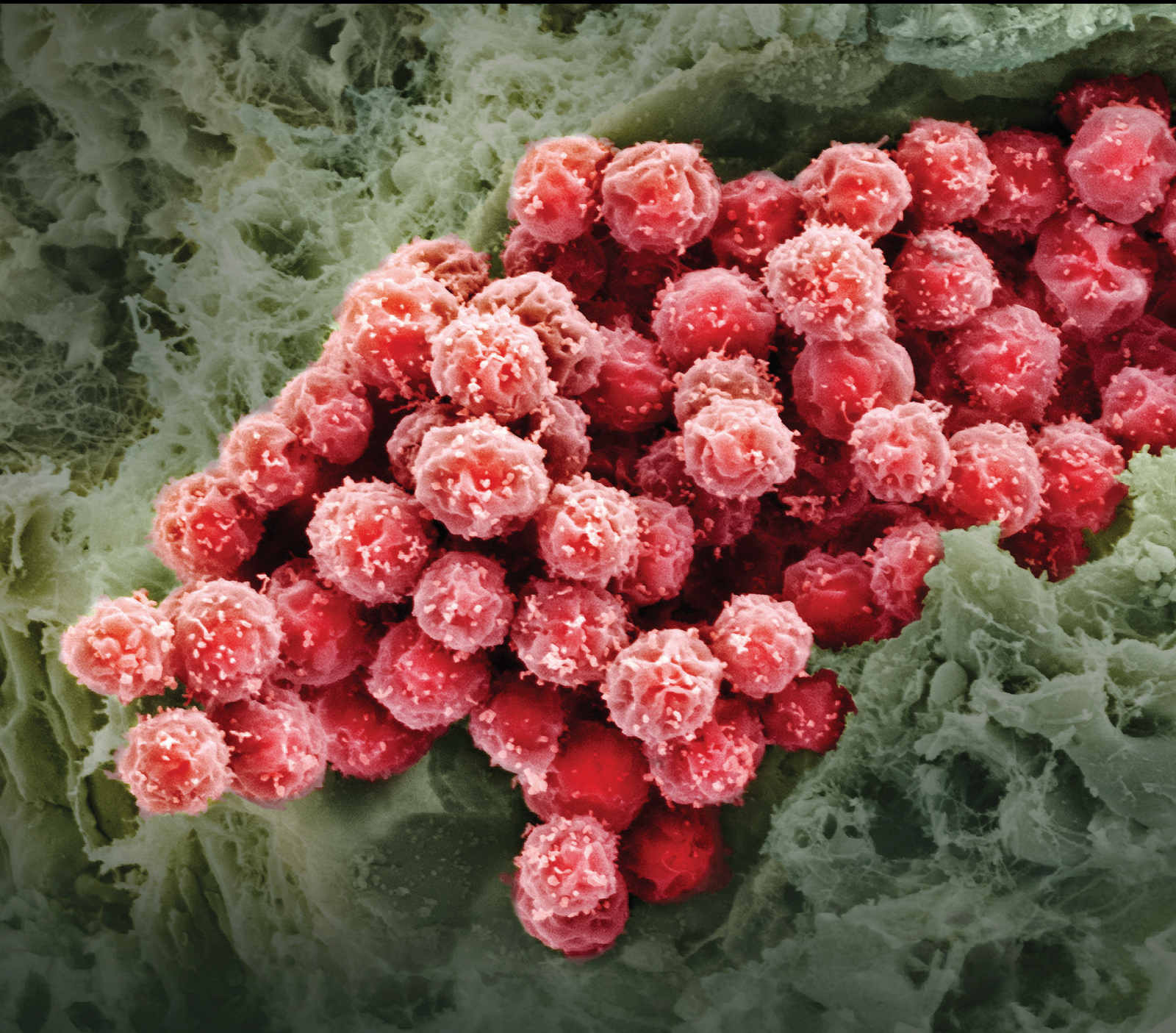


Molecular Imaging of Stems Cells: In Vivo Tracking and Clinical Translation

Guest Editors: Stefania Rizzo, Francesco Petrella, Letterio S. Politi, and Ping Wang





Molecular Imaging of Stems Cells: In Vivo Tracking and Clinical Translation

Molecular Imaging of Stems Cells: In Vivo Tracking and Clinical Translation

Guest Editors: Stefania Rizzo, Francesco Petrella,
Letterio S. Politi, and Ping Wang



Copyright © 2017 Hindawi Publishing Corporation. All rights reserved.

This is a special issue published in “Stem Cells International.” All articles are open access articles distributed under the Creative Commons Attribution License, which permits unrestricted use, distribution, and reproduction in any medium, provided the original work is properly cited.

Editorial Board

James Adjaye, Germany
Dominique Bonnet, UK
Marco Bregni, Italy
Silvia Brunelli, Italy
Bruce A. Bunnell, USA
Kevin D. Bunting, USA
Benedetta Bussolati, Italy
Yilin Cao, China
Kyunghee Choi, USA
Gerald A. Colvin, USA
Varda Deutsch, Israel
Leonard M. Eisenberg, USA
Marina Emborg, USA
Franca Fagioli, Italy
Tong-Chuan He, USA
Boon C. Heng, Hong Kong
Toru Hosoda, Japan
Xiao J. Huang, China
Thomas Ichim, USA
J. Itskovitz-Eldor, Israel
Pavla Jendelova, Czech Republic
Arne Jensen, Germany

Atsuhiko Kawamoto, Japan
Armand Keating, Canada
Mark D. Kirk, USA
Valerie Kouskoff, UK
Andrzej Lange, Poland
Laura Lasagni, Italy
Renke Li, Canada
Tao-Sheng Li, Japan
Susan Liao, Singapore
Shinn-Zong Lin, Taiwan
Gary E. Lyons, USA
Yupo Ma, USA
Athanasios Mantalaris, UK
Eva Mezey, USA
Claudia Montero-Menei, France
Karim Nayernia, UK
Sue O'Shea, USA
Bruno Péault, USA
Stefan Przyborski, UK
Peter J. Quesenberry, USA
Pranela Rameshwar, USA
Bernard A.J Roelen, Netherlands

Peter Rubin, USA
Hannele T. Ruohola-Baker, USA
Donald S. Sakaguchi, USA
Ghasem Hosseini Salekdeh, Iran
Heinrich Sauer, Germany
Coralie Sengenes, France
Ashok K. Shetty, USA
Shimon Slavin, Israel
Shay Soker, USA
Giorgio Stassi, Italy
Ann Steele, USA
Alexander Storch, Germany
Corrado Tarella, Italy
Yang D. Teng, USA
Antoine Toubert, France
Hung-Fat Tse, Hong Kong
Marc L. Turner, UK
Chia-Lin Wei, Singapore
Dominik Wolf, Austria
Qingzhong Xiao, UK
Zhaohui Ye, USA
Wen-Jie Zhang, China

Contents

Molecular Imaging of Stems Cells: In Vivo Tracking and Clinical Translation

Stefania Rizzo, Francesco Petrella, Letterio S. Politi, and Ping Wang
Volume 2017, Article ID 1783841, 2 pages

Molecular Imaging of Stem Cell Transplantation for Liver Diseases: Monitoring, Clinical Translation, and Theranostics

Ping Wang, Francesco Petrella, Luca Nicosia, Massimo Bellomi, and Stefania Rizzo
Volume 2016, Article ID 4058656, 8 pages

Towards Therapeutic Delivery of Extracellular Vesicles: Strategies for *In Vivo* Tracking and Biodistribution Analysis

Giuliana Di Rocco, Silvia Baldari, and Gabriele Toietta
Volume 2016, Article ID 5029619, 12 pages

Label-Free Imaging of Umbilical Cord Tissue Morphology and Explant-Derived Cells

Raf Donders, Kathleen Sanen, Rik Paesen, Eli Slenders, Wilfried Gyselaers, Piet Stinissen, Marcel Ameloot, and Niels Hellings
Volume 2016, Article ID 5457132, 15 pages

MRI-Based Assessment of Intralesional Delivery of Bone Marrow-Derived Mesenchymal Stem Cells in a Model of Equine Tendonitis

Alexandra Scharf, Shannon P. Holmes, Merrilee Thoresen, Jennifer Mumaw, Alaina Stumpf, and John Peroni
Volume 2016, Article ID 8610964, 13 pages

Dynamic Tracking Human Mesenchymal Stem Cells Tropism following Smoke Inhalation Injury in NOD/SCID Mice

MeiJuan Song, Qi Lv, XiuWei Zhang, Juan Cao, ShuLi Sun, PeiXin Xiao, ShiKe Hou, Hui Ding, ZiQuan Liu, WenLong Dong, JinQiang Wang, Xue Wang, ZhiGuang Sun, Man Tian, and HaoJun Fan
Volume 2016, Article ID 1691856, 13 pages

Dynamic Tracking of Injected Mesenchymal Stem Cells after Myocardial Infarction in Rats: A Serial 7T MRI Study

Xiuyu Chen, Minjie Lu, Ning Ma, Gang Yin, Chen Cui, and Shihua Zhao
Volume 2016, Article ID 4656539, 10 pages

Transplanted Endothelial Progenitor Cells Improve Ischemia Muscle Regeneration in Mice by Diffusion Tensor MR Imaging

Xin-Gui Peng, Yingying Bai, Judy R. James, Darya P. Shlapak, and Shenghong Ju
Volume 2016, Article ID 3641401, 10 pages

***In Vivo* Tracking of Systemically Administered Allogeneic Bone Marrow Mesenchymal Stem Cells in Normal Rats through Bioluminescence Imaging**

Juan Cao, Shike Hou, Hui Ding, Ziquan Liu, Meijuan Song, Xiaojing Qin, Xue Wang, Mengyang Yu, Zhiguang Sun, Jinyang Liu, Shuli Sun, Peixin Xiao, Qi Lv, and Haojun Fan
Volume 2016, Article ID 3970942, 11 pages

Editorial

Molecular Imaging of Stems Cells: In Vivo Tracking and Clinical Translation

Stefania Rizzo,¹ Francesco Petrella,² Letterio S. Politi,^{3,4} and Ping Wang⁵

¹*Department of Radiology, European Institute of Oncology, Milan, Italy*

²*Department of Thoracic Surgery, European Institute of Oncology, Milan, Italy*

³*Department of Hematology/Oncology and Department of Radiology, Boston Children's Hospital, Boston, MA, USA*

⁴*Department of Radiology, University of Massachusetts Medical School and University of Massachusetts Memorial Medical Center, Worcester, MA, USA*

⁵*Molecular Imaging Laboratory, MGH/MIT/HMS Athinoula A. Martinos Center for Biomedical Imaging, Department of Radiology, Massachusetts General Hospital, Harvard Medical School, Boston, MA, USA*

Correspondence should be addressed to Stefania Rizzo; stefania.rizzo@ieo.it

Received 12 December 2016; Accepted 13 December 2016; Published 2 January 2017

Copyright © 2017 Stefania Rizzo et al. This is an open access article distributed under the Creative Commons Attribution License, which permits unrestricted use, distribution, and reproduction in any medium, provided the original work is properly cited.

Once upon a time, there were diseases for which patients had to die without cure and to be treated only to relieve or retard symptoms, such as diabetes, myocardial infarction, postsurgical bronchopleural fistulas, Parkinson's disease, and Alzheimer's disease.

Then stem cells started to be intensively studied for infusion or transplantation into tissues for purposes of repair, revascularization, and other therapeutic actions [1, 2]. After systemic or local administration, stem cells may proliferate, migrate, and repopulate pathologic sites, bringing remarkable therapeutic effect. Indeed, several studies have demonstrated the capacity of adult stem cell transplantation to restore/induce bone repair and revascularization of the ischemic cardiac tissue *in vivo*, while investigations are underway on tissue neuroregeneration in disorders such as Parkinson's and Alzheimer's disease and diseases of the lung and airways [3–5], liver [6], diabetes, and other organs.

A risk that has been identified in early stem cell studies lays in the ability of undifferentiated human embryonic stem cells to produce tumors *in vivo*, such as teratomas and teratocarcinomas [7]. As a result, stem cell misbehavior after delivery has been regarded as a major obstacle for translation of stem cell-based therapies into clinical reality.

Furthermore, it has been demonstrated that, when injected systemically, mesenchymal stromal cells (MSCs) accumulate in the lungs and capillary beds of other tissues, thus decreasing the number of MSCs migrating to target

areas for treatment [8]. Molecular imaging can offer a better understanding of cell fate after transplantation, thus providing successful implementation of cell therapies.

For instance, J. Cao et al. demonstrated allogenic bone marrow MSCs home to the dorsal skin, apart from the lungs and kidneys, after tail-vein-injection, could not be detected 14 days later. M. Song et al. were able to track systemically transplanted human bone marrow-derived mesenchymal stromal cells mice with smoke inhalation injury through BLI, eventually demonstrating that MSC xenografts repaired smoke inhalation-induced lung injury in mice.

Magnetic Resonance Imaging (MRI), Positron Emission Tomography (PET), Single-Photon Emission Computed Tomography (SPECT), Fluorescence Imaging (FLI), and Bioluminescence Imaging (BLI) are multiple examples of imaging systems that can visualize signals generated from labelled cells, thus providing accurate and detailed information about cell fate, migration, and engraftment following transplantation.

In the specific setting of MRI, X.-G. Peng et al. demonstrated that Diffusion Tensor Imaging could be a useful tool for noninvasive evaluation of muscle tissue damage and repair in animal models and patient with ischemic diseases, while X. Chen et al. demonstrated that iron particles are not a reliable marker for *in vivo* tracking the fate of MSCs engraftment in case of myocardial infarction.

Cell tracking can be performed either by molecular probes entering the target cell by active/passive transport or by overexpression of reporter genes integrating into cellular genome [9].

As demonstrated by R. Donders et al., two-photon confocal laser scanning microscopy (TPM) and second harmonic generation (SHG) are alternative techniques that may enable the detection of cells and extracellular structures, based on intrinsic properties of the specific tissue and intracellular molecules under optical irradiation.

Molecular imaging may also play a role in defining the proper cell type, delivery method, cell dose, therapeutic window, and evaluation of toxicity to patients, by identification of early transformation of cell grafts into tumors, as well as imaging the proliferation and/or expression of tumor-specific markers, which cannot be detected by traditional imaging techniques.

Moreover, in vivo imaging of stem cells may disclose how cells survive and proliferate within the target tissue, as well as their differentiation and maturation, thus providing precious data to generate a dose-response curve to identify the optimal dose and dosing frequency of cell therapies [9].

For instance, in the specific setting of stem cell transplantation for liver diseases, there have been two main clinical applications of molecular imaging [10, 11]. In this special issue of this journal, the multiple possibilities of monitoring stem cell transplantation for liver diseases have been extensively exposed in a review article by P. Wang et al.

However, the serial visualization and tracking of transplanted stem cells, including their possible migration and/or retention in other sites, are still issues to be resolved before preclinical studies can be turned into clinical studies. For example, ultrasound-guided intralesional injection of MSCs is held as the benchmark for cell delivery in tendonitis because many reports have determined that local injury retains cells within a small radius of the site of injection. However, in this issue, A. Scharf et al. have demonstrated that there is a greater delocalization than expected, and relatively few cells are retained within collagenous tendon compared to surrounding fascia, underlying the need of further in vivo studies.

Similar issues are still unsolved about the use of extracellular vesicles (EVs), considered as paracrine mediators of the beneficial effects on tissue remodeling associated with cell therapy. The administration of MSCs-derived EVs may have the potential to open new and safer therapeutic avenues, alternative to cell-based approaches, for degenerative diseases, but studies about the biodistribution upon systemic delivery of EVs indicate in liver, spleen, and lungs preferential target organs. With this regard, G. Di Rocco et al. reviewed the existing strategies for in vivo tracking and targeting of EVs isolated from different cellular sources and the studies elucidating the biodistribution of exogenously administered EVs.

Although many examples of in vitro and in vivo studies have already been published, clinical applications of molecular imaging in stem cells therapies are still limited.

At the moment we are writing in the US more than 3,900 clinical trials with “stem cell transplantation” registered

(<https://www.clinicaltrials.gov>), 1,384 of which are open and are recruiting. Therefore, it is our opinion that in the forthcoming years the application of cell tracking studies in clinical research will dramatically increase and that the information gathered through cellular and molecular imaging techniques will play an important role in clinical trials design, in monitoring the cell delivery, in defining the fate of the transplantation, in interpreting the clinical data, and in understanding the reasons of success or failure of the trials.

After further evaluation of different possibilities of tracking stem cells, we do expect that many clinical questions, raised from applications of stem cells-based therapies, will find an answer in molecular imaging. Therefore, we do believe that stem cell-based therapies and molecular imaging will live together happily ever after.

Stefania Rizzo
Francesco Petrella
Letterio S. Politi
Ping Wang

References

- [1] R. McKay, “Stem cells: hype and hope,” *Nature*, vol. 406, no. 6794, pp. 361–364, 2000.
- [2] R. J. Deans and A. B. Moseley, “Mesenchymal stem cells: biology and potential clinical uses,” *Experimental Hematology*, vol. 28, no. 8, pp. 875–884, 2000.
- [3] F. Petrella, S. Rizzo, A. Borri, M. Casiraghi, and L. Spaggiari, “Current perspectives in mesenchymal stromal cell therapies for airway tissue defects,” *Stem Cells International*, vol. 2015, Article ID 746392, 7 pages, 2015.
- [4] F. Petrella, F. Toffalorio, S. Brizzola et al., “Stem cell transplantation effectively occludes bronchopleural fistula in an animal model,” *The Annals of Thoracic Surgery*, vol. 97, no. 2, pp. 480–483, 2014.
- [5] F. Petrella, L. Spaggiari, F. Acocella et al., “Airway fistula closure after stem-cell infusion,” *The New England Journal of Medicine*, vol. 372, no. 1, pp. 96–97, 2015.
- [6] P. Wang and A. Moore, “Theranostic magnetic resonance imaging of type 1 diabetes and pancreatic islet transplantation,” *Quantitative Imaging in Medicine and Surgery*, vol. 2, no. 3, pp. 151–162, 2012.
- [7] B. Blum and N. Benvenisty, “The tumorigenicity of diploid and aneuploid human pluripotent stem cells,” *Cell Cycle*, vol. 8, no. 23, pp. 3822–3830, 2009.
- [8] J. D. Glenn and K. A. Whartenby, “Mesenchymal stem cells: emerging mechanisms of immunomodulation and therapy,” *World Journal of Stem Cells*, vol. 6, no. 5, pp. 526–539, 2014.
- [9] P. K. Nguyen, J. Riegler, and J. C. Wu, “Stem cell imaging: from bench to bedside,” *Cell Stem Cell*, vol. 14, no. 4, pp. 431–444, 2014.
- [10] A. Gholamrezanezhad, S. Mirpour, M. Bagheri et al., “In vivo tracking of ¹¹¹In-oxine labeled mesenchymal stem cells following infusion in patients with advanced cirrhosis,” *Nuclear Medicine and Biology*, vol. 38, no. 7, pp. 961–967, 2011.
- [11] F. Defresne, T. Tondreau, X. Stéphenne et al., “Biodistribution of adult derived human liver stem cells following intraportal infusion in a 17-year-old patient with glycogenosis type 1A,” *Nuclear Medicine and Biology*, vol. 41, no. 4, pp. 371–375, 2014.

Review Article

Molecular Imaging of Stem Cell Transplantation for Liver Diseases: Monitoring, Clinical Translation, and Theranostics

Ping Wang,¹ Francesco Petrella,² Luca Nicosia,³ Massimo Bellomi,^{4,5} and Stefania Rizzo⁴

¹*Molecular Imaging Laboratory, MGH/MIT/HMS Athinoula A. Martinos Center for Biomedical Imaging, Department of Radiology, Massachusetts General Hospital, Harvard Medical School, Boston, MA 02129, USA*

²*Department of Thoracic Surgery, European Institute of Oncology, Via Ripamonti 435, 20141 Milan, Italy*

³*Postgraduation School in Radiodiagnostics, Università degli Studi di Milano, Via Festa del Perdono 7, 20122 Milan, Italy*

⁴*Department of Radiology, European Institute of Oncology, Via Ripamonti 435, 20141 Milan, Italy*

⁵*Department of Oncology, University of Milan, Via Festa del Perdono 7, 20142 Milan, Italy*

Correspondence should be addressed to Ping Wang; pwang3@mgh.harvard.edu and Stefania Rizzo; stefania.rizzo@ieo.it

Received 26 September 2016; Accepted 1 November 2016

Academic Editor: Gary E. Lyons

Copyright © 2016 Ping Wang et al. This is an open access article distributed under the Creative Commons Attribution License, which permits unrestricted use, distribution, and reproduction in any medium, provided the original work is properly cited.

Stem cell transplantation has been investigated to rescue experimental liver failure and is promising to offer an alternative therapy to liver transplantation for liver diseases treatment. Several clinical studies in this field have been carried out, but the therapeutic benefit of this treatment is still controversial. A major obstacle to developing stem cell therapies in clinic is being able to visualize the cells in vivo. Imaging modalities allow optimization of delivery, detecting cell survival and functionality by in vivo monitoring these transplanted graft cells. Moreover, theranostic imaging is a brand new field that utilizes nanometer-scale materials to glean diagnostic insight for simultaneous treatment, which is very promising to improve stem cell-based therapy for treatment of liver diseases. The aim of this review was to summarize the various imaging tools that have been explored with advanced molecular imaging probes. We also outline some recent progress of preclinical and clinical studies of liver stem cells transplantation. Finally, we discuss theranostic imaging for stem cells transplantation for liver dysfunction and future opportunities afforded by theranostic imaging.

1. Introduction

Acute liver failure and cirrhosis result from a variety of acute or chronic hepatic injuries [1, 2]. Up till now, liver transplantation has been considered as the primary treatment for acute liver failure and cirrhosis and various end-stage liver diseases. However, this procedure is hindered by the lack of donor organs, technical difficulties, complications associated with immune rejection, the requirement for lifelong immunosuppression, and financial considerations [3–5]. Therefore, to develop novel treatments that can either be effective curative and/or affect the underlying pathophysiology of the liver disease is urgently needed.

Stem cell transplantation has been suggested as an effective alternate approach for liver dysfunction [6–8]. For maximal efficacy, these therapies require transplanted cell delivery to targeted tissues followed by successful cell engraftment. So

far, numbers of clinic trials of stem cells transplantation for liver dysfunction have been carried out. By September 2016, more than 200 clinical trials had been registered when ClinicalTrials.gov was searched for the terms “stem cells AND liver diseases”. Among these clinical studies, some have indicated to be well tolerated and safe and confer beneficial effects in patients with liver failure, by enhancing liver function and reducing ascites and overall mortality without any major side effects [9–13]. However, the benefits of this emerging therapy for liver dysfunction in recent finished clinical trials are still conflicting. Some studies demonstrated there was no significant therapeutic effect to liver dysfunction [14]. Other concerns and critical issues remain unanswered regarding the long-term safety [9, 10, 12, 15–22]. Therefore, several meta-analyses have concluded that controversies remain in this rapidly developing field [23–26].

Meanwhile, several critical issues in clinical protocols require further investigation, such as the optimal type of cell types, the optimal therapeutic timing, the most effective stem cells amount, the best route of administration, and the primary endpoints. One thing is clear that there is an unmet clinical need to monitor the transplanted stem cells in vivo. Hence, in vivo visualization of transplanted stem cells with a robust, quantitative imaging method is essential for the monitoring of cell implantation, homing, and differentiation. The purpose of this current review is to summarize the latest developments of the various imaging modalities dedicated to monitor stem transplantation for liver dysfunctions; preclinical and clinic studies are emphasized; in addition, theranostic imaging and their future applications are also highlighted.

2. Imaging Methods to Monitor Transplanted Stem Cells in Animal Models

Noninvasive tracking of stem cells could facilitate its clinical translation. So far all major imaging modalities have been introduced to monitor transplanted stem cells for liver diseases. Numbers of animal studies have demonstrated that imaging modalities are essential for developing efficacious cell therapies for liver damage animal models.

2.1. Optical Imaging. Optical imaging, mainly based on retroviral vectors or enzymes to express fluorescent proteins, includes fluorescence imaging and bioluminescence imaging (BLI). Both these imaging methods have been tested for in vivo monitoring transplanted stem cells in liver.

Yukawa et al. investigated whether quantum dots (QDs) labeling using octa-arginine peptide (R8) for adipose tissue-derived stem cells (ASCs) could be applied for in vivo fluorescence imaging in mice with acute liver failure. The results demonstrated that heparin was effective in increasing the accumulation of transplanted ASCs in the liver using this imaging technology [27]. In another study, Akhan et al. conjugated a novel polymer based water-dispersible nanoparticles (CPN) with improved photostability, high fluorescent quantum yield, and noncytotoxicity compared to conventional dyes and quantum dots. The results showed that the labeled mesenchymal stem cells (MSCs) migrated to the liver and retained their labels in an in vivo liver regeneration model. These studies demonstrated that the utilization of fluorescence labeling could be a promising tool for the tracking of stem cells transplanted in liver to understand differentiation and homing mechanisms [28]. Wang et al. investigated upconversion nanoparticles- (UCNPs-) labeled mouse MSCs intravenous transplanted into mice and imaged using an in vivo upconversion luminescence (UCL) imaging system, observing the translocation of MSCs from lung where they initially accumulated, to liver [29]. Li et al. compared three-delivery routes for the MSCs transplantation to liver, including inferior vena cava (IVC), the superior mesenteric vein (SMV), and intrahepatic (IH) injection using in vivo BLI. Results showed that MSCs were firstly trapped inside the lungs, and no detectable homing to the liver and other organs was observed after IVC infusion; after SMV infusion,

MSCs were dispersedly distributed and stayed as long as 7-day posttransplantation in the liver. By IH injection, MSCs distribution was only localized in the injection region of the liver [30]. In another study reported by the same group, Liu et al. evaluated survival of transplanted human MSCs in the mice liver after intrahepatic transplantation and the role of intrahepatic natural killer (NK) cells by in vivo BLI. A gradual decline in bioluminescent signals from transplanted MSCs in liver was observed. Interestingly, compared to the control group, the survival time and retention of intrahepatic MSCs decreased more rapidly in the NK-activated group, which indicated that activated NK cells potentially accelerated the rejection of transplanted MSCs [31].

2.2. Nuclear Imaging. Wu et al. investigated the biodistribution of human placental deciduas basalis derived mesenchymal stem cells (PDB-MSCs) in nude mice after intravenous injection by carbon radioisotope labeling thymidine ((14) C-TdR), which was able to incorporate into new DNA strands during cell replication. Labeled PDB-MSCs grafts were found mainly in the lung, liver, spleen, stomach, and left femur of the recipient animals at the whole observation period. This work demonstrated that (14) C-TdR labeling did not alter the biological characteristics of human placental MSCs and that this labeling method had potential to be used to quantify the transplanted cells in preclinical studies [32].

2.3. Magnetic Resonance Imaging (MRI). Magnetic resonance imaging provides high-resolution (ranging from 50 μm in animals up to 300 μm in whole body clinical scanners) images capable of tracking stem cells in vivo without invasiveness and without the use of ionizing radiation. Stem cells need to be prelabeled with contrast probes for cell tracking studies by MRI. The probes for MRI noninvasively identification and tracking of transplanted cells include negative contrast agents, as superparamagnetic iron-oxide (SPIO) and ultra-small superparamagnetic iron-oxide (USPIO) particles, and positive contrast agents, such as gadolinium. They both have been tested in small animal models for stem cells transplantation studies.

An emerging approach to visualizing stem cells by MR is to label the stem cells with perfluorocarbon (PFC) nanoemulsions, which can be detected with ^{19}F MRI.

2.3.1. SPIO. Bos et al. evaluated in vivo tracking of intravascularly injected SPIO labeled MSCs using a conventional 1.5 T MR imaging system. After labeled MSC injection, damaged liver had diffuse granular appearance. Cells were detected for up to 12 days in liver. They concluded that MRI could in vivo monitor intravascularly administered SPIO labeled MSCs in liver [33]. Arbab et al. developed a method of delivering SPIO labeled MSCs to a targeted area in an animal model by applying an external magnet. SPIO labeled MSCs were injected intravenously to animals, and an external magnet was placed over the liver area of the animals. MRI signal intensity (SI) changes in the liver were monitored at different time points using MRI. Interestingly, SI decrease in the liver after injection of MSCs was greater in rats with external

magnets and returned gradually to that of control rat livers at approximately day 29. The results proved that the external magnets retained the labeled MSCs in the region of interest [34]. Cai et al. evaluated *in vivo* MRI for tracking the SPIO labeled MSCs transplanted into rat liver through hepatic arterial infusion. The labeled stem cells in liver could be detected and monitored *in vivo* with a 1.5 T clinical MR scanner for up to 7 days after transplantation [35]. Ju et al. tracked intrasplenically transplanted MSCs labeled with SPIO by using MRI *in vivo* in a liver damaged rat model. These studies demonstrated that MSCs could be effectively labeled with approximately 100% efficiency. Migration of transplanted labeled cells to the liver was successfully documented with *in vivo* MRI [36, 37]. Choi et al. labeled human MSCs with SPIO and green fluorescence protein (GFP). Labeled MSCs were transplanted into the portal veins of immunosuppressed, hepatic-damaged rat models. Serial MR imaging showed signal loss in the liver of transplanted cells in the early period of transplantation [38]. Zhong et al. assessed SPIO labeled MSCs that were transplanted via the portal vein to rats with hepatic fibrosis using MRI. T2*-weighted MR imaging indicated lower signal in liver [39]. Kim et al. used a fluorescent magnetic nanoparticle (MNP), which had both magnetic and optical features, containing a ferritin core and a silica shell, and the inner portion of silica shell filled fluorescent materials for stem cell tracking studies. Intrasplenically transplanted MSCs labeled with MNP in liver cirrhosis rat model were monitored with 3T MR scanner. The results showed that the liver-to-muscle contrast-to-noise ratios at 3 and 5 h after cell transplantation was significantly lower than that of preinjection group [40].

2.3.2. Gadolinium Based Probes. Shuai et al. transfected human umbilical cord derived MSCs with gadolinium-diethylenetriaminepentaacetic acid (Gd-DTPA) for *in vitro* MRI. The result showed that minimum 5×10^4 Gd-DTPA-labeled stem cells could be detected with MRI *in vitro*. The trace duration time was about 12 days without compromising either cell viability or cell differentiability [41]. The same group also determined double labeling of MSCs with Gd-DTPA and fluorescent dye PKH26. Gd-DTPA and PKH26 were used to label the stem cells. MRI and fluorescence microscopy were used to detect the double-labeled MSCs. Their *in vitro* studies demonstrated that the proliferation and differentiation abilities of MSCs were not affected by double labeling using Gd-DTPA and PKH26 [42]. Furthermore, Pan et al. assessed tracking Gd-DTPA and PKH26-labeled human umbilical cord MSCs using MRI *in vivo*. The T1 values and signal intensity on T1-weighted imaging of labeled cells were significantly higher than the control. The signal intensity on T1-weighted imaging of labeled cells was retained over 14 days *in vivo* [43]. The results demonstrated that this labeling method was reliable and efficient; the *in vivo* studies of transplanted cells in liver using this labeling method need to be further investigated.

2.3.3. Perfluorocarbon Based MRI. Another technique under evaluation for imaging injected stem cells *in vitro* and *in*

vivo is based on perfluorocarbon (PFC) formulations, whose advantage is the high specificity due to the virtual absence of fluor from the body. The fluorine signal can be accurately quantified from the MR images [44].

An emerging approach to imaging stem cells by MRI is to label the stem cells with perfluorocarbon nanoemulsions, which can be detected with ¹⁹F MRI [45–47]. The ¹⁹F nucleus is particularly suitable for labeling as its relative MR sensitivity is only 17% less than that of ¹H. Since the level of background ¹⁹F signal in host tissue is virtually absent [45], overlaying the ¹⁹F image on a conventional anatomical image allows for unambiguous, quantitative tracking of labeled cells *in vivo*.

A number of promising findings have been reported for the use of ¹⁹F labeling, including (1) intracellular labeling; (2) the lack of cellular toxicity; (3) the stability of cell labeling up to 21 days postlabeling; (4) positive signal with no background observed with ¹⁹F MRI; (5) biodistribution visualized by overlaying a ¹⁹F image of labeled cells on a ¹H anatomical image; (6) determination of the local concentration of labeled cells by quantitative ¹⁹F MRI [48].

2.4. Emerging Imaging Modality: Magnetic Particle Imaging (MPI). MPI is noninvasive and offers near-ideal image contrast, depth penetration, high sensitivity, and superb quantitative for single-cell tracking. Unlike MRI that applies magnetic resonance principles, MPI directly detects the iron-oxide nanoparticle-tagged cells using magnetic fields. These properties make MPI both ultrasensitive and linearly quantitative and very promising for monitoring transplanted cells *in vivo*. Conolly group from UC Berkeley firstly utilized MPI to monitor transplanted stem cells *in vivo* in animal model. Their first MPI cell tracking study demonstrated 200-cell detection limit *in vitro* and *in vivo* monitoring of graft clearance over 87 days in a rat model [49]. In a more recent study, this group imaged the intravenously transplanted MSCs using MPI. The results showed that labeled MSCs immediately entrapped in lung tissue posttransplantation and then relocated to the liver within one day. Longitudinal MPI-CT imaging demonstrated a clearance half-life of MSC iron-oxide labels in the liver at 4.6 days [50]. These first *in vivo* MPI results indicate that MPI offers strong utility for quantitating the transplanted stem cells labeled using SPIO.

3. Preclinic Imaging of Large Animal Models and Clinical Applications

Although stem cell transplantation based therapies have been clinically applied to patients, the fate of graft cells remains unknown. Small animal studies have demonstrated the feasibility and important role of *in vivo* imaging technologies for *in vivo* monitoring of transplanted stem cells. The next step is to conduct preclinic studies using large animals that are necessary for translation of these cutting edge imaging technologies to clinic.

3.1. Preclinic Imaging of Transplanted Stem Cells in Liver with Large Animal Models. Ito-Fujishiro et al. evaluated track

implanted peripheral blood mononuclear cells labeled with SPIO on days 0 and 7 after intravenous injection into a cynomolgus monkey using a 3T MRI scanner. Labeled cells were visualized in the liver on MR images T2-weighted sequences [51]. Shi et al. investigated tracking of SPIO labeled MSCs after intraportal transplantation to swine models of acute liver injury. Results showed that signal intensity loss in the livers of swine models by SPIO labeling on the T2*WI sequence persisted until 2 weeks after transplantation [52]. Spriet et al. compared the cell distribution and quantification shortly after intraportal vein, systemic intravenous and splenic injections of technetium-99m- (99mTc-) hexamethyl-propylene amine oxime (HMPAO) labeled MSCs in healthy beagle dogs. Scintigraphic images were obtained using gamma camera after cell transplantation to target the liver, which showed that, after the portal injection, diffuse homogeneous high uptake was observed through the liver; the systemic intravenous injection resulted in cells trapped in the lungs, whereas splenic injection led to MSCs mild splenic retention and homogeneous diffuse hepatic uptake [53].

3.2. The First Clinical Applications of Molecular Imaging on Stem Cells Transplantation for Liver Diseases. Gholam-rezanezhad et al. investigated the biodistribution of autologous ¹¹¹In-oxine labeled MSCs, after peripheral infusion in four cirrhotic patients was investigated using SPECT imaging. After intravenous infusion, the radioactivity was first observed to accumulate in the lungs of recipients. Then the radioactivity gradually increased in the liver and spleen in these four patients. Radiolabeled MSCs relocated in liver and spleen: radioactivity decreased from 33.5% to 2% in lung and increased from 2% to 42% in spleen. This first clinic imaging study demonstrated that cell labeling with ¹¹¹In-oxine was a suitable tool for tracking peripheral vein infused MSC distribution [54]. In a more recent case report study, Defresne et al. assessed biodistribution of ¹¹¹In-Indium DTPA labeled adult derived human liver stem cells (ADLHSC) from healthy donor using SPECT imaging after infusion through the portal vein in a patient with glycogenosis type 1A. Following infusion through the portal vein, SPECT imaging observed ADLHSC spread strictly within the targeted organ of liver until 5 days [55].

4. Theranostic Imaging of Stem Cells

The term “theranostics” refers to a rapidly developing approach that combines diagnostic imaging and molecular therapy [56]. By packaging the two modalities of diagnostic imaging and molecular therapy together, the application of theranostic imaging is promising to overcome undesirable selective biodistribution differences between diagnostic imaging probes and therapeutic agents [57–60]. To achieve higher sensitivity and increase molecular specificity, the novel two-in-one theranostic agents for various imaging tools have been developed. Not only can the novel imaging probes be functional as imaging tools, but they can also be useful as a carrier for controlled releasing of therapeutic moieties [61].

4.1. Improving Liver Function by Delivering Therapeutic Plasmid DNA. Pang et al. utilized a complex of SPIO nanoparticle coated with polyethylene glycol-grafted polyethylenimine (PEG-g-PEI-SPION) as an MRI probe that can track of rat bone MSCs and also act as a carrier for the plasmid DNA. The complex labeled MSCs were modified by a plasmid encoding human hepatocyte growth factor (HGF) attached in the MRI visible vector complex and transplanted into fibrotic rat livers. The results proved that these transplanted grafts effectively restored albumin production and significantly suppressed transaminase activities in the liver damaged animal models. Meanwhile, the transplanted MSCs displayed a sensitive signal on T2/T2*-weighted MR images, which enabled in vivo tracking of the cells for up to 14 days after transplantation [62].

4.2. Promoting Transplanted Cell Survival by Combined Cytokines Delivery. Kempen et al. designed a theranostic mesoporous silica nanoparticle that could offer ultrasound and MRI signal to guide transplanted cells and also served as a drug release reservoir of insulin-like growth factor (IGF) that could promote MSCs survival. The results showed that the presence of IGF increased cell survival up to 40% versus unlabeled cells in vitro [63]. Pulavendran et al. compared cirrhotic mice received either hematopoietic stem cells (HSC) or MSC with or without HGF incorporated chitosan nanoparticles (HGF-CNP). Serum levels of selected liver protein and enzymes were significantly increased in the combination of MSC and HGF-CNP (MSC+HGF-CNP) treated group. These findings indicated that HGF-CNP enhanced the differentiation of stem cells into hepatocytes. The results demonstrated MSCs transplantation in combination with HGF-CNP could be a promising treatment for liver cirrhosis [64].

4.3. In Vivo RNA Interference: siRNAs and microRNAs Delivery Carriers. RNA interference is a naturally occurring endogenous regulatory process where short double-stranded RNA including small interference RNA (siRNA) and microRNAs could induce sequence-specific posttranscriptional gene silencing. In vivo RNA interference therapy represents a promising therapeutic strategy, but the barriers for delivery siRNAs or microRNAs hamper this therapeutic method to reach their intended targets cells or tissues and to exert their gene silencing activity [65]. Theranostic probes labeled on the transplanted stem cells actually could serve as siRNA or microRNA carriers. Zhao et al. synthesized poly-sodium4-styrenesulfonate (PSS) and poly-allylamine hydrochloride (PAH) coated AuNR-based nanoparticles, which could deliver siRNA against LSD1 to induce the hepatocyte lineage differentiation of human MSCs in vitro [66]. These methods need to be further tested in vivo before it could eventually translate to clinical applications. MicroRNAs are endogenous small noncoding RNAs that regulate key processes of cells. Studies have been reported on the posttranscriptional regulation of hepatic differentiation and regenerative capacities in MSCs by microRNAs [67, 68]. Gomes et al. reported the use of biodegradable nanoparticles

containing perfluoro-1,5-crown ether (PFCE), a fluorine-based compound (NPI70-PFCE) that could track cells in vivo by MRI and efficiently release miRNA. NPI70-PFCE conjugated with miRNA132 could accumulate within the cell's endolysosomal compartment increased 3-fold the survival of endothelial cells (ECs) transplanted in vivo [69]. This novel theranostic technology potentially could be transferred to stem cells transplantation for liver diseases in future.

4.4. Stem Cells Can Be Used as a Unique Carrier for Therapeutic Agents. Zhao et al. loaded adipose-derived MSCs with SPIO-coated gold nanoparticles (SPIO@AuNPs), which is a MR contrast probe that can be activated to generate heat when irradiated with near-infrared laser, and tested their effects against liver injury and hepatocellular carcinoma (HCC) in mice. The results showed that in vivo MR imaging confirmed the active homing of AD-MSCs to liver. Upon laser irradiation, the SPIO@AuNP-loaded AD-MSCs could thermally ablate surrounding HCC tumor cells.

This study demonstrated that AD-MSC could act as an efficient carrier for therapeutic agents to liver injuries or HCC. The results showed that SPIO@AuNP-loaded AD-MSCs proved a promising theranostic agent for liver injury and HCC [70].

4.5. Preventing Teratoma Formation in Target Organs. One reason for controversial application of stem cell treatment is the possibility associated with tumor formation in the recipient. For promoting therapeutic effect, stem cells may undergo substantial manipulation such as differentiation and in vitro expansion, and this can lead to possible genetic aberrations and carcinogenesis [71]. To address the intractable issues such as the teratoma formation encountered in human embryonic stem cell (hESC) for therapeutic in clinic, Chung et al. hypothesized that serial manganese-enhanced MRI would have theranostic effect to assess hESC survival, teratoma formation, and hESC-derived teratoma reduction through intracellular accumulation of Mn²⁺. The study demonstrated that systemic administration of MnCl₂ enabled simultaneous monitoring and elimination of hESC-derived teratoma cells by higher intracellular accumulation of Mn²⁺ [72].

5. Conclusions and Future Perspectives

Stem cell therapy as a part of regenerative medicine provides promising alternatives for the treatment of liver injuries and diseases. The increasing application of stem cells transplantation for liver diseases treatments created the demand for long-term and quantitative in vivo cell tracking methods [71]. In this review, promising in vivo imaging methods for stem cell monitoring after transplantation in liver are shown. It is unlikely that one technique will answer all questions, but use of a multimodal approach will be the most appropriate approach to addressing the number of issues posed in this exciting field. The selection of a set or a combination of appropriate imaging approaches will depend on the goal of the experiment, on the experimental subject under study, and also on the availability of multimodality imaging facilities

and probes. In addition, new imaging modalities including Cherenkov illumination imaging (CLI), photoacoustic imaging (PAI), and surface enhanced Raman imaging (SERI) are developing rapidly. The application of these new strategies will also play a helpful role in the advancement of the field of stem cell therapy [73]. Mostly, although still in its infant stage of development, theranostic imaging definitely represents a promising new direction for in vivo stem cell transplantation. The maturation of multifunctional theranostic imaging may indeed revolutionize stem cell transplantation approach for liver diseases and beyond [74].

Competing Interests

The authors declare that there are no competing interests regarding the publication of this paper.

References

- [1] D. Schuppan and N. H. Afdhal, "Liver cirrhosis," *The Lancet*, vol. 371, no. 9615, pp. 838–851, 2008.
- [2] S. Berardis, P. D. Sattwika, M. Najimi, and E. M. Sokal, "Use of mesenchymal stem cells to treat liver fibrosis: current situation and future prospects," *World Journal of Gastroenterology*, vol. 21, no. 3, pp. 742–758, 2015.
- [3] T. K. Kuo, S.-P. Hung, C.-H. Chuang et al., "Stem cell therapy for liver disease: parameters governing the success of using bone marrow mesenchymal stem cells," *Gastroenterology*, vol. 134, no. 7, pp. 2111–2121.e3, 2008.
- [4] Z. Zhang and F. S. Wang, "Stem cell therapies for liver failure and cirrhosis," *Journal of Hepatology*, vol. 59, no. 1, pp. 183–185, 2013.
- [5] M. R. Lucey, N. Terrault, L. Ojo et al., "Long-term management of the successful adult liver transplant: 2012 practice guideline by the American Association for the Study of Liver Diseases and the American Society of Transplantation," *Liver Transplantation*, vol. 19, no. 1, pp. 3–26, 2013.
- [6] P. P. Wang, J. H. Wang, Z. P. Yan et al., "Expression of hepatocyte-like phenotypes in bone marrow stromal cells after HGF induction," *Biochemical and Biophysical Research Communications*, vol. 320, no. 3, pp. 712–716, 2004.
- [7] J. M. Luk, P. P. Wang, C. K. Lee, J. H. Wang, and S. T. Fan, "Hepatic potential of bone marrow stromal cells: development of in vitro co-culture and intra-portal transplantation models," *Journal of Immunological Methods*, vol. 305, no. 1, pp. 39–47, 2005.
- [8] V. Volarevic, J. Nurkovic, N. Arsenijevic, and M. Stojkovic, "Concise review: therapeutic potential of mesenchymal stem cells for the treatment of acute liver failure and cirrhosis," *Stem Cells*, vol. 32, no. 11, pp. 2818–2823, 2014.
- [9] M.-E. M. Amer, S. Z. El-Sayed, W. A. El-Kheir et al., "Clinical and laboratory evaluation of patients with end-stage liver cell failure injected with bone marrow-derived hepatocyte-like cells," *European Journal of Gastroenterology and Hepatology*, vol. 23, no. 10, pp. 936–941, 2011.
- [10] H. Salama, A.-R. N. Zekri, A. A. Bahnassy et al., "Autologous CD34⁺ and CD133⁺ stem cells transplantation in patients with end stage liver disease," *World Journal of Gastroenterology*, vol. 16, no. 42, pp. 5297–5305, 2010.
- [11] S. Nikeghbalian, B. Pournasr, N. Aghdami et al., "Autologous transplantation of bone marrow-derived mononuclear

- and CD133⁺ cells in patients with decompensated cirrhosis," *Archives of Iranian Medicine*, vol. 14, no. 1, pp. 12–17, 2011.
- [12] M. El-Ansary, I. Abdel-Aziz, S. Mogawer et al., "Phase II trial: undifferentiated versus differentiated autologous mesenchymal stem cells transplantation in Egyptian patients with HCV induced liver cirrhosis," *Stem Cell Reviews and Reports*, vol. 8, no. 3, pp. 972–981, 2012.
 - [13] A.-R. N. Zekri, H. Salama, E. Medhat et al., "The impact of repeated autologous infusion of haematopoietic stem cells in patients with liver insufficiency," *Stem Cell Research and Therapy*, vol. 6, no. 1, article 118, 2015.
 - [14] M. Mohamadnejad, K. Alimoghaddam, M. Bagheri et al., "Randomized placebo-controlled trial of mesenchymal stem cell transplantation in decompensated cirrhosis," *Liver International*, vol. 33, no. 10, pp. 1490–1496, 2013.
 - [15] R. P. H. Meier, Y. D. Müller, P. Morel, C. Gonelle-Gispert, and L. H. Bühler, "Transplantation of mesenchymal stem cells for the treatment of liver diseases, is there enough evidence?" *Stem Cell Research*, vol. 11, no. 3, pp. 1348–1364, 2013.
 - [16] M. Mohamadnejad, K. Alimoghaddam, M. Mohyeddin-Bonab et al., "Phase 1 trial of autologous bone marrow mesenchymal stem cell transplantation in patients with decompensated liver cirrhosis," *Archives of Iranian Medicine*, vol. 10, no. 4, pp. 459–466, 2007.
 - [17] Z. Zhang, H. Lin, M. Shi et al., "Human umbilical cord mesenchymal stem cells improve liver function and ascites in decompensated liver cirrhosis patients," *Journal of Gastroenterology and Hepatology*, vol. 27, no. s2, pp. 112–120, 2012.
 - [18] L. Peng, D.-Y. Xie, B.-L. Lin et al., "Autologous bone marrow mesenchymal stem cell transplantation in liver failure patients caused by hepatitis B: short-term and long-term outcomes," *Hepatology*, vol. 54, no. 3, pp. 820–828, 2011.
 - [19] H. Salama, A.-R. N. Zekri, E. Medhat et al., "Peripheral vein infusion of autologous mesenchymal stem cells in Egyptian HCV-positive patients with end-stage liver disease," *Stem Cell Research and Therapy*, vol. 5, no. 3, article no. 70, 2014.
 - [20] L. Xu, Y. Gong, B. Wang et al., "Randomized trial of autologous bone marrow mesenchymal stem cells transplantation for hepatitis B virus cirrhosis: regulation of Treg/Th17 cells," *Journal of Gastroenterology and Hepatology*, vol. 29, no. 8, pp. 1620–1628, 2014.
 - [21] M. Shi, Z. Zhang, R. Xu et al., "Human mesenchymal stem cell transfusion is safe and improves liver function in acute-on-chronic liver failure patients," *Stem Cells Translational Medicine*, vol. 1, no. 10, pp. 725–731, 2012.
 - [22] M. Vosough, S. Moossavi, S. Mardpour et al., "Repeated intra-portal injection of mesenchymal stem cells in combination with pioglitazone in patients with compensated cirrhosis: a clinical report of two cases," *Archives of Iranian Medicine*, vol. 19, no. 2, pp. 131–136, 2016.
 - [23] X.-N. Pan, L.-Q. Zheng, and X.-H. Lai, "Bone marrow-derived mesenchymal stem cell therapy for decompensated liver cirrhosis: a meta-analysis," *World Journal of Gastroenterology*, vol. 20, no. 38, pp. 14051–14057, 2014.
 - [24] X.-R. Ma, Y.-L. Tang, M. Xuan, Z. Chang, X.-Y. Wang, and X.-H. Liang, "Transplantation of autologous mesenchymal stem cells for end-stage liver cirrhosis: a meta-analysis based on seven controlled trials," *Gastroenterology Research and Practice*, vol. 2015, Article ID 908275, 10 pages, 2015.
 - [25] G. Kim, Y. W. Eom, S. K. Baik et al., "Therapeutic effects of mesenchymal stem cells for patients with chronic liver diseases: systematic review and meta-analysis," *Journal of Korean Medical Science*, vol. 30, no. 10, pp. 1405–1415, 2015.
 - [26] N. N. Than, C. L. Tomlinson, D. Haldar, A. L. King, D. Moore, and P. N. Newsome, "Clinical effectiveness of cell therapies in patients with chronic liver disease and acute-on-chronic liver failure: a systematic review protocol," *Systematic Reviews*, vol. 5, no. 1, article 100, 2016.
 - [27] H. Yukawa, M. Watanabe, N. Kaji et al., "Monitoring transplanted adipose tissue-derived stem cells combined with heparin in the liver by fluorescence imaging using quantum dots," *Biomaterials*, vol. 33, no. 7, pp. 2177–2186, 2012.
 - [28] E. Akhan, D. Tuncel, and K. C. Akcali, "Nanoparticle labeling of bone marrow-derived rat mesenchymal stem cells: their use in differentiation and tracking," *BioMed Research International*, vol. 2015, Article ID 298430, 9 pages, 2015.
 - [29] C. Wang, L. Cheng, H. Xu, and Z. Liu, "Towards whole-body imaging at the single cell level using ultra-sensitive stem cell labeling with oligo-arginine modified upconversion nanoparticles," *Biomaterials*, vol. 33, no. 19, pp. 4872–4881, 2012.
 - [30] Z. Li, X. Hu, J. Mao et al., "Optimization of mesenchymal stem cells (MSCs) delivery dose and route in mice with acute liver injury by bioluminescence imaging," *Molecular Imaging and Biology*, vol. 17, no. 2, pp. 185–194, 2015.
 - [31] J. J. Liu, X. J. Hu, Z. R. Li et al., "In Vivo bioluminescence imaging of transplanted mesenchymal stromal cells and their rejection mediated by intrahepatic NK cells," *Molecular Imaging and Biology*, 2016.
 - [32] C.-G. Wu, J.-C. Zhang, C.-Q. Xie et al., "In vivo tracking of human placenta derived mesenchymal stem cells in nude mice via ¹⁴C-TdR labeling," *BMC Biotechnology*, vol. 15, no. 1, article no. 55, 2015.
 - [33] C. Bos, Y. Delmas, A. Desmoulière et al., "In vivo MR imaging of intravascularly injected magnetically labeled mesenchymal stem cells in rat kidney and liver," *Radiology*, vol. 233, no. 3, pp. 781–789, 2004.
 - [34] A. S. Arbab, E. K. Jordan, L. B. Wilson, G. T. Yocum, B. K. Lewis, and J. A. Frank, "In vivo trafficking and targeted delivery of magnetically labeled stem cells," *Human Gene Therapy*, vol. 15, no. 4, pp. 351–360, 2004.
 - [35] J. Cai, X. Zhang, X. Wang, C. Li, and G. Liu, "In vivo MR imaging of magnetically labeled mesenchymal stem cells transplanted into rat liver through hepatic arterial injection," *Contrast Media & Molecular Imaging*, vol. 3, no. 2, pp. 61–66, 2008.
 - [36] S. Ju, G.-J. Teng, H. Lu et al., "In vivo MR tracking of mesenchymal stem cells in rat liver after intrasplenic transplantation," *Radiology*, vol. 245, no. 1, pp. 206–215, 2007.
 - [37] S. Ju, G.-J. Teng, H. Lu et al., "In vivo differentiation of magnetically labeled mesenchymal stem cells into hepatocytes for cell therapy to repair damaged liver," *Investigative Radiology*, vol. 45, no. 10, pp. 625–633, 2010.
 - [38] D. Choi, J. H. Kim, M. Lim et al., "Hepatocyte-like cells from human mesenchymal stem cells engrafted in regenerating rat liver tracked with in vivo magnetic resonance imaging," *Tissue Engineering Part C: Methods*, vol. 14, no. 1, pp. 15–23, 2008.
 - [39] Y. Zhong, Z. Tang, R. Xu et al., "Effect of transplantation route on stem cell migration to fibrotic liver of rats via cellular magnetic resonance imaging," *Cytotherapy*, vol. 15, no. 10, pp. 1266–1274, 2013.
 - [40] T. H. Kim, J. K. Kim, W. Shim, S. Y. Kim, T. J. Park, and J. Y. Jung, "Tracking of transplanted mesenchymal stem cells labeled with fluorescent magnetic nanoparticle in liver cirrhosis rat model

- with 3-T MRI," *Magnetic Resonance Imaging*, vol. 28, no. 7, pp. 1004–1013, 2010.
- [41] H.-L. Shuai, R.-L. Yan, H. Song, D.-L. Chen, and X. Luo, "Analysis of feasibility of in vitro nuclear magnetic resonance tracking human umbilical cord mesenchymal stem cells by Gd-DTPA labeled," *Magnetic Resonance Imaging*, vol. 32, no. 7, pp. 934–940, 2014.
 - [42] H. Shuai, C. Shi, J. Lan, D. Chen, and X. Luo, "Double labelling of human umbilical cord mesenchymal stem cells with Gd-DTPA and PKH26 and the influence on biological characteristics of hUCMSCs," *International Journal of Experimental Pathology*, vol. 96, no. 1, pp. 63–72, 2015.
 - [43] H. Pan, J. Lan, X. Luo, J. Gao, X. Xie, and H. Guo, "Biologic properties of gadolinium diethylenetriaminepentaacetic acid-labeled and PKH26-labeled human umbilical cord mesenchymal stromal cells," *Cytotherapy*, vol. 16, no. 1, pp. 74–83, 2014.
 - [44] E. J. Ribot, J. M. Gaudet, Y. Chen, K. M. Gilbert, and P. J. Foster, "In vivo MR detection of fluorine-labeled human MSC using the bSSFP sequence," *International Journal of Nanomedicine*, vol. 9, no. 1, pp. 1731–1739, 2014.
 - [45] E. T. Ahrens, R. Flores, H. Xu, and P. A. Morel, "In vivo imaging platform for tracking immunotherapeutic cells," *Nature Biotechnology*, vol. 23, no. 8, pp. 983–987, 2005.
 - [46] B. M. Helfer, A. Balducci, A. D. Nelson et al., "Functional assessment of human dendritic cells labeled for in vivo 19F magnetic resonance imaging cell tracking," *Cytotherapy*, vol. 12, no. 2, pp. 238–250, 2010.
 - [47] J. M. Janjic and E. T. Ahrens, "Fluorine-containing nanoemulsions for MRI cell tracking," *Wiley Interdisciplinary Reviews: Nanomedicine and Nanobiotechnology*, vol. 1, no. 5, pp. 492–501, 2009.
 - [48] J. Chen, G. M. Lanza, and S. A. Wickline, "Quantitative magnetic resonance fluorine imaging: today and tomorrow," *Wiley Interdisciplinary Reviews: Nanomedicine and Nanobiotechnology*, vol. 2, no. 4, pp. 431–440, 2010.
 - [49] B. Zheng, T. Vazin, P. W. Goodwill et al., "Magnetic particle imaging tracks the long-term fate of in vivo neural cell implants with high image contrast," *Scientific Reports*, vol. 5, Article ID 14055, 2015.
 - [50] B. Zheng, M. P. von See, E. Yu et al., "Quantitative magnetic particle imaging monitors the transplantation, biodistribution, and clearance of stem cells in vivo," *Theranostics*, vol. 6, no. 3, pp. 291–301, 2016.
 - [51] Y. Ito-Fujishiro, H. Koie, H. Shibata et al., "Tracking cells implanted into cynomolgus monkeys (*Macaca fascicularis*) using MRI," *Experimental Animals*, vol. 65, no. 3, pp. 311–318, 2016.
 - [52] X.-L. Shi, J.-Y. Gu, B. Han, H.-Y. Xu, L. Fang, and Y.-T. Ding, "Magnetically labeled mesenchymal stem cells after autologous transplantation into acutely injured liver," *World Journal of Gastroenterology*, vol. 16, no. 29, pp. 3674–3679, 2010.
 - [53] M. Spriet, G. B. Hunt, N. J. Walker, and D. L. Borjesson, "Scintigraphic tracking of mesenchymal stem cells after portal, systemic intravenous and splenic administration in healthy beagle dogs," *Veterinary Radiology and Ultrasound*, vol. 56, no. 3, pp. 327–334, 2015.
 - [54] A. Gholamrezanezhad, S. Mirpour, M. Bagheri et al., "In vivo tracking of ¹¹¹In-oxine labeled mesenchymal stem cells following infusion in patients with advanced cirrhosis," *Nuclear Medicine and Biology*, vol. 38, no. 7, pp. 961–967, 2011.
 - [55] F. Defresne, T. Tondreau, X. Stéphenne et al., "Biodistribution of adult derived human liver stem cells following intraportal infusion in a 17-year-old patient with glycogenosis type 1A," *Nuclear Medicine and Biology*, vol. 41, no. 4, pp. 371–375, 2014.
 - [56] S. S. Kelkar and T. M. Reineke, "Theranostics: combining imaging and therapy," *Bioconjugate Chemistry*, vol. 22, no. 10, pp. 1879–1903, 2011.
 - [57] S. M. Janib, A. S. Moses, and J. A. MacKay, "Imaging and drug delivery using theranostic nanoparticles," *Advanced Drug Delivery Reviews*, vol. 62, no. 11, pp. 1052–1063, 2010.
 - [58] J. V. Jokerst and S. S. Gambhir, "Molecular imaging with theranostic nanoparticles," *Accounts of Chemical Research*, vol. 44, no. 10, pp. 1050–1060, 2011.
 - [59] X. Ma, Y. Zhao, and X. J. Liang, "Theranostic nanoparticles engineered for clinic and pharmaceuticals," *Accounts of Chemical Research*, vol. 44, no. 10, pp. 1114–1122, 2011.
 - [60] P. Wang and A. Moore, "Theranostic magnetic resonance imaging of type 1 diabetes and pancreatic islet transplantation," *Quantitative Imaging in Medicine and Surgery*, vol. 2, no. 3, pp. 151–162, 2012.
 - [61] D. Yoo, J.-H. Lee, T.-H. Shin, and J. Cheon, "Theranostic magnetic nanoparticles," *Accounts of Chemical Research*, vol. 44, no. 10, pp. 863–874, 2011.
 - [62] P. Pang, C. Wu, F. Gong et al., "Nanovector for gene transfection and MR imaging of mesenchymal stem cells," *Journal of Biomedical Nanotechnology*, vol. 11, no. 4, pp. 644–656, 2015.
 - [63] P. J. Kempen, S. Greasley, K. A. Parker et al., "Theranostic mesoporous silica nanoparticles biodegrade after pro-survival drug delivery and ultrasound/magnetic resonance imaging of stem cells," *Theranostics*, vol. 5, no. 6, pp. 631–642, 2015.
 - [64] S. Pulavendran, C. Rose, and A. B. Mandal, "Hepatocyte growth factor incorporated chitosan nanoparticles augment the differentiation of stem cell into hepatocytes for the recovery of liver cirrhosis in mice," *Journal of Nanobiotechnology*, vol. 9, article no. 15, 2011.
 - [65] J. Wang, Z. Lu, M. G. Wientjes, and J. L.-S. Au, "Delivery of siRNA therapeutics: barriers and carriers," *AAPS Journal*, vol. 12, no. 4, pp. 492–503, 2010.
 - [66] X. Zhao, Q. Huang, and Y. Jin, "Gold nanorod delivery of LSD1 siRNA induces human mesenchymal stem cell differentiation," *Materials Science and Engineering C*, vol. 54, article no. 5448, pp. 142–149, 2015.
 - [67] E. Alizadeh, A. Akbarzadeh, M. B. Eslaminejad et al., "Up regulation of liver-enriched transcription factors HNF4a and HNF6 and liver-specific microRNA (miR-122) by inhibition of let-7b in mesenchymal stem cells," *Chemical Biology and Drug Design*, vol. 85, no. 3, pp. 268–279, 2015.
 - [68] K. D. Chen, K. T. Huang, C. C. Lin et al., "MicroRNA-27b enhances the hepatic regenerative properties of adipose-derived mesenchymal stem cells," *Molecular Therapy. Nucleic Acids*, vol. 5, article e285, 2016.
 - [69] R. S. M. Gomes, R. P. D. Neves, L. Cochlin et al., "Efficient pro-survival/angiogenic miRNA delivery by an MRI-detectable nanomaterial," *ACS Nano*, vol. 7, no. 4, pp. 3362–3372, 2013.
 - [70] J. Zhao, J. Vykoukal, M. Abdelsalam et al., "Stem cell-mediated delivery of SPIO-loaded gold nanoparticles for the theranosis of liver injury and hepatocellular carcinoma," *Nanotechnology*, vol. 25, no. 40, Article ID 405101, 2014.
 - [71] K. von der Haar, A. Lavrentieva, F. Stahl, T. Scheper, and C. Blume, "Lost signature: progress and failures in in vivo tracking of implanted stem cells," *Applied Microbiology and Biotechnology*, vol. 99, no. 23, pp. 9907–9922, 2015.

- [72] J. Chung, R. Dash, K. Kee et al., "Theranostic effect of serial manganese-enhanced magnetic resonance imaging of human embryonic stem cell derived teratoma," *Magnetic Resonance in Medicine*, vol. 68, no. 2, pp. 595–599, 2012.
- [73] M. Rodriguez-Porcel, "In vivo imaging and monitoring of transplanted stem cells: clinical applications," *Current Cardiology Reports*, vol. 12, no. 1, pp. 51–58, 2010.
- [74] D. Y. Lee and K. C. P. Li, "Molecular theranostics: a primer for the imaging professional," *American Journal of Roentgenology*, vol. 197, no. 2, pp. 318–324, 2011.

Review Article

Towards Therapeutic Delivery of Extracellular Vesicles: Strategies for *In Vivo* Tracking and Biodistribution Analysis

Giuliana Di Rocco, Silvia Baldari, and Gabriele Toietta

Department of Research, Advanced Diagnostic, and Technological Innovation, Translational Research Area, Regina Elena National Cancer Institute, Via E. Chianesi 53, 00144 Rome, Italy

Correspondence should be addressed to Gabriele Toietta; gabriele.toietta@ifo.gov.it

Received 21 June 2016; Revised 16 September 2016; Accepted 13 October 2016

Academic Editor: Letterio S. Politi

Copyright © 2016 Giuliana Di Rocco et al. This is an open access article distributed under the Creative Commons Attribution License, which permits unrestricted use, distribution, and reproduction in any medium, provided the original work is properly cited.

Extracellular vesicles (EVs), such as microvesicles and exosomes, are membranous structures containing bioactive material released by several cells types, including mesenchymal stem/stromal cells (MSCs). Increasing lines of evidences point to EVs as paracrine mediators of the beneficial effects on tissue remodeling associated with cell therapy. Administration of MSCs-derived EVs has therefore the potential to open new and safer therapeutic avenues, alternative to cell-based approaches, for degenerative diseases. However, an enhanced knowledge about *in vivo* EVs trafficking upon delivery is required before effective clinical translation. Only a few studies have focused on the biodistribution analysis of exogenously administered MSCs-derived EVs. Nevertheless, current strategies for *in vivo* tracking in animal models have provided valuable insights on the biodistribution upon systemic delivery of EVs isolated from several cellular sources, indicating in liver, spleen, and lungs the preferential target organs. Different strategies for targeting EVs to specific tissues to enhance their therapeutic efficacy and reduce possible off-target effects have been investigated. Here, in the context of a possible clinical application of MSC-derived EVs for tissue regeneration, we review the existing strategies for *in vivo* tracking and targeting of EVs isolated from different cellular sources and the studies elucidating the biodistribution of exogenously administered EVs.

1. Introduction

Mesenchymal stem cells (MSCs) are a heterogeneous subpopulation of cells with self-renewal and multilineage differentiation abilities, present in the stromal fraction of many adult tissues [1]. MSCs are expanded *in vitro* upon selection by adherence to plastic surfaces [2]. In order to define common standards, the International Society for Cellular Therapy set minimal criteria for defining MSCs and suggested the use of the term “mesenchymal stromal cells” (maintaining the acronym MSCs) for the designation of the plastic-adherent cells previously defined as “mesenchymal stem cells” [3, 4]. Indeed, the definition of MSCs is continuously evolving, taking into account more recent understanding in MSCs biology [5]. Several animal and human studies provided the proof-of-concept for the use of MSCs transplantation for the treatment of diseases associated with tissue degeneration

[6]. It was originally assumed that MSCs exert their therapeutic effect on tissue regeneration mainly by differentiating into specialized cells able to repopulate the injured tissue. Increasing evidences have demonstrated that the fraction of administered cells that actually survives upon transplantation, engrafts, differentiates, and provides functional support for tissue regeneration is minimal [7]. Moreover, some beneficial effects have been observed upon administration of factors secreted by MSCs [8]. These observations suggest that the prevalent mechanism by which MSCs exert their contribution to tissue regeneration is mostly associated with their paracrine activity [9–13]. Accordingly, MSCs secretome can be viewed as a remarkable tool for regenerative medicine, which poses reduced safety concerns and easier technological processes for production and storage compared to cell-based therapeutics [14, 15]. Indeed MSCs secrete a wide variety of factors with proangiogenic, anti-inflammatory,

antiapoptotic, and immunomodulatory properties [7]. Moreover, molecules secreted by MSCs include modulators of cellular growth, replication, differentiation, and adherence [16]. Several studies are currently focused on uncovering the nature of MSCs secretome [17, 18], which consists of both soluble factors such as cytokines, chemokines, growth factors, and other proteins, lipids, and nucleic acids, released within extracellular vesicles. How MSCs secretome exerts its beneficial effects on tissue regeneration has not been fully elucidated yet [19]. Due to the heterogeneous nature of MSCs also the mechanism of action of MSCs secretome can be multifaceted [10]. Paracrine factors may promote homing and activation of endogenous stem/progenitor cells, stimulate extracellular matrix remodeling, suppress apoptosis, limit local inflammation, reduce fibrosis, mediate chemoattraction, and support angiogenesis [7, 16]. A better understanding of the molecular and biochemical pathways targeted by MSCs paracrine effectors is crucial for clinical translation of secretome-based therapy approaches [14].

2. Cell-Derived Vesicles

Extracellular vesicles (EVs) are small membrane-enclosed particles derived from a variety of cell types including endothelial cells, dendritic, B and T cells, embryonic and mesenchymal stromal cells, neurons, oligodendrocytes, Schwann cells, intestinal epithelial cells, and platelets [20, 21]. EVs can be found in body fluids such as blood, urine, milk, saliva, amniotic, cerebrospinal, synovial and bronchial lavage fluids, and malignant effusions [22].

The definition “extracellular vesicles” encompasses vesicles with different origin, size, membrane composition, and content such as exosomes, microvesicles, microparticles, ectosomes, oncosomes, prostasomes, and apoptotic bodies [20, 23]. Distinction between different EV subgroups is difficult, due to the minimal physical and morphological differences, to the lack of specific markers, and to the fact that the same cellular source may dynamically produce different class of EVs in response to different conditions [21]. Currently there is no single method allowing for accurate characterization and discrimination of the different EVs classes [24, 25]. In fact, due to their small size, EVs cannot be resolved by light microscopy, neither be analyzed by conventional flow cytometry, but alternative, more cumbersome methods (recently reviewed by Rupert et al. [26]) should be used. In addition, differential centrifugation, which is considered the gold standard method used to isolate EVs, allows for enrichment, rather than purification of the various EVs populations [24, 27–29]. Other methods of isolation may result in different yields, making the direct comparison between various studies difficult [20].

In order to provide criteria for standardization of the nomenclature and the procedures for isolation and characterization of different EV subgroups, the International Society for Extracellular Vesicles has published in a position paper in 2004 [30]. International consensus has been achieved on the following classification: based on their biogenesis EVs

can be divided into three main subclasses: (i) microvesicles, which originate directly from the shedding of the plasma membrane; (ii) apoptotic bodies which are generated upon activation of apoptotic pathways; and (iii) exosomes which are secreted by reverse budding of multivesicular bodies. Interestingly, the existence of distinct subpopulations of exosomes has been recently described [31], but further research is required to fully define exosome subclasses. Detailed description of biogenesis, secretion, and intercellular interaction of EVs has been extensively reviewed elsewhere [32]. The different classes of EVs have also been defined by their approximate diameter size: apoptotic bodies (1–5 μm), microvesicles (100–1000 nm), and exosomes (40–100 nm) [33], but this classification is considered less accurate due to the intrinsic difficulties in performing precise measurements [34]. Further elucidation and a historical perspective on what can be defined as “exosome” were recently provided by Edgar [35]. Nonetheless, difficulties in accurately isolating and characterizing exosomes and other extracellular vesicles prompted some authors to apply the generic term “extracellular vesicles” to collectively denote vesicles obtained from biological samples or cell culture supernatants [34]. Accordingly, in this work we used the notation “extracellular vesicles” (EVs) for all secreted vesicles, although some of the cited articles specifically refer to “exosomes” or “microvesicles.”

Originally, EVs were considered as cellular debris without significant biological function. Actually, accumulating evidences indicate that EVs play a key role in intracellular signaling, exerting specific effects on homeostasis maintenance, modulation of the immune response, inflammation, cancer progression, angiogenesis, and coagulation, in both physiological and pathological conditions [21, 22, 33]. Detection of EVs in biological fluids can be used as diagnostic, prognostic, and treatment monitoring biomarker [36]. EVs lipid bilayer membrane includes transmembrane proteins and encloses soluble proteins and nucleic acids derived from the cell of origin [37]. EVs are able to shuttle protein, lipids, carbohydrates, messenger RNAs, long noncoding RNAs, microRNAs, mitochondrial DNA, and chromosomal DNA into target cells [38, 39]. Transferring distinct biomolecules, EVs mediate different signals between cells and organs, promoting tolerance to external stress stimuli such as inflammation, hypoxia, and oxidative and shear stress [40]. For this reason, EVs have increasingly been under investigation as novel modulators for different therapeutic purposes, including anticancer strategies, vaccination, targeted drug delivery, immunomodulation, and tissue regeneration [22, 41, 42]. Therefore, several possible applications for EVs-mediated therapy have been proposed (Figure 1) [14, 43–49].

Albeit several regulatory and technical issues in achieving highly purified and extensively characterized EVs preparations suitable for use in humans need to be solved [37, 50], several clinical trials have been conducted. Ohno et al. [41] recently reviewed the results of the phase I clinical trials of EVs-based therapies. Overall, no serious acute events have been associated with EVs administration [24, 50]. These preliminary trials have generated great expectation for ongoing and future clinical trials using EVs isolated from MSCs for tissue regenerative purposes [51].

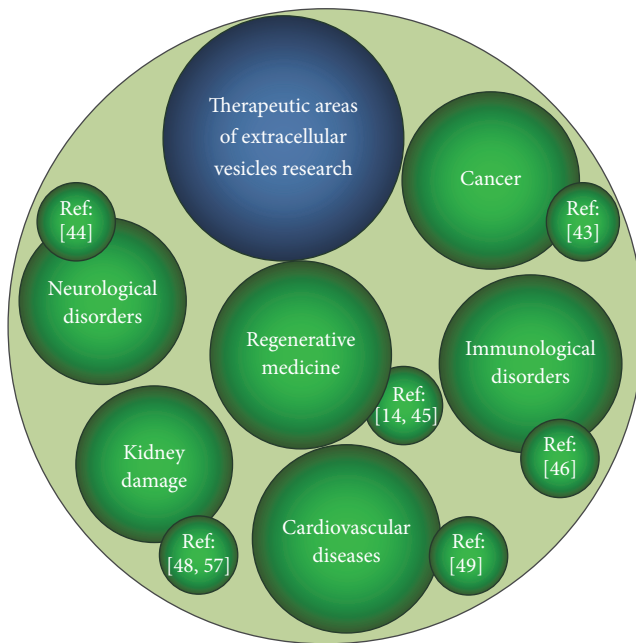


FIGURE 1: Main areas of potential therapeutic use of mesenchymal stem/stromal cells-derived extracellular vesicles.

3. Mesenchymal Stem/Stromal Cells-Derived Extracellular Vesicles and Tissue Regeneration

Studies using MSCs are the most prevalent among the cell-based therapies being tested for tissue regeneration, the reason being that (i) MSCs can be isolated from different, easily accessible, adult tissue sources, including bone marrow [83] and adipose tissue [84]; (ii) they can be cultured *in vitro*; and (iii) they can be induced into osteogenic, chondrogenic, adipogenic, endothelial, cardiovascular, neurogenic, and hepatic differentiation. The ability of MSCs to secrete a variety of growth factors, cytokines, and chemokines potentially involved in tissue repair and remodeling is well-established, being described for the first time 20 years ago [85]. Nonetheless, elucidating the factors that contribute to the regenerative ability of MSCs remains one of the most relevant but unresolved issues in the field. Therefore, in recent years, the attempts for identifying MSCs-secreted mediators with therapeutic potential have shifted from growth factor and cytokines to extracellular vesicles [86]. The existence of EVs is well-documented since the description of extracellular vesicles, termed “exosomes,” was first published nearly 30 years ago [87]. However, more recent studies demonstrating the ability of MSC-secreted EVs in providing protection against acute kidney damage [88], hepatic fibrosis [89], and myocardial [90] injury have sprouted a new interest on possible exploitation of EVs as therapeutic vehicles [22]. EVs may play a role in local tissue repair affecting progenitor cell proliferation, recruitment, and differentiation; promoting extracellular matrix remodeling and angiogenesis; overpowering apoptosis and immunological responses [45, 91].

EVs play a pivotal role in stem cell plasticity and tissue regeneration, possibly contributing to the paracrine action observed upon MSCs cell transplant [92, 93]. Purification of EVs released from cultured MSCs and their delivery to damaged tissues may represent a novel “acellular” therapeutic approach in the arena of regenerative medicine [14, 51]. This strategy can be considered as an alternative to cell-based therapeutic approaches [94], albeit MSCs are still necessary as EVs source. MSCs are a proficient source of EVs, including exosomes, which therefore can be obtained in a clinical relevant scale with procedures compliant with good manufacturing process standards [95]. Also immortalized MSCs produce considerable amounts of exosomes and microvesicles, making possible the generation of stable cell lines for consistent production of EVs [96]. In addition, genetic manipulation of producer cells might be used in order to increase production or to generate “tailored” EVs [79, 97]. EVs can be isolated from cells obtained from each patient, posing no question of immunocompatibility and allowing for repeated administration. Moreover, EVs-mediated delivery of biological material has improved safety profile compared to the current methods of delivery based on liposome and viral based vehicles. Favorably, EVs are fairly stable under different storage conditions [98], making them easier to store and deliver compared with living cells used in cell-based therapies.

4. Investigating Extracellular Vesicles Biodistribution by Molecular Imaging

The use of MSC-derived EVs for regenerative therapy requires production and isolation of a suitable quantity of clinical grade EVs from cultured MSCs [94]. For safe and successful clinical applications of EVs-based therapies for tissue regeneration, a better understanding of EVs biodistribution upon administration is needed [50]. A large amount of pre-clinical studies on the therapeutic potential of MSCs-derived EVs (recently reviewed by Akyurekli et al. [99]) has been performed. Nonetheless, current knowledge of the biodistribution of EVs upon administration in animal models is limited. To our knowledge, only one work evaluated the biodistribution of human bone marrow-derived MSC in murine models [58]. In the current section, we review the methods for EVs labeling and the biodistribution studies, including those performed by administration of EVs collected from cellular sources other than MSCs.

4.1. Methods for Extracellular Vesicles Labeling. Several strategies have been employed for *in vivo* tracking to determine EVs biodistribution upon systemic delivery in different animal models (Table 1) [100]. The ideal method should be specific, have a high signal-to-noise ratio, and mirror EVs half-life. Unfortunately, the methods currently used present some limitations. One approach consists, for instance, in loading EVs with superparamagnetic iron oxide nanoparticles for high resolution and sensitive magnetic resonance analysis [56]. Radioisotope labeling of EVs using clinically validated radio tracers and nuclear imaging have also been used for tracing EVs in murine experimental models [54, 55]. These techniques provide for accurate detection also in deep organs,

TABLE 1: Imaging studies investigating extracellular vesicles (EVs) biodistribution *in vivo*.

Imaging technique	EVs labeling	EVs source	Administration route	Biodistribution	Ref
PET	^{68}Ga and ^{64}Cu	Breast cancer cells (4T1)	Tail vein and foot pad	Lung, liver, spleen, lymph nodes	[52]
SPECT/CT	$^{99\text{m}}\text{Tc}$	Erythrocytes	Tail vein	Liver and spleen	[53]
	$^{99\text{m}}\text{Tc}$ -HMPAO	Macrophages	Tail vein	Liver and spleen	[54]
	^{125}I	Melanoma cells (B16BL6)	Intravenous injection	Liver, spleen, lungs	[55]
MRI	Paramagnetic cation probes	Melanoma cells (B16-F10)	Food pad	Lymph node	[56]
	Infrared dye	Mouse lymphoma cell line (EL-4)	Intraperitoneal	Kidney, liver, spleen, lungs	[57]
	Near-infrared dye; GFP labeling	Dendritic cells, MSCs from bone marrow	Tail vein, intraperitoneal, subcutaneous	Liver, spleen, gastrointestinal tract, lungs	[58]
	Near-infrared dye	MSCs	Intravenous injection	Kidney in acute kidney injured mice	[59]
Optical imaging	PKH67 dye	Embryonic kidney cells (HEK293T)	Intravenous injection	Tumor targeting	[60]
	Fluorescent dye and ^{111}In	Breast cancer cells (4T1)	Tail vein	Liver and spleen	[61]
	gLuc-lactadherin	Melanoma cells (B16BL6)	Tail vein	Liver and lungs	[62]
	gLuc-lactadherin and PKH67 dye	Melanoma cells (B16BL6)	Tail vein	Macrophages in liver and spleen; endothelial cells in lungs	[63]
	gLuc-B and streptavidin-Alexa680	Embryonic kidney cells (HEK293T)	Tail vein	Spleen, liver, lungs, kidney	[64]
Optical imaging and radiolabelling	GFP-tagged CD63	Orthotopically transplanted breast cancer cells	—	Tumor	[65]
Intra vital imaging	Cre-GFP-RFP	Orthotopically transplanted MDA-MB-231	—	Tumor	[66]
	PalmGFP, PalmtdTomato	Mouse lymphoma cell line (EL-4)	Intratumor injection	Tumor	[67]

HMPAO: hexamethylpropyleneamine oxime. gLuc-lactadherin: Gaussia luciferase and a truncated lactadherin reporter. gLuc-B: fusion between a membrane-bound variant of the Gluc reporter and a biotin acceptor peptide.

but require instruments not available in many research departments.

Alternatively, EVs can be conveniently labeled with fluorescent dyes; both dyes selective for DNA and RNA contained in the EVs [101] and lipophilic dyes for labeling membrane components have been used [102–104]. Near-infrared (NIR) dyes are ideal for *in vivo* applications due to their high signal/noise ratio, the minimal autofluorescence of biological tissue in the 700–900 nm spectral range, and the strong tissue penetration of the near-IR light. In particular, the carbocyanine DiOC18(7) (DiR) is a lipophilic dye weakly fluorescent in water, but particularly fluorescent and photostable when incorporated into lipid-membranes. Lipophilic NIR dyes

have been quite extensively employed for labeling of EVs isolated from different sources and administered into different animal models (Table 2). The major limitation, however, is that lipophilic dyes labeling promotes EVs aggregation and may give rise to artifacts, especially *in vivo* [59]. Moreover, extensive washing steps, needed to reduce the presence of dye residues which might result in nonspecific signals, can cause significant EVs loss. Nonetheless, valuable information on localization of EVs administered by different routes has been acquired using this labeling strategy followed by *in vivo* fluorescence optical imaging. Little is known about EVs' half-life after systemic administration. Recent evidences, obtained following miR loaded EVs expression, suggest that, in the

TABLE 2: Extracellular vesicles targeting studies.

Target cells	Ligand	Receptor	Main reference
APCs	Lactadherin-fusion	Antigen targeting	[68, 69]
Neurons	RVG-Lamp2b fusion	Acetylcholine receptor	[70–72]
B cells	EBV glycoprotein 350	CD19	[73]
Breast cancer	PDGFR-GE11 peptide fusion	EGFR	[60]
	RGD-	$\alpha v \beta 3$ integrins	[74]
Cancer cells	Iron oxide nanoparticles	Magnetic targeting	[75]
Carcinoma cells	Nanobodies anti-EGFR fused to GPI anchors	EGFR	[76]
	Nanobodies anti-EGFR conjugated with PEG		[77]
	Viral envelope proteins	Dependent on the type of the virus	[78]
Different targets	Exosome fusion with liposomes	Dependent on the type of the hybrid exosome	[79, 80]
	Click chemistry modification	Dependent on the type of the functionalization	[81, 82]

blood, EVs are detectable as early as 5 min after intravenous administration, decrease by ~50% in 30 minutes, and become undetectable after 4 hours [105]. On the other hand, lipophilic dye staining is quite stable, with an *in vivo* half-life estimated in several days. Therefore, in long-term studies the extended half-life of the lipophilic dye may result in the maintenance of the fluorescent signal for longer than the EVs persistence itself [58]. To circumvent this problem, we have developed a method for EVs labeling without the use of fluorescent dye. The strategy is based on the genetic modification of the EVs-producing cells with a lentiviral vector derived from the X-Pack plasmid (System Biosciences, Palo Alto, CA) in which the coding sequence of the fluorescent protein TurboFP635 (Katushka red) (Evrogen, Moscow, Russia) has been cloned in frame with a specific peptide sequence that targets the protein into the EVs (Baldari et al., unpublished data). The choice of the Katushka far red fluorescent protein makes this labeling strategy suitable for *in vivo* imaging studies, due to reduced auto fluorescence in biological tissue in the near-infrared-shifted emission spectra [106]. This labeling method allows for the generation of a producer cell line which continuously secretes EVs containing the reporter protein of choice for downstream applications. Another method of EVs labeling has been recently used by Lai et al. directing the expression of fluorescent markers into the exosomal membrane by the generation of enhanced green (EGFP) and tandem dimer tomato (tdTomato) fluorescent proteins containing specific palmitoylation signals, which promote the membrane association of the proteins [67]. Albeit the range of fluorescent probes suitable for EVs labeling is continuously expanding, one of the major limitations for *in vivo* tracking studies is associated with the fact that fluorescent markers should have an emission peak not coinciding with the fluorescence emission of biological tissues, in order to overcome the autofluorescence background. Moreover, the use of fluorescent conjugated markers directed against specific proteins, such as CD63-GFP, may restrict labeling to specific subpopulations of EVs [58]. On the other side, fluorescent dyes for EV lipid labeling, such as the most commonly used PKH67 [60], are not EV-specific [67]. Consequently, they not only label EVs but also can be retained in association with other lipid entities for

long periods, eventually forming aggregates or micelles, thus inducing false positive results [59]. In contrast, the palmitoylated fluorescent EV reporters, like PalmGFP and PalmtdTomato, have increased specificity compared with CD63-GFP and to PKH67 dye, allowing for labeling and semiquantification of multiple and different sized EV types, irrespective of their biogenesis, time-lapse live-cell imaging of EV release and uptake, and EV exchange between different cell populations [67].

Compared to fluorescent-based imaging, bioluminescent optical imaging (BLI), which uses luciferase enzymes as imaging reporters, has an extremely low signal-to-noise ratio, since the autoluminescence in mammalian tissue is negligible. In particular, the adapted bioluminescence reporters, such as Gaussia luciferase, being over 1,000-fold brighter than firefly luciferase, are useful tools to study temporal properties of minute biological processes because of their sensitivity, low background and independence from an excitation source to emit light. Therefore, BLI has been extensively evaluated in the development of cell-based therapies to determine cellular distribution, survival, proliferation, and differentiation after transplantation [107, 108]. BLI has also been described for the analysis of EVs associated with a luciferase enzyme. In particular, Takahashi et al. generated a fusion protein named gLuc-lactadherin consisting of the Gaussia luciferase (gLuc) enzyme combined with portions of the membrane protein lactadherin which are required for the protein translocation into the exosomal compartment and for retention on the exosomal membrane [62]. Cellular expression of gLuc-lactadherin results in production of EVs containing Gaussia luciferase on their membrane, which can be therefore detected by BLI. Using a similar approach Lai et al. generated a fusion between a membrane-bound variant of the gLuc reporter and a biotin acceptor peptide [64]. These reporters were instrumental for performing *in vivo* biodistribution studies upon administration of exogenously purified EVs into animal models (Table 1). Recently, imaging of live animals at microscopic resolution (intravital imaging) was used to investigate exosomal cellular trafficking *in vivo* suggesting that EVs take part in the dissemination of cancer cells [66, 67].

4.2. *In Vivo* Biodistribution of Exogenously Administered Extracellular Vesicles. The nature and the physiological state of the vesicle-producing cell affect the tropism of produced EVs [58, 109]. Moreover, the characteristics of EVs purified from a defined cellular source cultured *in vitro* may be different from EVs endogenously released from the same source [110]. The lack of standardization in EVs isolation procedures and in the methods for the characterization of the purified fraction hampers direct comparison between different studies. In fact, the isolation method used may substantially affect EVs purity and function and consequently have an impact on the *in vivo* biodistribution. For instance, collection of EVs by ultracentrifugation results in vesicles aggregation [111]. In biodistribution studies, the dosage of administered EVs is mainly assessed by determining the protein content in EVs preparations, which, due to suboptimal isolation protocols, may suffer from protein aggregates contaminations [112]. Furthermore, EVs display an intrinsic broad size distribution and heterogeneity, which may determine differential targeting [37]. Differential posttranslational modifications of EVs membrane proteins are an additional source of variability, which might have a functional role in EVs specific targeting [113]. In addition, purified EVs used for biodistribution studies *in vivo* need to be labeled, and the labeling procedure may modify EVs tropism. Accordingly, the EVs labeling procedure determines the detection method used, with its own advantages and limitations. Further complication in assessing exogenously administered EVs biodistribution is represented by the partial knowledge of the mechanisms of cellular uptake of EVs, recently reviewed by Mulcahy et al. [114]. Nonetheless, from studies summarized in Table 1, some valuable information on pharmacodynamics and biodistribution of administered EVs can be obtained.

Due to their presence in most of biological fluids, it was supposed that EVs may be quite stable in circulation. Unexpectedly, dynamic distribution studies have demonstrated that blood levels of EVs decreased by more than a half from 30 to 60 minutes upon intravenous administration [64]. Pharmacokinetics studies performed by Takahashi et al. suggest a rapid clearance of systemically administered EVs, with half-life of few minutes and complete disappearance from circulation within 4 hours after injection [62]. These results are in accordance with studies performed on systemic administration of liposomes of similar size and charge [110]. Exogenously administered EVs are rapidly cleared predominantly by the macrophages of the mononuclear phagocyte system [62, 63]. Accordingly, EVs clearance is significantly reduced in macrophage depleted animals, compared to animal not subjected to macrophage depletion treatment [63]. In particular, exogenously administered EVs accumulate mainly in liver, spleen, and lungs, organs rich in macrophages (Table 1). Interaction between macrophages and EVs may be mediated by specific phosphatidylserine recognition on the outer portion of the membrane [114, 115]. In the liver, in addition to a predominant clearance by macrophages (Kupffer cells), also direct EVs uptake by hepatocytes has been suggested [63]. Presence of high amounts of systemically delivered EVs into

the spleen was attributed to circulating lymphocytes and macrophages, which bind EVs in the blood and then migrate to the spleen [63]. It was observed that EVs are retained in the lungs longer than in other organs, being detectable approximately 4 hours after intravenous delivery [62]. In some experimental conditions, EVs accumulation in the lungs observed after systemic delivery was due to aggregation subsequent to EVs labeling [54]. Exogenously administered EVs may also be internalized by kidney cells and released into the urine [59]. Biodistribution of systemically administered EVs is a dynamic process: a rapid phase of distribution in liver, spleen, and lungs within approximately 30 min upon administration is followed by an elimination phase via hepatic and renal processing, removing EVs in 1 to 6 hours after administration [64, 67].

The route of administration determines EVs biodistribution [58]. For instance, administration into the footpad resulted in EVs localization into lymph nodes [56]; intranasal administration delivered EVs to the brain, across the blood brain barrier [70], opening exciting opportunities on the exploitation of EVs as drug delivery system to the brain [116]; periocular injection of EVs reached the neurosensory retina [117]. Furthermore, it is likely that clearance and organ uptake of EVs may be different in healthy recipients compared to subject suffering some sort of disease or trauma, even if more detailed comparative studies addressing this issue are needed [21].

5. Targeting Extracellular Vesicles Delivery

In vivo tracking studies have pointed out that, upon systemic delivery, EVs are sequestered within a few minutes by circulating macrophages in the liver, spleen, and lungs [21]. Hence, to achieve a longer half-life of circulating EVs it might be necessary to modify EVs in order to escape macrophage recognition. On the other hand, receptors and ligands exposed on the external part of the lipid bilayer of the membrane play key roles in target cell recognition and EVs uptake [114], although the exact mechanism of specific recipient cell selection has not been fully elucidated [118]. Therefore, detargeting from macrophages or targeting of EVs to specific tissues may enhance their therapeutic efficacy and reduce possible off-target effects. In order to achieve targeted delivery different strategies to modify EVs' natural tropism have been developed (Table 2) [119–121]. Some approaches require the functionalization of the cellular source to generate “tailored” EVs (Figure 2). For instance, targeting restricted cellular receptors can be achieved by genetic modification of the EVs-producing cells, in order to express specific ligands or peptides in the outer portion of a transmembrane protein, such as lactadherin, lysosome-associated membrane protein-2b (LAMP-2b), and platelet-derived growth factor receptor (PDGFR) (Table 2). Using these approaches EVs have been directed to clinical relevant targets such as EGFR-expressing tumors [60], antigen presenting cells [68], and brain [70]. Interestingly, fusion of membrane proteins with specific viral proteins can direct EVs towards specific target cells. Accordingly,

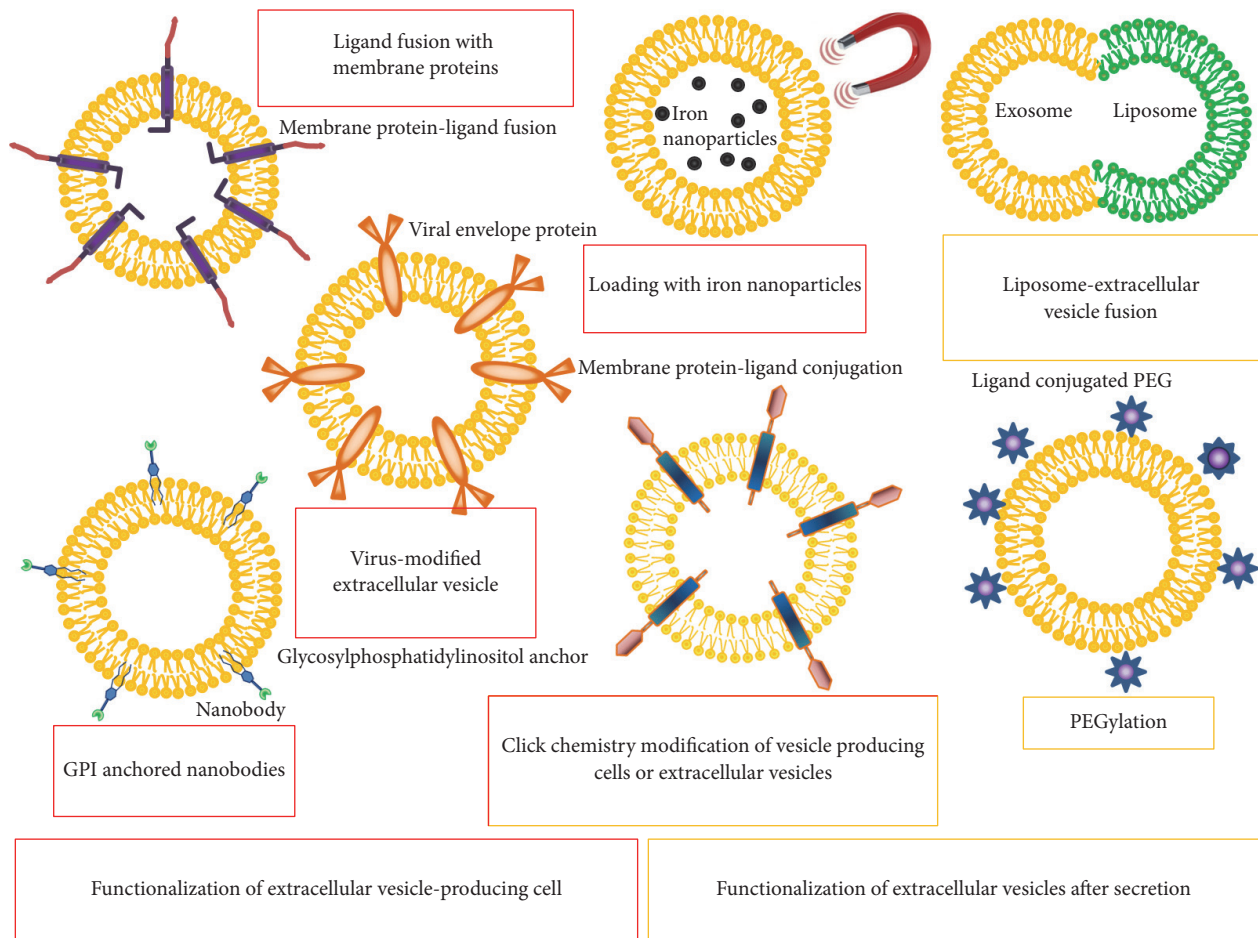


FIGURE 2: Schematic representation of different methods to promote tissue- or cell-type-specific targeting of extracellular vesicles (EVs). EVs can be targeted to particular cellular receptor either by modifications of EVs-producing cells (red squares) or modification of EVs after secretion (yellow squares). In the first case, EVs-producing cells can be modified: expressing ligands, peptides, or viral-derived envelop proteins in the outer portion of a transmembrane protein; loading cells with iron oxide particles to allow for magnetic targeting. Alternatively, secreted EVs can be modified linking cell-specific peptides to the EVs surface via association with polyethylene glycol (PEG) polymer chains or by EVs-liposome fusion. Click chemistry can be used to modify both EVs-producing cells and purified EVs.

Koppers-Lalic and collaborators suggested producing EVs with modified tropism by genetic modification of EVs-secreting cells in order to overexpress viral-derived envelop proteins, taking advantage of viral proteins specific binding to target cell receptors [78]. Albeit effective, it should be considered that such targeting strategies may compromise the function of the EVs, and consequently their therapeutic efficacy, or promote their aggregation [21].

Approaches requiring genetic modification of EVs-secreting cells are cumbersome and time-consuming. In addition, some peptides fused to EVs transmembrane proteins are not effectively exposed or adequately stable to provide for efficient target recognition [122]. Moreover, in some EVs-producing cells, especially primary cells, it might be difficult to achieve a satisfactory level of transgene expression, using both viral and nonviral methods of transduction. To avoid genetic manipulation, Silva et al. loaded the EVs-secreting cells with iron oxide particles to produce EVs-containing magnetic nanoparticles suitable for magnetic

targeting [75]. Alternatively, a series of approaches aiming at modifying the EVs after secretion, without the need of manipulating the EVs-producing cells, have been recently pursued (Figure 2). For instance, it is possible to link cell-specific peptides to the EVs surface via association with polyethylene glycol (PEG) polymer chains [77]. The resulting PEGylated EVs are coated with the desired ligand, allowing for specific targeting. PEGylation has the advantage of reducing EVs recognition by the mononuclear phagocytic system. A limitation to the clinical translation of the use of PEGylated EVs for therapeutic purposes is represented by the fact that approximately 25% of healthy subjects are positive to anti-PEG neutralizing antibodies, due to exposure to PEG contained in cosmetic products [123]. Recent studies have provided evidences that click chemistry can be efficiently used to modify EVs-producing cells [81] or purified EVs [82] in order to generate “tailored” vesicles.

Altogether these reports established the possibility to manipulate EV tropism, fostering future studies, in both

academia and the pharmaceutical industry, to actively pursue the development of an efficient system with improved target specificity suitable for safe clinical translation.

6. Conclusive Remarks

In recent years, stem/stromal mesenchymal cells-derived extracellular vesicles, in particular exosomes, have gained increasing interest and their potential use in regenerative therapies has greatly expanded. Addressing both technical and regulatory issues to bring EVs-based therapies from bench to bedside is an ongoing process. Nonetheless, the exact mechanism of *in vivo* action of exogenously administered EVs, their biodistribution, pharmacokinetics, and possibility of targeted delivery are not fully elucidated. Imaging techniques may help in filling this gap of knowledge and further promoting clinical translation of EVs-based regenerative therapy.

Competing Interests

The authors declare that there is no conflict of interests regarding the publication of this paper.

Acknowledgments

This work was supported by the Ministero della Salute (Ricerca Finalizzata Grant no. RF-2011-02347907 to Gabriele Toietta) and, in part, by IRE 5x1000.

References

- [1] L. da Silva Meirelles, P. C. Chagastelles, and N. B. Nardi, "Mesenchymal stem cells reside in virtually all post-natal organs and tissues," *Journal of Cell Science*, vol. 119, no. 11, pp. 2204–2213, 2006.
- [2] A. I. Caplan, "Mesenchymal stem cells," *Journal of Orthopaedic Research*, vol. 9, no. 5, pp. 641–650, 1991.
- [3] M. Dominici, K. Le Blanc, I. Mueller et al., "Minimal criteria for defining multipotent mesenchymal stromal cells. The International Society for Cellular Therapy position statement," *Cytotherapy*, vol. 8, no. 4, pp. 315–317, 2006.
- [4] E. M. Horwitz, K. Le Blanc, M. Dominici et al., "Clarification of the nomenclature for MSC: The International Society for Cellular Therapy position statement," *Cytotherapy*, vol. 7, no. 5, pp. 393–395, 2005.
- [5] A. Keating, "Mesenchymal stromal cells: new directions," *Cell Stem Cell*, vol. 10, no. 6, pp. 709–716, 2012.
- [6] J.-F. Stoltz, N. De Isla, Y. P. Li et al., "Stem cells and regenerative medicine: myth or reality of the 21st century," *Stem Cells International*, vol. 2015, Article ID 734731, 19 pages, 2015.
- [7] L. da Silva Meirelles, A. M. Fontes, D. T. Covas, and A. I. Caplan, "Mechanisms involved in the therapeutic properties of mesenchymal stem cells," *Cytokine and Growth Factor Reviews*, vol. 20, no. 5–6, pp. 419–427, 2009.
- [8] P. Smedo, M. Burgos-Silva, C. Donizetti-Oliveira, and N. O. S. Camara, "How do mesenchymal stem cells repair?" in *Stem Cells in Clinic and Research*, A. Gholamrezanezhad, Ed., chapter 4, pp. 83–104, InTech, Rijeka, Croatia, 2011.
- [9] T. Wu, Y. Liu, B. Wang, and G. Li, "The roles of mesenchymal stem cells in tissue repair and disease modification," *Current Stem Cell Research and Therapy*, vol. 9, no. 5, pp. 424–431, 2014.
- [10] M. Gnecci, P. Danieli, G. Malpasso, and M. C. Ciuffreda, "Paracrine mechanisms of mesenchymal stem cells in tissue repair," in *Mesenchymal Stem Cells: Methods and Protocols*, M. Gnecci, Ed., vol. 1416 of *Methods in Molecular Biology*, pp. 123–146, Springer, Berlin, Germany, 2016.
- [11] X. Liang, Y. Ding, Y. Zhang, H.-F. Tse, and Q. Lian, "Paracrine mechanisms of mesenchymal stem cell-based therapy: current status and perspectives," *Cell Transplantation*, vol. 23, no. 9, pp. 1045–1059, 2014.
- [12] C. P. Hodgkinson, A. Bareja, J. A. Gomez, and V. J. Dzau, "Emerging concepts in paracrine mechanisms in regenerative cardiovascular medicine and biology," *Circulation Research*, vol. 118, no. 1, pp. 95–107, 2016.
- [13] T. J. Burdon, A. Paul, N. Noiseux, S. Prakash, and D. Shum-Tim, "Bone marrow stem cell derived paracrine factors for regenerative medicine: current perspectives and therapeutic potential," *Bone Marrow Research*, vol. 2011, Article ID 207326, 14 pages, 2011.
- [14] V. B. R. Konala, M. K. Mamidi, R. Bhonde, A. K. Das, R. Pochampally, and R. Pal, "The current landscape of the mesenchymal stromal cell secretome: a new paradigm for cell-free regeneration," *Cytotherapy*, vol. 18, no. 1, pp. 13–24, 2016.
- [15] T. Katsuda and T. Ochiya, "Molecular signatures of mesenchymal stem cell-derived extracellular vesicle-mediated tissue repair," *Stem Cell Research and Therapy*, vol. 6, no. 1, article 214, 2015.
- [16] C. Tran and M. S. Damaser, "Stem cells as drug delivery methods: application of stem cell secretome for regeneration," *Advanced Drug Delivery Reviews*, vol. 82–83, pp. 1–11, 2015.
- [17] H. Kupcova Skalnikova, "Proteomic techniques for characterisation of mesenchymal stem cell secretome," *Biochimie*, vol. 95, no. 12, pp. 2196–2211, 2013.
- [18] M. Makridakis, M. G. Roubelakis, and A. Vlahou, "Stem cells: insights into the secretome," *Biochimica et Biophysica Acta*, vol. 1834, no. 11, pp. 2380–2384, 2013.
- [19] J. R. Lavoie and M. Rosu-Myles, "Uncovering the secretomes of mesenchymal stem cells," *Biochimie*, vol. 95, no. 12, pp. 2212–2221, 2013.
- [20] G. Raposo and W. Stoorvogel, "Extracellular vesicles: exosomes, microvesicles, and friends," *Journal of Cell Biology*, vol. 200, no. 4, pp. 373–383, 2013.
- [21] M. Yáñez-Mó, P. R. Siljander, Z. Andreu et al., "Biological properties of extracellular vesicles and their physiological functions," *Journal of Extracellular Vesicles*, vol. 4, Article ID 27066, 2015.
- [22] H. Kalra, G. P. C. Drummen, and S. Mathivanan, "Focus on extracellular vesicles: introducing the next small big thing," *International Journal of Molecular Sciences*, vol. 17, no. 2, article 170, 2016.
- [23] E. van der Pol, A. N. Böing, P. Harrison, A. Sturk, and R. Nieuwland, "Classification, functions, and clinical relevance of extracellular vesicles," *Pharmacological Reviews*, vol. 64, no. 3, pp. 676–705, 2012.
- [24] R. Xu, D. W. Greening, H.-J. Zhu, N. Takahashi, and R. J. Simpson, "Extracellular vesicle isolation and characterization: toward clinical application," *The Journal of Clinical Investigation*, vol. 126, pp. 1152–1162, 2016.
- [25] E. van der Pol, A. G. Hoekstra, A. Sturk, C. Otto, T. G. van Leeuwen, and R. Nieuwland, "Optical and non-optical

- methods for detection and characterization of microparticles and exosomes,” *Journal of Thrombosis and Haemostasis*, vol. 8, no. 12, pp. 2596–2607, 2010.
- [26] D. L. Rupert, V. Claudio, C. Lässer, and M. Bally, “Methods for the physical characterization and quantification of extracellular vesicles in biological samples,” *Biochimica et Biophysica Acta (BBA)—General Subjects*, 2016.
- [27] F. Momen-Heravi, L. Balaj, S. Alian et al., “Current methods for the isolation of extracellular vesicles,” *Biological Chemistry*, vol. 394, no. 10, pp. 1253–1262, 2013.
- [28] C. Théry, S. Amigorena, G. Raposo, and A. Clayton, “Isolation and characterization of exosomes from cell culture supernatants and biological fluids,” in *Current Protocols in Cell Biology*, chapter 3, unit 3.22, John Wiley & Sons, New York, NY, USA, 2006.
- [29] R. Szatanek, J. Baran, M. Siedlar, and M. Baj-Krzyworzeka, “Isolation of extracellular vesicles: determining the correct approach,” *International Journal of Molecular Medicine*, vol. 36, no. 1, pp. 11–17, 2015.
- [30] J. Lötvall, A. F. Hill, F. Hochberg et al., “Minimal experimental requirements for definition of extracellular vesicles and their functions: a position statement from the International Society for Extracellular Vesicles,” *Journal of Extracellular Vesicles*, vol. 3, Article ID 26913, 2014.
- [31] E. Willms, H. J. Johansson, I. Mäger et al., “Cells release subpopulations of exosomes with distinct molecular and biological properties,” *Scientific Reports*, vol. 6, Article ID 22519, 2016.
- [32] M. Colombo, G. Raposo, and C. Théry, “Biogenesis, secretion, and intercellular interactions of exosomes and other extracellular vesicles,” *Annual Review of Cell and Developmental Biology*, vol. 30, pp. 255–289, 2014.
- [33] S. El Andaloussi, I. Mäger, X. O. Breakefield, and M. J. A. Wood, “Extracellular vesicles: biology and emerging therapeutic opportunities,” *Nature Reviews Drug Discovery*, vol. 12, no. 5, pp. 347–357, 2013.
- [34] S. J. Gould and G. Raposo, “As we wait: coping with an imperfect nomenclature for extracellular vesicles,” *Journal of Extracellular Vesicles*, vol. 2, Article ID 20389, 2013.
- [35] J. R. Edgar, “Q&A: what are exosomes, exactly?” *BMC Biology*, vol. 14, article 46, 2016.
- [36] J. Lin, J. Li, B. Huang et al., “Exosomes: novel biomarkers for clinical diagnosis,” *Scientific World Journal*, vol. 2015, Article ID 657086, 8 pages, 2015.
- [37] S. W. Ferguson and J. Nguyen, “Exosomes as therapeutics: the implications of molecular composition and exosomal heterogeneity,” *Journal of Controlled Release*, vol. 228, pp. 179–190, 2016.
- [38] H. Valadi, K. Ekström, A. Bossios, M. Sjöstrand, J. J. Lee, and J. O. Lötvall, “Exosome-mediated transfer of mRNAs and microRNAs is a novel mechanism of genetic exchange between cells,” *Nature Cell Biology*, vol. 9, no. 6, pp. 654–659, 2007.
- [39] M. Z. Ratajczak and J. Ratajczak, “Horizontal transfer of RNA and proteins between cells by extracellular microvesicles: 14 years later,” *Clinical and Translational Medicine*, vol. 5, article 7, 2016.
- [40] M. Eldh, K. Ekström, H. Valadi et al., “Exosomes communicate protective messages during oxidative stress; possible role of exosomal shuttle RNA,” *PLoS ONE*, vol. 5, no. 12, Article ID e15353, 2010.
- [41] S.-I. Ohno, G. P. C. Drummen, and M. Kuroda, “Focus on extracellular vesicles: development of extracellular vesicle-based therapeutic systems,” *International Journal of Molecular Sciences*, vol. 17, no. 2, p. 172, 2016.
- [42] B. György, M. E. Hung, X. O. Breakefield, and J. N. Leonard, “Therapeutic applications of extracellular vesicles: clinical promise and open questions,” *Annual Review of Pharmacology and Toxicology*, vol. 55, pp. 439–464, 2015.
- [43] N. Tominaga, Y. Yoshioka, and T. Ochiya, “A novel platform for cancer therapy using extracellular vesicles,” *Advanced Drug Delivery Reviews*, vol. 95, pp. 50–55, 2015.
- [44] A. Jarmalavičiūtė and A. Pivoriūnas, “Exosomes as a potential novel therapeutic tools against neurodegenerative diseases,” *Pharmacological Research*, 2016.
- [45] O. G. de Jong, B. W. M. van Balkom, R. M. Schiffelers, C. V. C. Bouten, and M. C. Verhaar, “Extracellular vesicles: potential roles in regenerative medicine,” *Frontiers in Immunology*, vol. 5, article 608, 2014.
- [46] G. Natasha, B. Gundogan, A. Tan et al., “Exosomes as immunotherapeutic nanoparticles,” *Clinical Therapeutics*, vol. 36, no. 6, pp. 820–829, 2014.
- [47] L. Biancone, S. Bruno, M. C. Derigibus, C. Tetta, and G. Camussi, “Therapeutic potential of mesenchymal stem cell-derived microvesicles,” *Nephrology Dialysis Transplantation*, vol. 27, no. 8, pp. 3037–3042, 2012.
- [48] K. Yao and S. D. Ricardo, “Mesenchymal stem cells as novel micro-ribonucleic acid delivery vehicles in kidney disease,” *Nephrology*, vol. 21, no. 5, pp. 363–371, 2016.
- [49] C. Gallina, V. Turinetto, and C. Giachino, “A new paradigm in cardiac regeneration: the mesenchymal stem cell secretome,” *Stem Cells International*, vol. 2015, Article ID 765846, 10 pages, 2015.
- [50] T. Lener, M. Gimona, L. Aigner et al., “Applying extracellular vesicles based therapeutics in clinical trials—an ISEV position paper,” *Journal of Extracellular Vesicles*, vol. 4, Article ID 30087, 2015.
- [51] A. Fuster-Matanzo, F. Gessler, T. Leonardi, N. Iraci, and S. Pluchino, “Acellular approaches for regenerative medicine: On the verge of clinical trials with extracellular membrane vesicles? Extracellular vesicles and regenerative medicine,” *Stem Cell Research and Therapy*, vol. 6, no. 1, article 227, 2015.
- [52] K. O. Jung, H. Youn, M. J. Kim et al., “In vivo PET imaging of radiolabeled exosomes from breast cancer cells,” *Journal of Nuclear Medicine*, vol. 56, p. 11, 2015.
- [53] Z. Varga, I. Gyurkó, K. Pálóczi et al., “Radiolabeling of extracellular vesicles with (99m)Tc for quantitative in vivo imaging studies,” *Cancer Biother Radiopharm*, vol. 31, no. 5, pp. 168–173, 2016.
- [54] D. W. Hwang, H. Choi, S. C. Jang et al., “Noninvasive imaging of radiolabeled exosome-mimetic nanovesicle using 99m Tc-HMPAO,” *Scientific Reports*, vol. 5, article 15636, 2015.
- [55] M. Morishita, Y. Takahashi, M. Nishikawa et al., “Quantitative analysis of tissue distribution of the B16BL6-derived exosomes using a streptavidin-lactadherin fusion protein and Iodine-125-labeled biotin derivative after intravenous injection in mice,” *Journal of Pharmaceutical Sciences*, vol. 104, no. 2, pp. 705–713, 2015.
- [56] L. Hu, S. A. Wickline, and J. L. Hood, “Magnetic resonance imaging of melanoma exosomes in lymph nodes,” *Magnetic Resonance in Medicine*, vol. 74, no. 1, pp. 266–271, 2015.

- [57] D. Sun, X. Zhuang, X. Xiang et al., "A novel nanoparticle drug delivery system: the anti-inflammatory activity of curcumin is enhanced when encapsulated in exosomes," *Molecular Therapy*, vol. 18, no. 9, pp. 1606–1614, 2010.
- [58] O. P. Wiklander, J. Z. Nordin, A. O'Loughlin et al., "Extracellular vesicle in vivo biodistribution is determined by cell source, route of administration and targeting," *Journal of Extracellular Vesicles*, vol. 4, Article ID 26316, 2015.
- [59] C. Grange, M. Tapparo, S. Bruno et al., "Biodistribution of mesenchymal stem cell-derived extracellular vesicles in a model of acute kidney injury monitored by optical imaging," *International Journal of Molecular Medicine*, vol. 33, no. 5, pp. 1055–1063, 2014.
- [60] S.-I. Ohno, M. Takanashi, K. Sudo et al., "Systemically injected exosomes targeted to EGFR deliver antitumor microRNA to breast cancer cells," *Molecular Therapy*, vol. 21, no. 1, pp. 185–191, 2013.
- [61] T. Smyth, M. Kullberg, N. Malik, P. Smith-Jones, M. W. Graner, and T. J. Anchordoquy, "Biodistribution and delivery efficiency of unmodified tumor-derived exosomes," *Journal of Controlled Release*, vol. 199, pp. 145–155, 2015.
- [62] Y. Takahashi, M. Nishikawa, H. Shinotsuka et al., "Visualization and in vivo tracking of the exosomes of murine melanoma B16-BL6 cells in mice after intravenous injection," *Journal of Biotechnology*, vol. 165, no. 2, pp. 77–84, 2013.
- [63] T. Imai, Y. Takahashi, M. Nishikawa et al., "Macrophage-dependent clearance of systemically administered B16BL6-derived exosomes from the blood circulation in mice," *Journal of Extracellular Vesicles*, vol. 4, article 26238, 2015.
- [64] C. P. Lai, O. Mardini, M. Ericsson et al., "Dynamic biodistribution of extracellular vesicles in vivo using a multimodal imaging reporter," *ACS Nano*, vol. 8, no. 1, pp. 483–494, 2014.
- [65] A. Suetsugu, K. Honma, S. Saji, H. Moriwaki, T. Ochiya, and R. M. Hoffman, "Imaging exosome transfer from breast cancer cells to stroma at metastatic sites in orthotopic nude-mouse models," *Advanced Drug Delivery Reviews*, vol. 65, no. 3, pp. 383–390, 2013.
- [66] A. Zomer, C. Maynard, F. J. Verweij et al., "In vivo imaging reveals extracellular vesicle-mediated phenocopying of metastatic behavior," *Cell*, vol. 161, no. 5, pp. 1046–1057, 2015.
- [67] C. P. Lai, E. Y. Kim, C. E. Badr et al., "Visualization and tracking of tumour extracellular vesicle delivery and RNA translation using multiplexed reporters," *Nature Communications*, vol. 6, article 7029, 2015.
- [68] I. S. Zeelenberg, M. Ostrowski, S. Krumeich et al., "Targeting tumor antigens to secreted membrane vesicles in vivo induces efficient antitumor immune responses," *Cancer Research*, vol. 68, no. 4, pp. 1228–1235, 2008.
- [69] Z. C. Hartman, J. Wei, O. K. Glass et al., "Increasing vaccine potency through exosome antigen targeting," *Vaccine*, vol. 29, no. 50, pp. 9361–9367, 2011.
- [70] L. Alvarez-Erviti, Y. Seow, H. Yin, C. Betts, S. Lakhal, and M. J. A. Wood, "Delivery of siRNA to the mouse brain by systemic injection of targeted exosomes," *Nature Biotechnology*, vol. 29, no. 4, pp. 341–345, 2011.
- [71] Y. Liu, D. Li, Z. Liu et al., "Targeted exosome-mediated delivery of opioid receptor Mu siRNA for the treatment of morphine relapse," *Scientific Reports*, vol. 5, Article ID 17543, 2015.
- [72] J. M. Cooper, P. B. O. Wiklander, J. Z. Nordin et al., "Systemic exosomal siRNA delivery reduced alpha-synuclein aggregates in brains of transgenic mice," *Movement Disorders*, vol. 29, no. 12, pp. 1476–1485, 2014.
- [73] R. Ruiss, S. Jochum, R. Mocikat, W. Hammerschmidt, and R. Zeidler, "EBV-gp350 confers B-cell tropism to tailored exosomes and is a neo-antigen in normal and malignant B cells—a new option for the treatment of B-CLL," *PLoS ONE*, vol. 6, no. 10, Article ID e25294, 2011.
- [74] Y. Tian, S. Li, J. Song et al., "A doxorubicin delivery platform using engineered natural membrane vesicle exosomes for targeted tumor therapy," *Biomaterials*, vol. 35, no. 7, pp. 2383–2390, 2014.
- [75] A. K. A. Silva, N. Luciani, F. Gazeau et al., "Combining magnetic nanoparticles with cell derived microvesicles for drug loading and targeting," *Nanomedicine: Nanotechnology, Biology, and Medicine*, vol. 11, no. 3, pp. 645–655, 2015.
- [76] S. A. Kooijmans, C. G. Aleza, S. R. Roffler, W. W. van Solinge, P. Vader, and R. M. Schiffelers, "Display of GPI-anchored anti-EGFR nanobodies on extracellular vesicles promotes tumour cell targeting," *Journal of Extracellular Vesicles*, vol. 5, no. 0, 2016.
- [77] S. A. A. Kooijmans, L. A. L. Fliervoet, R. Van Der Meel et al., "PEGylated and targeted extracellular vesicles display enhanced cell specificity and circulation time," *Journal of Controlled Release*, vol. 224, pp. 77–85, 2016.
- [78] D. Koppers-Lalic, M. M. Hogenboom, J. M. Middeldorp, and D. M. Pegtel, "Virus-modified exosomes for targeted RNA delivery; A new approach in nanomedicine," *Advanced Drug Delivery Reviews*, vol. 65, no. 3, pp. 348–356, 2013.
- [79] Y. T. Sato, K. Umezaki, S. Sawada et al., "Engineering hybrid exosomes by membrane fusion with liposomes," *Scientific Reports*, vol. 6, article 21933, 2016.
- [80] J. Lee, H. Lee, U. Goh et al., "Cellular engineering with membrane fusogenic liposomes to produce functionalized extracellular vesicles," *ACS Applied Materials & Interfaces*, vol. 8, no. 11, pp. 6790–6795, 2016.
- [81] M. Wang, S. Altinoglu, Y. S. Takeda, and Q. Xu, "Integrating protein engineering and bioorthogonal click conjugation for extracellular vesicle modulation and intracellular delivery," *PLoS ONE*, vol. 10, no. 11, article e0141860, 2015.
- [82] T. Smyth, K. Petrova, N. M. Payton et al., "Surface functionalization of exosomes using click chemistry," *Bioconjugate Chemistry*, vol. 25, no. 10, pp. 1777–1784, 2014.
- [83] Y. Jiang, B. N. Jahagirdar, R. L. Reinhardt et al., "Pluripotency of mesenchymal stem cells derived from adult marrow," *Nature*, vol. 418, no. 6893, pp. 41–49, 2002.
- [84] A. Trivisonno, M. Abecassis, M. Monti, G. Toietta, and A. Bachir, "Adipose tissue: from energy reservoir to a source of cells for epithelial tissue engineering," in *Stem Cells in Aesthetic Procedures*, M. A. Shiffman, A. Di Giuseppe, and F. Bassetto, Eds., pp. 303–326, Springer, Berlin, Germany, 2014.
- [85] S. E. Haynesworth, M. A. Baber, and A. I. Caplan, "Cytokine expression by human marrow-derived mesenchymal progenitor cells in vitro: effects of dexamethasone and IL-1 α ," *Journal of Cellular Physiology*, vol. 166, no. 3, pp. 585–592, 1996.
- [86] G. Camussi, M. C. Deregibus, and V. Cantaluppi, "Role of stem-cell-derived microvesicles in the paracrine action of stem cells," *Biochemical Society Transactions*, vol. 41, no. 1, pp. 283–287, 2013.
- [87] R. M. Johnstone, M. Adam, J. R. Hammond, L. Orr, and C. Turbide, "Vesicle formation during reticulocyte maturation. Association of plasma membrane activities with released vesicles (exosomes)," *Journal of Biological Chemistry*, vol. 262, no. 19, pp. 9412–9420, 1987.
- [88] S. Bruno, C. Grange, M. C. Deregibus et al., "Mesenchymal stem cell-derived microvesicles protect against acute tubular injury,"

- Journal of the American Society of Nephrology*, vol. 20, no. 5, pp. 1053–1067, 2009.
- [89] T. Li, Y. Yan, B. Wang et al., “Exosomes derived from human umbilical cord mesenchymal stem cells alleviate liver fibrosis,” *Stem Cells and Development*, vol. 22, no. 6, pp. 845–854, 2013.
 - [90] R. C. Lai, F. Arslan, M. M. Lee et al., “Exosome secreted by MSC reduces myocardial ischemia/reperfusion injury,” *Stem Cell Research*, vol. 4, no. 3, pp. 214–222, 2010.
 - [91] A. Marote, F. G. Teixeira, B. Mendes-Pinheiro, and A. J. Salgado, “MSCs-derived exosomes: cell-secreted nanovesicles with regenerative potential,” *Frontiers in Pharmacology*, vol. 7, article 231, 2016.
 - [92] C. Tetta, S. Bruno, V. Fonsato, M. C. Deregibus, and G. Camussi, “The role of microvesicles in tissue repair,” *Organogenesis*, vol. 7, no. 2, pp. 105–115, 2011.
 - [93] J. Stephen, E. L. Bravo, D. Colligan, A. R. Fraser, J. Petrik, and J. D. M. Campbell, “Mesenchymal stromal cells as multifunctional cellular therapeutics—a potential role for extracellular vesicles,” *Transfusion and Apheresis Science*, vol. 55, no. 1, pp. 62–69, 2016.
 - [94] S. Rani, A. E. Ryan, M. D. Griffin, and T. Ritter, “Mesenchymal stem cell-derived extracellular vesicles: toward cell-free therapeutic applications,” *Molecular Therapy*, vol. 23, no. 5, pp. 812–823, 2015.
 - [95] T. S. Chen, F. Arslan, Y. Yin et al., “Enabling a robust scalable manufacturing process for therapeutic exosomes through oncogenic immortalization of human ESC-derived MSCs,” *Journal of Translational Medicine*, vol. 9, article 47, 2011.
 - [96] R. W. Y. Yeo, R. C. Lai, B. Zhang et al., “Mesenchymal stem cell: an efficient mass producer of exosomes for drug delivery,” *Advanced Drug Delivery Reviews*, vol. 65, no. 3, pp. 336–341, 2013.
 - [97] S. Rana, S. Yue, D. Stadel, and M. Zöller, “Toward tailored exosomes: the exosomal tetraspanin web contributes to target cell selection,” *International Journal of Biochemistry and Cell Biology*, vol. 44, no. 9, pp. 1574–1584, 2012.
 - [98] V. Sokolova, A.-K. Ludwig, S. Hornung et al., “Characterisation of exosomes derived from human cells by nanoparticle tracking analysis and scanning electron microscopy,” *Colloids and Surfaces B: Biointerfaces*, vol. 87, no. 1, pp. 146–150, 2011.
 - [99] C. Akyurekli, Y. Le, R. B. Richardson, D. Fergusson, J. Tay, and D. S. Allan, “A systematic review of preclinical studies on the therapeutic potential of mesenchymal stromal cell-derived microvesicles,” *Stem Cell Reviews and Reports*, vol. 11, no. 1, pp. 150–160, 2015.
 - [100] H. Choi and D. S. Lee, “Illuminating the physiology of extracellular vesicles,” *Stem Cell Research & Therapy*, vol. 7, article 55, 2016.
 - [101] A. J. Ullal, D. S. Pisetsky, and C. F. Reich III, “Use of SYTO 13, a fluorescent dye binding nucleic acids, for the detection of microparticles in vitro systems,” *Cytometry Part A*, vol. 77, no. 3, pp. 294–301, 2010.
 - [102] T. Tian, Y. Wang, H. Wang, Z. Zhu, and Z. Xiao, “Visualizing of the cellular uptake and intracellular trafficking of exosomes by live-cell microscopy,” *Journal of Cellular Biochemistry*, vol. 111, no. 2, pp. 488–496, 2010.
 - [103] K. Laulagnier, H. Vincent-Schneider, S. Hamdi, C. Subra, D. Lankar, and M. Record, “Characterization of exosome subpopulations from RBL-2H3 cells using fluorescent lipids,” *Blood Cells, Molecules, and Diseases*, vol. 35, no. 2, pp. 116–121, 2005.
 - [104] E. J. van der Vlist, E. N. M. Nolte-’t Hoen, W. Stoorvogel, G. J. A. Arksteijn, and M. H. M. Wauben, “Fluorescent labeling of nano-sized vesicles released by cells and subsequent quantitative and qualitative analysis by high-resolution flow cytometry,” *Nature Protocols*, vol. 7, no. 7, pp. 1311–1326, 2012.
 - [105] S. Bala, T. Csak, F. Momen-Heravi et al., “Biodistribution and function of extracellular miRNA-155 in mice,” *Scientific Reports*, vol. 5, article 10721, 2015.
 - [106] D. Shcherbo, E. M. Merzlyak, T. V. Chepurnykh et al., “Bright far-red fluorescent protein for whole-body imaging,” *Nature Methods*, vol. 4, no. 9, pp. 741–746, 2007.
 - [107] J. E. Kim, S. Kalimuthu, and B.-C. Ahn, “In vivo cell tracking with bioluminescence imaging,” *Nuclear Medicine and Molecular Imaging*, vol. 49, no. 1, pp. 3–10, 2015.
 - [108] G. Di Rocco, A. Gentile, A. Antonini et al., “Analysis of biodistribution and engraftment into the liver of genetically modified mesenchymal stromal cells derived from adipose tissue,” *Cell Transplantation*, vol. 21, no. 9, pp. 1997–2008, 2012.
 - [109] R. C. Lai, S. S. Tan, R. W. Yeo et al., “MSC secretes at least 3 EV types each with a unique permutation of membrane lipid, protein and RNA,” *Journal of Extracellular Vesicles*, vol. 5, Article ID 29828, 2016.
 - [110] R. van der Meel, M. H. A. M. Fens, P. Vader, W. W. Van Solinge, O. Eniola-Adefeso, and R. M. Schiffelers, “Extracellular vesicles as drug delivery systems: lessons from the liposome field,” *Journal of Controlled Release*, vol. 195, pp. 72–85, 2014.
 - [111] R. Linares, S. Tan, C. Gounou, N. Arraud, and A. R. Brisson, “High-speed centrifugation induces aggregation of extracellular vesicles,” *Journal of Extracellular Vesicles*, vol. 4, article 29509, 2015.
 - [112] B. György, K. Módos, É. Pállinger et al., “Detection and isolation of cell-derived microparticles are compromised by protein complexes resulting from shared biophysical parameters,” *Blood*, vol. 117, no. 4, pp. e39–e48, 2011.
 - [113] O. Moreno-Gonzalo, C. Villarroja-Beltri, and F. Sánchez-Madrid, “Post-translational modifications of exosomal proteins,” *Frontiers in Immunology*, vol. 5, article 383, 2014.
 - [114] L. A. Mulcahy, R. C. Pink, and D. R. Carter, “Routes and mechanisms of extracellular vesicle uptake,” *Journal of Extracellular Vesicles*, vol. 3, Article ID 24641, 2014.
 - [115] D. Feng, W.-L. Zhao, Y.-Y. Ye et al., “Cellular internalization of exosomes occurs through phagocytosis,” *Traffic*, vol. 11, no. 5, pp. 675–687, 2010.
 - [116] D. Ha, N. Yang, and V. Nadihe, “Exosomes as therapeutic drug carriers and delivery vehicles across biological membranes: current perspectives and future challenges,” *Acta Pharmaceutica Sinica B*, vol. 6, no. 4, pp. 287–296, 2016.
 - [117] A. R. Hajrasouliha, G. Jiang, Q. Lu et al., “Exosomes from retinal astrocytes contain antiangiogenic components that inhibit laser-induced choroidal neovascularization,” *Journal of Biological Chemistry*, vol. 288, no. 39, pp. 28058–28067, 2013.
 - [118] H. M. van Dongen, N. Masoumi, K. W. Witwer, and D. M. Pegtel, “Extracellular vesicles exploit viral entry routes for cargo delivery,” *Microbiology and Molecular Biology Reviews*, vol. 80, no. 2, pp. 369–386, 2016.
 - [119] M. Kotmakçı and V. B. Çetintaş, “Extracellular vesicles as natural nanosized delivery systems for small-molecule drugs and genetic material: steps towards the future nanomedicines,” *Journal of Pharmacy and Pharmaceutical Sciences*, vol. 18, no. 3, pp. 396–413, 2015.
 - [120] S. EL Andaloussi, S. Lakhali, I. Mäger, and M. J. A. Wood, “Exosomes for targeted siRNA delivery across biological barriers,” *Advanced Drug Delivery Reviews*, vol. 65, no. 3, pp. 391–397, 2013.

- [121] S. A. Kooijmans, R. M. Schiffelers, N. Zarovni, and R. Vago, "Modulation of tissue tropism and biological activity of exosomes and other extracellular vesicles: new nanotools for cancer treatment," *Pharmacological Research*, vol. 111, pp. 487–500, 2016.
- [122] M. E. Hung and J. N. Leonard, "Stabilization of exosome-targeting peptides via engineered glycosylation," *The Journal of Biological Chemistry*, vol. 290, no. 13, pp. 8166–8172, 2015.
- [123] R. P. Garay, R. El-Gewely, J. K. Armstrong, G. Garratty, and P. Richette, "Antibodies against polyethylene glycol in healthy subjects and in patients treated with PEG-conjugated agents," *Expert Opinion on Drug Delivery*, vol. 9, no. 11, pp. 1319–1323, 2012.

Research Article

Label-Free Imaging of Umbilical Cord Tissue Morphology and Explant-Derived Cells

Raf Donders,¹ Kathleen Sanen,¹ Rik Paesen,¹ Eli Slenders,¹ Wilfried Gyselaers,^{1,2} Piet Stinissen,¹ Marcel Ameloot,¹ and Niels Hellings¹

¹Biomedical Research Institute, Hasselt University and School of Life Sciences, Transnational University Limburg, Agoralaan Building C, 3590 Diepenbeek, Belgium

²Ziekenhuis Oost-Limburg, Campus St. Jan, Schiepse Bos 6, 3600 Genk, Belgium

Correspondence should be addressed to Niels Hellings; niels.hellings@uhasselt.be

Received 14 May 2016; Revised 28 July 2016; Accepted 31 July 2016

Academic Editor: Francesco Petrella

Copyright © 2016 Raf Donders et al. This is an open access article distributed under the Creative Commons Attribution License, which permits unrestricted use, distribution, and reproduction in any medium, provided the original work is properly cited.

In situ detection of MSCs remains difficult and warrants additional methods to aid with their characterization *in vivo*. Two-photon confocal laser scanning microscopy (TPM) and second harmonic generation (SHG) could fill this gap. Both techniques enable the detection of cells and extracellular structures, based on intrinsic properties of the specific tissue and intracellular molecules under optical irradiation. TPM imaging and SHG imaging have been used for label-free monitoring of stem cells differentiation, assessment of their behavior in biocompatible scaffolds, and even cell tracking *in vivo*. In this study, we show that TPM and SHG can accurately depict the umbilical cord architecture and visualize individual cells both *in situ* and during culture initiation, without the use of exogenously applied labels. In combination with nuclear DNA staining, we observed a variance in fluorescent intensity in the vessel walls. In addition, antibody staining showed differences in Oct4, α SMA, vimentin, and ALDH1A1 expression *in situ*, indicating functional differences among the umbilical cord cell populations. In future research, marker-free imaging can be of great added value to the current antigen-based staining methods for describing tissue structures and for the identification of progenitor cells in their tissue of origin.

1. Introduction

Stem cells originating from perinatal tissues such as the umbilical cord (UC) are being intensively studied for application in regenerative medicine. Due to their intrinsic growth promoting abilities mediated via self-renewal, multilineage differentiation, and trophic factor production, as well as their immune modulatory functions [1, 2], these perinatal stem cells are put forward as potent alternatives to adult stem cell sources for both autologous and allogeneic application. As a result, UC-derived stromal cells are currently under evaluation as cellular therapy for multiple degenerative diseases and as an immune modulatory approach for diseases involving aberrant immunological responses, such as multiple sclerosis, Parkinson's disease, graft-versus-host disease, type 1 diabetes, or stroke [3–6].

The UC is a rich source of stem cells, since a variety of progenitors can be harvested from different compartments of the

tissue, for example, cord blood, perivascular space, and tissue matrix [7, 8]. The derivation of multipotent cells from the UC matrix or Wharton's jelly (WJ) was first described about a decade ago by Mitchell et al. and Romanov et al., reporting the isolation of stromal cells with a mesenchymal-like phenotype (WJ-MSCs) [9, 10]. Following their discovery, their potent preclinical potential as well as their superior culture properties over adult (bone-marrow-derived) mesenchymal stem cells (MSCs) has been extensively described [11–16]. In contrast to this extensive characterization in culture, the biology of WJ-MSCs *in situ* and their transition from tissue into culture remain poorly understood.

At present, the identification of mesenchymal-like cells derived from a specific tissue of origin relies on *in vitro* assays which usually involve the dissociation of the tissue and isolation and culturing of cells first. Classically, MSCs are defined by the ability to adhere to plastic, the expression of

specific surface marker antigens, and multipotent differentiation potential [17]. To assess cell differentiation and function at specific time points or within a certain tissue, techniques such as western blots, quantitative polymerase chain reaction, and immunohistochemistry are the most commonly utilized. Although these approaches are highly sensitive and specific, their destructive nature does not allow for dynamic or real-time assessments of cells within intact tissues [18]. As such, the *in situ* identification of MSCs remains difficult and requires additional imaging methods.

Nonlinear optical microscopy techniques, such as multiphoton microscopy and higher harmonic generation, are emerging tools for intravital noninvasive imaging of cells and tissues [19–21]. These techniques allow for marker-free visualization and characterization of cells and tissue structures without fixation or staining procedures [19, 22]. Accordingly, two-photon excitation can provoke the emission of photons from intrinsic fluorophores within the cell, such as nicotinamide adenine dinucleotides (NADH) and flavins, a phenomenon called autofluorescence (AF) [23, 24]. In addition, asymmetric molecules such as collagen type I and elastin can produce light at exactly twice the frequency (or half the wavelength) of the pulsed excitation beam, a feature that is referred to as second harmonic generation (SHG) [21, 25]. SHG does not suffer from photobleaching and allows for extended periods of observation [26]. Moreover, the two-photon laser excitation beams can penetrate deeper into the tissue allowing imaging and tracking of cells in relatively thick samples of up to 1 mm [20, 27, 28]. By monitoring AF and SHG, stem cell differentiation, cell behavior in 3D biological scaffolds (e.g., collagen matrices), and *in vivo* tracking of cells (untouched or transgenic) and regenerative processes have been visualized [28–37].

The aim of the present study is to assess the potential of label-free imaging for the visualization of cells within umbilical cord tissue and for monitoring stromal cells during explant isolation and in culture. Our data show that two-photon fluorescence microscopy (TPM) and SHG imaging can be used to detect cells *in situ* without exogenously applied labeling molecules. We were able to visualize the UC architecture along with explant attachment and primary cell outgrowth. In parallel, chondrogenic pellets were imaged to validate the procedure, showing collagen rich deposits and cells in cleft-like structures after differentiation of WJ-MSCs. Furthermore, AF and SHG imaging was used in combination with nuclear DNA staining, revealing differential intensities in nuclear fluorescence in the umbilical vessel walls. As such, we show that TPM is an elegant tool to characterize UC stem cells *in situ*, with the potential for parallel use with conventional imaging and staining techniques.

2. Material and Methods

2.1. Umbilical Cord Tissue Processing. The collection and experimental use of human UC tissues were approved by the Medical Ethical Committees of Hasselt University and Ziekenhuis Oost-Limburg. UC tissues ($n = 5$) were obtained aseptically from full-term uncomplicated pregnancies with

planned cesarean section, after informed consent. Cords were drained of blood and subsequently stored in sterile phosphate-buffered saline (PBS; Lonza, Verviers, Belgium) supplemented with 1% penicillin-streptomycin (P/S; 10000:10000 U; Gibco®, Life Technologies, Gent, Belgium) and 0.2% Fungizone® (250 µg/mL; Gibco, Life Technologies). Tissues were processed within 24 hours for cell isolation or sectioning. Fresh cord fragments were processed for cell isolation (see below) or fixed overnight with 4% paraformaldehyde (PFA; Sigma-Aldrich, Bornem, Belgium) followed by paraffin embedding. For subsequent *in situ* analysis, 7 µm sections were deparaffinized in xylene (VWR, Heverlee, Belgium) and rehydrated in graded ethanol series until submerged in PBS.

2.2. Wharton's Jelly Stem Cell Culture. Stromal cells were isolated from the WJ using explant tissue culturing as was previously described [4]. In brief, after removal of the vessels, the cord matrix was cut into 2 mm³ fragments and cultured in KnockOut™ Dulbecco's modified Eagle's medium with F12 (Gibco, Life Technologies) supplemented with 1% P/S, 1% GlutaMAX™ (200 mM; Gibco, Life Technologies), and 10% fetal bovine serum (Biochrom AG, Berlin, Germany). When cellular outgrowth from the explants was observed, fresh medium was added every 3 days. For imaging, explants were seeded in 8-well chamber slides (µ-slide, Ibidi, Martinsried, Germany). Wharton's jelly-derived stem cells (WJ-MSCs) were collected at 80% confluence using StemPro® accutase (Gibco, Life Technologies) and seeded either in T75 flasks (Nunc™; VWR) for further expansion, on glass coverslips (Menzel-Gläser; Braunschweig, Germany) for characterization experiments, or in 8-well chamber slides for TPM and SHG imaging.

2.3. Trilineage Differentiation. Differentiation was performed as previously described [38], using the human Mesenchymal Stem Cell Functional Identification Kit (SC006; R&D Systems, Abingdon, Oxfordshire, UK). For adipogenic and osteogenic differentiation, WJ-MSCs were cultured for 3 weeks in 24-well plates (Nunc) on sterile glass coverslips, in their respective complete differentiation medium according to the kit instructions. Medium was changed every 3 days after which cells were fixed with 4% PFA and stored in PBS at 4°C until microscopy imaging. To validate the monolayer differentiation cultures, adipogenic coverslips were stained with Oil Red O (ORO; Sigma-Aldrich) as previously described [38], whereas osteogenic coverslips were stained with the anti-osteocalcin antibody from the differentiation kit. For chondrogenic differentiation, freshly harvested WJ-MSCs were transferred to 15 mL conical tubes containing 0.5 mL complete chondrogenic differentiation medium. After centrifugation, pellets were cultured for 3 weeks with medium changed every 3 days. After that, chondrogenic pellets were fixed with 4% PFA and stored in PBS at 4°C until microscopic imaging and Alcian Blue staining. For multiphoton microscopy, whole chondropellets were submerged in PBS in chamber slides. To further validate the differentiation process, pellets were snap frozen and sectioned into 7 µm tissue

slices using a Leica CM1900UV cryostat (Leica Microsystems, Diegem, Belgium). Thawed cryosections were hydrated with distilled water and stained with Alcian Blue (generated in-house) for 30 minutes in the dark. Next, the sections were washed and counterstained with Nuclear Fast Red (NFR; Sigma-Aldrich) for 5 minutes, dehydrated, and mounted with glass coverslips using DPX (Merck, Darmstadt, Germany). Bright field images were taken using a Nikon Eclipse 80i microscope and processed with NIS Elements BR 4.0 software (Nikon Instruments BeLux, Brussels, Belgium).

2.4. Multiphoton Microscopy and SHG Imaging. AF and SHG imaging of the UC tissue slices, explants, and stem cells was performed with a Zeiss LSM 510 META mounted on an Axiovert 200 M (Carl Zeiss, Jena, Germany) and equipped with a femtosecond pulsed laser excitation source (Mai Tai DeepSee, Spectra-Physics, CA, USA) tuned to a central wavelength of 810 nm. For scanning an entire UC section, a 10x/0.3 objective (Plan-Neofluar 10x/0.3, Carl Zeiss) was used. Detailed images were taken through a 40x/1.1 water immersion objective (LD C-Apochromat 40x/1.1 W Korr UV-VIS-IR, Carl Zeiss). As a control for cellular location, UC tissue slices ($n = 2$) were counterstained with 0.1% 4',6-diamidino-2-phenylindole (DAPI; 1 mg/mL; Molecular Probes®, Life Technologies) in distilled water. For imaging the explant process, WJ-MSCs in culture, or the chondrogenic pellets, a 20x/0.75 objective was selected (Plan-Apochromat 20x/0.75, Carl Zeiss). Both AF and SHG were detected in backward nondescanned mode by analogue photomultipliers. The signals were first separated from the excitation beam using a long pass dichroic mirror with an edge at 685 nm. Next, the SHG and AF were separated from each other by a long pass dichroic mirror with an edge at 442 nm. The SHG signal then passed through a 10 nm narrow band pass filter with a central wavelength of 405 nm. In the AF channel, a wide band pass filter ranging from 450 nm to 650 nm was used to clean out any possible leaked excitation and SHG light. 3D images were obtained after digitally combining Z-stack optical sections. All images were processed using ZEN 2009 Light Edition software (Carl Zeiss).

2.5. Immunohistochemistry. For marker expression analysis, 7 μ m thick tissue slices were microwaved for antigen retrieval in 10 mM sodium citrate buffer at pH 6.0 (Sigma-Aldrich). Next, specific antigen expression was detected using the peroxidase-based EnVision™+ system (Dako, Heverlee, Belgium) according to the manufacturer's instructions. Prior to labeling with the primary antibody, tissues were permeabilized in Tris-buffered saline (VWR) with 0.05% Tween-20 (Merck Chemicals, Overijse, Belgium) (TBS-T), after which endogenous peroxidase activity was quenched with 0.5% hydrogen peroxide. Nonspecific binding sites were blocked using 10% normal goat serum (Dako) in TBS-T. Subsequently, tissues were incubated for 2 hours in TBS-T with primary antibodies directed against human octamer-binding transcription factor 4 (Oct4; 1/250; rabbit polyclonal ab19857; Abcam, Cambridge, UK), aldehyde dehydrogenase family 1 member A1 (ALDH1A1; 1 μ g/mL; rabbit polyclonal ab23375;

Abcam), alpha smooth muscle actin (α SMA; 1/50; mouse monoclonal α sm-1; Novocastra™, Leica), vimentin (1/100; mouse monoclonal V9; Dako), and pan cytokeratin (pan-CK; 1/100; mouse monoclonal MNF116; Dako), followed by 30-minute incubation with horseradish peroxidase- (HRP-) conjugated goat anti-rabbit or goat anti-mouse secondary antibody (Envision kit). To visualize binding of the antibodies, diaminobenzidine (DAB) chromogen substrate was added after which the tissues were counterstained with Mayer's hematoxylin (Leica) or NFR in case of nuclear antigen detection. Stainings without primary antibody served as negative controls. Next, stained sections were dehydrated and mounted with glass coverslips using DPX. Sections were examined using a Mirax Desk photomicroscope slide scanner and images were processed with Mirax Viewer software (Carl Zeiss).

2.6. Immunocytochemistry. WJ-MSCs were seeded on sterile glass coverslips in a 24-well plate and grown until 80% confluence. WJ cells were fixed with 4% PFA before antibody staining with the EnVision™+ system. The cell membrane was permeated and nonspecific binding sites were blocked using PBS supplemented with 0.3% Triton X-100 (Sigma-Aldrich), 1% bovine serum albumin (US Biological, Swampscott, MA, USA), and 10% normal goat serum (blocking buffer) at room temperature for 45 minutes. Next, the cells were incubated for 2 hours with 5 μ g/mL Oct4 (ab19857; Abcam), 1 μ g/mL ALDH1A1 (ab23375; Abcam), or α SMA (1/100, α sm-1; Novocastra, Leica) in blocking buffer. The negative controls were incubated without the primary antibody. Subsequently, the coverslips were washed and incubated for 1 hour with HRP-conjugated goat anti-rabbit or goat anti-mouse secondary antibody of the Envision kit. After washing the cells, nuclear counterstaining with Mayer's hematoxylin or NFR was performed, and coverslips were subsequently mounted on glass slides using Aquatex (Merck). Stained cells were examined using a Nikon Eclipse 80i microscope and images processed with NIS Elements BR 4.0 software (Nikon Instruments BeLux, Brussels, Belgium).

3. Results

3.1. Detailed Visualization of Different Anatomical Compartments within the Umbilical Cord Using TPM and SHG Detection. Based on AF and SHG signals, a detailed image of the UC architecture was generated. Figure 1(a) shows a composition of serial scanned sections of cord tissue after TPM imaging. Without any additional labeling agents, we clearly observed the overall cord composition and the cellular organization of the umbilical cord vessels, WJ, and subamniotic zone. The UC is mainly composed of a gelatinous matrix of different types of collagen supporting the two arteries and vein [39]. We detected the different tissue layers of the umbilical vein and arteries, as is depicted in Figure 1(a) and detailed in Figures 1(b) and 1(d). Within the stromal clefts lining the vessels, slender myofibroblast-like cells were observed (Figures 1(c) and 1(d)). Furthermore, we detected the presence of tripolar-shaped cells within the WJ and

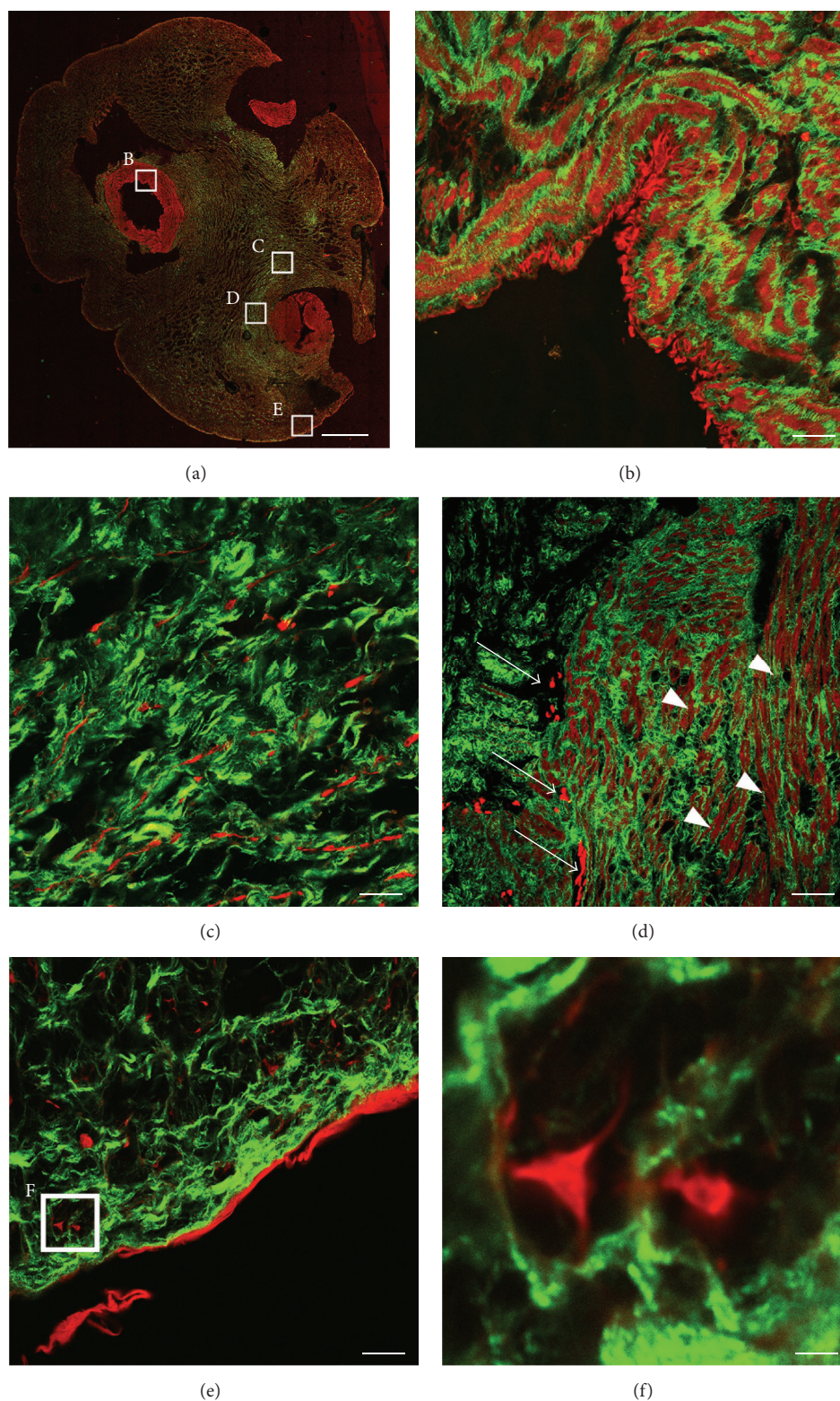


FIGURE 1: Label-free imaging of umbilical cord tissue compartments. (a) Image composition derived from multiple fields of view for AF (red) and SHG (green) in unstained cord tissue, scale bar = 1 mm. (B–E) Detailed image sections of (a), scale bars = 20 μ m. (b) Lamina intima and media of the umbilical vein. (c) Wharton's jelly and perivascular zone of an umbilical artery. (d) Umbilical artery media and adventitia showing intensely fluorescent cells (arrows) and less bright smooth muscle cell bodies (arrowheads). (e) Subamnion and amniotic epithelial layer. (F) Detailed image of (e) displaying tripolar cells within the subamniotic zone, scale bar = 2 μ m. Representative images from 3 independent donors are shown.

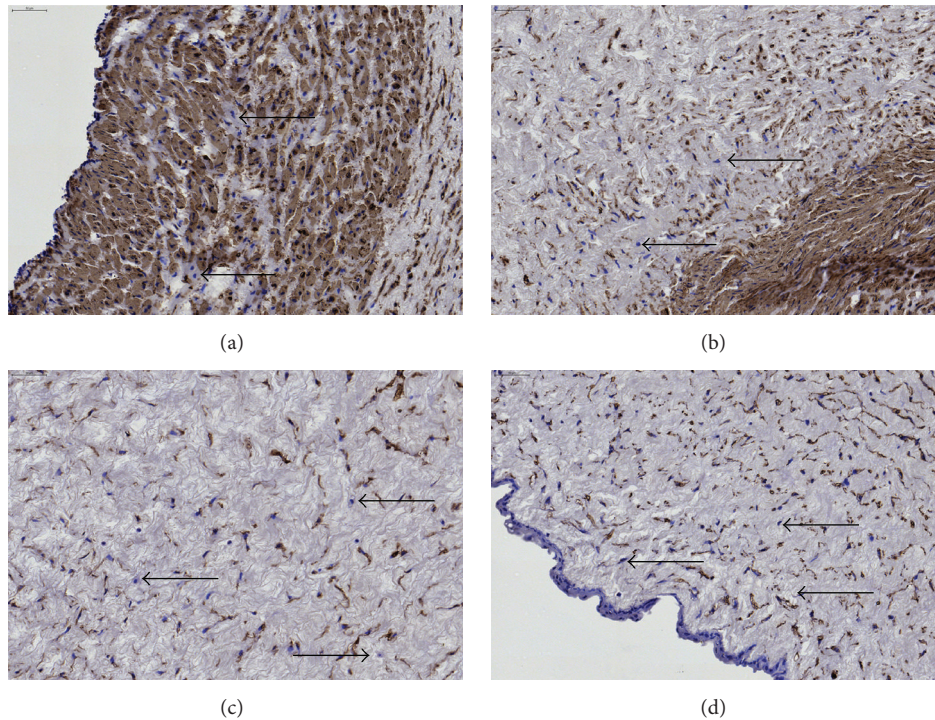


FIGURE 2: Staining of umbilical cord tissue for α SMA expression (brown). Images are shown for umbilical cord areas: (a) vein, (b) arteries, (c) Wharton's jelly, and (d) cord edge and amniotic epithelium. Slides were counterstained using Mayer's hematoxylin (dark blue = cell nuclei). Scale bars = 50 μ m. Unstained cells (black arrows) are found in all anatomical compartments of the cord. Representative images of 3 different experiments are shown. Images of control staining without primary antibody are available in the electronic Supplementary Material, Figure S1, available online at <http://dx.doi.org/10.1155/2016/5457132>. Scale bars = 50 μ m (top left corner).

subamniotic region (Figures 1(c), 1(e), and 1(f)). Finally, some hollow areas surrounding the vessels were observed (Figure 1(a)), likely caused by the presence of extraluminal blood that was washed out during sectioning.

3.2. Cellular Autofluorescence Does Not Discriminate between Stromal Cells but Is Less Bright in Vascular Smooth Muscle Cells. Autofluorescence was observed throughout the entire umbilical cord and was more localized to the vessel walls (Figure 1). This fluorescence signal originated from the highly abundant smooth muscle cells residing in the collagen deposits of the media, as was shown in parallel by α SMA staining (Figure 2 and Figure S1). Although autofluorescence was more confined to the vessels due to higher cell numbers, it was observed that the signal intensity of the surrounding stromal cells was higher compared to that of the smooth muscle fibers (Figure 1(d)). Nevertheless, no major difference in autofluorescence was observed between the stromal cells populations residing in the other compartments (Figure 1). Additionally, the vessels were further examined for cellular presence by nuclear staining with DAPI. Surprisingly, we observed a variance in nuclear fluorescent signal intensity amongst the cells residing in different areas of the vessel wall. As seen in Figure 3, cells located in the smooth muscle and collagen rich media of the vessel wall (red and green fluorescence, resp., Figures 3(a) and 3(b)) show higher

nuclear fluorescence intensity compared to cells from the perivascular adventitia (Figure 3(c)).

3.3. Imaging of Live WJ Explants and Cellular Outgrowth. Attached WJ explants were obtained approximately 10 days after isolation and subsequently imaged with TPM. In a label-free manner, we were able to visualize both the attached tissue structure and the outgrowing cells (Figure 4(b)). Our observation correlated with the cellular outgrowth visualized by bright field microscopy (Figure 4(a)). By scanning the explant attachment area (Z-stack; Figures 4(c) and 4(d)), we found a cellular migration pattern, showing a sloped downward outgrowth from the globular explant to the culture surface.

3.4. Validation of WJ-MSCs Chondrogenic Differentiation. To confirm the validity of our imaging approach, chondrogenic differentiation of WJ-MSCs was assessed. Detection of SHG after stem cell differentiation has already been reported for adult stromal cells [40, 41]. The chondrogenic pellet consists of a complex matrix containing glycosaminoglycans, collagen, and proteoglycans with stromal cells scattered throughout the matrix scaffold, as was shown in Figure 5(a) by Alcian Blue staining. Indeed, based on their autofluorescence, WJ-MSCs were observed in the pellet's cleft-like structures visualized by SHG (Figures 5(c) and 5(d)). Furthermore,

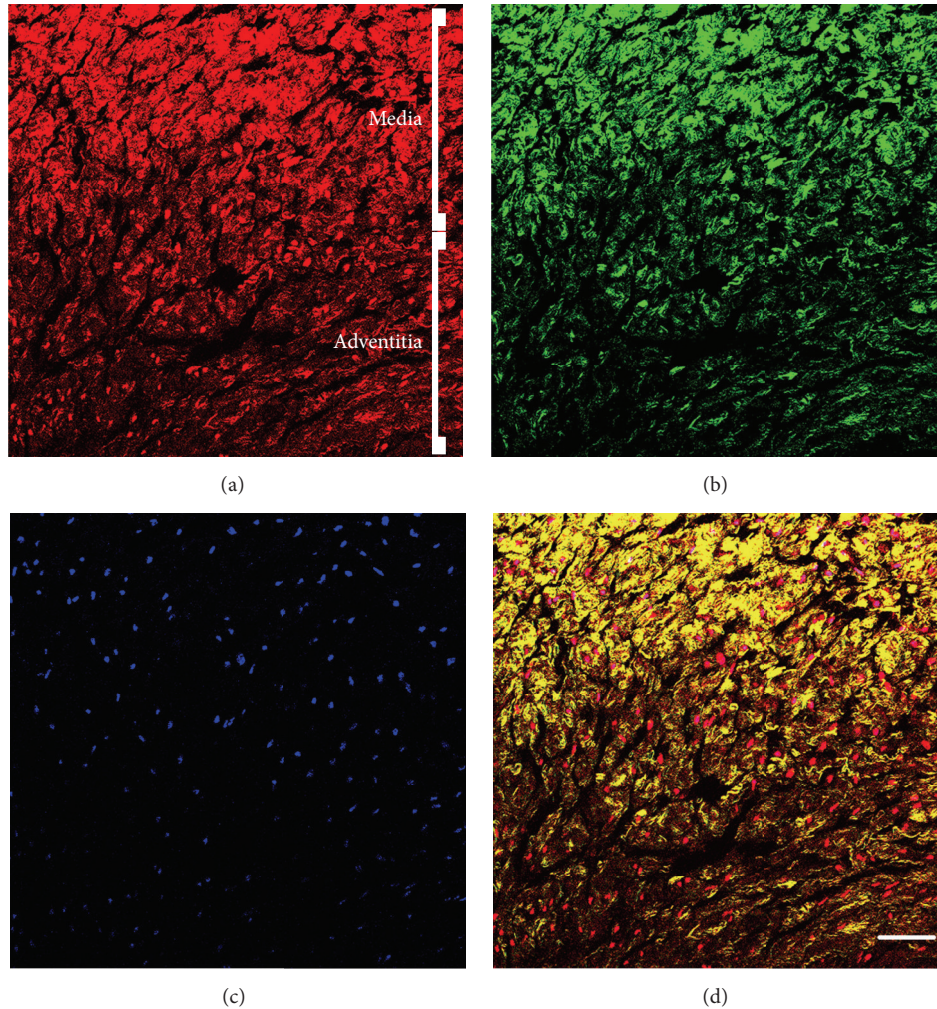


FIGURE 3: TPM and SHG imaging of DAPI stained umbilical cord vein showing a differential staining intensity for DAPI. (a) AF signal and (b) SHG derived from the vessel media and adventitia. Increased AF density originates from the media smooth muscle cells. In addition, more SHG is observed in the media due to higher collagen content, as expected. (c) An increasing gradient in DAPI fluorescence was observed towards the media of the umbilical vein. (d) Merged image. Scale bar = 50 μm .

a bright nodule composed of a cellular center surrounded by collagen could be observed at the edge of the pellet (Figures 5(b) and 5(c)). In addition, we imaged the adipogenic and osteogenic differentiation end state (Figure S3). After adipogenic differentiation (Figures S3a and S3c), confirmed by ORO staining, we observed the typical voids in fluorescent signal due to lipid droplet accumulation. For the osteogenic differentiation (Figures S3b and S3d), low SHG signal was detected, originating from collagen deposition in the ECM during differentiation. Validity of the differentiation was shown by *de novo* osteocalcin expression.

3.5. TPM Imaging of WJ-MSCs in Culture Indicates That Autofluorescence Originates from the Perinuclear Organelles. Besides umbilical cord tissue, cultures of explant-derived cells were also visualized using TPM. As shown in Figure S2, WJ-MSCs have a fibroblast-like morphology and possess large nuclei and multiple nucleoli and have their organelles

confined to the perinuclear region of the cytoplasm. The latter was also shown by Struys et al. at the ultrastructural level [38]. Interestingly, in this study, we observed autofluorescence originating from the perinuclear zone of live cells in culture (Figures 6(b) and 6(d)). Few SHG scatter could be observed (Figure 6(c)).

3.6. Differences in Oct4, αSMA , Vimentin, Pan-CK, and ALDH1A1 Expression In Situ. As was previously shown by us and others, cultured WJ-MSCs express several surface and intracellular markers, such as the classical MSCs phenotype panel, but also several other, for instance, multipotency markers (e.g., Oct4, nucleus), adhesion molecules (e.g., CD54, membrane), or immune modulatory molecules (e.g., IDO-1, cytosol) [4, 42, 43]. Here, we attempted to localize the WJ-MSCs *in situ* by assessing the expression of Oct4, a transcription factor related to the pluripotent stem cell state [44]. In addition, we performed stainings for αSMA , in

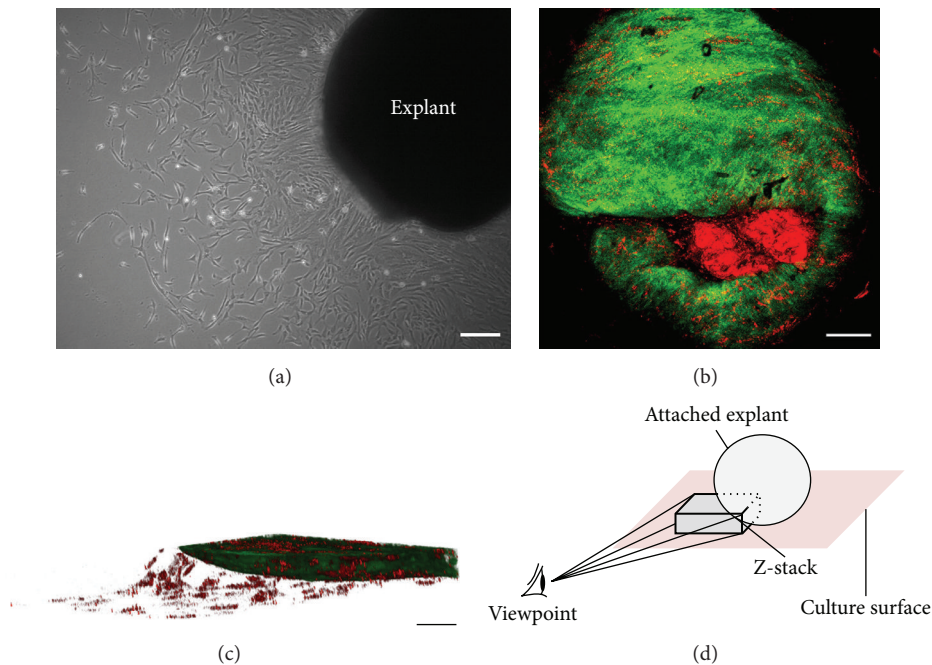


FIGURE 4: Marker-free visualization of Wharton's jelly explant tissue and cell outgrowth. (a) Phase contrast image of an attached explant with outgrowing WJ-MSCs, scale bar = 200 μm . (b) AF (red) and SHG (green) of an attached explant (attachment site, bottom view), scale bar = 100 μm . (c) 2D image of cellular outgrowth from explant tissue at the attachment site (side view), scale bar = 50 μm . The images were derived from a Z-stack composition of the SHG and AF signals of (b). (d) Schematic view of the visualization plane of (c). Representative images for 3 independent experiments are shown.

order to assess the perivascular niche of smooth muscle and myofibroblast-like cells, and ALDH1A1 which is expressed in various stem cell populations [45]. Furthermore, we assessed the expression of cytoskeletal proteins by staining for pan-CK and vimentin (an intermediate filament found in cells of mesenchymal origin) [38, 46]. We could not correlate a specific expression pattern for these markers to a particular anatomical location within the umbilical cord, as both positive and negative cells were found in all areas (Figures 7–9 and Figure S4). Respective negative control stainings are depicted in the electronic Supplementary Material, Figures S1, S4c, S4f, S4i, and S4l.

αSMA expression was intensely observed in the umbilical vessels, as was to be expected because of the smooth muscle cells presented there. Interestingly, also WJ stromal cells expressed αSMA (Figures 7(a) and 2); however, we could not observe increased cellular staining within the perivascular zone compared to other areas (data not shown). Analysis of vimentin and pan-CK expression indicated that positive cells are scattered throughout the entire umbilical cord, including the perivascular areas (Figures S4a–S4f), stroma (Figures S4g–S4i), and subamniotic zone (Figures S4j–S4l). Of note, the cord lining epithelial membrane did not express vimentin *in situ* but showed intense pan-CK staining. Oct4 was expressed in cultured WJ cells (Figure 7(c)) and also *in situ* by most perivascular cells, stromal cells, and even amniotic epithelial cells (Figure 8). ALDH1A1 staining is more confined to the media of the umbilical vessels, but also WJ matrix cells express the protein (Figure 9). Interestingly,

in WJ cell cultures, all cells were positive for ALDH1A1 (Figure 7(b)), indicating that either a specific cell population is isolated into culture or a culture induced expression occurs. Moreover, we observed a variable expression intensity within the heterogeneous culture, where mainly the smaller cells displayed a darker staining pattern.

4. Discussion

Multiphoton and higher harmonic generation imaging offers a high-resolution characterization tool for tissues and stem cells, because of its noninvasive and marker-free nature, whereas traditional assessments of tissue structure are destructive at both the molecular and the structural level (e.g., protein expression and extracellular matrix degradation). Consequently, this nondestructive, label-free approach offers a powerful high-content characterization tool for optimizing tissue engineering protocols and assessing engineered tissue implants [47]. Furthermore, the possibility for noninvasive optical tracking of cells and tissue structure *in vitro* can be applied in future studies to assess tissue development, drug toxicity screening, or other therapeutic interventions (e.g., cellular implants) [27, 48, 49].

In this study, the first steps towards label-free identification of umbilical cord tissue and stem cell culturing were assessed. By measuring AF and SHG after TPM, we were able to visualize the major anatomical compartments of the human UC. A detailed description of these anatomic locations, their composition, and their potential stem cell

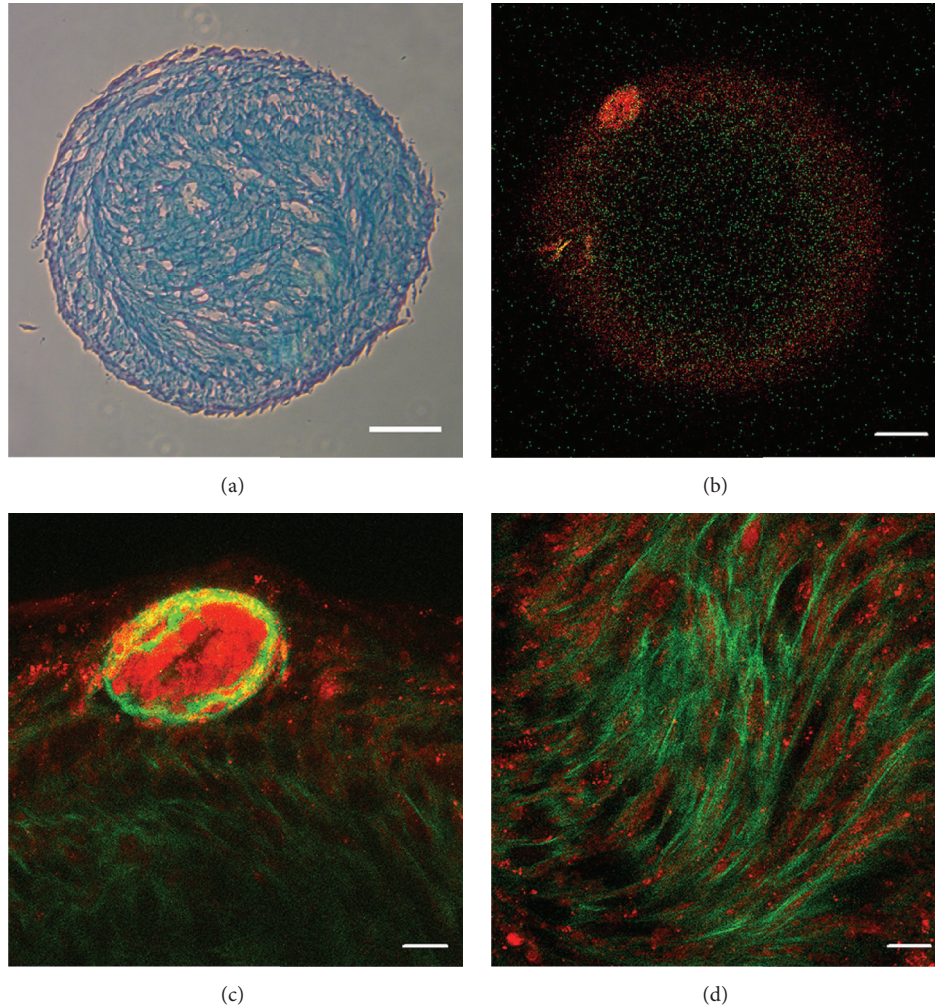


FIGURE 5: TPM and SHG imaging of WJ-MSCs chondrogenic differentiation. (a) Alcian Blue staining of a chondrogenic pellet section, visualizing the nuclei (red) and chondrogenic matrix (blue), scale bar = 200 μm . (b–d) AF (red) and SHG (green) imaging of an intact chondrogenic pellet of ± 1 mm diameter. (b) Chondrogenic pellet center, scale bar = 100 μm . (c) Cell and matrix nodule at the pellet border, scale bar = 20 μm . (d) Differentiated cells within their collagen rich matrix in the center of the pellet, scale bar = 20 μm . Representative images for 2 independent experiments are shown.

content can be found elsewhere [2, 8, 13]. We clearly observed the cellular arrangement in the perivascular zones and vessel walls. In addition, we detected stromal cells within the less densely populated cord matrix and subamniotic zone. Our findings closely relate to a number of histological studies, which already described differences in radial distribution of stromal cells and extracellular matrix (ECM) components [39, 50]. Similar structures and cellular distribution patterns could be observed by our imaging approach, for example, the presence of tripolar cells in the subamniotic zone. Of note, our study visualized the cellular and structural arrangement throughout the cord using only the intrinsic fluorescence of cells and tissue components generated after pulsed laser excitation, without additional manipulation of the samples.

In contrast to a previous report by Uchugonova and König, who imaged different subpopulations of cells using a label-free setup [41], we could not discriminate between possible subpopulations of cells based on differences in

autofluorescence signal intensity. Although AF was highly abundant in the walls of the umbilical vessels, individual cells did not show increased or decreased intensities compared to cells in other UC areas. Nevertheless, we conducted an additional experiment to stain for nuclei within the tissue to investigate the colocalization of cells and AF. Surprisingly, we observed a differential fluorescent intensity in DNA stain (DAPI). We assume that such discrepancy is suggestive of differences in DNA content between the smooth muscle cells and the adventitial cells, given that the staining efficiency is equal for the different cell types mentioned. Previous studies showed that the integrated fluorescence intensity of DAPI gives a good measure of DNA content [51, 52]. This is likely due to differences in metabolic state of the aforementioned cells, with smooth muscle cells being more active than the surrounding supportive cells. To further assess this finding, immunological staining but also ultrastructural analysis of the chromatin using transmission electron microscopy

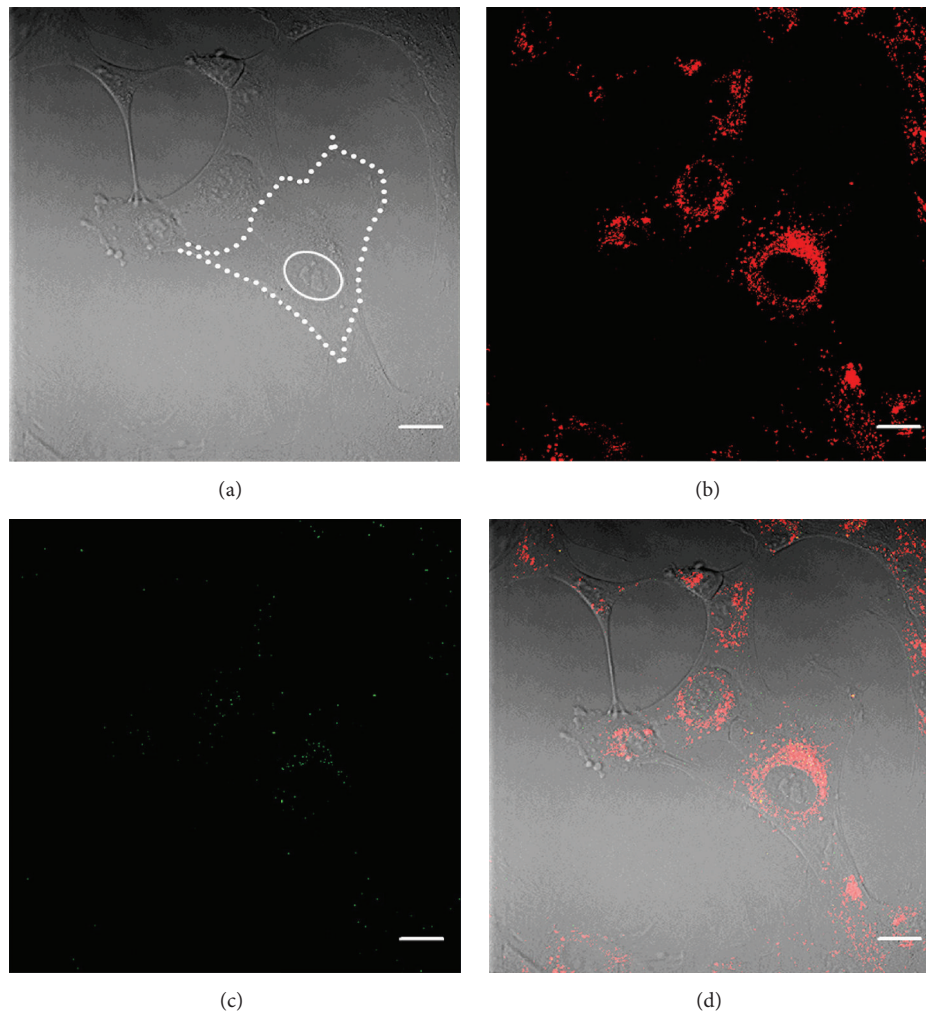


FIGURE 6: Autofluorescence originates from the perinuclear organelles in WJ-MSCs. (a) Bright field image of explant-derived WJ-MSCs. For reference, the cell boundary is delineated by a dotted white line and the nucleus is outlined by a full white line. (b) AF signal (red) and (c) SHG after two-photon excitation of the same cells. (d) Merged image. A perinuclear area of organelles is visible (view also the electronic Supplementary Material, Figure S2). Scale bars = 20 μm .

should be performed. Furthermore, others have documented the isolation of multipotent stem cells from the umbilical vein perivascular zone [53]. As such, it should be investigated whether DNA content correlates with the presence of multipotent progenitor cells, using, for example, the TPM/SHG imaging approach in conjunction with fluorescently labeled antibodies against multiple progenitor population-related markers (e.g., SSEA-4, CD271, and CD133).

To validate our imaging approach, we included the analysis of chondrogenic differentiated WJ-MSCs pellets. Rice et al. reported the quantitative use of two-photon excitation fluorescence and SHG for noninvasively monitoring MSCs differentiation [40]. They indicated that, by measuring the endogenous sources of contrast such as collagen, changes in cell metabolic activity, morphology, and extracellular matrix production can be visualized. As such, we could clearly detect the chondrogenic pellet and distinguish the newly formed matrix and cells scattered throughout the scaffold. Additionally, we imaged monolayer cultures of WJ-MSCs

that were fully differentiated towards the adipogenic and osteogenic lineage. Two-photon excitation fluorescence and SHG imaging of adipo- and osteogenic differentiation were already reported for human bone-marrow-derived MSCs cultures [35, 40]. After adipogenic differentiation, we observed similar voids in the fluorescent signal due to lipid droplet accumulation. For the osteogenic differentiation, low SHG signal was detected, originating from collagen deposition in the ECM during differentiation. In this case, we did not expect dramatic signal changes, since our previous report indicated that WJ-MSCs represent an immature progenitor of *in vitro* osteogenesis [38]. Furthermore, our cultures were differentiated at normal oxygen levels, while Rice et al. observed increased collagen deposition under hypoxic differentiation conditions [40]. Nevertheless, our label-free and IHC analyses confirm the trilineage differentiation potential of our WJ-MSCs cultures.

Apart from imaging the UC tissue, we were able to visualize WJ-derived cells, both during isolation and in culture.

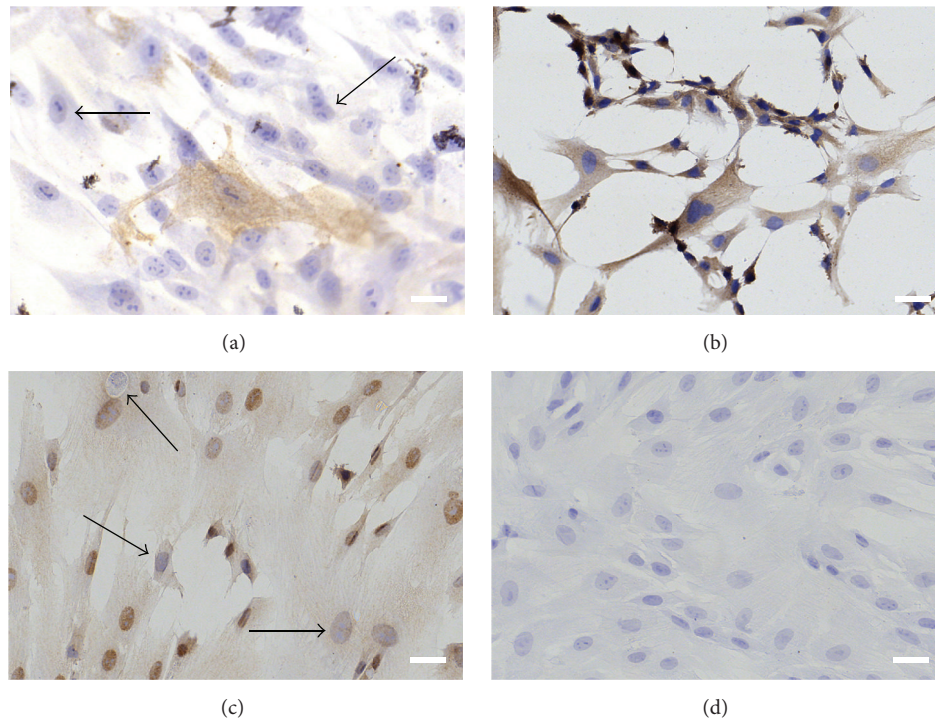


FIGURE 7: Staining of WJ-MSCs in culture for (a) α SMA, (b) ALDH1A1, and (c) Oct4 expression. (d) Representative control staining without primary antibody. All cells stain positive (brown) for ALDH1A1, but not for α SMA and Oct4 (black arrows), indicating that a heterogeneous cell isolate was obtained. Scale bars = 50 μ m. Representative images of at least 3 donors are shown.

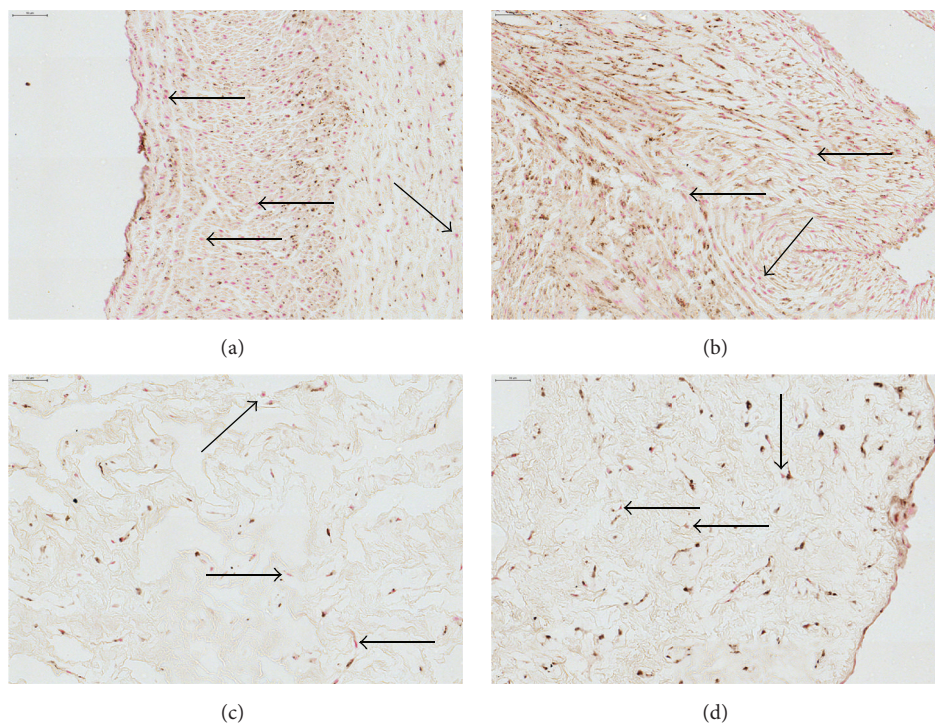


FIGURE 8: Staining of umbilical cord tissue for Oct4 expression (brown). Nuclei (red) were visualized using NFR counterstain. Images are shown for umbilical cord areas: (a) vein, (b) arteries, (c) Wharton's jelly, and (d) cord edge and amniotic epithelium. Scale bars = 50 μ m. Unstained cells (black arrows) are found in all anatomical compartments of the cord. Representative images of 3 different experiments are shown. Images of control staining without primary antibody are available in the electronic Supplementary Material, Figure S1. Scale bars = 50 μ m (top left corner).

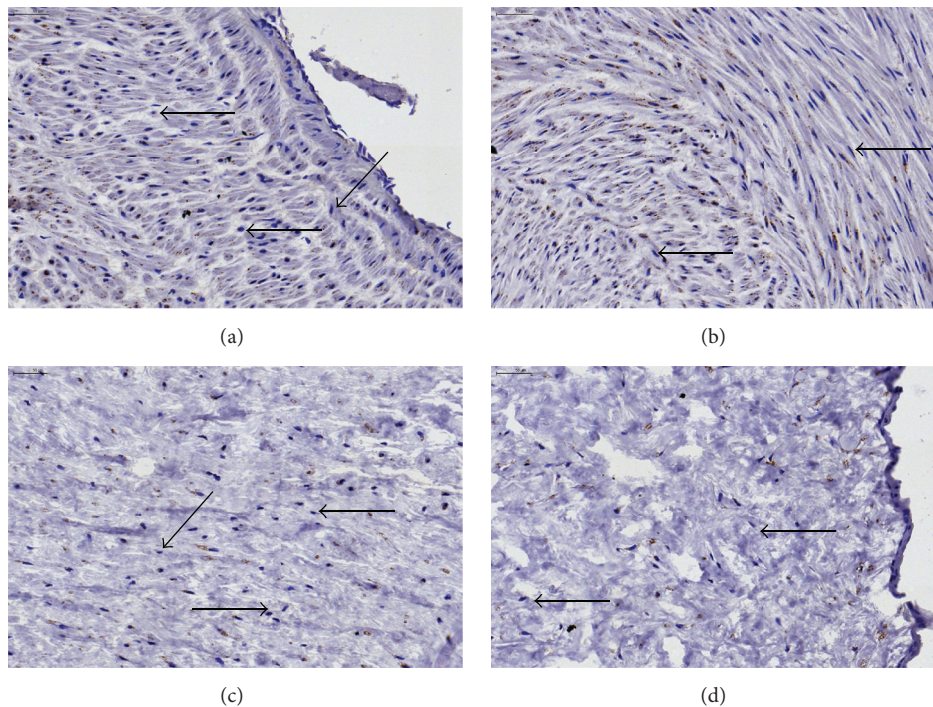


FIGURE 9: Staining of umbilical cord tissue for ALDH1A1 expression (brown). Images are shown for umbilical cord areas: (a) vein, (b) arteries, (c) Wharton's jelly, and (d) cord edge and amniotic epithelium. Slides were counterstained using Mayer's hematoxylin (dark blue = cell nuclei). Scale bars = 50 μm . Unstained cells (black arrows) are found in all anatomical compartments of the cord. Representative images of 3 different experiments are shown. Images of control staining without primary antibody are available in the electronic Supplementary Material, Figure S1. Scale bars = 50 μm (top left corner).

While the cultured cells mainly presented without SHG, AF signal originated from the organelle rich perinuclear zone. Such finding is of interest since it could allow for the detection of cells based on their specific intracellular molecules. Using flow cytometry, Molinos et al. recently reported the detection of three distinct cell subsets based on a difference in autofluorescent signal [54]. Exploiting endogenous fluorophores as biomarkers for cell detection might be of beneficial use for veterinary research of the umbilical cord, since immunomarkers are not always available (e.g., equine or canine research) [31]. Further studies are required to validate different laser imaging setups (e.g., flow cytometry versus confocal laser scanning microscopy) and characterize the specific signals originating from the cells.

Besides the visualization of growing cells on coverslips, our AF and SHG based imaging approach is ideally suited to visualizing the initiation of explant cell cultures. Both the collagen rich explant fragments (SHG) and outgrowing cells (AF) were easily detected upon attachment to the culture chamber. Furthermore, the explant culturing technique preserves the initial WJ tissue (cellular niche) from which the cells arise. Consequently, we suggest that such label-free analysis can prove useful in discovering the origin of outgrowing cells, while imaging the explant culture process in real time.

It is currently unclear whether a specific tissue compartment of the UC contains multipotent stromal cells. Until now, it has not been possible to pinpoint a stem cell niche and

subsequently follow the migration of the desired multipotent cells out of that tissue compartment. Their identification still occurs when cells are already in culture. Consequently, it still proves difficult to isolate specific populations of progenitors. A number of studies have attempted to address the *in situ* to *in vitro* transition of umbilical cord stem cells by correlating marker expression of cell cultures to their tissue origin [46, 55–57]. Yet, several issues further complicate such research, for example, the appearance of various cell populations with different isolation techniques (e.g., type I and type II cells) but also possible contamination by other cells and the lack of a specific multipotent stem cell biomarker, giving no conclusive results [50, 58]. Furthermore, for some markers, protein expression was induced or gradually diminished upon culturing, making it difficult to trace back the cells to their point of origin within the tissue [46]. We assessed the expression of multiple candidate stem cell markers for expression *in situ* and in culture. Initially, we assessed the expression of Oct4, a marker for pluripotent stem cells [44], αSMA , a marker commonly expressed by smooth muscle cells but also mesenchymal stromal cells [59], and ALDH1A1 which is expressed in both normal and cancer stem cell populations [45]. Using standard immunohistochemistry, we tried to localize differences in antigen expression patterns; however, we were not able to confine the markers to specific UC areas. Of note, in all cord compartments unstained cells could be observed, indicating that *in situ* differences in marker expression already preexist. Our findings are in line

with previous reports, showing α SMA expression located in the umbilical vessels and WJ [60] and indicating the presence of Oct4 expressing cells within the WJ [43]. Additionally, we assessed the expression of vimentin, a cytoskeletal filament expressed by MSCs. Vimentin was abundantly expressed throughout the entire umbilical cord tissue except for the amniotic membrane. Our *in situ* analysis and previous reported cell culture data [38] confirm the recent report of Coskun and Can, in which they show that explants-derived cells originate from the UC stroma and not from the amniotic membrane as determined by their positive expression of vimentin and α SMA in culture [46].

In our explant cell cultures, a variable expression pattern was shown for α SMA and Oct4. In contrast to these markers, ALDH1A1 was expressed in all cultured cells. Furthermore, differences in ALDH1A1 intensity were observed between the smaller tripolar-shaped cells and the larger fibroblast-like cells. Whether those cells can be traced back to the tripolar cells in the subamniotic zone remains to be determined in ongoing experiments. Other studies already showed ALDH expression in primitive multipotent stem cells isolates [61–63]. Because of the differential expression pattern in umbilical cord tissue and isolated cells, more studies on the expression of this enzyme during culture initiation should be performed. Moreover, several stem cell related markers are difficult to trace back to their tissue of origin as their expression is influenced by both the isolation and the culture methods used (phenotype change) [46, 57, 64]. Cells derived from different compartments of the human umbilical cord were shown to express different amounts of CK subtypes in culture, depending on their isolation method [64]. We found expression of pan-CK at multiple sites in the umbilical cord, similar to the recently reported *in situ* study by Coskun and Can [46]. The pan-CK antibody used in this study, which contains CK 5, 6, 8, 17, and 19 subtypes, stained positive in all stromal cells and perivascular areas, but the highest staining intensity was observed for the amniotic epithelial cells lining the cord.

Other MSCs confined markers such as N-cadherin or desmin [56] are interesting candidates for tracking studies of explants in combination with the label-free imaging setup. We suggest that, by using AF and SHG imaging combined with specific antibody labeling, cellular outgrowth from the explants can be followed in real time (fluorescence lifetime imaging) with the potential to identify different cell subtypes. Such approach is already used in cancer research, imaging both cancer cell migration and ECM remodeling [65–67].

Collectively, this study shows that AF and SHG detection is a potent and easy approach for the visualization of stem cells *in situ* and may form a starting point for further biological studies of umbilical cord-derived stem cells. AF and SHG are optimally suited for visualization of live explants in culture. As such, the imaging approach can be a useful tool for assessing the *in situ* to culture transition of stem cells as well as for determining optimal isolation and culturing conditions. We speculate that AF and SHG imaging could prove useful in discovering the origin of outgrowing cells, while imaging the explant culture process in real time. Furthermore, the potential for high-resolution live imaging

should be further explored in conjunction with other modern labeling techniques, such as antibodies conjugated to near-infrared excitable fluorophores [68, 69], quantum dots [70], or other nanoparticles [71, 72], provided there is no spectral overlap. Label-free monitoring of stem cells, in combination with such advanced staining techniques, opens perspectives for better cells characterization both *in situ* and *ex vivo*, by simultaneously visualizing resident cells and extracellular components. Hence, AF and SHG imaging can be a vital additional tool for unraveling the stem cell niche within the umbilical cord and other tissues.

Abbreviations

α SMA:	Alpha smooth muscle actin
AF:	Autofluorescence
ALDH1A1:	Aldehyde dehydrogenase family 1 member A1
DAB:	Diaminobenzidine
DAPI:	4',6-Diamidino-2-phenylindole
ECM:	Extracellular matrix
HRP:	Horseradish peroxidase
MSCs:	Mesenchymal stem cells
NFR:	Nuclear Fast Red
Oct4:	Octamer-binding transcription factor 4
pan-CK:	Pan cytokeratin
P/S:	Penicillin-streptomycin
PBS:	Phosphate-buffered saline
PFA:	Paraformaldehyde
SHG:	Second harmonic generation
TBS-T:	Tris-buffered saline with 0.05% Tween-20
TPM:	Two-photon confocal laser scanning microscopy
UC:	Umbilical cord
WJ:	Wharton's jelly
WJ-MSCs:	Wharton's jelly-derived mesenchymal stem cells.

Competing Interests

The authors declare that they have no competing interests.

Acknowledgments

The authors would like to thank Ms. Katrien Wauterickx, Dr. Petra Hilken, and Ms. Jeanine Santermans for assistance with the immunohistochemical staining and paraffin embedding of the umbilical cord tissues. This research was financially supported by the agency for Innovation through Science and Technology (Agentschap voor Innovatie door Wetenschap en Technologie, IWT), the Research Foundation-Flanders (Fonds Wetenschappelijk Onderzoek Vlaanderen, FWO), the Transnational University Limburg, Hasselt University, and the Belgian Charcot Foundation. The Province of Limburg (Belgium) is acknowledged for financial support within the tUL IMPULS FASE II program, allowing for the upgrading of the laser source used in this work.

References

- [1] R. R. Taghizadeh, K. J. Cetrulo, and C. L. Cetrulo, "Wharton's Jelly stem cells: future clinical applications," *Placenta*, vol. 32, supplement 4, pp. S311–S315, 2011.
- [2] D. L. Troyer and M. L. Weiss, "Wharton's Jelly-derived cells are a primitive stromal cell population," *Stem Cells*, vol. 26, no. 3, pp. 591–599, 2008.
- [3] J. P. McGuirk and M. L. Weiss, "Promising cellular therapeutics for prevention or management of graft-versus-host disease (a review)," *Placenta*, vol. 32, supplement 4, pp. S304–S310, 2011.
- [4] R. Donders, M. Vanheusden, J. F. J. Bogie et al., "Human Wharton's jelly-derived stem cells display immunomodulatory properties and transiently improve rat experimental autoimmune encephalomyelitis," *Cell Transplantation*, vol. 24, no. 10, pp. 2077–2098, 2015.
- [5] M. L. Weiss, S. Medicetty, A. R. Bledsoe et al., "Human umbilical cord matrix stem cells: preliminary characterization and effect of transplantation in a rodent model of Parkinson's disease," *Stem Cells*, vol. 24, no. 3, pp. 781–792, 2006.
- [6] G. Yu, C. V. Borlongan, C. E. Stahl et al., "Systemic delivery of umbilical cord blood cells for stroke therapy: a review," *Restorative Neurology and Neuroscience*, vol. 27, no. 1, pp. 41–54, 2009.
- [7] M. T. Conconi, R. D. Liddo, M. Tommasini, C. Calore, and P. P. Parnigotto, "Phenotype and differentiation potential of stromal populations obtained from various zones of human umbilical cord: an overview," *Open Tissue Engineering and Regenerative Medicine Journal*, vol. 4, no. 1, pp. 6–20, 2011.
- [8] A. Can and S. Karahuseyinoglu, "Concise review: human umbilical cord stroma with regard to the source of fetus-derived stem cells," *Stem Cells*, vol. 25, no. 11, pp. 2886–2895, 2007.
- [9] Y. A. Romanov, V. A. Svintsitskaya, and V. N. Smirnov, "Searching for alternative sources of postnatal human mesenchymal stem cells: candidate MSC-like cells from umbilical cord," *STEM CELLS*, vol. 21, no. 1, pp. 105–110, 2003.
- [10] K. E. Mitchell, M. L. Weiss, B. M. Mitchell et al., "Matrix cells from Wharton's jelly form neurons and glia," *Stem Cells*, vol. 21, no. 1, pp. 50–60, 2003.
- [11] L.-F. Wu, N.-N. Wang, Y.-S. Liu, and X. Wei, "Differentiation of Wharton's jelly primitive stromal cells into insulin-producing cells in comparison with bone marrow mesenchymal stem cells," *Tissue Engineering—Part A*, vol. 15, no. 10, pp. 2865–2873, 2009.
- [12] L. Wang, I. Tran, K. Seshareddy, M. L. Weiss, and M. S. Detamore, "A comparison of human bone marrow-derived mesenchymal stem cells and human umbilical cord-derived mesenchymal stromal cells for cartilage tissue engineering," *Tissue Engineering Part A*, vol. 15, no. 8, pp. 2259–2266, 2009.
- [13] D.-W. Kim, M. Staples, K. Shinozuka, P. Pantcheva, S.-D. Kang, and C. V. Borlongan, "Wharton's jelly-derived mesenchymal stem cells: phenotypic characterization and optimizing their therapeutic potential for clinical applications," *International Journal of Molecular Sciences*, vol. 14, no. 6, pp. 11692–11712, 2013.
- [14] S. Balasubramanian, P. Venugopal, S. Sundarraj, Z. Zakaria, A. S. Majumdar, and M. Ta, "Comparison of chemokine and receptor gene expression between Wharton's jelly and bone marrow-derived mesenchymal stromal cells," *Cytotherapy*, vol. 14, no. 1, pp. 26–33, 2012.
- [15] R. Anzalone, M. L. Iacono, S. Corrao et al., "New emerging potentials for human Wharton's jelly mesenchymal stem cells: immunological features and hepatocyte-like differentiative capacity," *Stem Cells and Development*, vol. 19, no. 4, pp. 423–438, 2010.
- [16] I. Kalaszczynska and K. Ferdyn, "Wharton's jelly derived mesenchymal stem cells: future of regenerative medicine? Recent findings and clinical significance," *BioMed Research International*, vol. 2015, Article ID 430847, 11 pages, 2015.
- [17] M. Dominici, K. Le Blanc, I. Mueller et al., "Minimal criteria for defining multipotent mesenchymal stromal cells. The International Society for Cellular Therapy position statement," *Cytotherapy*, vol. 8, no. 4, pp. 315–317, 2006.
- [18] K. P. Quinn, G. V. Sridharan, R. S. Hayden, D. L. Kaplan, K. Lee, and I. Georgakoudi, "Quantitative metabolic imaging using endogenous fluorescence to detect stem cell differentiation," *Scientific Reports*, vol. 3, article 3432, 2013.
- [19] B. Bruneel, M. Mathä, R. Paesen, M. Ameloot, W. J. Weninger, and A. Huysseune, "Imaging the zebrafish dentition: from traditional approaches to emerging technologies," *Zebrafish*, vol. 12, no. 1, pp. 1–10, 2015.
- [20] J. Mertz, "Nonlinear microscopy: new techniques and applications," *Current Opinion in Neurobiology*, vol. 14, no. 5, pp. 610–616, 2004.
- [21] P. Friedl, K. Wolf, G. Harms, and U. H. von Andrian, "Biological second and third harmonic generation microscopy," *Current Protocols in Cell Biology*, 2007.
- [22] G. Cox, E. Kable, A. Jones, I. Fraser, F. Manconi, and M. D. Gorrell, "3-Dimensional imaging of collagen using second harmonic generation," *Journal of Structural Biology*, vol. 141, no. 1, pp. 53–62, 2003.
- [23] I. Georgakoudi and K. P. Quinn, "Optical imaging using endogenous contrast to assess metabolic state," *Annual Review of Biomedical Engineering*, vol. 14, pp. 351–367, 2012.
- [24] S. W. Perry, R. M. Burke, and E. B. Brown, "Two-photon and second harmonic microscopy in clinical and translational cancer research," *Annals of Biomedical Engineering*, vol. 40, no. 2, pp. 277–291, 2012.
- [25] G. Cox and E. Kable, "Second-harmonic imaging of collagen," *Methods in Molecular Biology*, vol. 319, pp. 15–35, 2006.
- [26] G. Cox, "Biological applications of second harmonic imaging," *Biophysical Reviews*, vol. 3, no. 3, pp. 131–141, 2011.
- [27] A. Mauri, M. Perrini, J. M. Mateos et al., "Second harmonic generation microscopy of fetal membranes under deformation: normal and altered morphology," *Placenta*, vol. 34, no. 11, pp. 1020–1026, 2013.
- [28] I. Georgakoudi, W. L. Rice, M. Hronik-Tupaj, and D. L. Kaplan, "Optical spectroscopy and imaging for the noninvasive evaluation of engineered tissues," *Tissue Engineering Part B: Reviews*, vol. 14, no. 4, pp. 321–340, 2008.
- [29] E. Güç, M. Fankhauser, A. W. Lund, M. A. Swartz, and W. W. Kilarski, "Long-term intravital immunofluorescence imaging of tissue matrix components with epifluorescence and two-photon microscopy," *Journal of Visualized Experiments*, no. 86, Article ID e51388, 2014.
- [30] H. Lim, D. Sharoukhov, I. Kassim, Y. Zhang, J. L. Salzer, and C. V. Melendez-Vasquez, "Label-free imaging of Schwann cell myelination by third harmonic generation microscopy," *Proceedings of the National Academy of Sciences of the United States of America*, vol. 111, no. 50, pp. 18025–18030, 2014.
- [31] G. Santin, M. Paulis, P. Vezzoni, G. Pacchiana, G. Bottiroli, and A. C. Croce, "Autofluorescence properties of murine embryonic stem cells during spontaneous differentiation phases," *Lasers in Surgery and Medicine*, vol. 45, no. 9, pp. 597–607, 2013.

- [32] J. Herz, M. Paterka, R. A. Niesner et al., "In vivo imaging of lymphocytes in the CNS reveals different behaviour of naïve T cells in health and autoimmunity," *Journal of Neuroinflammation*, vol. 8, article 131, 2011.
- [33] K. König, A. Uchugonova, and E. Gorjup, "Multiphoton fluorescence lifetime imaging of 3D-stem cell spheroids during differentiation," *Microscopy Research and Technique*, vol. 74, no. 1, pp. 9–17, 2011.
- [34] H.-S. Lee, S.-W. Teng, H.-C. Chen et al., "Imaging human bone marrow stem cell morphogenesis in polyglycolic acid scaffold by multiphoton microscopy," *Tissue Engineering*, vol. 12, no. 10, pp. 2835–2841, 2006.
- [35] W. L. Rice, D. L. Kaplan, and I. Georgakoudi, "Quantitative biomarkers of stem cell differentiation based on intrinsic two-photon excited fluorescence," *Journal of Biomedical Optics*, vol. 12, no. 6, Article ID 060504, 2007.
- [36] R. Dittmar, E. Potier, M. van Zandvoort, and K. Ito, "Assessment of cell viability in three-dimensional scaffolds using cellular auto-fluorescence," *Tissue Engineering Part C: Methods*, vol. 18, no. 3, pp. 198–204, 2012.
- [37] R. Dittmar, B. G. M. Van Dijk, M. A. M. J. Van Zandvoort, and K. Ito, "In situ label-free cell viability assessment of nucleus pulposus tissue," *Journal of Orthopaedic Research*, vol. 32, no. 4, pp. 545–550, 2014.
- [38] T. Struys, M. Moreels, W. Martens, R. Donders, E. Wolfs, and I. Lambrechts, "Ultrastructural and immunocytochemical analysis of multilineage differentiated human dental pulp- and umbilical cord-derived mesenchymal stem cells," *Cells Tissues Organs*, vol. 193, no. 6, pp. 366–378, 2011.
- [39] A. K. Nanaev, G. Kohnen, A. P. Milovanov, S. P. Domogatsky, and P. Kaufmann, "Stromal differentiation and architecture of the human umbilical cord," *Placenta*, vol. 18, no. 1, pp. 53–64, 1997.
- [40] W. L. Rice, D. L. Kaplan, and I. Georgakoudi, "Two-photon microscopy for non-invasive, quantitative monitoring of stem cell differentiation," *PLoS ONE*, vol. 5, no. 4, Article ID e10075, 2010.
- [41] A. Uchugonova and K. König, "Two-photon autofluorescence and second-harmonic imaging of adult stem cells," *Journal of Biomedical Optics*, vol. 13, no. 5, article 054068, 2008.
- [42] A. K. Batsali, M.-C. Kastrinaki, H. A. Papadaki, and C. Pontikoglou, "Mesenchymal stem cells derived from Wharton's jelly of the umbilical cord: biological properties and emerging clinical applications," *Current Stem Cell Research and Therapy*, vol. 8, no. 2, pp. 144–155, 2013.
- [43] G. La Rocca, R. Anzalone, S. Corrao et al., "Isolation and characterization of Oct-4⁺/HLA-G⁺ mesenchymal stem cells from human umbilical cord matrix: differentiation potential and detection of new markers," *Histochemistry and Cell Biology*, vol. 131, no. 2, pp. 267–282, 2009.
- [44] G. Shi and Y. Jin, "Role of Oct4 in maintaining and regaining stem cell pluripotency," *Stem Cell Research and Therapy*, vol. 1, article 39, 2010.
- [45] J. S. Moreb, "Aldehyde dehydrogenase as a marker for stem cells," *Current Stem Cell Research and Therapy*, vol. 3, no. 4, pp. 237–246, 2008.
- [46] H. Coskun and A. Can, "The assessment of the in vivo to in vitro cellular transition of human umbilical cord multipotent stromal cells," *Placenta*, vol. 36, no. 2, pp. 232–239, 2015.
- [47] K. P. Quinn, E. Bellas, N. Fourligas, K. Lee, D. L. Kaplan, and I. Georgakoudi, "Characterization of metabolic changes associated with the functional development of 3D engineered tissues by non-invasive, dynamic measurement of individual cell redox ratios," *Biomaterials*, vol. 33, no. 21, pp. 5341–5348, 2012.
- [48] A. Ward, K. P. Quinn, E. Bellas, I. Georgakoudi, and D. L. Kaplan, "Noninvasive metabolic imaging of engineered 3D human adipose tissue in a perfusion bioreactor," *PLoS ONE*, vol. 8, no. 2, Article ID e55696, 2013.
- [49] M. L. Greenberg, J. G. Weinger, M. P. Matheu et al., "Two-photon imaging of remyelination of spinal cord axons by engrafted neural precursor cells in a viral model of multiple sclerosis," *Proceedings of the National Academy of Sciences of the United States of America*, vol. 111, no. 22, pp. E2349–E2355, 2014.
- [50] S. Karahuseyinoglu, O. Cinar, E. Kilic et al., "Biology of stem cells in human umbilical cord stroma: in situ and in vitro surveys," *Stem Cells*, vol. 25, no. 2, pp. 319–331, 2007.
- [51] F. M. K. Corke, C. L. Hedley, P. J. Shaw, and T. L. Wang, "An analysis of seed development in *Pisum sativum* V. Fluorescence triple staining for investigating cotyledon cell development," *Protoplasma*, vol. 140, no. 2-3, pp. 164–172, 1987.
- [52] M. I. Highett, D. J. Rawlins, and P. J. Shaw, "Different patterns of rDNA distribution in *Pisum sativum* nucleoli correlate with different levels of nucleolar activity," *Journal of Cell Science*, vol. 104, no. 3, pp. 843–852, 1993.
- [53] R. Sarugaser, D. Lickorish, D. Baksh, M. M. Hosseini, and J. E. Davies, "Human umbilical cord perivascular (HUCPV) cells: a source of mesenchymal progenitors," *Stem Cells*, vol. 23, no. 2, pp. 220–229, 2005.
- [54] M. Molinos, C. R. Almeida, R. M. Gonçalves, and M. A. Barbosa, "Improvement of bovine nucleus pulposus cells isolation leads to identification of three phenotypically distinct cell subpopulations," *Tissue Engineering—Part A*, vol. 21, no. 15-16, pp. 2216–2227, 2015.
- [55] T. Margossian, L. Reppel, N. Makdissy, J.-F. Stoltz, D. Bensoussan, and C. Huselstein, "Mesenchymal stem cells derived from Wharton's jelly: comparative phenotype analysis between tissue and in vitro expansion," *Bio-Medical Materials and Engineering*, vol. 22, no. 4, pp. 243–254, 2012.
- [56] Y.-J. Ryu, H. S. Seol, T. J. Cho, T. J. Kwon, S. J. Jang, and J. Cho, "Comparison of the ultrastructural and immunophenotypic characteristics of human umbilical cord-derived mesenchymal stromal cells and in situ cells in Wharton's jelly," *Ultrastructural Pathology*, vol. 37, no. 3, pp. 196–203, 2013.
- [57] R. C. Schugar, S. M. Chirieleison, K. E. Wescoe et al., "High harvest yield, high expansion, and phenotype stability of CD146 mesenchymal stromal cells from whole primitive human umbilical cord tissue," *Journal of Biomedicine and Biotechnology*, vol. 2009, Article ID 789526, 11 pages, 2009.
- [58] K. Seshareddy, D. Troyer, and M. L. Weiss, "Method to isolate mesenchymal-like cells from Wharton's jelly of umbilical cord," *Methods in Cell Biology*, vol. 86, pp. 101–119, 2008.
- [59] P. Bianco, M. Riminucci, S. Gronthos, and P. G. Robey, "Bone marrow stromal stem cells: nature, biology, and potential applications," *STEM CELLS*, vol. 19, no. 3, pp. 180–192, 2001.
- [60] K. Kobayashi, T. Kubota, and T. Aso, "Study on myofibroblast differentiation in the stromal cells of Wharton's jelly: expression and localization of α -smooth muscle actin," *Early Human Development*, vol. 51, no. 3, pp. 223–233, 1998.
- [61] S. Corti, F. Locatelli, D. Papadimitriou et al., "Identification of a primitive brain-derived neural stem cell population based on aldehyde dehydrogenase activity," *STEM CELLS*, vol. 24, no. 4, pp. 975–985, 2006.

- [62] R. Koninckx, A. Daniëls, S. Windmolders et al., "The cardiac atrial appendage stem cell: a new and promising candidate for myocardial repair," *Cardiovascular Research*, vol. 97, no. 3, pp. 413–423, 2013.
- [63] R. W. Storms, A. P. Trujillo, J. B. Springer et al., "Isolation of primitive human hematopoietic progenitors on the basis of aldehyde dehydrogenase activity," *Proceedings of the National Academy of Sciences of the United States of America*, vol. 96, no. 16, pp. 9118–9123, 1999.
- [64] I. Garzón, C. A. Alfonso-Rodríguez, C. Martínez-Gómez et al., "Expression of epithelial markers by human umbilical cord stem cells. A topographical analysis," *Placenta*, vol. 35, no. 12, pp. 994–1000, 2014.
- [65] P. Friedl, "Dynamic imaging of cellular interactions with extracellular matrix," *Histochemistry and Cell Biology*, vol. 122, no. 3, pp. 183–190, 2004.
- [66] G.-J. Bakker, V. Andresen, R. M. Hoffman, and P. Friedl, "Fluorescence lifetime microscopy of tumor cell invasion, drug delivery, and cytotoxicity," *Methods in Enzymology*, vol. 504, pp. 109–125, 2012.
- [67] M. R. Fein and M. Egeblad, "Caught in the act: revealing the metastatic process by live imaging," *Disease Models & Mechanisms*, vol. 6, no. 3, pp. 580–593, 2013.
- [68] X. Zhang, S. Bloch, W. Akers, and S. Achilefu, "Near-infrared molecular probes for in vivo imaging," *Current Protocols in Cytometry*, vol. 60, pp. 12.27.1–12.27.20, 2012.
- [69] H. S. Choi, S. L. Gibbs, J. H. Lee et al., "Targeted zwitterionic near-infrared fluorophores for improved optical imaging," *Nature Biotechnology*, vol. 31, no. 2, pp. 148–153, 2013.
- [70] X. Michalet, F. F. Pinaud, L. A. Bentolila et al., "Quantum dots for live cells, in vivo imaging, and diagnostics," *Science*, vol. 307, no. 5709, pp. 538–544, 2005.
- [71] C. Bouzigues, T. Gacoin, and A. Alexandrou, "Biological applications of rare-earth based nanoparticles," *ACS Nano*, vol. 5, no. 11, pp. 8488–8505, 2011.
- [72] K. Douma, R. T. A. Megens, and M. A. M. J. van Zandvoort, "Optical molecular imaging of atherosclerosis using nanoparticles: shedding new light on the darkness," *Wiley Interdisciplinary Reviews: Nanomedicine and Nanobiotechnology*, vol. 3, no. 4, pp. 376–388, 2011.

Research Article

MRI-Based Assessment of Intralesional Delivery of Bone Marrow-Derived Mesenchymal Stem Cells in a Model of Equine Tendonitis

Alexandra Scharf,^{1,2} Shannon P. Holmes,³ Merrilee Thoresen,¹ Jennifer Mumaw,¹ Alaina Stumpf,¹ and John Peroni¹

¹Department of Large Animal Medicine, College of Veterinary Medicine, University of Georgia, Athens, GA 30602, USA

²Department of Biological and Agricultural Engineering, College of Engineering, University of Georgia, Athens, GA 30602, USA

³Veterinary Biosciences and Diagnostic Imaging, College of Veterinary Medicine, University of Georgia, Athens, GA 30602, USA

Correspondence should be addressed to John Peroni; jperoni@uga.edu

Received 6 June 2016; Accepted 15 August 2016

Academic Editor: Franca Fagioli

Copyright © 2016 Alexandra Scharf et al. This is an open access article distributed under the Creative Commons Attribution License, which permits unrestricted use, distribution, and reproduction in any medium, provided the original work is properly cited.

Ultrasound-guided intralesional injection of mesenchymal stem cells (MSCs) is held as the benchmark for cell delivery in tendonitis. The primary objective of this study was to investigate the immediate cell distribution following intralesional injection of MSCs. Unilateral superficial digital flexor tendon (SDFT) lesions were created in the forelimb of six horses and injected with 10×10^6 MSCs labeled with superparamagnetic iron oxide nanoparticles (SPIOs) under ultrasound guidance. Assays were performed to confirm that there were no significant changes in cell viability, proliferation, migration, or trilineage differentiation due to the presence of SPIOs. Limbs were imaged on a 1.5-tesla clinical MRI scanner postmortem before and after injection to determine the extent of tendonitis and detect SPIO MSCs. Clusters of labeled cells were visible as signal voids in 6/6 subjects. Coalescing regions of signal void were diffusely present in the peritendinous tissues. Although previous reports have determined that local injury retains cells within a small radius of the site of injection, our study shows greater than expected delocalization and relatively few cells retained within collagenous tendon compared to surrounding fascia. Further work is needed if this is a reality *in vivo* and to determine if directed intralesional delivery of MSCs is as critical as presently thought.

1. Introduction

The incidence of athletic, overuse injury continues to rise with the popularity of recreational and competitive sports in both human and veterinary patients. At this time, over 50 US clinical trials investigating the effects of biological therapeutics including platelet-rich plasma or stem cells on tendon or ligament injury are active or have recently been completed in humans (ClinicalTrials.gov). A comprehensive review of tendinopathies in the equine and human athlete has shown striking similarities and concluded that the horse provides a robust preclinical model for translational therapies [1]. The use of mesenchymal stem cells (MSCs) for tendon therapy in the horse has shown encouraging results, including superior tissue organization, composition, and mechanics

compared to untreated controls [2–6]. Direct, intralesional injection of MSCs under ultrasound guidance is held as the benchmark for MSCs therapy in tendonitis [3, 4, 6–8], although little is known about the efficacy of this delivery technique.

Current tracking studies rely heavily on postmortem histological validation [9–11] or utilize low resolution imaging modalities such as nuclear scintigraphy [12, 13] and low field magnetic resonance imaging [14, 15]. Such studies report low cell retention and survival in tendon following injection of MSCs, reporting <25% cells totally retained after the first 24 hours [12, 13] and fewer than 5% of the original bolus after 10 days as confirmed by histology [11]. However, little is known about the discrete localization of cells after injection or their ability to migrate into injured tissues over time.

This study represents part of an effort to establish a model of tendon injury that can be paired with nanotechnology-based cell tracking methods to track MSCs following ultrasound-guided injection into damaged tissues [16]. Superparamagnetic iron oxide nanoparticles (SPIOs) have the ability to image and monitor cells using MRI. SPIOs are nontoxic at low concentrations and biodegradable and do not emit ionizing agents and are readily endocytosed by adherent cells in culture [17–20]. At this time, SPIOs have safely been implemented as an intracellular label for stem cell studies in the liver [21], heart [22], spinal cord and brain [19, 23], and articular cartilage [24] to study spatial distribution and migration after implantation using MRI over periods of time ranging from weeks to months [18, 25–27].

The major aims of this study were to validate the safety of labeling equine BM-derived MSCs with SPIOs and to investigate the immediate distribution of cells following ultrasound-guided, intralesional injection of MSCs into an established model of iatrogenic, flexor tendon injury in the horse [28, 29]. This model was chosen to reflect the environment associated with acute tendon injury and provide reproducible areas of tissue contrast on MRI that could be used to enhance intralesional detection of SPIOs. The hypotheses of this research were that (i) equine BM-MSCs would be unaltered by SPIO labeling, (ii) SPIOs labeled MSCs could be tracked immediately after injection in an equine tendonitis model, and (iii) MSCs would be localized within the tendon lesion following ultrasound-guided injection. This study represents the first effort to track cells in an iatrogenic model of tendon injury on a high field, clinical scanner with potential for translation into longitudinal studies of experimental and naturally occurring disease models.

2. Materials and Methods

2.1. In Vitro Validation. All experiments were performed in triplicate using cryopreserved, bone marrow-derived equine mesenchymal stem cells from 3 horses below passage 6. Cells were cryopreserved in 10% (v/v) DMSO in cell culture medium and thawed for 1 minute in a 37°C water bath. Cells were diluted in 10 mL MSC culture medium (low glucose Dulbecco's Modified Eagle Medium (DMEM), 10% Fetal Bovine Serum, 1% L-glutamine, 50 U/mL penicillin, and 50 µg/mL streptomycin), centrifuged, and plated for culture at 10,000 cells/cm². Cells were maintained at 37°C and 5% CO₂ in MSC culture medium. At 70% confluency, MSCs were treated with 25 µg/mL Molday ION C6Amine (Biopal, Inc.) suspended in 0.1 mL/cm² MSC culture medium for 4 or 16 hours, as noted. Untreated cells were used as a control. Following treatment, cells were trypsinized, centrifuged, and manually counted for use in the following assays.

2.1.1. Cell Viability following SPIO Treatment. For cell viability, cells were labeled with SPIOs as described above for 4 or 16 hours. Cells were harvested and evaluated immediately after treatment and 24 hours following completion of treatment. A Trypan Blue (Cellgro®) exclusion assay was performed for viability according to the manufacturer's protocol. Results were analyzed with one-way analysis of variance (ANOVA)

and Dunnett's multiple comparisons test using untreated cells as the control. Bonferroni's multiple comparison test was used to compare cells immediately after treatment to cells after 24 hours of recovery.

2.1.2. Iron Content and Cell Proliferation. For qualitative assessment, cells were fixed with 4% paraformaldehyde over ice for 10 minutes, incubated for 10 minutes with Prussian Blue reagents (Biopal, Inc.), and Prussian Blue-positive, intracellular deposits of SPIOs were confirmed with light microscopy. For quantitative assessment, cells were harvested, counted, and digested in dilute aqueous nitric acid for analysis by inductively coupled plasma-mass spectrometry with a VG Plasmaquad 3 (VG Instruments) to determine iron content. To measure proliferation, cells were plated in flat bottom, 96-well plates and the CyQuant® (Life Technologies) assay was performed according to the manufacturer's microplate protocol and analyzed at 0, 24, 48, and 72 hours. Results were analyzed with two-way ANOVA using Dunnett's multiple comparisons test and untreated cells as the control.

2.1.3. Trilineage Differentiation. For osteogenic and adipogenic differentiation experiments, SPIO-labeled cells were plated in flat bottom, 96-well plates at a density of 28,000 cells/cm² and cultured in MSC culture medium for 24 hours. Fresh MSCs (undifferentiated) were included as controls for all experiments. Osteogenic induction cultures were replenished with Hyclone® AdvanceSTEM™ osteogenic medium every 2–3 days for 28 days. Osteogenic differentiation was determined using Calcium Liquicolor® Test (Stanbio) according to the manufacturer's protocol. Calcium was extracted from the differentiated cultures with 0.6 N HCl overnight at 4°C. The supernatant was combined at a ratio of 1:20 in an equal portion mixture of the color and base reagents from the Calcium Liquicolor Test and read on a plate reader at 550 nm (Biotek Synergy 4).

Adipogenic induction cultures were replenished with Hyclone AdvanceSTEM adipogenic medium for 14 days and then switched to an adipogenic medium modified from Vidal et al. (2006) consisting of DMEM, 10% FBS, 5% rabbit serum, 0.5 µM dexamethasone, 60 µM indomethacin, 0.5 mM IBMX, 1 µM insulin, 50 U/mL penicillin, and 50 µg/mL streptomycin for the remaining 14 days with medium changes every 2–3 days [30]. Adipogenic cells were fixed with 4% paraformaldehyde for 10 minutes over ice and stained with Oil Red O to identify lipid deposits.

For chondrogenic differentiation, 100,000 cells/well were plated in conical bottom, 96-well plates, centrifuged for 10 minutes, and replenished with Hyclone AdvanceSTEM chondrogenic medium every 2–3 days for 28 days. Chondrogenic pellets were fixed with methanol, stained with 0.2% Alcian Blue in 0.1 M HCl overnight, extracted with 0.1 mL 6 M guanidine/HCl for 2 hours, and read at 650 nm in a plate reader (Biotek Synergy 4).

2.1.4. Scratch Test. The scratch test was modified from the protocol outlined by Liang et al. [31]. Cells were plated at

confluency in a 24-well plate. A p200 pipet tip was used to scratch a line through the cells. Light microscopy images were taken at 0, 8, 16, and 24 hours. Image analysis was performed using ImageJ. Distance was measured as number of pixels between 3 sets of cells per well per time point. Results were analyzed with two-way ANOVA repeated measures analysis and Bonferroni's multiple comparisons test at a significance level of 0.05.

2.1.5. Inflammatory Modulation and Cytokine Production.

Equine peripheral blood mononuclear cells (PBMCs) were obtained by collecting 60 mL of peripheral blood from a healthy horse into a syringe with ethylenediaminetetraacetic acid (EDTA) as an anticoagulant. Blood was layered onto Histopaque-1077 and centrifuged at 20°C for 30 min, and the PBMC layer was removed by aspiration. Cells were washed twice in phosphate buffered saline (PBS), resuspended in monocyte media (RPMI-1641 with 10% equine serum, 50 U/mL penicillin, and 50 µg/mL streptomycin) at 4×10^6 /mL, and plated. PBMCs were incubated for 2 hours, after which nonadherent cells were washed off and adherent PBMCs were harvested for the following assays.

To assess the ability of MSCs to modulate the inflammatory response, 100,000 MSCs were plated in 12-well transwell plates and allowed to adhere for approximately 12 hours. At this time, MSC media were exchanged for 1.5 mL monocyte media/well. Next, 400,000 monocytes were added to each upper transwell in 0.5 mL monocyte media supplemented with 50 ng/mL *E. coli* LPS and allowed to incubate for 16 hours overnight. Monocytes stimulated with LPS were used as control. Results of monocytes without LPS are not reported. Supernatant was collected and used for analysis by ELISA for production of interleukin-10 (IL-10, Abcam®) and prostaglandin E₂ (PGE₂, Enzo® Life Sciences) according to manufacturer's protocols. An ELISA for tumor necrosis factor-α (TNF-α) was performed as previously described by Sun et al. [32]. ELISA plates were coated with anti-equine TNF-α polyclonal antibody overnight, washed, and incubated with samples. Plates were washed again, incubated with anti-equine TNF-α biotin-labeled polyclonal antibody, washed, incubated with avidin-horseradish peroxidase, washed again, incubated with a peroxidase substrate (ABTS®), and read at 405 nm on a plate reader (Biotek Synergy 4).

2.2. MRI Study. MRI was performed using a Siemens Symphony with TIM technology 1.5 T MRI unit with B17 software. All imaging was performed with limb centered in a 15-channel knee coil with receiver bandwidth of 130 kHz. Proton density- (PD-) weighted turbo spin-echo (TSE), true fast imaging with steady-state free precession (TRUFI) sequences, T2*, and multiecho spin-echo (MSE) T2-weighted sequences were acquired for cell phantoms and all subjects (Table 1). Analysis was performed with Osirix DICOM software and ImageJ.

2.2.1. In Vitro Phantom Study. A preliminary study was performed to establish the sensitivity and limits of MRI detection

of SPIO-labeled MSCs. Cell phantoms were prepared by suspending 0.01, 0.1, 0.25, 0.5, and 1×10^6 cells in 200 µL of 1% agar in the wells of a 96-well plate. Mean signal intensities (MSI) of labeled cells were measured using a circular ROI of 8.44 mm² on 4 contiguous slices acquired from TRUFI images. Signal-to-noise ratio (SNR) was calculated by dividing the MSI by the standard deviation of the background noise. A second study was performed in normal tendon. Tissue was collected from 1 horse euthanized for purposes unrelated to this study. Beginning proximally, 1, 5, 10, and 20×10^6 cells were serially injected into the SDFT and scanned as described above.

2.2.2. In Vivo MRI Analysis of Intralesional Cell Injection.

All work performed in this study was done in accordance with the University of Georgia Institutional Animal Care and Use committee guidelines. All horses were scheduled to be euthanized for reasons unrelated to this project.

(1) Pilot Lesion. An iatrogenic lesion was made in the forelimb of one horse scheduled for anesthesia and subsequent euthanasia. While under general anesthesia, the metacarpal region was circumferentially clipped and aseptically prepared. The limb was desensitized with a ring block performed using 10 mL of 2% lidocaine infused subcutaneously just distally to the carpus. A 1 cm incision was made on the caudal aspect of the metacarpus and into the SDFT just above the proximal extent of the digital flexor tendon sheath. A 4.5 mm Steinmann pin was inserted within the SDFT and advanced 5 cm 5 times and withdrawn and the skin sutured. The horse was euthanized under general anesthesia. 10×10^6 SPIO-labeled MSCs were injected into the lesion under ultrasound guidance and imaged as described above.

(2) Model of Tendon Injury. Unilateral SDFT lesions were created in the forelimb of six horses. A protocol was modified from Schramme et al. [28] with horses in a standing position. Horses were premedicated with i.v. flunixin meglumine (1.1 mg/kg) and then sedated with a combination of detomidine hydrochloride (10 µg/kg) and butorphanol (20 µg/kg) administered intravenously. The limb was surgically prepped as described above. A 1 cm incision was made on the caudal aspect of the metacarpus and into the SDFT just above the proximal extent of the digital flexor tendon sheath. While holding the limb off the ground, a 4.5 mm Steinmann pin was inserted within the SDFT and advanced 5 cm. The pin was extracted and replaced with a 5 mm arthroscopic burr. The burr was activated at 2500 rpm and inserted and withdrawn within the SDFT 5 times. The skin incision was closed with surgical staples and the forelimb was bandaged. Horses were maintained on stall rest and walked by hand two times per day and subsequently euthanized 10 days following induction of the lesion. Cell injections and MRI were performed immediately following euthanasia and removal of the limb.

Cryopreserved, BM-derived equine MSCs below passage 10 were thawed and plated 3–5 days prior to treatment for culture as described above. The day prior to imaging, cells were treated with 25 µg/mL C6Amine Molday ION

TABLE 1: Parameters for MRI sequences acquired.

Sequence, plane	PD TSE, sagittal	PD TSE, transverse	TRUFI, sagittal and dorsal	T2*, transverse	T2 MSE, sagittal
TR (ms)	1830	3020	11.8	695	400
TE (ms)	56	39	5	22.5	4.8, 13, 21.3, 29.6, 37.8
Slice thickness (mm)	2.5	3.0	0.3	2.5	2.5
Flip angle	150	180	28	30	60
FOV (cm)	16 × 16	15 × 15	11 × 16	12.2 × 15	11.4 × 14
Matrix size	320 × 320	320 × 320	352 × 512	260 × 320	260 × 320

suspended in MSC culture media for 4 hours. At the time of injection, cells were harvested and 10×10^6 cells were counted. Cells were suspended in 0.25 to 0.75 mL PBS for injection, depending on the size of the lesion as determined by MRI and ultrasound.

Immediately following euthanasia, the injured forelimb was placed in a 15-channel knee coil with the palmar side up and imaged on a Siemens 1.5 T MRI scanner. PD images were acquired in the sagittal and transverse planes and TRUFI was acquired in the dorsal plane prior to injection as described in Table 1. Next, the limb was removed from the scanner and placed on a flat surface in a horizontal position, with palmar side up for evaluation by ultrasound. This position was chosen to mimic cell injections performed on a non-weight-bearing limb, with minimal tension on the flexor tendons so as to permit the largest volume of fluid within the core lesion. Cells were delivered via a 20-gauge needle placed into the lesion under ultrasound guidance using a 7.5 MHz probe connected to a Micromaxx Ultrasound System (SonoSite, Inc., 21919 30th Drive SE, Bothell, WA 98021, USA). The cell bolus was not delivered unless the tip of the needle could be verified within the core of the lesion on transverse and longitudinal planes. Following injection, limbs were returned to MRI and scanned with all sequences described in Table 1.

The extent of hypointense signal or signal void associated with SPIO-labeled MSC dispersion was measured using Osirix software on isotropic TRUFI images proximally and distally to the site of injection. The depth of signal into the subcutaneous tissue surrounding normal tendon was also measured. Relative pixel intensity (RPI) was measured on every other slice in T2* transverse images from the most proximal and distal aspects where signal voids could be observed. Histograms were generated on ImageJ to quantify the RPI from the distal aspect of the suspensory to the palmar surface of the limb. Histograms were also generated from the SDFT and deep digital flexor tendons (DDFT), which were subsequently subtracted from the total RPI to quantify the amount of RPI that was likely associated with SPIOs in the paratendinous fascia and subcutaneous tissues. Pixel values >100 were excluded from analysis.

2.2.3. Histology. Following MRI, 3.5–4.0 cm of affected area of the SDFT was excised at the site of injection, embedded in OCT compound (Tissue-Tek®), and longitudinally sectioned on a cryostat (Leica) at $12 \mu\text{m}$. Sections were mounted, fixed with 4% paraformaldehyde, incubated with Prussian Blue reagents (Biopal, Inc.) to evaluate the presence of iron

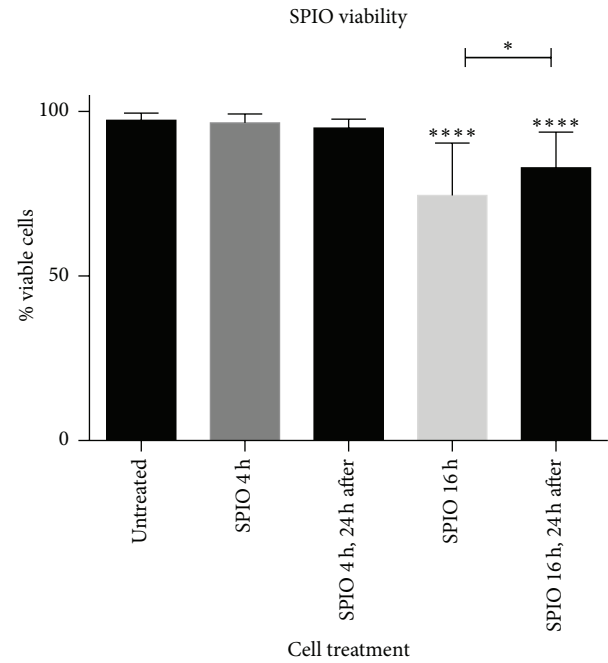


FIGURE 1: *Cell Viability.* Shown after labeling with SPIOs for 4 or 16 hours as compared to untreated cells. Measurements were recorded immediately and 24 hours after treatment (**** $p < 0.0001$, * $p < 0.05$).

nanoparticles, and counterstained with Nuclear Fast Red to visualize tissue morphology with light microscopy.

2.3. Statistical Analysis. Results were analyzed with one-way ANOVA and Bonferroni's multiple comparison tests at a significance level of 0.05 using Prism 6 software, unless otherwise noted above. Cells isolated from 3 horses were analyzed at each time point with measurements performed in triplicate. Error is reported in figures as standard error (SE) of the mean.

3. Results

3.1. In Vitro Validation

3.1.1. Cell Viability following SPIO Treatment. Untreated MSCs and MSCs treated for 4 hours showed 97.35 ± 0.36 (SE) and $96.56 \pm 0.64\%$ viability, respectively (Figure 1). Viability of equine MSCs treated for 4 hours did not differ at 24 hours following treatment (Figure 1). MSCs showed a significant

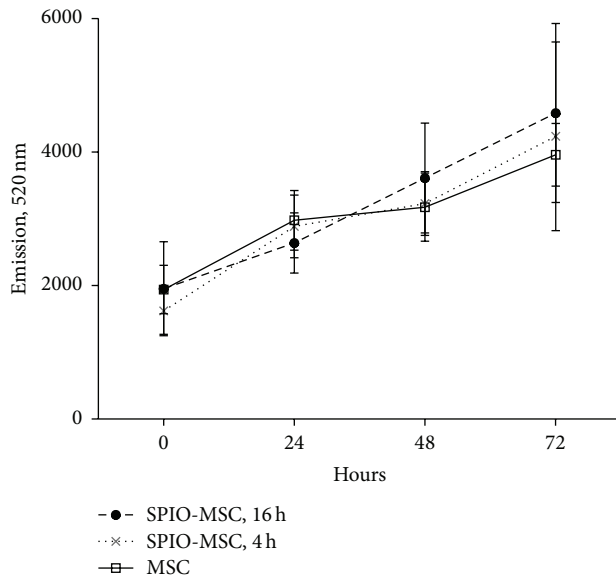


FIGURE 2: Cell proliferation shown over 72 hours after labeling with SPIOs for 4 or 16 hours as compared with untreated cells.

decrease in viability following treatment for 16 hours ($74.53 \pm 4.11\%$, $p < 0.0001$). Cells treated for 16 hours demonstrated an increase in viability 24 hours later ($82.92 \pm 2.55\%$) as compared to viability immediately following treatment ($p < 0.05$).

3.1.2. Iron Content and Cell Proliferation. Iron content was determined to be 3.99 ± 0.35 (SE) and 18.64 ± 1.25 (SE) pg/cell in cells treated for 4 and 16 hours, respectively. Untreated and treated MSCs demonstrated an increasing, linear relationship proliferative capacity over 72 hours after treatment. Cell proliferation was not significantly different in untreated cells as compared to cells treated for 4 or 16 hours (Figure 2).

3.1.3. Trilineage Differentiation. Due to the significant difference in viability between cells labeled for 4 versus 16 hours, only cells treated for 4 hours were used in the remaining experiments. Untreated and treated cells successfully demonstrated osteogenic ($p < 0.0001$) and chondrogenic differentiation ($p < 0.01$ untreated, $p < 0.0001$ treated) as compared to undifferentiated control cells (Figures 3(a) and 3(b)). Additionally, treated and untreated cells both demonstrated adipogenic differentiation as assessed by Oil Red O staining of lipid vacuoles at 28 days after treatment (Figure 3(c)).

3.1.4. Scratch Test. The scratch test showed no significant difference in the ability of treated and untreated MSCs to close the distance of the wound gap over 24 hours (Figure 4).

3.1.5. Inflammatory Modulation and Cytokine Production. Treated and untreated MSCs successfully upregulated PGE_2 ($p < 0.0001$), downregulated $\text{TNF}\alpha$ ($p < 0.0001$), and upregulated IL-10 production (ns) when cocultured with PBMCs stimulated with LPS (Figure 5).

3.2. MRI Study

3.2.1. In Vitro Study. Phantom models indicated that MR signal intensity decreased with increasing labeled cell numbers. All cell concentrations were qualitatively discernible compared to cell-free gel (CFG) on TRUFI and PD-weighted images showing distinct loss of signal (Figure 6(a)). The signal-to-noise ratio (SNR) for all cell concentrations were significantly different as compared to cell-free gel ($p < 0.0001$), but only 10,000 ($p < 0.0001$); 100,000 ($p < 0.0001$); and 250,000 cells ($p < 0.01$) were discernible from background (BG) signal (Figure 6(b)). Cells could not be visualized within normal tendon. Areas of hypointense signal were visible in the paratendinous fascia and subcutaneous tissues and were concentrated near sites of injection following injection into normal tendon (Figure 6(c)).

3.2.2. In Vivo MRI Analysis of Intralesional Cell Injection

(1) Pilot Study. Iatrogenic injury was localized and consisted of a focal area of fiber disruption and edema at the site of surgical incision in the transverse and sagittal plane. Although a small amount of contrast was produced, contrast was not evident proximally to the site of surgical incision. The extent of cell delivery into the lesion could not be determined (Figure 7(a)). At this time, the model was redesigned such that cells would be injected 10 days following surgery to allow edema to develop and more closely mimic clinical disease. Current studies routinely inject cells 1-2 weeks following iatrogenic injury, which supports the implementation of this timeframe [2, 10, 11, 14, 33, 34].

(2) Model of Tendon Injury. Prior to injection, tendon injuries were detectable as small, focal areas of hyperintensity localized to the SDFT in the transverse plane (Figures 8(a) and 8(e)) and were visible as longitudinal, linear segments of hyperintense signal in the dorsal plane (Figures 8(b) and 8(f)) in 5/6 subjects. The lesions were measured to be 5.41 ± 0.36 (SE) cm in length, on average. On TRUFI images, clusters of labeled cells were visible as hypointense, signal voids in 6/6 subjects. Coalescing regions of signal void were diffusely present throughout the site of injury, in the paratendinous, subcutaneous, and fibrous scar tissues surrounding the SDF (Figures 8(c), 8(d), 8(g), and 8(h)). Cell retention within the lesions varied greatly, with 1/6 subjects demonstrating little to no cell retention within the lesion (Figures 8(f)–8(h)). Substantial leakage of labeled cells outside of the SDFT was observed. High numbers of low intensity pixel values likely associated with SPIO-labeled cells were quantifiable throughout the tissue surrounding the SDFT and DDFT in 6/6 subjects (Figure 9). Cells were located at 1.89 ± 0.33 (SE) cm proximally and distally to the site of injection and were found at a depth of 3.13 ± 0.40 (SE) mm into the surrounding tissues.

3.2.3. Histology. Tendon lesions were grossly visible as areas of mechanical disruption with little to no fiber density. No scar tissue was present within the lesioned area. The margin surrounding the injury was delineated by dense irregular connective tissue with increased cellularity. The tissue

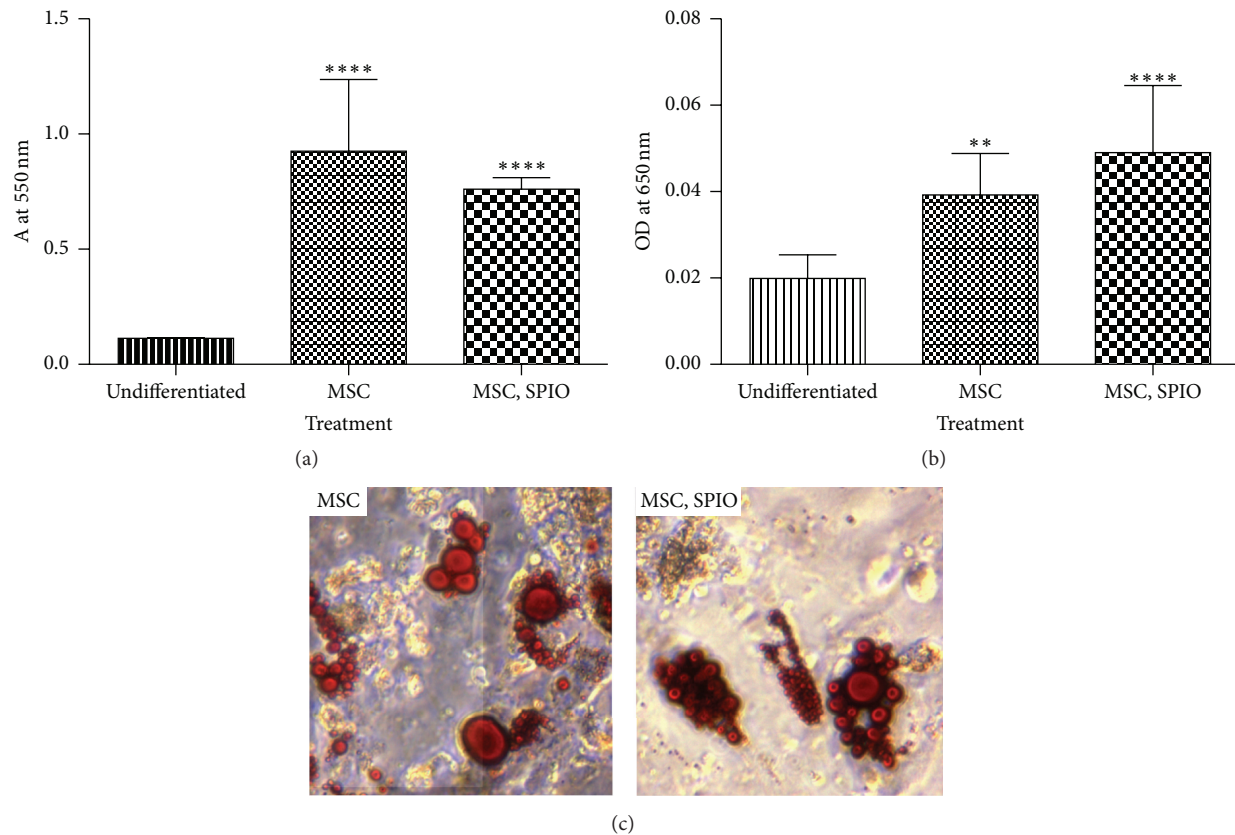


FIGURE 3: Trilineage differentiation data demonstrating (a) osteogenesis as measured by calcium production (**** $p < 0.0001$), (b) chondrogenesis as measured by Alcian Blue uptake in cell pellets (** $p < 0.01$, **** $p < 0.0001$), and (c) adipogenesis as noted by lipid deposition visualized with Oil Red O.

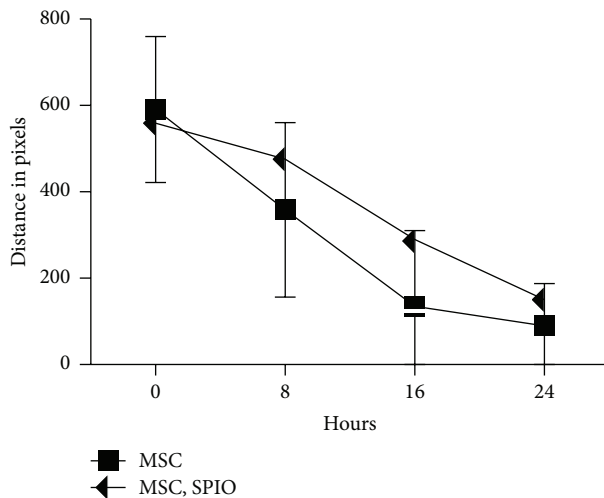


FIGURE 4: Cell migration as measured by a scratch test over 24 hours.

surrounding the lesion was normal with no inflammatory cell infiltrate and demonstrated crimp and fiber patterns characteristic of normal tendon. Prussian Blue-positive, iron-containing cells were detectable within the lesioned area and adherent to the bordering, dense, irregular connective tissue

(Figure 10). Few Prussian Blue-positive cells were located within the normal tendon tissue surrounding the lesion.

4. Discussion

This study represents a comprehensive evaluation of the characteristics of SPIO-labeled equine MSCs *in vitro*. We aimed to standardize a technique for safely loading equine BM-MSCs with SPIOs and to ensure that MSCs would not be functionally altered by SPIO labeling. A positive correlation was observed between time of incubation with SPIO-treated media and iron load per cell. A previous study demonstrated a linear relationship between SPIO concentration in media and iron load per cell [17]. Increasing time of incubation may provide a more economical alternative to increasing iron load per cell. Our data shows that a higher iron load of 19 pg/cell can be achieved by overnight incubation, but this was detrimental to cell viability. Care must be taken to avoid interference with cell migration and survival when performing cell tracking studies. Subsequent imaging demonstrated robust detectability of clinically relevant cell numbers following only 4 hours of incubation in SPIO-treated media. To ensure maximum cell viability and functionality in future cell tracking studies, we employed a lower iron load of 4 pg/cell for labeling and tracking BM-MSCs although higher loads of 10–12 pg/cell have been validated in prior work [17]. Interestingly, even with this

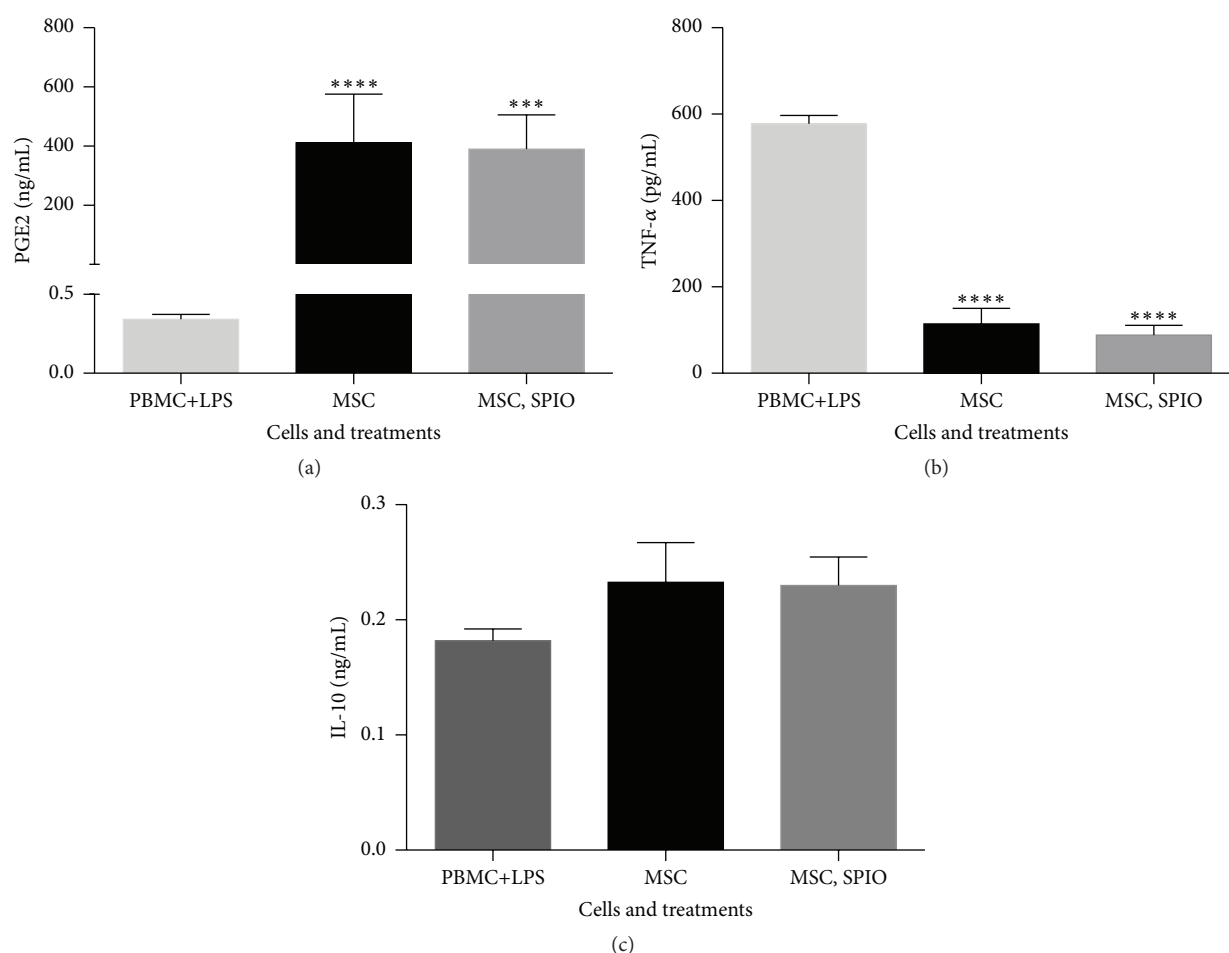


FIGURE 5: Graphs representative of (a) prostaglandin-E2 (PG-E2), (b) tumor necrosis factor- α (TNF- α), and (c) interleukin-10 (IL-10) production in MSC coculture with peripheral blood mononuclear cells (PBMCs) following stimulation with LPS (**** $p < 0.0001$, *** $p < 0.01$).

low iron burden, trilineage differentiation showed increased potential for chondrogenesis (ns) and decreased potential for osteogenesis (ns) and an increase in cell proliferation (ns) was noted in SPIO-labeled cells. Previous studies report similar conflicts in trilineage potential and the mechanism of action remains unclear [35–38]. Another study associated changes in cell proliferation with free Fe in the lysosome leading to an increase in cell cycle progression [39]. As such, SPIO-labeled cells should be considered a feasible method for cell tracking *in vivo*, but care should be taken when interpreting results.

The second aim of this study was to establish a clinically relevant, reproducible model for cell detection and tracking in equine tendon injury. The model of iatrogenic injury described by Schramme et al. (2010) has been well characterized on several imaging modalities [28, 29]. However, pathologic tendon is characterized by heterogeneous areas of high and low signal intensity on T2-weighted images, which can be difficult to discern from SPIO-associated signal [14, 15]. SPIOs are nearly undetectable in normal tendon and can only be differentiated in proximity to the subcutaneous tissues where their dipolar effect may disrupt normal tendon

borders on MRI. A high field magnet can enhance this effect and is valuable in the interpretation of cell distribution in tissues with low contrast, like tendon.

Previous work with high field MRI showed that ultrasmall SPIOs could effectively be used to track umbilical cord-derived MSCs and BM-MSCs in equine tendons with collagenase defects [40]. Our study implemented a similar imaging approach with the addition of a 15-channel transmit-receive coil, which more closely matches the anatomy of the equine distal limb. High field MRI details pathology more accurately and improves contrast and tissue margins, thus enhancing the ability to monitor cell tracking concurrent with tissue healing [41]. Other studies have attempted to track cells with low field magnets in standing horses [14, 15]. Our choice of equipment and sequences enabled imaging at 0.3 mm slice thickness, approaching a resolution close to that of MR microscopy. This is the first study to achieve this feat using only clinical equipment in the equine distal limb.

This work was designed with the goal of efficient translation into long-term imaging studies that allow simultaneous tracking of cells and tendon healing. Other research relies

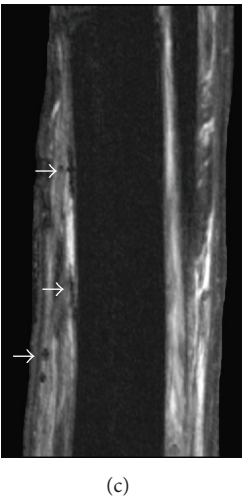
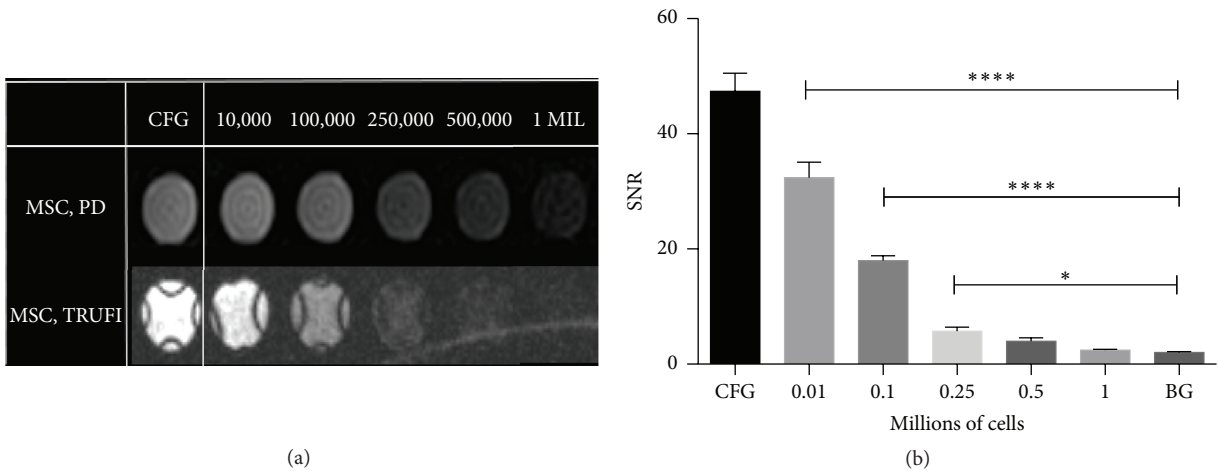


FIGURE 6: MRI data from cell suspensions in agar gel showing (a) PD (top row) and TRUFI (bottom row) images ranging from cell-free gel (CFG) up to 1×10^6 cells in a 96-well plate. (b) Signal-to-noise ratios (SNR) corresponding to the TRUFI images in (a). (c) Normal tendon following serial injection of 20, 10, 5, and 1×10^6 SPIO-labeled MSCs in order along the palmar aspect of the limb. SPIO-associated signal is only visible in the tissues surrounding the SDFT (arrows) (**** $p < 0.0001$, * $p < 0.05$).

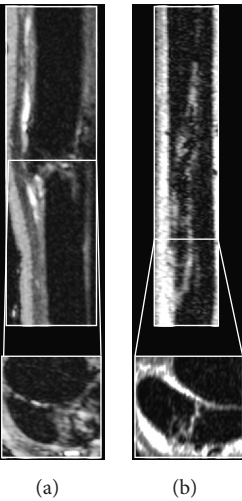


FIGURE 7: TRUFI images demonstrate SDFT lesions (a) induced immediately prior to and (b) 10 days prior to injection in the sagittal (top) and transverse (bottom) planes.

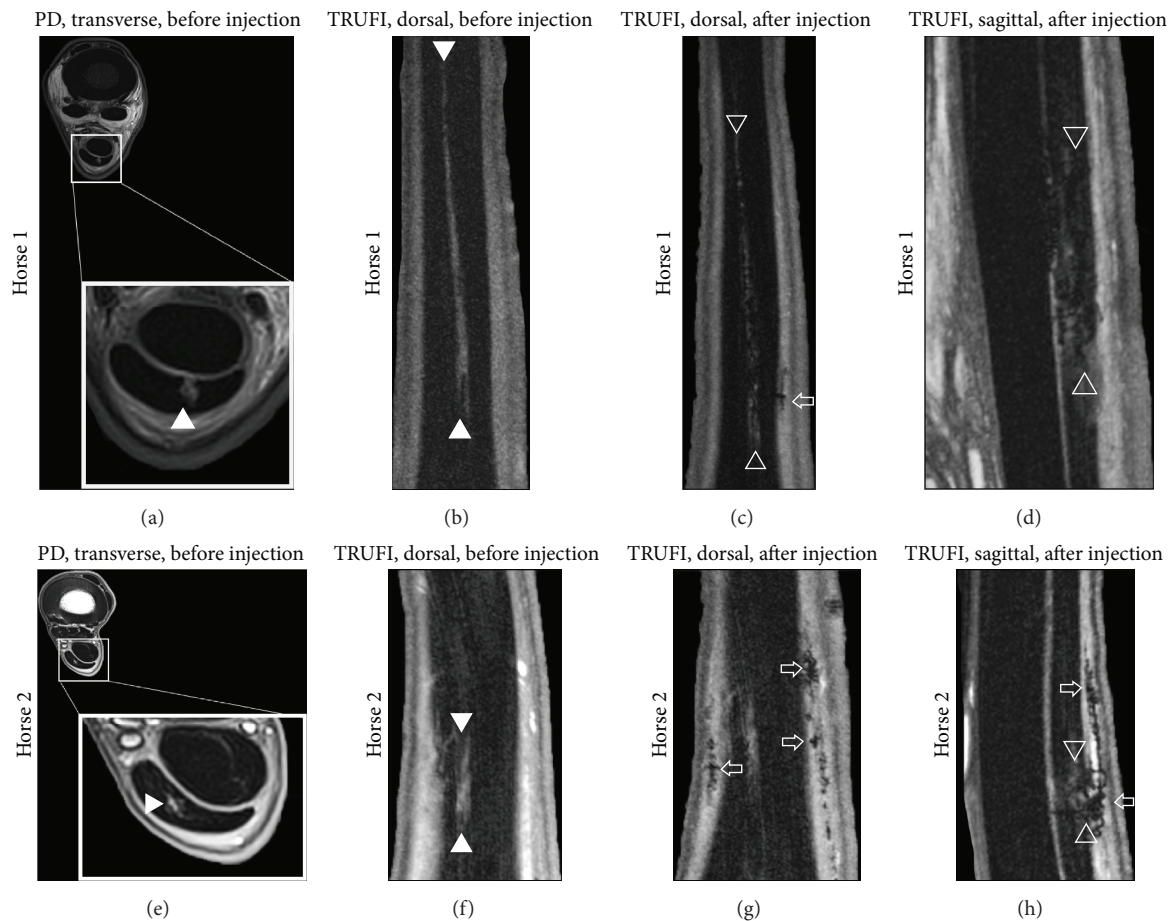


FIGURE 8: MRI of iatrogenic, SDFT lesions before (a, b, e, f) and after (c, d, g, h) injection of SPIO-treated cells. Solid arrowheads delineate the tendon lesion in preinjection images. Open arrowheads indicate SPIO-treated cells within the tendon lesion after injection. The SPIO-treated cells are seen as small, heterogeneous clusters of dark signal. The open, horizontal arrows indicate SPIO-treated cells distributed throughout the tissue layers surrounding the tendon.

heavily on T2- and T2*-weighted gradient echo sequences [15, 40]. However, T2-weighting enhances the artifacts produced by iron-labeled cells, which may distort the surrounding anatomy and be easily confused with other inhomogeneities in the magnetic field including hemorrhage. Both iatrogenic and collagenase tendon injury models are associated with moderate-to-severe swelling, vascular damage, and induction of the inflammatory cascade. For this reason, the implementation of sequences that offer clear discrimination between hemorrhage and labeled cells is essential. To overcome these challenges, our protocol utilizes three types of MRI sequences: PD-weighted TSE sequences, which enhance pathologic changes in tendon and minimize dephasing caused by labeled cells; TRUFI sequences, which maximize the contrast between signal voids produced by labeled cells while maintaining sufficient SNR and reducing artifact [42]; and T2-weighted sequences, which maximize signal artifacts and are routinely used for imaging SPIOs.

The animal model used in this study is most representative of acute, focal injury to the SDFT and can successfully be used to monitor a large bolus of labeled MSCs after injection by MRI. The use of a mechanical model of injury

enhanced detection of MSCs by providing soft tissue contrast within the lesion associated with the absence and disruption of collagen fibers and mild edema. The efflux of cells into the subcutaneous tissues was easily detectable due to the high signal intensity of the fat contrast associated with these surrounding areas. In the future, these cells can easily be tracked and monitored for cell survival and migration into the tendon, as determined by diminution of the hypointense signal and redistribution within the tissues. Longer term *in vivo* tracking studies will also have to consider the effects of biomechanical tendon loads, motion, and gravity on cell movement and distribution.

Our third objective was to characterize the distribution of cells at the time of injection. In contrast to our stated hypothesis, our data suggest that there is a substantial variation in cell distribution among study subjects even though the injection is performed with precise ultrasound triangulation technique. Postinjection T2*-weighted images in the transverse plane demonstrated heterogeneous and inconsistent cell localization within the tendon lesions when compared to preinjection images and showed consistent leakage of the labeled cells into the tissue surrounding the

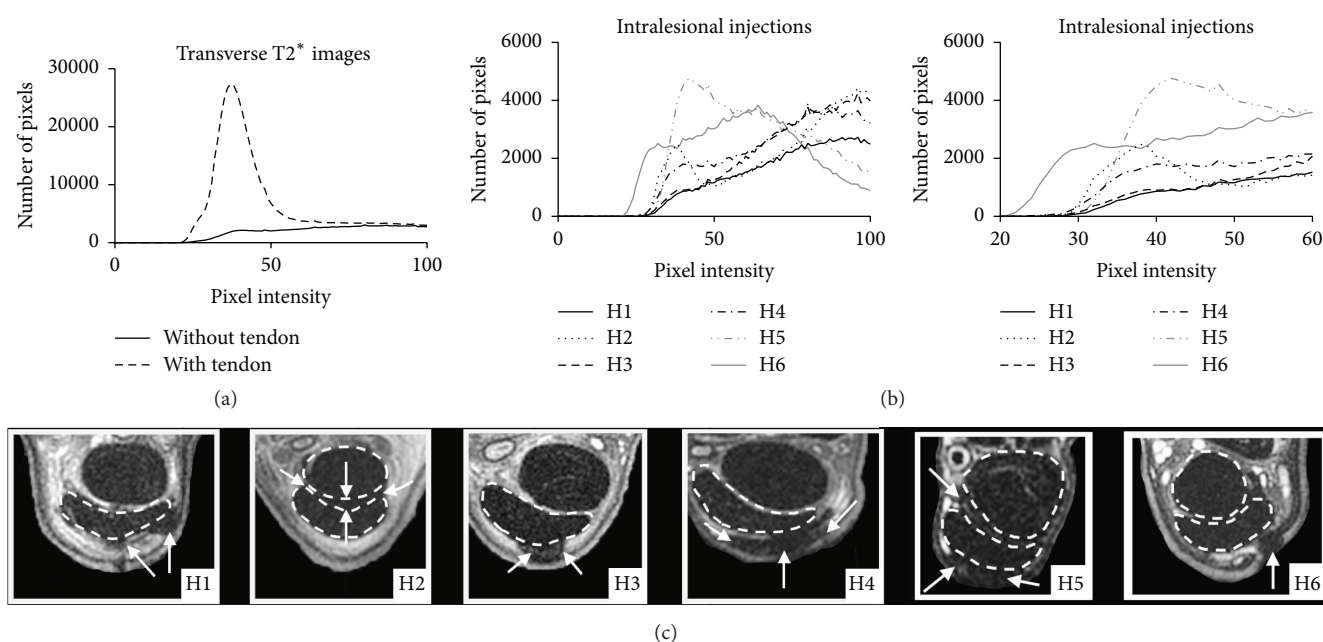


FIGURE 9: Transverse MRI of SDFT and quantification of low MRI signal as measured on 8-bit, grayscale images. (a) Graph showing summation of low signal intensity pixels before and after subtraction of DDFT and SDFT from transverse images. (b) Summation of low signal intensity pixels in the subcutaneous and surrounding soft tissues in all 6 subjects with a magnified view of the x -axis displayed on the right. (c) TRUFI images demonstrating substantial efflux of cells into the paratendinous and surrounding tissues. Arrows indicate hypointense areas of MRI signal representative of SPIO-treated cells. Dotted lines estimate the boundaries of the SDFT and DDFT.

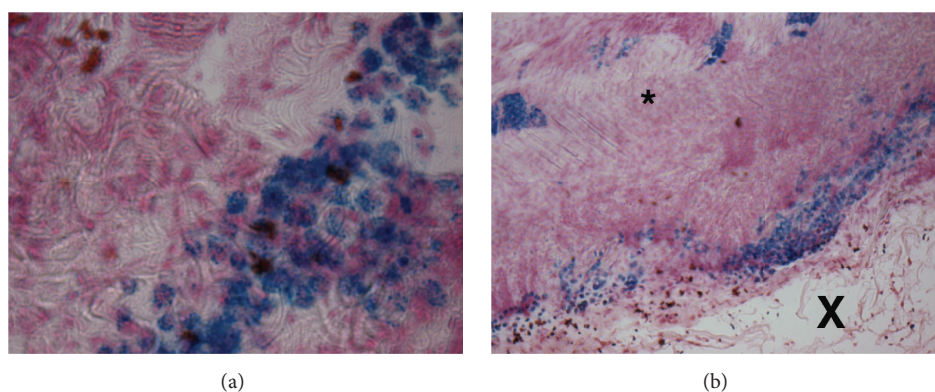


FIGURE 10: Histology of iron-labeled cells. Tissue sections demonstrate dense areas of Prussian Blue-positive, SPIO-treated MSCs lining the tendon lesion. Markers indicate the tendon lesion (X) and the tendon matrix (*). Images shown are at (a) 10x and (b) 40x.

SDFT, including the paratenon and subcutaneous tissues, in all subjects.

Histological evaluation confirmed that some cells were also retained within the core lesion. The histologic appearance of the lesioned areas suggests fluid filling that increases interstitial tissue pressure and causes cells to flow retrogradely along the needle surface into the fascial layers surrounding the tendons. It is interesting to note that most equine studies suspend cells in a volume of 1-2 mL for injection into flexor tendon injuries [3, 4, 6, 7, 34], whereas we injected less than 1 mL and still observed poor intralesional cellular retention. The clinical presumption that the majority of a cell bolus is retained within the core lesion is incorrect and further studies should be performed to investigate the degree to which cells

migrate within the tendon after injection and if healing is affected by the degree of cell delocalization.

5. Limitations

This study performed all imaging and injections postmortem for economical and logistical reasons. Limbs were not injected in weight-bearing conformation, which is common practice in the clinic. However, it is possible that when the flexor tendons are in slack position there is less risk of iatrogenic damage from the incoming fluid and needle stick. If injections are performed in standing position, cells will flow distally to the site of needle placement due to the effects of gravity, as opposed to flowing both proximally and distally

when the leg is placed in a horizontal position. The influence of circulation on cell viability within the tendon lesion will also have to be considered in future studies. It is possible that cells engrafted into the subcutaneous tissues may exhibit higher rates of survival than those in the lesion because of higher vascular perfusion and nutrient supply.

Due to the inherent low signal intensity of normal tendon, it is not possible to perform a quantitative evaluation of SPIO signal or to compare the ratio of cells within and surrounding the tendon lesion. However, the images provide a cohesive albeit qualitative assessment regarding the distribution of MSCs following ultrasound-guided, intralesional tendon injections. Although this question has not been raised in the literature in the past, several studies have already begun to investigate cell migration and survival using histology or other methods [2, 10, 11, 14]. The delocalization of cells immediately following cell injection suggests *in vivo* imaging methods will be far superior for analyzing these data. Additionally, since the patterns of cell distribution determined in this study were wider than expected or reported, changes in MSC administration may be needed. However, confirmation of cell location and *in vivo* effect on tendon repair, through tissue biopsy in large animal studies, is needed to better establish a protocol for cellular therapies.

6. Conclusion

Although previous reports have determined that local injury retains cells within a small radius of the site of injection, our study shows greater than expected delocalization and that relatively few cells are retained within collagenous tendon compared to surrounding fascia. The theories of MSC mechanism of action may need to consider greater contribution from MSCs outside of collagenous tissue. The regional retention of MSCs may have important implications regarding the healing of injuries. Further work is needed if this is a reality *in vivo* and therefore to determine if directed intralesional delivery of MSCs is as critical as presently thought.

Abbreviations

MRI: Magnetic resonance imaging
SPIO: Superparamagnetic iron oxide nanoparticle
MSCs: Mesenchymal stem cells.

Disclosure

John Peroni present address is Department of Large Animal Medicine, College of Veterinary Medicine, University of Georgia, 501 DW Brooks Drive, Athens, GA 30602.

Competing Interests

The authors declare that there are no competing interests regarding the publication of this paper.

Acknowledgments

The authors would like to thank the American Quarter Horse Association, Morris Animal Foundation, and the University

of Georgia Interdisciplinary Grant for their financial support of this project.

References

- [1] J. C. Patterson-Kane, D. L. Becker, and T. Rich, "The pathogenesis of tendon microdamage in athletes: the horse as a natural model for basic cellular research," *Journal of Comparative Pathology*, vol. 147, no. 2-3, pp. 227–247, 2012.
- [2] A. Crovace, L. Lacitignola, G. Rossi, and E. Francioso, "Histological and immunohistochemical evaluation of autologous cultured bone marrow mesenchymal stem cells and bone marrow mononucleated cells in collagenase-induced tendinitis of equine superficial digital flexor tendon," *Veterinary Medicine International*, vol. 2010, Article ID 250978, 10 pages, 2010.
- [3] E. E. Godwin, N. J. Young, J. Dudhia, I. C. Beamish, and R. K. W. Smith, "Implantation of bone marrow-derived mesenchymal stem cells demonstrates improved outcome in horses with overstrain injury of the superficial digital flexor tendon," *Equine Veterinary Journal*, vol. 44, no. 1, pp. 25–32, 2012.
- [4] S. Pacini, S. Spinabella, L. Trombi et al., "Suspension of bone marrow-derived undifferentiated mesenchymal stromal cells for repair of superficial digital flexor tendon in race horses," *Tissue Engineering*, vol. 13, no. 12, pp. 2949–2955, 2007.
- [5] L. V. Schnabel, M. E. Lynch, M. C. H. Van Der Meulen, A. E. Yeager, M. A. Kornatowski, and A. J. Nixon, "Mesenchymal stem cells and insulin-like growth factor-I gene-enhanced mesenchymal stem cells improve structural aspects of healing in equine flexor digitorum superficialis tendons," *Journal of Orthopaedic Research*, vol. 27, no. 10, pp. 1392–1398, 2009.
- [6] R. K. W. Smith, N. J. Werling, S. G. Dakin, R. Alam, A. E. Goodship, and J. Dudhia, "Beneficial effects of autologous bone marrow-derived mesenchymal stem cells in naturally occurring tendinopathy," *PLoS ONE*, vol. 8, no. 9, Article ID e75697, 2013.
- [7] A. D. M. Carvalho, P. R. Badial, L. E. C. Álvarez et al., "Equine tendonitis therapy using mesenchymal stem cells and platelet concentrates: a randomized controlled trial," *Stem Cell Research & Therapy*, vol. 4, no. 4, article 85, 2013.
- [8] L. E. Richardson, J. Dudhia, P. D. Clegg, and R. Smith, "Stem cells in veterinary medicine—attempts at regenerating equine tendon after injury," *Trends in Biotechnology*, vol. 25, no. 9, pp. 409–416, 2007.
- [9] L. Lacitignola, F. Staffieri, G. Rossi, E. Francioso, and A. Crovace, "Survival of bone marrow mesenchymal stem cells labelled with red fluorescent protein in an ovine model of collagenase-induced tendinitis," *Veterinary and Comparative Orthopaedics and Traumatology*, vol. 27, no. 3, pp. 204–209, 2014.
- [10] D. J. Guest, M. R. W. Smith, and W. R. Allen, "Monitoring the fate of autologous and allogeneic mesenchymal progenitor cells injected into the superficial digital flexor tendon of horses: preliminary study," *Equine Veterinary Journal*, vol. 40, no. 2, pp. 178–181, 2008.
- [11] D. J. Guest, M. R. W. Smith, and W. R. Allen, "Equine embryonic stem-like cells and mesenchymal stromal cells have different survival rates and migration patterns following their injection into damaged superficial digital flexor tendon," *Equine Veterinary Journal*, vol. 42, no. 7, pp. 636–642, 2010.
- [12] P. Becerra, M. A. Valdes Vazquez, J. Dudhia et al., "Distribution of injected technetium(99m)-labeled mesenchymal stem cells in horses with naturally occurring tendinopathy," *Journal of Orthopaedic Research*, vol. 31, no. 7, pp. 1096–1102, 2013.

- [13] A. Sole, M. Spriet, L. D. Galuppo et al., "Scintigraphic evaluation of intra-arterial and intravenous regional limb perfusion of allogeneic bone marrow-derived mesenchymal stem cells in the normal equine distal limb using ^{99m}Tc -HMPAO," *Equine Veterinary Journal*, vol. 44, no. 5, pp. 594–599, 2012.
- [14] F. Geburek, K. Mundle, S. Conrad et al., "Tracking of autologous adipose tissue-derived mesenchymal stromal cells with in vivo magnetic resonance imaging and histology after intralesional treatment of artificial equine tendon lesions—A Pilot Study," *Stem Cell Research and Therapy*, vol. 7, no. 1, article 21, 2016.
- [15] D. Berner, W. Brehm, K. Gerlach et al., "Longitudinal cell tracking and simultaneous monitoring of tissue regeneration after cell treatment of natural tendon disease by low-field magnetic resonance imaging," *Stem Cells International*, vol. 2016, Article ID 1207190, 13 pages, 2016.
- [16] A. Scharf, S. Holmes, M. Thoresen, J. Mumaw, A. Stumpf, and J. Peroni, "Superparamagnetic iron oxide nanoparticles as a means to track mesenchymal stem cells in a large animal model of tendon injury," *Contrast Media & Molecular Imaging*, vol. 10, no. 5, pp. 388–397, 2015.
- [17] B. Addicott, M. Willman, J. Rodriguez et al., "Mesenchymal stem cell labeling and in vitro MR characterization at 1.5 T of new SPIO contrast agent: molday ION Rhodamine-B™," *Contrast Media and Molecular Imaging*, vol. 6, no. 1, pp. 7–18, 2011.
- [18] E. Farrell, P. Wielopolski, P. Pavljasevic et al., "Effects of iron oxide incorporation for long term cell tracking on MSC differentiation *in vitro* and *in vivo*," *Biochemical and Biophysical Research Communications*, vol. 369, no. 4, pp. 1076–1081, 2008.
- [19] L. E. Gonzalez-Lara, X. Xu, K. Hofstetrova et al., "The use of cellular magnetic resonance imaging to track the fate of iron-labeled multipotent stromal cells after direct transplantation in a mouse model of spinal cord injury," *Molecular Imaging and Biology*, vol. 13, no. 4, pp. 702–711, 2011.
- [20] C. McFadden, C. L. Mallett, and P. J. Foster, "Labeling of multiple cell lines using a new iron oxide agent for cell tracking by MRI," *Contrast Media and Molecular Imaging*, vol. 6, no. 6, pp. 514–522, 2011.
- [21] J. Kriz, D. Jirak, D. White, and P. Foster, "Magnetic resonance imaging of pancreatic islets transplanted into the right liver lobes of diabetic mice," *Transplantation Proceedings*, vol. 40, no. 2, pp. 444–448, 2008.
- [22] D. L. Kraitchman, D. A. Kedziorek, and J. W. Bulte, "MR imaging of transplanted stem cells in myocardial infarction," in *Molecular Imaging: Methods and Protocols*, vol. 680 of *Methods in Molecular Biology*, pp. 141–152, Springer, Berlin, Germany, 2011.
- [23] C. Heyn, J. A. Ronald, L. T. Mackenzie et al., "In vivo magnetic resonance imaging of single cells in mouse brain with optical validation," *Magnetic Resonance in Medicine*, vol. 55, no. 1, pp. 23–29, 2006.
- [24] G. M. van Buul, G. Kotek, P. A. Wielopolski et al., "Clinically translatable cell tracking and quantification by MRI in cartilage repair using superparamagnetic iron oxides," *PLoS ONE*, vol. 6, no. 2, Article ID e17001, 2011.
- [25] J. A. Frank, B. R. Miller, A. S. Arbab et al., "Clinically applicable labeling of mammalian and stem cells by combining superparamagnetic iron oxides and transfection agents," *Radiology*, vol. 228, no. 2, pp. 480–487, 2003.
- [26] I. K. Ko, H.-T. Song, E.-J. Cho, E. S. Lee, Y.-M. Huh, and J.-S. Suh, "In vivo MR imaging of tissue-engineered human mesenchymal stem cells transplanted to mouse: a preliminary study," *Annals of Biomedical Engineering*, vol. 35, no. 1, pp. 101–108, 2007.
- [27] L. Ferreira, J. M. Karp, L. Nobre, and R. Langer, "New opportunities: the use of nanotechnologies to manipulate and track stem cells," *Cell Stem Cell*, vol. 3, no. 2, pp. 136–146, 2008.
- [28] M. Schramme, S. Hunter, N. Campbell, A. Blikslager, and R. Smith, "A surgical tendonitis model in horses: technique, clinical, ultrasonographic and histological characterisation," *Veterinary and Comparative Orthopaedics and Traumatology*, vol. 23, no. 4, pp. 231–239, 2010.
- [29] M. Schramme, Z. Kerekes, S. Hunter, and R. Labens, "Mr imaging features of surgically induced core lesions in the equine superficial digital flexor tendon," *Veterinary Radiology & Ultrasound*, vol. 51, no. 3, pp. 280–287, 2010.
- [30] M. A. Vidal, G. E. Kilroy, J. R. Johnson, M. J. Lopez, R. M. Moore, and J. M. Gimble, "Cell growth characteristics and differentiation frequency of adherent equine bone marrow-derived mesenchymal stromal cells: adipogenic and osteogenic capacity," *Veterinary Surgery*, vol. 35, no. 7, pp. 601–610, 2006.
- [31] C.-C. Liang, A. Y. Park, and J.-L. Guan, "In vitro scratch assay: a convenient and inexpensive method for analysis of cell migration in vitro," *Nature Protocols*, vol. 2, no. 2, pp. 329–333, 2007.
- [32] W.-C. Sun, J. N. Moore, D. J. Hurley et al., "Adenosine A2A receptor agonists inhibit lipopolysaccharide-induced production of tumor necrosis factor- α by equine monocytes," *Veterinary Immunology and Immunopathology*, vol. 121, no. 1–2, pp. 91–100, 2008.
- [33] A. Crovace, L. Lacitignola, E. Francioso, and G. Rossi, "Histology and immunohistochemistry study of ovine tendon grafted with cBMSCs and BMNCs after collagenase-induced tendinitis," *Veterinary and Comparative Orthopaedics and Traumatology*, vol. 21, no. 4, pp. 329–336, 2008.
- [34] A. E. Watts, A. E. Yeager, O. V. Kopyov, and A. J. Nixon, "Fetal derived embryonic-like stem cells improve healing in a large animal flexor tendonitis model," *Stem Cell Research & Therapy*, vol. 2, no. 1, article 4, 2011.
- [35] L. Kostura, D. L. Kraitchman, A. M. Mackay, M. F. Pittenger, and J. M. W. Bulte, "Feridex labeling of mesenchymal stem cells inhibits chondrogenesis but not adipogenesis or osteogenesis," *NMR in Biomedicine*, vol. 17, no. 7, pp. 513–517, 2004.
- [36] C. B. Foldager, M. Pedersen, S. Ringgaard, C. Bünger, and M. Lind, "Chondrocyte gene expression is affected by very small iron oxide particles-labeling in long-term in vitro MRI tracking," *Journal of Magnetic Resonance Imaging*, vol. 33, no. 3, pp. 724–730, 2011.
- [37] E. Farrell, P. Wielopolski, P. Pavljasevic et al., "Cell labelling with superparamagnetic iron oxide has no effect on chondrocyte behaviour," *Osteoarthritis and Cartilage*, vol. 17, no. 7, pp. 961–967, 2009.
- [38] Y.-C. Chen, J.-K. Hsiao, H.-M. Liu et al., "The inhibitory effect of superparamagnetic iron oxide nanoparticle (Ferucarbotran) on osteogenic differentiation and its signaling mechanism in human mesenchymal stem cells," *Toxicology and Applied Pharmacology*, vol. 245, no. 2, pp. 272–279, 2010.
- [39] D.-M. Huang, J.-K. Hsiao, Y.-C. Chen et al., "The promotion of human mesenchymal stem cell proliferation by superparamagnetic iron oxide nanoparticles," *Biomaterials*, vol. 30, no. 22, pp. 3645–3651, 2009.
- [40] C. A. Bourzac, J. B. Koenig, K. A. Link, S. G. Nykamp, and T. G. Koch, "Evaluation of ultrasmall superparamagnetic iron oxide contrast agent labeling of equine cord blood and bone marrow mesenchymal stromal cells," *American Journal of Veterinary Research*, vol. 75, no. 11, pp. 1010–1017, 2014.

- [41] R. C. Murray, T. S. Mair, C. E. Sherlock, and A. S. Blunden, "Comparison of high-field and low-field magnetic resonance images of cadaver limbs of horses," *Veterinary Record*, vol. 165, no. 10, pp. 281–288, 2009.
- [42] E. J. Ribot, F. M. Martinez-Santesteban, C. Simedrea et al., "In vivo single scan detection of both iron-labeled cells and breast cancer metastases in the mouse brain using balanced steady-state free precession imaging at 1.5 T," *Journal of Magnetic Resonance Imaging*, vol. 34, no. 1, pp. 231–238, 2011.

Research Article

Dynamic Tracking Human Mesenchymal Stem Cells Tropism following Smoke Inhalation Injury in NOD/SCID Mice

MeiJuan Song,¹ Qi Lv,² XiuWei Zhang,¹ Juan Cao,² ShuLi Sun,² PeiXin Xiao,² ShiKe Hou,² Hui Ding,² ZiQuan Liu,² WenLong Dong,² JinQiang Wang,² Xue Wang,² ZhiGuang Sun,² Man Tian,³ and HaoJun Fan²

¹Respiratory Department, Affiliated Jiangning Hospital, Nanjing Medical University, Jiangsu, China

²Institute of Disaster Medicine and Public Health, Affiliated Hospital of Logistic University of Chinese People's Armed Police Force, Tianjin 300162, China

³Respiratory Department, Affiliated Nanjing Children's Hospital, Nanjing Medical University, Jiangsu, China

Correspondence should be addressed to Man Tian; tmsweet@163.com and HaoJun Fan; haojunfan86@163.com

Received 21 March 2016; Revised 22 June 2016; Accepted 28 June 2016

Academic Editor: Francesco Petrella

Copyright © 2016 MeiJuan Song et al. This is an open access article distributed under the Creative Commons Attribution License, which permits unrestricted use, distribution, and reproduction in any medium, provided the original work is properly cited.

Multiple preclinical evidences have supported the potential value of mesenchymal stem cells (MSCs) for treatment of acute lung injury (ALI). However, few studies focus on the dynamic tropism of MSCs in animals with acute lung injury. In this study, we track systemically transplanted human bone marrow-derived mesenchymal stem cells (hBMSCs) in NOD/SCID mice with smoke inhalation injury (SII) through bioluminescence imaging (BLI). The results showed that hBMSCs systemically delivered into healthy NOD/SCID mouse initially reside in the lungs and then partially translocate to the abdomen after 24 h. Compared with the uninjured control group treated with hBMSCs, higher numbers of hBMSCs were found in the lungs of the SII NOD/SCID mice. In both the uninjured and SII mice, the BLI signals in the lungs steadily decreased over time and disappeared by 5 days after treatment. hBMSCs significantly attenuated lung injury, elevated the levels of KGF, decreased the levels of TNF- α in BALF, and inhibited inflammatory cell infiltration in the mice with SII. In conclusion, our findings demonstrated that more systemically infused hBMSCs localized to the lungs in mice with SII. hBMSC xenografts repaired smoke inhalation-induced lung injury in mice. This repair was maybe due to the effect of anti-inflammatory and secreting KGF of hMSCs but not associated with the differentiation of the hBMSCs into alveolar epithelial cells.

1. Introduction

Smoke inhalation injury (SII) is caused by smoke-induced damage of the respiratory tract and lung parenchyma, with or without additional heat-induced damage. SII is a major cause of morbidity and mortality in victims of fire tragedies [1], affecting approximately 22% of all burn patients and resulting in at least 30% of all fire-related mortality [2]. Moreover, 80% to 90% of fire-related fatalities have been attributed to smoke inhalation [3]. The major harmful components of smoke include heat, systemic toxins (e.g., CO and cyanide), and respiratory irritants [4], which damage the respiratory tract and lung tissue. This results in laryngeal/pulmonary edema, airway obstruction, and ventilation/perfusion mismatch [5].

Severe cases may develop acute respiratory distress syndrome (ARDS) [3]. Determining the best method for treating burn victims, especially during the early stages of smoke inhalation-induced acute lung injury (ALI), remains to be a difficult problem in the field of first aid medicine. Current treatments for SII mainly focus on oxygen administration, airway management, fluid resuscitation, mechanical ventilation, and the use of specific medications [1, 4, 6]. Although many drugs are effective in reducing lung injury in animal models, only a few drugs, including anticoagulants, β 2-agonists, antioxidants, and inflammatory mediator agonists, are currently applied in the clinical setting [6, 7].

Mesenchymal stem cells (MSCs) are self-renewing, multipotent progenitor cells that have the potential to differentiate

into multiple different mesodermal lineages. It has been shown in many different animal models that MSCs have a remarkable ability to localize to sites of injury and exert non-immunogenic and immunosuppressive characteristics [8, 9]. Based on these properties, MSCs offer a promising source for cell-based treatment of various complicated disorders, such as graft-versus-host disease [10, 11], cardio/cerebrovascular disease [12], spinal cord injury [13], hepatic disease [14], and respiratory disease [15, 16]. Furthermore, many studies have indicated that MSCs exert protective effects against ALI via their secretion of multiple paracrine factors, including endothelial and epithelial growth factors, anti-inflammatory cytokines, and antimicrobial peptides [17–20]. However, these studies have mainly focused on endotoxin-induced ALI, and researches focusing on the effects of MSCs on smoke inhalation-induced ALI still lack. Furthermore, uncertainties remain regarding the localization and persistence of MSCs in vivo following their administration into subjects with ALI.

Bioluminescent imaging (BLI), a recently developed technique that enables the noninvasive study of ongoing biological processes in small laboratory animals, can be used to track luciferase- (Luc-) expressing cells implanted into living animals in real time. In a previous study, Kidd et al. used BLI to track the dynamic distribution of firefly Luc-expressing human MSCs (hMSCs) following their systemic injection into healthy mice, mice subjected to inflammatory insults, and mice bearing tumors. The hMSCs were found to initially localize to the lungs and later moved into the liver and spleen. Additionally, the Luc signal produced by the hMSCs decreased over time. In wounded mice and tumor-bearing mice, the hMSCs were found to localize to injured tissue or tumors after systemic administration [21]. Although it has been shown that MSCs initially localize to the lungs following systemic delivery, studies examining the dynamic distribution of MSCs after their intravenous injection into mice with SII are lacking. In the current study, we modified human bone marrow-derived MSCs (hBMSCs) to stably coexpress Luc and green fluorescent protein (GFP) reporter genes (Luc-GFP-hBMSCs). We then used BLI to track the dynamics of the cells' localization patterns for 14 days following their systemic administration into normal mice and mice with SII. Our results provide experimental support for the use of MSCs to treat SII.

2. Materials and Methods

2.1. Cells and Animals. hMSCs were purchased from Cyagen Biosciences (Guangzhou, China) and grown in Dulbecco's modified Eagle's medium (DMEM) (Cyagen Biosciences) supplemented with 10% heat-inactivated fetal bovine serum (FBS) (Cyagen) at 37°C under 5% CO₂.

Male NOD/SCID mice, aged between 6 and 8 weeks and ranging in weight from 25 to 30 g, were purchased from Wei Tong Li Hua Experimental Animal Technology Co., Ltd (Beijing, China). The mice were used in accordance with institutional guidelines and following approved protocols.

2.2. Lentiviral Vector Construction and MSC Transduction. Lentiviral vectors carrying a Luc and GFP dual-fusion

reporter gene were constructed and purified by Shanghai GeneChem Co., Ltd. For transduction, hMSCs were seeded into 25 cm² flasks containing appropriate growth medium and grown to 20%–30% confluence. Then, the GFP-Luc lentivirus vectors were added at a multiplicity of infection (MOI) of 10 to a 2.5 mL aliquot of hMSCs in growth medium containing 5 µg/mL polybrene. The cells were incubated with the viruses for 8–12 h, after which fresh medium was added to each flask, and the cells were incubated for an additional 48–72 h. The cells were passaged 1:2 and grown to 80–100% confluence. Three days after transduction, the cells were viewed on a Leica DMI4000 inverted microscope equipped with a fluorescence source and a charge-coupled device (CCD) camera. Transduction efficiency was determined by fluorescence-activated cell sorting (FACS) analysis of GFP expression using previously described settings [22].

2.3. Flow Cytometry Analysis. Luc-GFP-hBMSCs were harvested with 0.25% trypsin-EDTA and resuspended in phosphate-buffered saline (PBS) supplemented with 2% FBS. Approximately 1×10^6 cells were stained with 1 µg of antibody for 30 minutes at 4°C and then analyzed on a FACS Caliber flow cytometer (Becton Dickinson, Franklin Lakes, NJ). Human antibodies against the following proteins were used for this analysis: CD105, CD29, CD73, CD44, CD90, CD34, CD45, and CD11c (BD Biosciences).

2.4. Multilineage Differentiation of Transduced hMSCs. To determine the multilineage differentiation potential of the transduced hMSCs, we cultured the cells in various types of differentiation media according to manufacturer recommendations (Cyagen Biosciences, Guangzhou, China, <http://www.cyagen.com/>). To induce adipogenic differentiation, Luc-GFP-hBMSCs were subcultured in six-well plates at 2×10^4 cells/cm² in growth medium containing 10% FBS, 5% penicillin-streptomycin, and 2 mM L-glutamine. The culture medium was replaced every 3 days until the cells reached 100% confluence, after which the growth medium was replaced with induction medium (2 mL per well) containing FBS, penicillin-streptomycin, glutamine, insulin, rosiglitazone, and dexamethasone. Three days later, the medium was replaced with maintenance medium consisting of FBS, penicillin-streptomycin, and insulin. After 24 h, the maintenance medium was changed back to induction medium, and this cycle was repeated three times. After five cycles of induction/maintenance, the cells were cultured in maintenance medium for 3 days. Three weeks later, adipose cells were stained for visualization with Oil Red O.

To induce osteogenic differentiation, Luc-GFP-hBMSCs were cultured in growth medium at a density of 3×10^4 cells/cm² for 1 day at 37°C in a 5% CO₂ humidified incubator. Following this, the growth medium was aspirated and replaced with osteogenic differentiation medium (2 mL per well) containing FBS, penicillin-streptomycin, glutamine, ascorbate, β-glycerophosphate, and dexamethasone. The medium was replaced every three days. Three weeks later, the cells were fixed with 2 mL of 4% formaldehyde solution and stained with Alizarin red. A light microscope was used to visualize and capture images of the stained cells.

To induce chondrogenic differentiation, human MSCs at subconfluent conditions were trypsinized and aliquots of 2×10^5 cells per well were added to a 15 mL centrifuge tube, and the plate was spun at $400 \times g$ for 5 min. For differentiation into chondrocytes, cells were cultured in a commercialized chondrogenic induction medium in the presence of 10 ng/mL recombinant human TGF- β 3. The cell pellets formed free-floating aggregates within the first 24 h. The medium was replaced every 2–3 days, and aggregates were cultured for 28 days and collected for paraffin section following Alcian Blue staining.

2.5. Establishment of Smoke Inhalation Mouse Model. All animals used in this study received humane care in compliance with the Guide for the Care and Use of Laboratory Animals published by the National Institutes of Health. The study protocol was approved by the Laboratory Animal Ethics Committee of the Affiliated Hospital of Logistical College of Chinese People's Armed Police Forces. All surgeries were performed under sodium pentobarbital anesthesia, and all efforts were made to minimize suffering.

Models of SII were established using a previously described device that was constructed in-house [23]. To accomplish this, awake male NOD/SCID mice were exposed to combustion smoke generated by smoldering wood shavings in a smoke-generating container connected to a 20 L transparent exposure chamber. The mice were subjected to the smoke for 0, 3, 5, 7, and 9 min. The establishment of severe SII was assessed by blood carboxyhemoglobin (COHb) concentration, blood gas analysis, measurement of the wet/dry (W/D) weight ratio of lung tissue, and lung histopathology. Blood was collected from a subset of mice that were killed 1 h after smoke exposure to measure COHb concentration with an oximeter (482 CO-Oximeter) [24] and analyze blood gas content using a Radiometer ABL 625 Blood Gas Analyzer (Copenhagen, Denmark) [25]. Another subset of mice were killed 3 d after smoke exposure, and their lungs were isolated to measure W/D ratios and for histological analysis.

2.6. Luc-GFP-hBMSC Administration and Bioluminescent Imaging. At 24 h after smoke inhalation, 100 μ L aliquots of Luc-GFP-hBMSCs (3×10^5 cells) were injected into the tail veins of control and SII NOD/SCID mice. The mice were then submitted to BLI to visualize the localization of the Luc-GFP-hBMSCs at 1.5, 2.5, 5, 7.5, 10, and 24 h and 3 and 5 days after injection [21].

To monitor Luc-GFP-hBMSC localization to the lungs, we submitted mice to isoflurane anesthesia and then intraperitoneally injected them with D-luciferin firefly potassium salt substrate (150 mg/kg body weight in 100 μ L PBS). Then, we placed the animals into an IVIS system in a supine position (Caliper Life Sciences, Hopkinton, MA). The animals were imaged over a 10 min time period with 1 min acquisition intervals [26]. To quantify light emission, a region of interest (ROI) was manually selected based on signal intensity. The area of the ROI was kept constant while the signal intensity was recorded as average photons per second

per square centimeter per steradian as previously described [21].

2.7. Analysis of Wet/Dry Weight Ratio of Lung Tissue. After treatment as described above, the mice were killed, and their left lungs were isolated. After blotting off blood and other contaminants, the wet weights of the lung tissue samples were measured. Then, the lungs were dried in a 70°C oven for 72 h, and their dry weights were measured. The W/D weight ratios of the lungs were then calculated as previously described [25].

2.8. Histology and Immunohistochemistry. The right lungs of the mice treated as described above were isolated, and their upper and middle lobes were fixed in 10% formalin for 24 h. The tissue samples were then dehydrated, embedded in paraffin, and cut into 5 mm thick sections. Following this, the samples were stained with hematoxylin and eosin (H&E) after deparaffinization and evaluated under an optical microscope (Olympus BX51, Japan).

Luc-GFP-hBMSCs in lung tissue were detected by immunostaining for GFP. After deparaffinization and rehydration, paraffin sections were placed into a pressure cooker containing antigen retrieval buffer (0.01 M citrate buffer, pH 6.0) under full pressure for 2 minutes to unmask antigens. Immunostaining was performed by incubating the sections with a rabbit anti-GFP monoclonal antibody (1:100, Abcam, MA) overnight at 4°C, followed by incubation with a biotin-conjugated secondary antibody (ZSGB-bio, China) at 37°C for 1 h and horseradish peroxidase-conjugated streptavidin (ZSGB-bio, China) at 37°C for 30 min. The sections were stained with a DAB kit, which were counterstained with hematoxylin to visualize cell nuclei. Images were obtained with an Olympus BX51 microscope, and the proportion of positively stained cells was determined using Image-Pro Plus version 5.1. For histological and immunohistochemical analysis, the slides were labeled with numbers, and double-blinded examinations were performed by two independent pathologists.

2.9. Semiquantitative PCR. Total RNA for PCR was extracted using an RNeasy kit (Solarbio, Beijing, China), which included a DNase digestion step to remove any contaminating DNA. Semiquantitative reverse transcription PCR was performed using a thermal cycler (Thermo), and amplified products were visualized using agarose gels. The following primers were used for PCR:

Luciferase forward: ACTGGGACGAAGACGAAC-AC.

Luciferase reverse: GGCGACGTAATCCACGAT-CT.

β -actin forward: GTGGGGCGCCCCAGGCACCA.

β -actin reverse: CTCCTTAATGTCACGCACGA-TTTC.

2.10. Analysis of TNF- α and KGF Levels in Bronchoalveolar Lavage Fluid. Bronchoalveolar lavage (BAL) was performed by instilling and withdrawing sterile physiological saline

(1 mL) through a tracheal cannula using a 20-gauge Surflo i.v. catheter. This procedure was repeated three times, and the three BAL fluid (BALF) samples were pooled. The BALF was centrifuged ($300 \times g$, 5 min), and the supernatant portions were stored at -80°C for further examination. For the detections of TNF- α and keratinocyte growth factor (KGF), the supernatant of BALF was analyzed by using mouse TNF- α ELISA kit (eBioscience, San Diego, CA, USA) and KGF ELISA kit (Nanjing Jiancheng Bioengineering Institute, Nanjing, China) following the instructions of manufacturer.

2.11. Statistical Analysis. All data were processed using SPSS version 13.0 statistical software. The data are shown as the mean \pm standard deviation ($\bar{x} \pm s$). Sample measurement data between groups were compared using independent samples *t*-tests, and group data were compared using paired *t*-tests. $P < 0.05$ was considered significant.

3. Results

3.1. hMSC Transduction. Lenti-GFP-Luc with a 2.00×10^8 TU/mL titer was used at an MOI of 10 to infect hMSCs. Transduction efficiency was approximately 90% after 48 h based on fluorescence and phase-contrast microscopy (Figures 1(a) and 1(b)). GFP expression remained stable for at least 30 d under constant culture conditions (data not shown). In vitro Luc activity was assessed using BLI following the application of D-luciferin. Only the transduced cells showed Luc activity and not the control cells (Figure 1(c)).

3.2. Characterization of Luc-GFP-hBMSCs. After transduction with Lenti-GFP-Luc, FACS analysis demonstrated that Luc-GFP-hBMSCs expressed high levels of CD105, CD29, CD73, CD44, and CD90 and low levels of CD34, CD45, and CD11c. These proteins were chosen for analysis because they represent well-established phenotypic markers for hMSCs (Figure 2(a)) [23]. The expression patterns were consistent across all hMSCs tested, and the tested hMSCs were used in the following experiments. Additionally, we subjected transduced hMSCs to adipogenic and osteoblastic differentiation assays. In all cases, cells positively stained for Oil Red O and Alizarin red were detected after culture in differentiation medium, suggesting that the cells maintained differentiation potential regardless of lentiviral transduction (Figures 2(b) and 2(c)). Furthermore, chondrogenic differentiation of transduced hMSCs was confirmed by staining the acid mucopolysaccharide of chondrocytes with Alcian Blue (Figure 2(d)).

3.3. Establishment of Mouse Model of Smoke Inhalation Injury. To establish a mouse model of SII, a smoke generator constructed in-house was utilized, as previously described [23]. To optimize the experimental conditions for inducing SII, mice were subjected to smoke for 0, 3, 5, 7, and 9 min. 85% of mice exposed to smoke for 9 min died of hypoxia, so this time point was excluded in the following detections. COHb concentration and blood gas content were measured immediately after smoke exposure and again 1 h later. As the smoke exposure time increased, the COHb concentration

increased, while the PaO_2 and $\text{PaO}_2/\text{FiO}_2$ content in blood decreased (Figure 1(a)). The $\text{PaO}_2/\text{FiO}_2$ ratio was below 300 at 7 min in the SII group, which is within the standard for mild ARDS according to the Berlin Definition [27].

The W/D weight ratio was used as an index of water accumulation in the lung, which is an indicator of lung edema. At 3 d after smoke exposure, the lung W/D ratios in the 7 min SII group were significantly elevated relative to the control group; however, there were no differences noted in the 3 or 5 min SII groups (Figure 3(a)). Accordingly, histopathology results showed that exposure to smoke for 7 min led to the most serious pathological changes in the lungs, including narrowed alveolar space, thickened alveolar and bronchiole walls, and inflammatory cell infiltration around the airway (Figure 3(b)). Based on these results, we used a 7 min smoke exposure protocol for the following studies.

3.4. Dynamics of hMSC Distribution after Injection into Mice with SII. Luc-GFP-hBMSCs (3×10^5 cells/animal) were intravenously injected into NOD/SCID mice with or without SII. Live-animal BLI was then used to monitor Luc-GFP-hBMSC localization patterns over time. As shown in Figure 4, luciferase expression was initially detected in the lungs in both the control and the SII plus Luc-hBMSC groups (Figure 4(a)). Compared with the control group, stronger BLI signals were produced in the SII group. The BLI signals in the lungs peaked at 7.5 h after infusion of hBMSCs and then gradually diminished with time (Figure 4(b)). At 24 h after infusion of hBMSCs, the bioluminescent signals began to shift to the abdomen in the control group. However, the signals were still primarily in the lungs in the mice with SII. Five days after injection of hBMSCs, the BLI signals disappeared completely from the lungs, and the abdomens of the mice in the control group showed only weak BLI signals. Fourteen days after injection, no signals were detected in either the control group or the SII group (Figures 4(a) and 4(b)).

3.5. PCR and Immunohistochemistry Detection of hBMSC Engraftment. Fourteen days after the injection of Luc-GFP-hBMSCs, the injected mice were sacrificed, and PCR was used to detect Luc expression in liver and lung tissues. Consistent with the BLI results described above, no Luc expression was detected in either the control group or the SII group that underwent hBMSC administration (Figure 5(a)). Accordingly, no GFP-positive cells were found in the lung tissue samples collected from these mice (Figure 5(b)).

3.6. Protective Effects of hBMSC Xenografts in SII Mice. Fourteen days after the injection of hBMSCs into mice with SII, we evaluated the effects produced by the cells by measuring lung W/D weight ratios and evaluating pathological changes in lung tissue samples. There were no significant differences in W/D weight ratio in the control group before and after injection. The lung W/D ratio in the SII + hBMSC group was significantly lower than that in the untreated SII group ($P < 0.01$), indicating that pretreatment with hBMSCs could decrease the degree of lung edema produced by smoke inhalation (Figure 6(a)). Moreover, PaO_2 and $\text{PaO}_2/\text{FiO}_2$ were

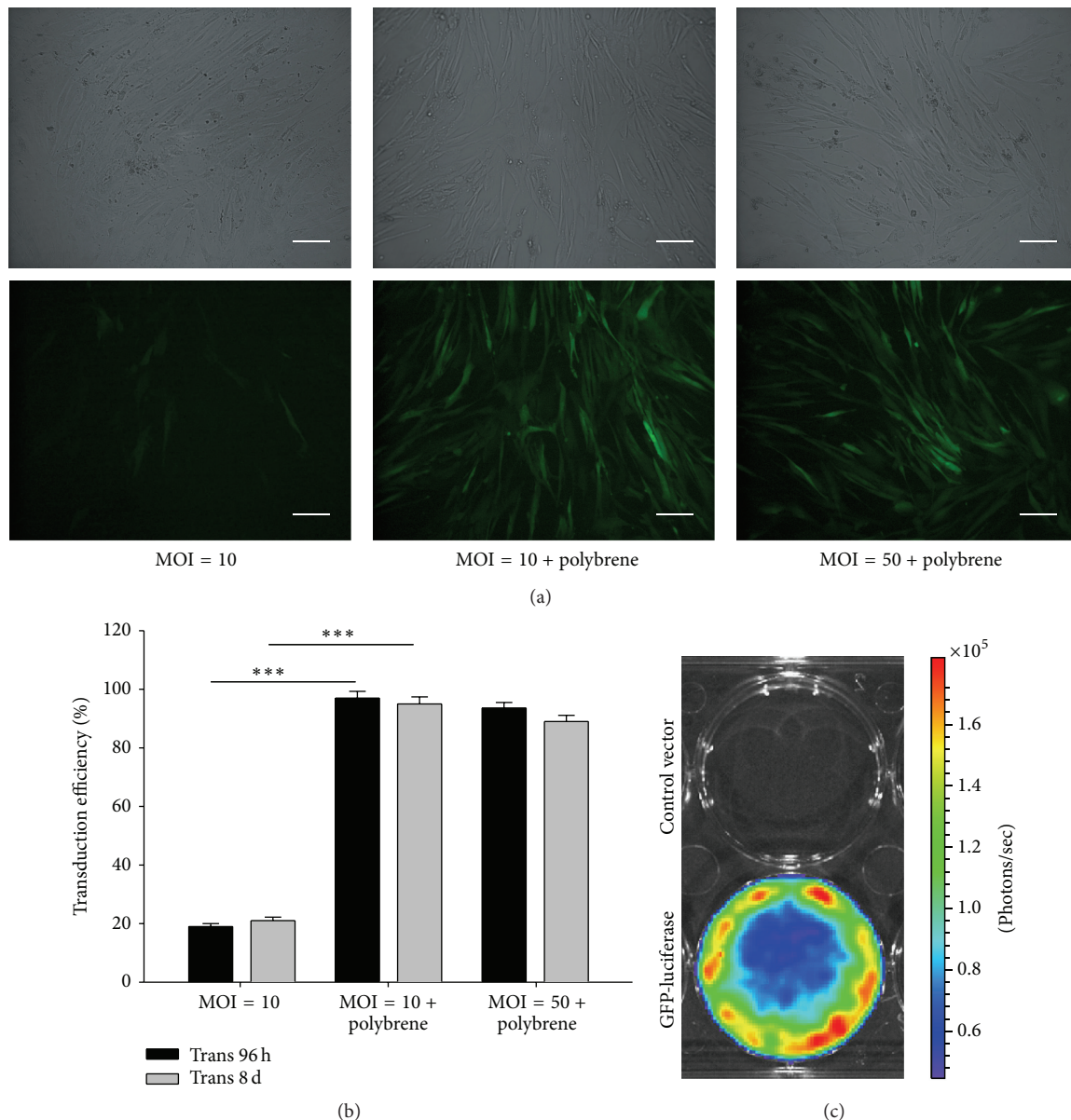


FIGURE 1: Characterization of human mesenchymal stem cells expressing firefly luciferase and green fluorescent protein reporter genes. (a) Human mesenchymal stem cells (hMSCs) were transduced with a lentiviral vector carrying luciferase (Luc) and green fluorescent protein (GFP) reporter genes, and GFP expression within the cytosol was measured. (b) Transduction efficiencies of Luc-GFP lentiviral vector-transduced hMSCs after 96 h and 8 d. *** indicates $P < 0.01$ between the indicated groups. (c) Firefly Luc-expressing cells showed specific activity after treatment with D-luciferin and coelenterazine in vitro.

significantly improved after hBMSCs treatment compared with SII group ($P < 0.01$) (Figures 6(b) and 6(c)).

As shown in Figure 6(d), there were no obvious differences in lung tissue samples collected from mice treated with hBMSCs compared to untreated mice. In the SII group, the alveolar walls burst, and the alveolar space was narrowed. In addition, there was significant infiltration of polymorphonuclear leukocytes (PMNs) around the airway. The administration of hBMSCs markedly reduced the severity of pulmonary injury induced by smoke inhalation. In the lungs of the mice in the SII + hBMSCs group, the alveolar space was widened,

there was less PMN infiltration, and there were thinner alveolar septa compared to the lungs of the untreated mice with SII. These results indicated that the hBMSC xenografts protected mice from damage associated with SII.

3.7. Analysis of KGF and $TNF-\alpha$ Levels in BALF. Previous studies have reported that MSCs could repair ALI-induced impaired alveolar fluid clearance (AFC) by secreting KGF [20]. We next measured the concentration of KGF in BALF and culture supernatant of hBMSCs. Consistent with several studies, the secret of KGF by hBMSCs was detected in

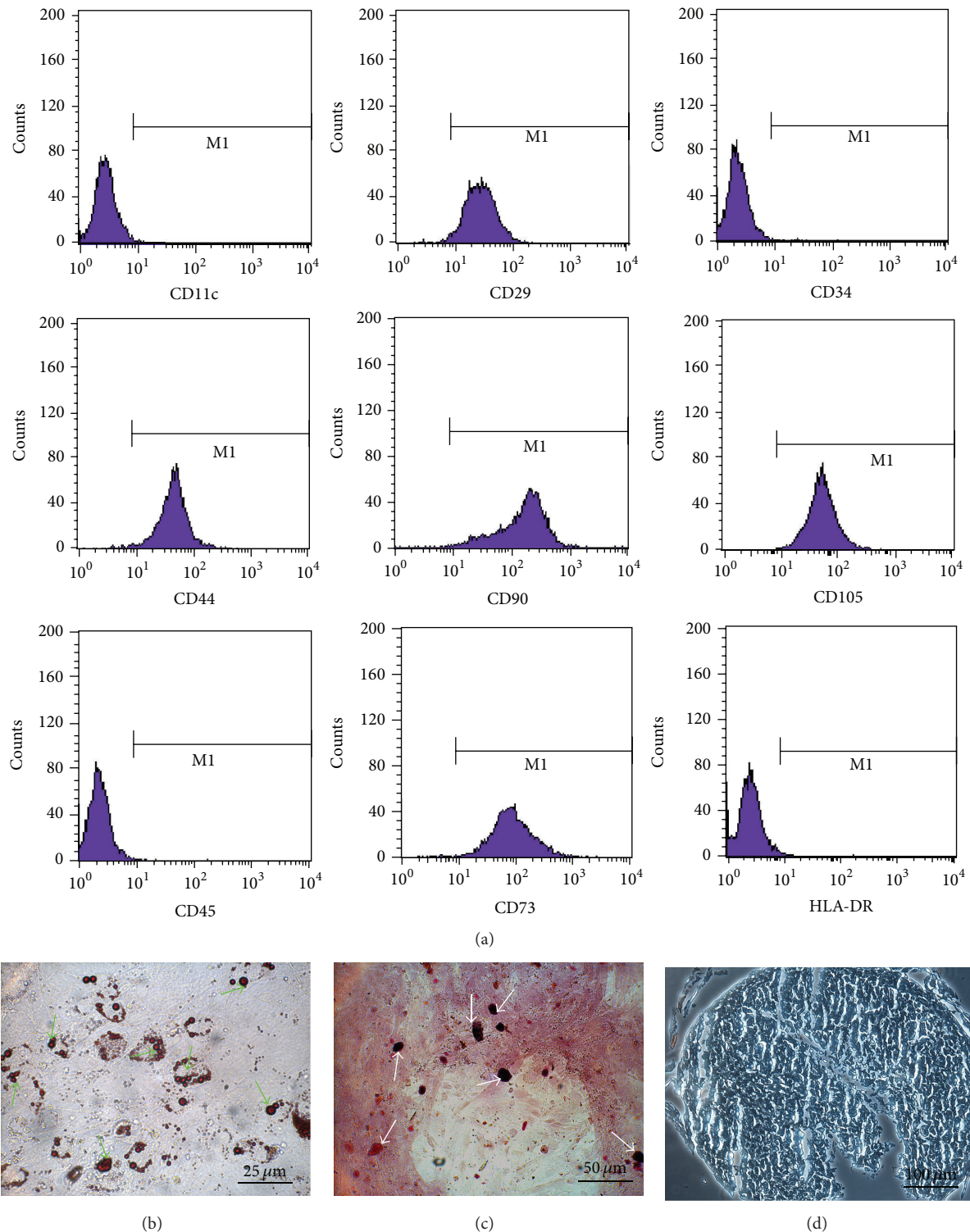
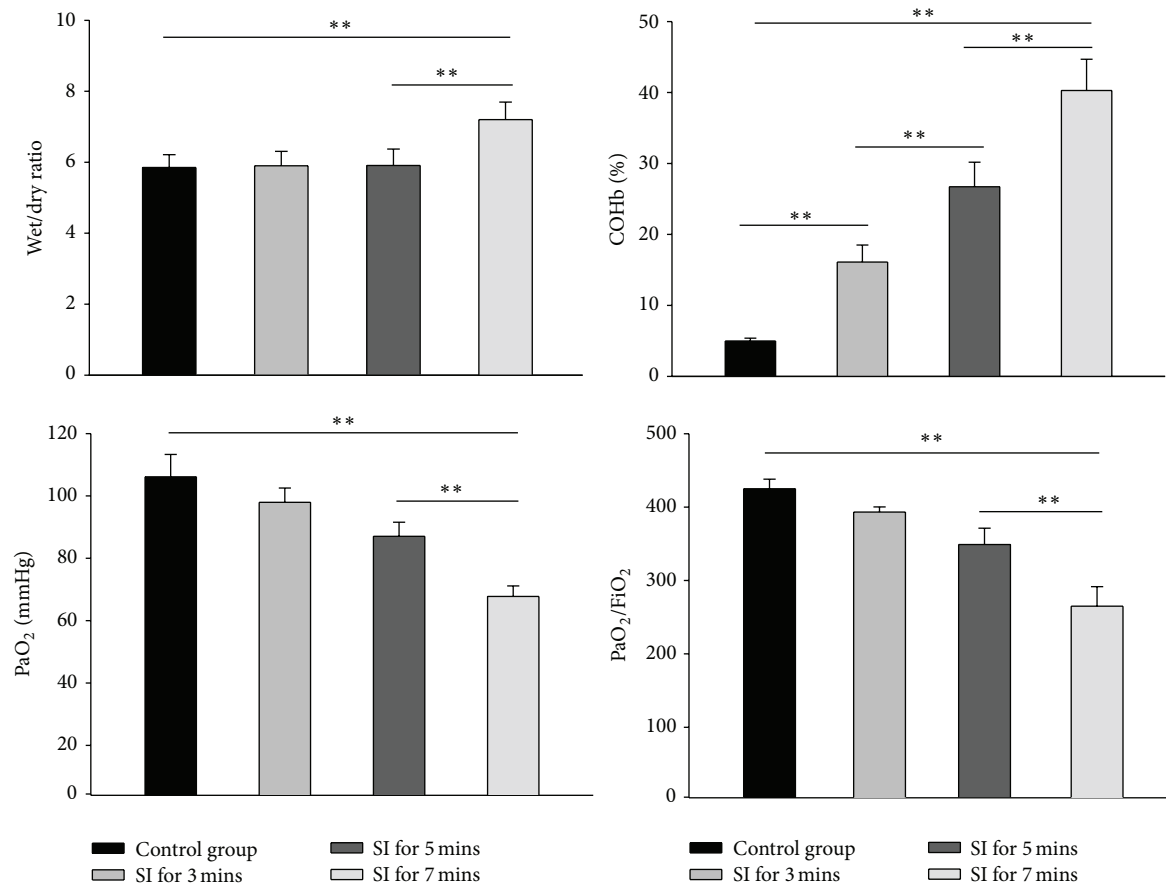
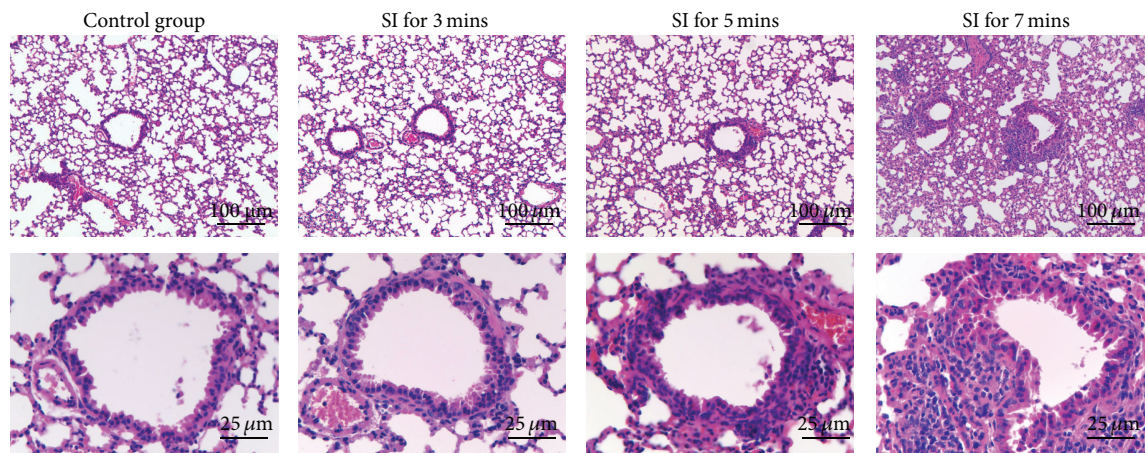


FIGURE 2: Characterization of human bone marrow-derived stem cells coexpressing luciferase and green fluorescent protein reporter genes (Luc-GFP-hBMSCs). (a) Flow cytometric analysis of Luc-GFP-hBMSCs. Luc-GFP-hBMSCs were harvested with 0.25% trypsin-EDTA and resuspended in phosphate-buffered saline supplemented with 2% fetal bovine serum. Following this, the expression levels of CD90, CD105, CD29, CD73, CD44, CD34, CD45, CD11c, and HLA-DR were measured by fluorescence-activated cell sorting analysis. (b)–(d) Luc-GFP-BMSCs were able to differentiate into adipocytes, osteoblasts, and chondrocytes in vitro as shown by positive Oil Red O staining (b), Alizarin red staining (c), and Alcian Blue staining (d). The green arrows indicate lipid droplets stained with Oil Red O, and the white arrows indicate calcium nodules stained with Alizarin red. Acid mucopolysaccharide of chondrocytes could be stained by Alcian Blue.



(a)



(b)

FIGURE 3: Establishment of smoke inhalation NOD/SCID mouse model. NOD/SCID mice ($n = 6$) were subjected to 0, 3, 5, 7, and 9 min of smoke exposure. (a) Wet/dry (W/D) weight ratios, blood carboxyhemoglobin (COHb), PaO₂, and PaO₂/FiO₂ were measured at the indicated time points. ** indicates $P < 0.01$ between the indicated groups. (b) Representative histological images of lung sections from mice with or without smoke inhalation injury ($n = 6$).

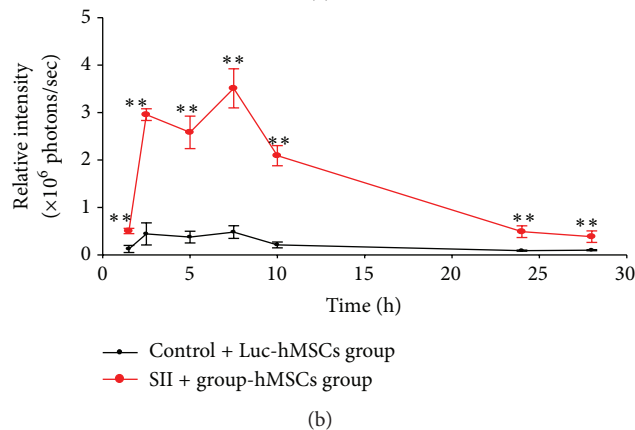
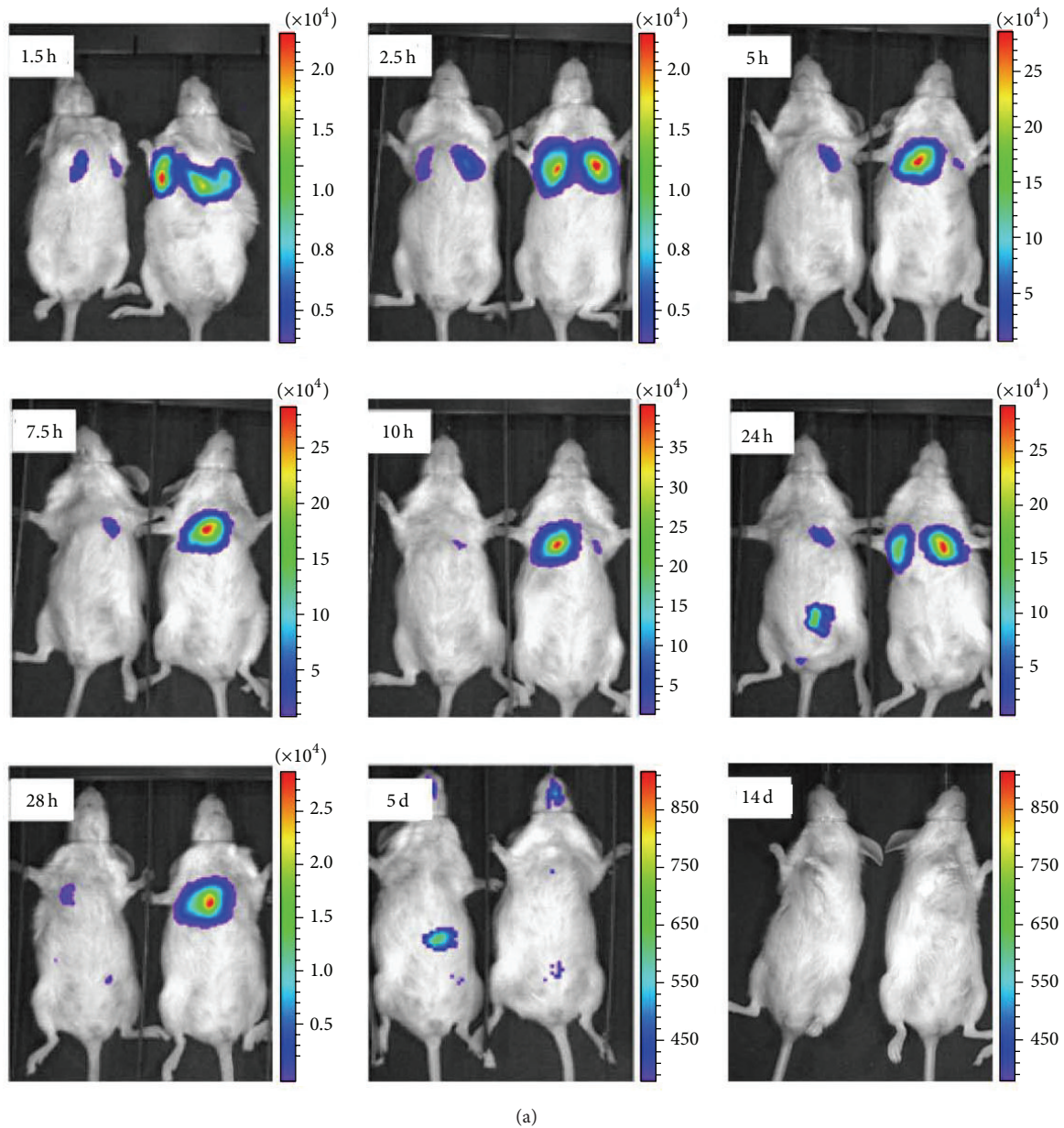


FIGURE 4: Biodistribution of human bone marrow-derived stem cells coexpressing luciferase and green fluorescent protein reporter genes in mice with or without smoke inhalation injury. Human bone marrow-derived stem cells coexpressing luciferase and green fluorescent protein reporter genes (Luc-GFP-hBMSCs) were intravenously injected into NOD/SCID mice and imaged at 1.5, 2.5, 5, 7.5, 10, 24, and 28 h and 5 and 14 d after injection. (a) The Luc-GFP-hBMSCs initially localized to the lung and then migrated to the abdomen by 24 h. Reporter gene expression completely disappeared by 14 d after injection. (b) Quantification of the bioluminescent signal over this time period indicated that a greater number of systemically infused Luc-GFP-hBMSCs localized to the lungs in mice with smoke inhalation injury compared to uninjured mice ($n = 6$). ** indicates $P < 0.01$ compared with the uninjured control group treated with Luc-GFP-hBMSCs.

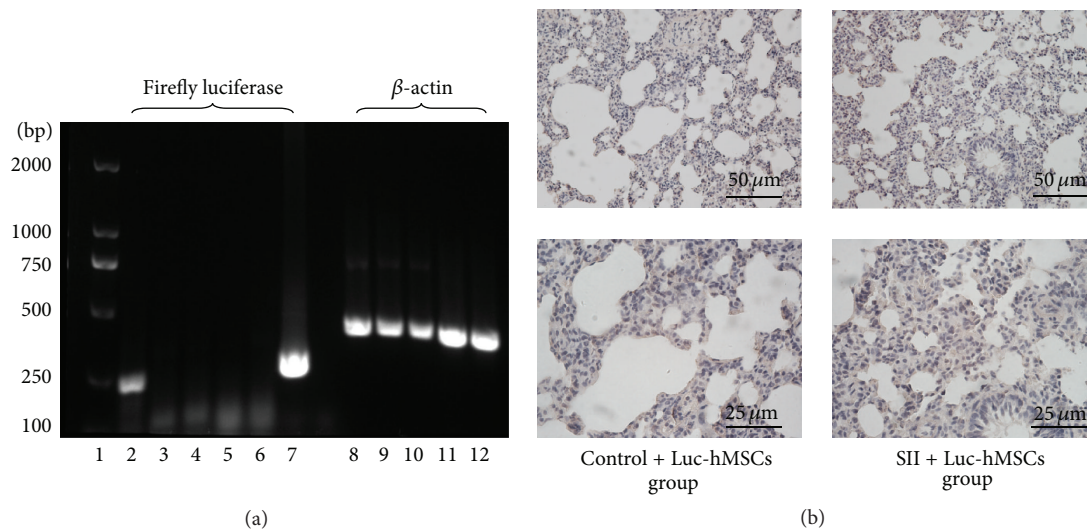


FIGURE 5: Detection of human bone marrow-derived stem cells coexpressing luciferase and green fluorescent protein reporter genes in mouse tissues at 14 days after injection. (a) Expression of the firefly luciferase gene was detected by PCR. β -actin was used as a loading control. Panel 1: DNA marker. Panels 2–7: from left to right, human bone marrow-derived stem cells coexpressing luciferase and green fluorescent protein reporter genes (Luc-GFP-hBMSCs), liver from a control mouse treated with Luc-GFP-hBMSCs, liver from a mouse with smoke inhalation injury (SII) treated with Luc-GFP-hBMSCs, lung from a control mouse treated with Luc-GFP-hBMSCs, and lung from a mouse with SII treated with Luc-GFP-hBMSCs. Panels 8–12: corresponding β -actin levels from panels 2–6. Representative images from at least three independent experiments. (b) Luc-GFP-hBMSCs were detected by immunohistochemistry (anti-GFP) in the lung at day 14 after injection into mice with SII ($n = 6$).

the culture supernatant. Moreover, 1 day after injection of hBMSCs, the levels of KGF in BALF were increased compared with control and SII groups ($P < 0.05$) (Figure 7(a)).

MSC could downregulate expressions of proinflammatory factors to protect the host from extraordinary inflammatory damage [18]. Our results found that systemic treatment with hMSCs could significantly decrease the levels of TNF- α in BALF (Figure 7(b)), which may contribute to downregulating inflammatory responses and tissue injury.

4. Discussion

In China, ALI caused by smoke inhalation is the most common cause of death among victims of fire tragedies. At least 85% of deaths from fire disasters occur because of excessive inhalation of smoke and toxic gases [28]. Characterized by acute onset, rapid progression, severe illness, and high mortality, severe respiratory disease resulting from smoke inhalation is commonly seen in clinical practice [29].

ALI is a severe pathological condition clinically characterized by respiratory distress, refractory hypoxemia, and non-cardiogenic pulmonary edema. A number of factors can lead to the development of ALI; these include sepsis, pneumonia, trauma, aspiration of gastric contents, and exposure to large amounts of smoke from fires [30]. Smoke inhalation-induced ALI has unique pathophysiological features that differ from ALI caused by sepsis or pneumonia. Components found within smoke, including particulate materials, systemic toxins, and respiratory irritants, trigger the production of a cascade of inflammatory mediators within the airway mucosa and lung parenchyma, causing damage to mucosal lining

and leading to peribronchial inflammation, which ultimately can result in pulmonary edema and ventilation/perfusion mismatch [1, 3–5]. During this process, intrapulmonary leukocyte aggregation following activation of the classic complement cascade releases even more chemokines and cytokines, leading to airway cast formation and widespread plugging. Moreover, the resultant induction of nitric oxide (NO) synthase in respiratory epithelial cells and alveolar macrophages leads to NO production, which increases bronchial blood flow, decreases hypoxic pulmonary vasoconstriction in poorly ventilated regions within the lung, and results in ventilation/perfusion mismatch. NO also forms peroxynitrite (ONOO^-) by combining with superoxide (O_2^-) produced by neutrophils, which can lead to DNA damage and alveolar epithelial cell death [4, 5].

As with the other factors that cause ALI, efficient and specific therapies are needed for smoke inhalation-induced ALI. To develop these therapies, additional studies are needed because the pathological mechanisms underlying ALI remain poorly understood, and the current supportive methods used to treat the condition, including basic mechanical ventilation, fluid resuscitation, and oxygen administration, are not as effective as desired [1, 4, 6]. Different types of cell therapies are expected to have the ability to cure a wide variety of diseases, substantially improving the routine therapies currently used in the clinic [31]. Due to their low expression levels of immune antigens, MSCs are an attractive cell resource for the treatment of various complicated and refractory diseases [32]. Preclinical studies in small (mouse and rat) and large (sheep) animal models, as well as ex vivo studies using perfused human lungs, have demonstrated the potential

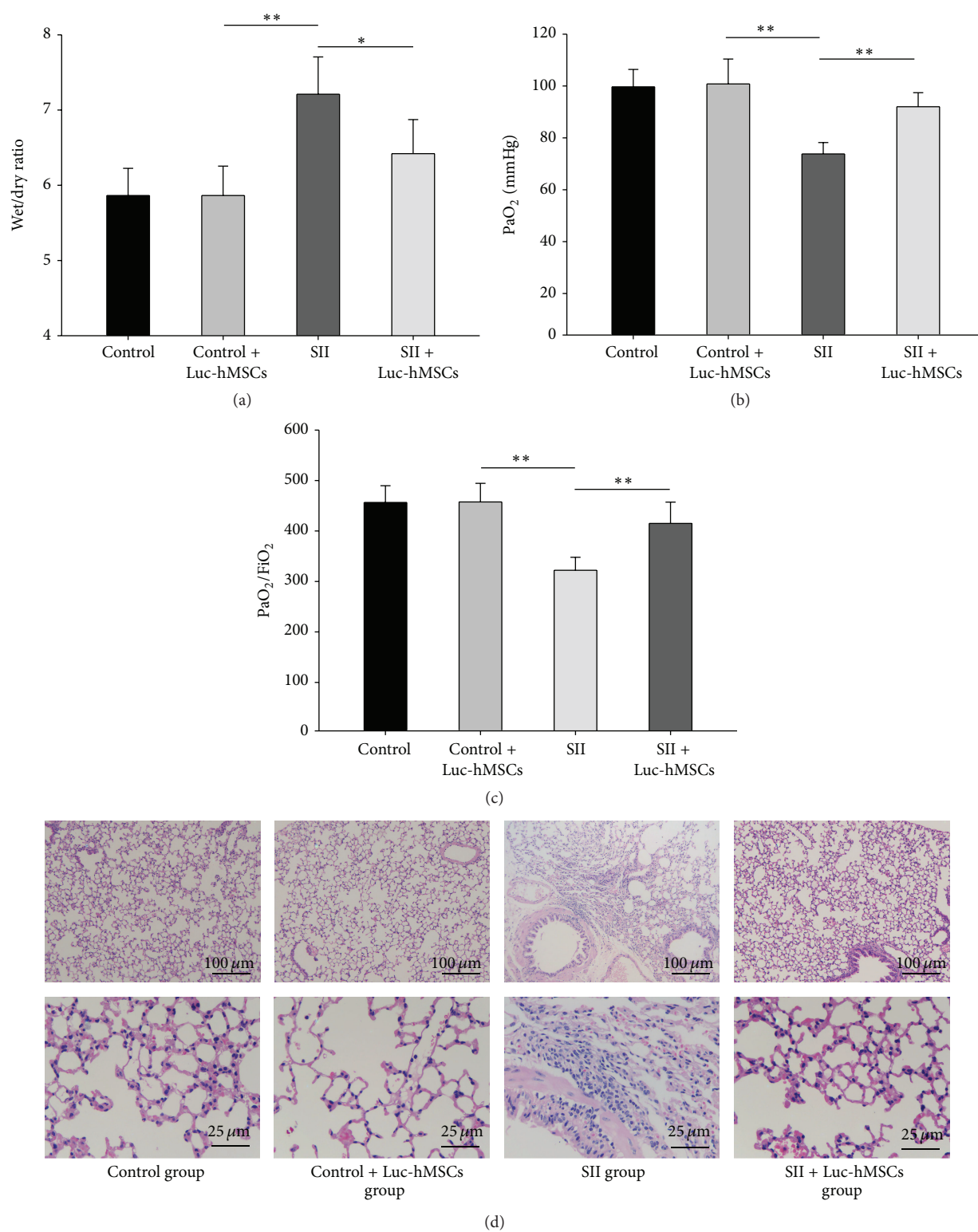


FIGURE 6: Evaluation of the protective effects of hMSCs against smoke inhalation lung injury in mice. (a)–(c) Wet/dry (W/D) weight ratios, PaO₂, and PaO₂/FiO₂ were measured at 14 days after injection of hBMSCs into mice with or without SII ($n = 6$). * $P < 0.05$, ** $P < 0.01$ between the indicated groups. (d) Representative pictures of histological examinations of lung sections from the indicated groups.

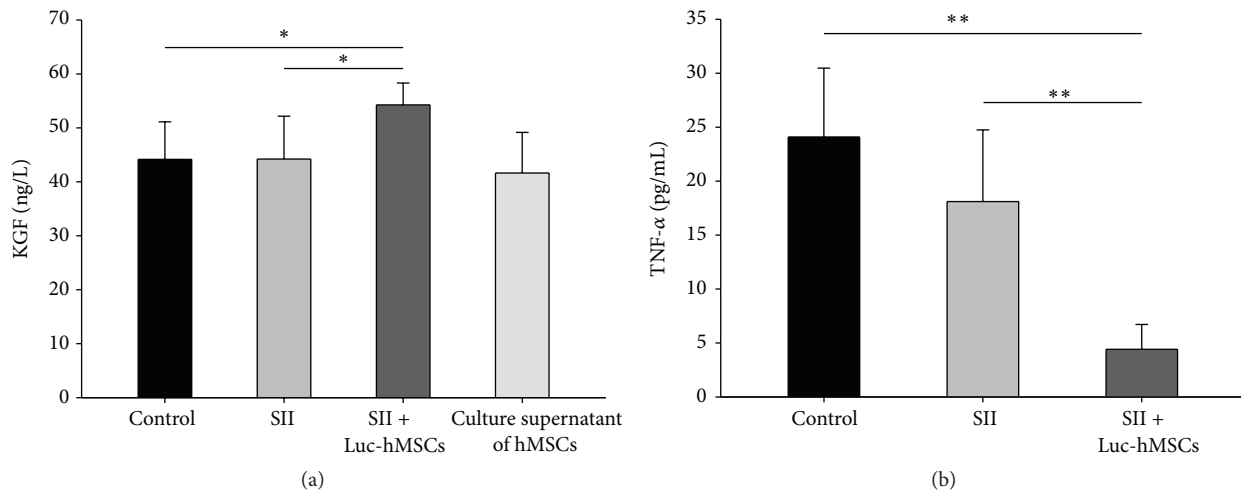


FIGURE 7: The effects of hMSCs treatment on the levels of TNF- α and KGF in BALF of mice with SII. At one day after injection of hMSCs, (a) the concentrations of keratinocyte growth factor (KGF) in the BALF were measured for control, SII, and Luc-hMSCs treatment groups. The culture supernatant of hBMSC was used as a positive control. (b) The concentrations of TNF- α in the BALF were measured for the indicated groups ($n = 6$). * $P < 0.05$, ** $P < 0.01$ between the indicated groups.

efficacy and safety of MSC administration for the treatment of ALI/ARDS [17–20, 33]. In the current study, we demonstrated that hMSCs exert a protective effect on mice with smoke inhalation-induced ALI, suggesting that these cells may offer a therapeutic strategy for SII.

Despite recent interest in the use of adult stem cell therapy due to the multipotent nature of bone marrow-derived stem cells, findings regarding the engraftment process of systemically administered hBMSCs in lung injury models have varied. The majority of studies on experimental lung injuries have demonstrated an MSC engraftment rate of less than 1–5% [34–36]. In the current study, using BLI, we tracked the distribution dynamics of systemically administered hBMSCs in immunodeficient mice with SII. The results showed that a greater number of hBMSCs were found in the lung tissues of SII mice compared with control mice, a finding that is similar to previous studies [21] of mice exposed to trauma or bearing tumors. Our results further confirmed that hBMSCs innately traffic to sites of inflammation, which are concordant with previous studies of MSC localization patterns in trauma, cancer, and following exposure to radiation [37–39]. However, we found no hBMSC engraftment in the lung, which was demonstrated by the complete disappearance of BLI signal at 14 days after hBMSC administration. This result indicates that engraftment of the cells into the lung is not a major driving force behind the beneficial effects that were noted.

Growing evidence has indicated that the effects of MSCs with regard to lung tissue repair are not attributable to the differentiation capacity of these cells but rather to their activation of a protective mechanism and their stimulation of endogenous regeneration factors [18, 40]. MSCs produce soluble bioactive factors known to reduce alveolocapillary membrane permeability, inhibit apoptosis and fibrosis, decrease inflammation, and enhance tissue repair. Impaired AFC (alveolar fluid clearance) is common in patients with ALI/ARDS and leads to pulmonary edema. BMSCs also

produce several epithelial growth factors, including vascular endothelial growth factor (VEGF), keratinocyte growth factor (KGF), and hepatocyte growth factor (HGF). KGF has been shown to improve alveolar fluid transport in part by upregulating aENaC gene expression [41] and Na-K-ATPase activity [42]. As such, KGF is important in the resolution of lung injury. In a set of ex vivo experiments, Matthay MA and colleagues found that siRNA-mediated inhibition of KGF expression decreased the beneficial effects of MSCs in restoring AFC in injured, perfused human lungs by approximately 80% [19]. In the current study, we found that MSCs significantly attenuated pulmonary edema induced by smoke inhalation. The paracrine secretion of KGF leading to the restoration of AFC may be a possible mechanism for this finding.

The immunomodulatory effects of MSCs are well-established, and MSCs exert protection against inflammatory damage by downregulating the expression of proinflammatory factors, such as IL-1b, IL-8, interferon- (INF-) γ , and TNF- α [43]. MSCs also secrete anti-inflammatory agents such as IL-4 and IL-10 to regulate the development of lung inflammation [44], reduce neutrophil infiltration into the lung, and reduce the quantity of proinflammatory cytokines in circulation, collectively maintaining a balance between inflammatory and anti-inflammatory responses [45]. Our results showed that hMSCs could significantly decrease the levels of TNF- α in BALF after 1 day after injection. Correspondingly, smoke inhalation resulted in inflammatory cell infiltration around the airway, which was significantly attenuated by the administration of hBMSCs. Thus, immunomodulation plays an important role in downregulating inflammatory responses and attenuating tissue injury in SII.

In summary, our study demonstrated that systemically administered hBMSCs mainly localized to the lungs of mice with SII. The hBMSCs attenuated the lung injury induced by smoke inhalation, and this may be due to the effect of

anti-inflammatory and secreting KGF of hMSCs but not associated with the differentiation potential of the cells.

Competing Interests

The authors declare that they have no competing interests.

Authors' Contributions

MeiJuan Song and Qi Lv contributed equally to this paper.

Acknowledgments

This research was partially supported by the National Natural Science Foundation of China (81202105 and 71533008) and the Tianjin Science and Technology Project (15JCYBJC28500, 13JCQNJC12900-2013, and 14ZCDZSY00033). The authors appreciate the help provided by the Chinese Academy of Medical Sciences and the Medical University of Tianjin's basic medical school.

References

- [1] R. H. Demling, "Smoke inhalation lung injury: an update," *Eplasty*, vol. 8, article e27, 2008.
- [2] D. L. Smith, B. A. Cairns, F. Ramadan et al., "Effect of inhalation injury, burn size, and age on mortality: a study of 1447 consecutive burn patients," *Journal of Trauma—Injury, Infection and Critical Care*, vol. 37, no. 4, pp. 655–659, 1994.
- [3] E. C. Kimmel and K. R. Still, "Acute lung injury, acute respiratory distress syndrome and inhalation injury: an overview," *Drug and Chemical Toxicology*, vol. 22, no. 1, pp. 91–128, 1999.
- [4] M. H. Toon, M. O. Maybauer, J. E. Greenwood, D. M. Maybauer, and J. F. Fraser, "Management of acute smoke inhalation injury," *Critical Care and Resuscitation*, vol. 12, no. 1, pp. 53–61, 2010.
- [5] M. O. Maybauer, S. Rehberg, D. L. Traber, D. N. Herndon, and D. M. Maybauer, "Pathophysiology of acute lung injury in severe burn and smoke inhalation injury," *Anaesthetist*, vol. 58, no. 8, pp. 805–812, 2009.
- [6] The Chinese Medical Association, *Clinical Diagnosis and Treatment Guidelines: Burns Booklet*, 2007.
- [7] N. Nugent and D. N. Herndon, "Diagnosis and treatment of inhalation injury," *Total Burn Care*, vol. 3, pp. 262–272, 2007.
- [8] B. J. Jones and S. J. Mctaggart, "Immunosuppression by mesenchymal stromal cells: from culture to clinic," *Experimental Hematology*, vol. 36, no. 6, pp. 733–741, 2008.
- [9] M. R. Reagan and D. L. Kaplan, "Concise review: Mesenchymal stem cell tumor-homing: detection methods in disease model systems," *Stem Cells*, vol. 29, no. 6, pp. 920–927, 2011.
- [10] M. Introna, G. Lucchini, E. Dander et al., "Treatment of graft versus host disease with mesenchymal stromal cells: a phase I study on 40 adult and pediatric patients," *Biology of Blood and Marrow Transplantation*, vol. 20, no. 3, pp. 375–381, 2014.
- [11] I. B. Resnick, C. Barkats, M. Y. Shapira et al., "Treatment of severe steroid resistant acute GVHD with mesenchymal stromal cells (MSC)," *American Journal of Blood Research*, vol. 3, no. 3, pp. 225–238, 2013.
- [12] J. Bartunek, A. Behfar, D. Dolatabadi et al., "Cardiopietic stem cell therapy in heart failure: The C-CURE (cardiopietic stem cell therapy in heart failure) multicenter randomized trial with lineage-specified biologics," *Journal of the American College of Cardiology*, vol. 61, no. 23, pp. 2329–2338, 2013.
- [13] S. Forostyak, P. Jendelova, and E. Sykova, "The role of mesenchymal stromal cells in spinal cord injury, regenerative medicine and possible clinical applications," *Biochimie*, vol. 95, no. 12, pp. 2257–2270, 2013.
- [14] M.-E. M. Amer, S. Z. El-Sayed, W. A. El-Kheir et al., "Clinical and laboratory evaluation of patients with end-stage liver cell failure injected with bone marrow-derived hepatocyte-like cells," *European Journal of Gastroenterology and Hepatology*, vol. 23, no. 10, pp. 936–941, 2011.
- [15] A. Skrahin, R. K. Ahmed, G. Ferrara et al., "Autologous mesenchymal stromal cell infusion as adjunct treatment in patients with multidrug and extensively drug-resistant tuberculosis: an open-label phase 1 safety trial," *The Lancet Respiratory Medicine*, vol. 2, no. 2, pp. 108–122, 2014.
- [16] J. G. Wilson, K. D. Liu, H. Zhuo et al., "Mesenchymal stem (stromal) cells for treatment of ARDS: a phase 1 clinical trial," *The Lancet Respiratory Medicine*, vol. 3, no. 1, pp. 24–32, 2015.
- [17] G. Yin, G. Hu, R. Wan et al., "Role of bone marrow mesenchymal stem cells in L-arg-induced acute pancreatitis: effects and possible mechanisms," *International Journal of Clinical and Experimental Pathology*, vol. 8, no. 5, pp. 4457–4468, 2015.
- [18] J. W. Lee, X. Fang, A. Krasnodembskaya, J. P. Howard, and M. A. Matthay, "Concise review: mesenchymal stem cells for acute lung injury: role of paracrine soluble factors," *Stem Cells*, vol. 29, no. 6, pp. 913–919, 2011.
- [19] M. A. Matthay, B. T. Thompson, E. J. Read et al., "Therapeutic potential of mesenchymal stem cells for severe acute lung injury," *Chest*, vol. 138, no. 4, pp. 965–972, 2010.
- [20] J. W. Lee, X. Fang, N. Gupta, V. Serikov, and M. A. Matthay, "Allogeneic human mesenchymal stem cells for treatment of E. coli endotoxin-induced acute lung injury in the ex vivo perfused human lung," *Proceedings of the National Academy of Sciences of the United States of America*, vol. 106, no. 38, pp. 16357–16362, 2009.
- [21] S. Kidd, E. Spaeth, J. L. Dembinski et al., "Direct evidence of mesenchymal stem cell tropism for tumor and wounding microenvironments using in vivo bioluminescent imaging," *STEM CELLS*, vol. 27, no. 10, pp. 2614–2623, 2009.
- [22] D. Zhao, Y. Tu, L. Wan et al., "In vivo monitoring of angiogenesis inhibition via down-regulation of Mir-21 in a VEGFR2-luc murine breast cancer model using bioluminescent imaging," *PLoS ONE*, vol. 8, article e71472, 2013.
- [23] F. Zhu, X. Qiu, J. Wang et al., "A rat model of smoke inhalation injury," *Inhalation Toxicology*, vol. 24, no. 6, pp. 356–364, 2012.
- [24] R. Yu, X. Guo, L. Huang, Z. Zeng, and H. Zhang, "The novel peptide PACAP-TAT with enhanced traversing ability attenuates the severe lung injury induced by repeated smoke inhalation," *Peptides*, vol. 38, no. 1, pp. 142–149, 2012.
- [25] S. Hou, H. Ding, Q. Lv et al., "Therapeutic effect of intravenous infusion of perfluorocarbon emulsion on LPS-induced acute lung injury in rats," *PLoS ONE*, vol. 9, no. 1, Article ID e87826, 2014.
- [26] S. Bhaumik, X. Z. Lewis, and S. S. Gambhir, "Optical imaging of *Renilla* luciferase, synthetic *Renilla* luciferase, and firefly luciferase reporter gene expression in living mice," *Journal of Biomedical Optics*, vol. 9, no. 3, pp. 578–586, 2004.
- [27] V. M. Ranieri, G. D. Rubenfeld, B. T. Thompson et al., "Acute respiratory distress syndrome: the Berlin definition," *The Journal*

- of the American Medical Association, vol. 307, no. 23, pp. 2526–2533, 2012.
- [28] L. Yan and H. J. Fan, “Advances in bone marrow mesenchymal stem cells in the treatment of acute lung injury,” *Chinese Journal of Emergency Medicine*, vol. 21, pp. 328–331, 2012.
 - [29] S. Lei, L. Daibo, and C. Jia, “Advances in drug therapy for acute smoke inhalation induced lung injury,” *Chinese Journal of Asthma*, vol. 4, pp. 292–297, 2011.
 - [30] L. B. Ware and M. A. Matthay, “The acute respiratory distress syndrome,” *The New England Journal of Medicine*, vol. 342, no. 18, pp. 1334–1349, 2000.
 - [31] A. Tyndall, “Mesenchymal stem cell treatments in rheumatology: a glass half full?” *Nature Reviews Rheumatology*, vol. 10, no. 2, pp. 117–124, 2014.
 - [32] F. Gao, S. M. Chiu, D. A. Motan et al., “Mesenchymal stem cells and immunomodulation: current status and future prospects,” *Cell Death and Disease*, vol. 7, no. 1, article e2062, 2016.
 - [33] S. Asmussen, H. Ito, D. L. Traber et al., “Human mesenchymal stem cells reduce the severity of acute lung injury in a sheep model of bacterial pneumonia,” *Thorax*, vol. 69, no. 9, pp. 819–825, 2014.
 - [34] N. Gupta, X. Su, B. Popov, J. W. Lee, V. Serikov, and M. A. Matthay, “Intrapulmonary delivery of bone marrow-derived mesenchymal stem cells improves survival and attenuates endotoxin-induced acute lung injury in mice,” *Journal of Immunology*, vol. 179, no. 3, pp. 1855–1863, 2007.
 - [35] M. Rojas, J. Xu, C. R. Woods et al., “Bone marrow-derived mesenchymal stem cells in repair of the injured lung,” *American Journal of Respiratory Cell and Molecular Biology*, vol. 33, no. 2, pp. 145–152, 2005.
 - [36] D. N. Kotton, A. J. Fabian, and R. C. Mulligan, “Failure of bone marrow to reconstitute lung epithelium,” *American Journal of Respiratory Cell and Molecular Biology*, vol. 33, no. 4, pp. 328–334, 2005.
 - [37] H. Wang, F. Cao, A. De et al., “Trafficking mesenchymal stem cell engraftment and differentiation in tumor-bearing mice by bioluminescence imaging,” *Stem Cells*, vol. 27, no. 7, pp. 1548–1558, 2009.
 - [38] M. Studeny, F. C. Marini, J. L. Dembinski et al., “Mesenchymal stem cells: potential precursors for tumor stroma and targeted-delivery vehicles for anticancer agents,” *Journal of the National Cancer Institute*, vol. 96, no. 21, pp. 1593–1603, 2004.
 - [39] A. H. Klopp, E. L. Spaeth, J. L. Dembinski et al., “Tumor irradiation increases the recruitment of circulating mesenchymal stem cells into the tumor microenvironment,” *Cancer Research*, vol. 67, no. 24, pp. 11687–11695, 2007.
 - [40] K.-Y. Yang, H.-C. Shih, C.-K. How et al., “IV delivery of induced pluripotent stem cells attenuates endotoxin-induced acute lung injury in mice,” *Chest*, vol. 140, no. 5, pp. 1243–1253, 2011.
 - [41] Y. Wang, H. G. Folkesson, C. Jayr, L. B. Ware, and M. A. Matthay, “Alveolar epithelial fluid transport can be simultaneously upregulated by both KGF and β -agonist therapy,” *Journal of Applied Physiology*, vol. 87, no. 5, pp. 1852–1860, 1999.
 - [42] B. P. H. Guery, C. M. Mason, E. P. Dobard, G. Beaucaire, W. R. Summer, and S. Nelson, “Keratinocyte growth factor increases transalveolar sodium reabsorption in normal and injured rat lungs,” *American Journal of Respiratory and Critical Care Medicine*, vol. 155, no. 5, pp. 1777–1784, 1997.
 - [43] M. Hayes, G. Curley, B. Ansari, and J. G. Laffey, “Clinical review: stem cell therapies for acute lung injury/acute respiratory distress syndrome—hope or hype?” *Critical Care*, vol. 16, article 205, 2012.
 - [44] Z.-X. Liang, J.-P. Sun, P. Wang, Q. Tian, Z. Yang, and L.-A. Chen, “Bone marrow-derived mesenchymal stem cells protect rats from endotoxin-induced acute lung injury,” *Chinese Medical Journal*, vol. 124, no. 17, pp. 2715–2722, 2011.
 - [45] S. S. Iyer and M. Rojas, “Anti-inflammatory effects of mesenchymal stem cells: novel concept for future therapies,” *Expert Opinion on Biological Therapy*, vol. 8, no. 5, pp. 569–581, 2008.

Research Article

Dynamic Tracking of Injected Mesenchymal Stem Cells after Myocardial Infarction in Rats: A Serial 7T MRI Study

Xiuyu Chen,¹ Minjie Lu,¹ Ning Ma,² Gang Yin,¹ Chen Cui,¹ and Shihua Zhao¹

¹Department of Radiology, State Key Laboratory of Cardiovascular Disease, Fuwai Hospital, National Center for Cardiovascular Diseases, Chinese Academy of Medical Sciences and Peking Union Medical College, Beijing 100037, China

²Department of Ultrasound, Anzhen Hospital, Beijing 100029, China

Correspondence should be addressed to Shihua Zhao; zhaoshihua0202@126.com

Received 7 May 2016; Accepted 25 July 2016

Academic Editor: Ping Wang

Copyright © 2016 Xiuyu Chen et al. This is an open access article distributed under the Creative Commons Attribution License, which permits unrestricted use, distribution, and reproduction in any medium, provided the original work is properly cited.

Purpose. To track the fate of micron-sized particles of iron oxide (MPIO) labeled mesenchymal stem cells (MSCs) in vivo in a rat myocardial infarction model using 7T magnetic resonance imaging (MRI) scanner. **Materials and Methods.** Male MSCs ($2 \times 10^6/50 \mu\text{L}$) dual-labeled with MPIO and CM-DiI were injected into the infarct periphery 7 days after myocardial infarction (MI). The control group received cell-free media injection. The temporal stem cell location, signal intensity, and cardiac function were dynamically assessed using a 7T MRI at 24 h before transplantation (baseline), 3 days, 2 weeks, and 4 weeks after transplantation, respectively. **Results.** MR hypointensities caused by MPIOs were observed on T2⁺-weighted images at all time points after MSCs injection. Cine-MRI showed that MSCs moderated progressive left ventricular remodeling. Double staining for iron and CD68 revealed that most of the iron-positive cells were CD68-positive macrophages. Real-time PCR for rat SRY gene showed the number of survival MSCs considerably decreased after transplantation. MSC-treated hearts had significantly increased capillary density in peri-infarct region and lower cardiomyocytes apoptosis and fibrosis formation. **Conclusions.** Iron particles are not a reliable marker for in vivo tracking the long-term fate of MSCs engraftment. Despite of poor cell retention, MSCs moderate left ventricular remodeling after MI.

1. Introduction

Stem cell-based therapy has been currently introduced as a potentially promising approach to treat myocardial infarction (MI) and heart failure. As multipotent progenitor cells, bone-marrow-derived mesenchymal stem cells (MSCs) are easy to obtain and expand in vitro and have been considered to be an ideal option for clinical and basic applications [1]. According to previous studies, MSCs transplantation was proved to be able to attenuate left ventricular remodeling and cardiac dysfunction without significant safety concerns [2, 3]. However, noticeable concerns have been raised and yet to be studied, such as the fate of transplanted cells and the underlying mechanisms of the functional benefits.

Magnetic resonance imaging (MRI) is currently considered as a standard tool to evaluate the cardiac morphology and function due to its versatility, accuracy, and reproducibility and has been most frequently applied in the clinical trials

[4–8]. However, echocardiography was more commonly used instead of MRI in rodent hearts studies because of their quite small size and high heart rate (>300 beats/min) [9–13]. The measurements by echocardiography are less accurate than cine-MRI especially when applied to asymmetric, infarcted rat hearts [14–16]. Furthermore, T2⁺-weighted imaging is able to determine whether iron-labeled cells were successfully transplanted into the target sites of infarcted hearts as well as the initial cell retention, which is crucial for the following therapeutic effects on cardiac function and therefore makes MRI an potentially ideal monitoring imaging modality for tracking the fate of engrafted MSCs.

Our preliminary study has revealed that MRI scanner with ultra-high magnetic field (7.0T) could accurately evaluate the cardiac function and morphology in MI models of rats whereas superparamagnetic iron oxide nanoparticles were unable to reliably track the fate of engrafted MSCs

[17]. However, the effect of MSCs after injection and the value of tracking MSCs by MRI remain as a controversial issue to be resolved. Hence, we aimed to use a 7.0T MRI scanner to dynamically track the fate of fluorescent micron-sized particles of iron oxide (MPIO) labeled MSCs and simultaneously to assess the effects on cardiac function after injection into the infarcted rat heart and the possible underlying mechanisms as well.

2. Materials and Methods

2.1. Animals. All animal studies were approved by the Institutional Animal Care and Use Committee at our hospital and all experiments were performed in accordance with the “Guide for the Care and Use of Laboratory Animals” published by the US National Institutes of Health (publication number 85-23, revised 1996).

2.2. MSCs Preparation and Labeling. Rat male MSCs were isolated and cultured using the methods as previously described [18]. A previous study has analyzed and tested the surface antigen profiles and potentials for multilineage differentiation [19]. In brief, we isolated MSCs from femurs and tibias of male Sprague Dawley rats (4 weeks, 60–80 g). The cells were subsequently seeded in Iscove’s modified Dulbecco’s medium (IMDM) culture medium (Gibco) with L-glutamine mixed with 10% fetal bovine serum (FBS, Gibco) on flasks. We replaced culture medium after 2 days and changed it twice a week afterward. 0.25% trypsin (EDTA, Sigma) was used to dissociate cells once they covered the 95% of the flask and then were replated to expand cells for successive passages. In terms of cell labeling, MSCs were incubated with fluorescent micron-sized particles of iron oxide (MPIO, 10 μ L of 1% stock solution per mL medium, Bangs Laboratories Inc.) in a humidified 5% CO₂ incubator at 37°C for 24 h and followed by washing three times in phosphate-buffered saline (PBS) to rinse off spare MPIO particles. The label efficiency of MPIO was assessed by Prussian blue staining as well as microscopic examination. Before transplantation, cells were stained with CM-DiI (Invitrogen) in PBS for 30 minutes [20, 21]. The viability of the dual-labeled cells was assessed by trypan-blue exclusion before transfer. The transplanted MSCs were passage 3~4.

2.3. Myocardial Infarction and Cell Transfer. MI model was established using the method as previously described [18]. Briefly, SD female rats (200–250 g, $n = 113$) were anesthetized with intraperitoneal injection of chloral hydrate. Intubation and mechanical ventilation were subsequently performed using a small animal ventilation apparatus (model 683; Harvard Apparatus). With the heart exposed by a 2 cm lateral thoracotomy, the left coronary artery was permanently ligated a few millimeters below its origin with a 6-0 Prolene stitch. MI model was considered successfully established when myocardial blanching was visualized within the downstream myocardium. The thorax closure was done with three layers of sutures. 7 days after MI, the chest was reopened and

rats were randomized to receive 1~2 sites direct injection of $2 \times 10^6/50 \mu$ L dual-labeled MSCs (MSCs group) or 50 μ L PBS (control group) into the peri-infarct region.

2.4. MRI Protocol. Serial MRI was performed with a 7T horizontal-bore animal scanner (Varian NMR systems imaging with VnmrJ 2.1B software) at 24 h before cell transfer (baseline), 3 days, 2 and 4 weeks after cell transfer, respectively. Animals were anesthetized with isoflurane (3% for induction and 1.5–2% for maintenance) in oxygen. During image acquisition, small animal ECG electrodes (SA Instruments) were attached to the forelimbs of rats and a respiration-detection cushion was placed under the thorax in order to monitor and trigger ECG and respiration signals. For detecting the susceptibility artifacts (hypointensities) generated by the MPIO-labeled cells, T2*-weighted gradient echo sequence was acquired using the following parameters: FOV 40 \times 40 mm, matrix 196 \times 196, TE 2.83 ms, TR 56.32 ms, slice thickness 1.0 mm, and flip angle 20°. For assessing cardiac function, a stack of contiguous short-axis cine-MRI images were acquired to cover the entire left ventricle using the following parameters: FOV 40 \times 40 mm, matrix 196 \times 196, TE 1.8 ms, TR 10 ms, slice thickness 1.0 mm, 20° pulse, 4 averages, 10 cardiac phases, and 12 frames/cardiac cycle.

2.5. MRI Analysis. The left ventricular (LV) end-diastolic (EDV) and end-systolic (ESV) volumes were measured using ImageJ (NIH, Bethesda, MD). Stroke volume [8] was calculated as EDV minus ESV. LV ejection fraction (LVEF) was calculated as the SV divided by the EDV. The relative infarct size was calculated from the average of the endocardial and epicardial circumferential lengths of the thinned area of all slices, measured at diastolic stage and expressed as a percentage of the total myocardial surface. The signal intensity (SI) and hypointensive area were measured on the slice with maximum hypointensities area on T2*-weighted images using ImageJ (NIH, Bethesda, MD). A circular ROI of 11 pixels (0.70 mm²) was selected within hypointensive area and normal myocardium, respectively [20]. The signal contrast ratio was calculated as $\text{signal contrast ratio} = (\text{SI}_{\text{normal myocardium}} - \text{SI}_{\text{hypointensive area}}) / \text{SI}_{\text{normal myocardium}} \times 100\%$. Relative change (%) was calculated as $[(\text{follow-up parameter} - \text{baseline parameter}) / \text{baseline parameter}] \times 100$.

2.6. Histology and Immunohistochemistry. At each time point after MRI scans, 3 animals from each group were sacrificed by overdose of pentobarbitone. Hearts were sectioned into 3 to 4 transverse slices and fixed with 4% buffered formalin, embedded in paraffin, and then sectioned with a microtome (5- μ m thick). Prussian blue staining was conducted to detect iron particles. To further identify the cells that had taken up the iron particles, antibody staining for the macrophage marker CD68 (Sigma) was performed in consecutive sections. Masson’s-Trichrome staining was performed to assess myocardial fibrosis, and the fibrosis score was calculated as collagen fiber area/total view area \times 100%. Apoptosis

was assessed by the terminal deoxynucleotidyl transferase-mediated dUTP nick end-labeling (TUNEL) assay kit (Roche, Indiana, USA), and the apoptosis score was calculated as the number of TUNEL-positive cardiomyocytes/the total number of cardiomyocytes $\times 100\%$. Angiogenesis was assessed by counting the number of vessels immunostained for the endothelial cell marker CD31 (rabbit polyclonal, Abcam, UK). Random fields ($n = 20$) around each peri-infarct area were selected and numbers of vessels were counted.

2.7. Transmission Electron Microscopy. The heart tissues were cut into approximately 1 mm cubes and fixed with 2.5% glutaraldehyde in 0.1 M phosphate buffer at 4°C for 2 h. After washing with sodium cacodylate buffer, samples were postfixed with 1% osmium tetroxide at 4°C for 2 h. Samples were then dehydrated by a serial gradient ethanol and then embedded in Epon-812 (Electron Microscopy Sciences). Ultrathin sections were cut using an ultramicrotome (Leica, Leica EM UC7) on uncoated copper grids and stained with 0.2% lead citrate/1% uranyl acetate. Images were recorded under a transmission electron microscope (JEM1400; JEOL).

2.8. Real-Time PCR. For assessing the MSCs retention after transplantation, RT-PCR analysis for the rat Y-chromosome-specific SRY gene was performed from infarcted hearts of 3 female recipients treated with male MSCs at each time point. Total RNA was extracted by the Trizol reagent method (Invitrogen), and first strand cDNA was synthesized with SuperScript II (Invitrogen). The primer sequence for rat SRY gene were forward primer 5'-AGGGTTAAAGTGCCACAG-AGGA-3' and reverse primer 5'-GCTTTTCTGGTTCTT-GGAGGAC-3'. The primers and probe for GAPDH gene were forward primer 5'-AACCTGCCAAGTATGATGACA-TCA-3' and reverse primer 5'-TTCCACTGATATCCC-AGCTGCT-3'. PCR products were electrophoresed through 1.5% agarose gels containing ethidium bromide. Quantitative real-time PCR involved the iCycler iQ system (Bio-Rad).

2.9. Statistical Analyses. Data were presented as means \pm standard deviation. Differences between the two groups were made using unpaired Student's *t*-test; Statistical comparisons among different time points in each group were made using repeated measures ANOVA. All statistical analyses were conducted using SPSS 16.0 (SPSS, Chicago, IL). A value of $p < 0.05$ was considered significant.

3. Results

3.1. Establishment of Myocardial Infarction Model and Mortality. Myocardial infarction (MI) surgery was successfully performed on 113 rats. Of them, 20 died within 24 hours of the surgical operations (17% postoperative mortality) due to procedure-related complications. Absence of or minimal MI was revealed by baseline MRI (defined as LVEF $> 60\%$) in 7 rats, which were further excluded in the study. Therefore, the remaining qualified 86 rats were randomized into two groups, MSCs engrafted and control group. During cell injection,

a total of 16 rats died, 9 in the MSCs group and 7 in the control group. Thus, 70 rats were included in the final analysis (34 rats in the MSCs group, 36 rats in the control group).

3.2. MSCs Labeling and Morphology. MSCs were efficiently labeled ($>98\%$) in culture at a concentration of 10 μ L MPIO stock per mL of medium for 24 h, confirmed by phase contrast microscopy (Figures 1(a) and 1(b)) and iron staining (Figure 1(c)). Fluorescence microscopy demonstrated MSCs were efficiently dual-labeled with MPIO and CM-DiI. The dragon green fluorescence of the MPIOs was clearly detected in the cytoplasm and the red of CM-DiI in the membrane of cells (Figures 1(d)–1(f)). By trypan-blue exclusion assay, almost 99% of the cells remained viable before transplantation.

3.3. MRI Measurement of Cardiac Morphology and Function. Cine images were acquired to assess the cardiac morphology and function at baseline (24 h before transplantation), 3 days, and 2 and 4 weeks after cell injection. The typical course after myocardial infarction including progressive scar thinning, left ventricular dilatation and functional deterioration were observed in both groups at baseline (Figure 2(a)), and there were no significant differences between the two groups in terms of LVEF, EDV, and ESV. Although both groups showed pronounced LV dilatation, both EDV and ESV in MSCs group were significantly smaller than that of control group 4 weeks after transplantation (3.6 ± 0.4 mL versus 4.8 ± 0.4 mL, $p < 0.05$ and 1.8 ± 0.4 mL versus 2.8 ± 0.3 mL, $p < 0.05$, resp.). Meanwhile, the LVEF in control group was significantly lower than that of MSCs-treated hearts ($41 \pm 5\%$ versus $49 \pm 6\%$, $p < 0.05$). Relative infarct size was similar between the groups at the first 3 time points, which then increased significantly in control hearts but not in MSCs-treated hearts at 4 weeks ($18 \pm 2\%$ versus $14 \pm 2\%$, $p < 0.05$) (Figure 2(b)). Furthermore, the relative changes of LVEF, EDV, ESV, and infarct size in MSCs group between baseline and 4 weeks after cell delivery were significantly smaller than controls (Figure 2(c)).

3.4. MRI Tracking of the Injected MSCs. T2*-weighted images were acquired to in vivo tracking MPIO-labeled cells at 3 days and 2 and 4 weeks after injection into the peri-infarct region of LV anterior wall, respectively. Persistent hypointensities ("black spots") generated by MPIO particles were detected in all animals that received MSCs transplantation. 3 days later, large well-defined hypointensities which extended beyond the whole LV wall could be visualized at the site of injection, while the virtual area of MPIO-labeled cells was smaller, which was called blooming effect. However, as time progressed, the signal of "black spot" gradually weakened and the area decreased (Figure 3(a)). There was a significant decrease both in signal contrast ratio (%) and in the low signal area (mm^2) at 4 weeks (95.27 ± 20.10 versus 62.14 ± 13.58 and 5.34 ± 0.80 versus 2.53 ± 0.93 , $p < 0.05$, resp.) than those at 3 days after transfer; no statistic differences were observed between 3 days and 2 weeks (Figure 3(b)). For control hearts, no "black spot" was detected on T2* weighted images.

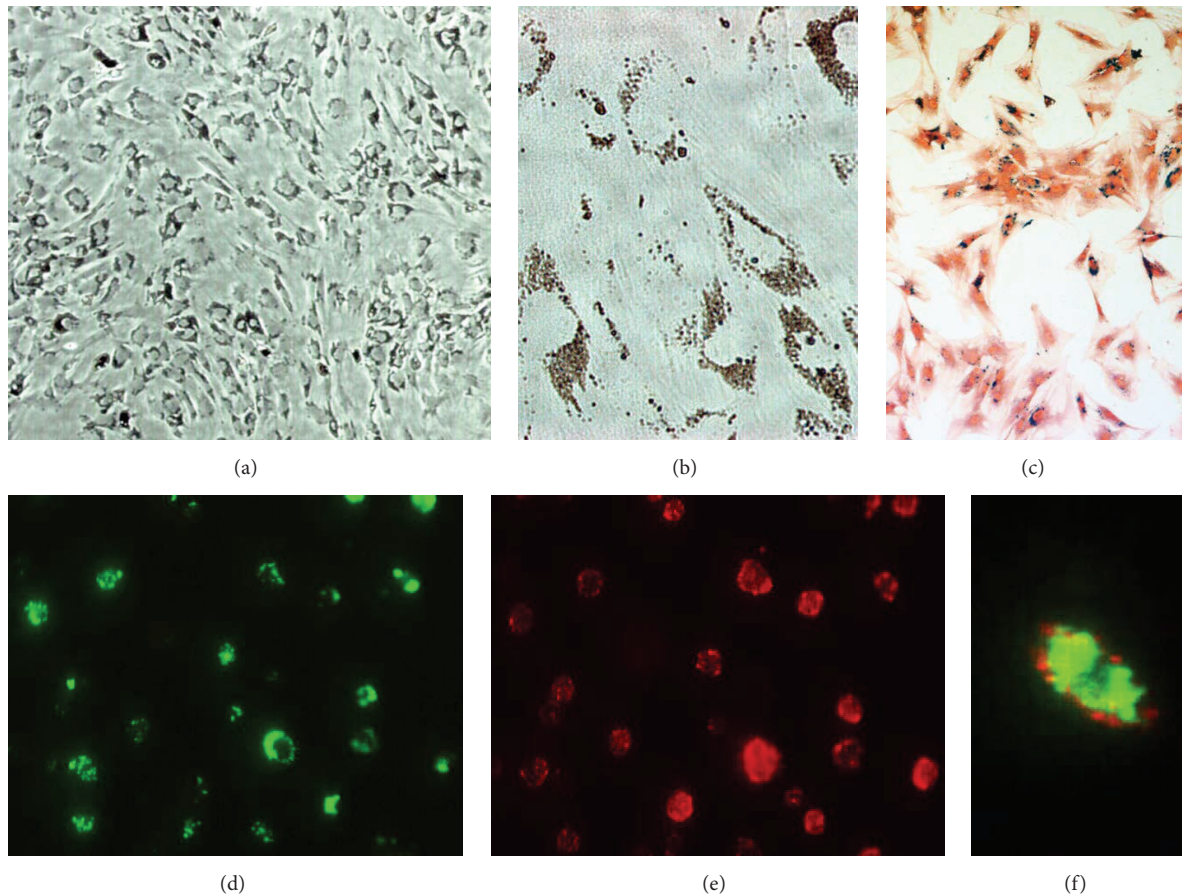


FIGURE 1: Dual-labeled mesenchymal stem cells (MSCs). (a) Phase contrast images showed almost 99% of the cells labeled with MPIO (original magnification $\times 100$). (b) The iron particles gathered in the cytoplasm and perinuclear area (original magnification $\times 400$). (c) Iron staining demonstrated high MPIO labeling efficiency ($>98\%$) represented as numerous blue granules in the cytoplasm (original magnification $\times 100$). (d)–(f) The green fluorescence of the MPIOs was clearly detected in the cytoplasm (d and f) and the red CM-DiI in the membrane of MSCs (e and f), original magnification $\times 400$.

3.5. Distribution and Retention of Injected MSCs in Hearts.

The detection of dual-labeled MSCs was confirmed by colocalization of two markers, green fluorescent MPIOs and red CM-DiI at the site of MSCs injection, which demonstrated successful cell transplantation. However, the number of positive cells significantly reduced over time, and almost no positive dual-labeled cells were found in MSCs group at 4 weeks after cell delivery (Figure 4(a)). Double staining for iron and CD68 (a marker of resident macrophage) at 4 weeks revealed that most iron-positive cells were also CD68 positive (Figure 4(b)). This was further confirmed by transmission electron microscopy, which demonstrated iron particles inside the macrophages (Figure 4(c)). Consistently, Real-time PCR analysis for the rat Y-chromosome-specific SRY gene demonstrated the retention of survival MSCs reduced significantly after injection: 3 days after the injection of 2×10^6 MSCs ($n = 3$), 11.5% of the initially engrafted cells were detected. After 2 weeks, this number dropped to 1.2% ($n = 3$) and further declined to $\sim 0.1\%$ at 4 weeks ($n = 3$).

3.6. Cardiac Fibrosis, Apoptosis, and Capillary Density in Peri-Infarcted Region. The degree of fibrosis determined by

Masson staining was much severer in the control group, and the fibrosis score was significantly higher than that in MSCs group ($18.5 \pm 3.1\%$ versus $7.5 \pm 2.2\%$, $p < 0.05$) (Figure 5). TUNEL staining demonstrated high level of apoptosis in both groups after MI. But MSCs injection significantly reduced apoptotic cell death at 4 weeks after transplantation ($9.4 \pm 2.1\%$ versus $20.3 \pm 5.2\%$, $p < 0.05$) (Figure 6(a)). CD31 staining showed that no significant difference regarding the number of capillaries was observed between the two groups until 4 weeks. Compared with the control group ($255.3 \pm 29.1/\text{mm}^2$), the number of capillaries was significantly increased by 30% ($p < 0.05$) in the MSC-treated hearts ($370.6 \pm 31.5/\text{mm}^2$) at 4 weeks (Figure 6(b)).

4. Discussion

The main findings of current study are that iron particles are not a reliable marker for in vivo tracking the long-term fate of MSCs engraftment. However, despite poor cell retention, MSCs moderate left ventricular remodeling after MI due to the enhanced angiogenesis, inhibition of cardiomyocytes apoptosis, and fibrosis.

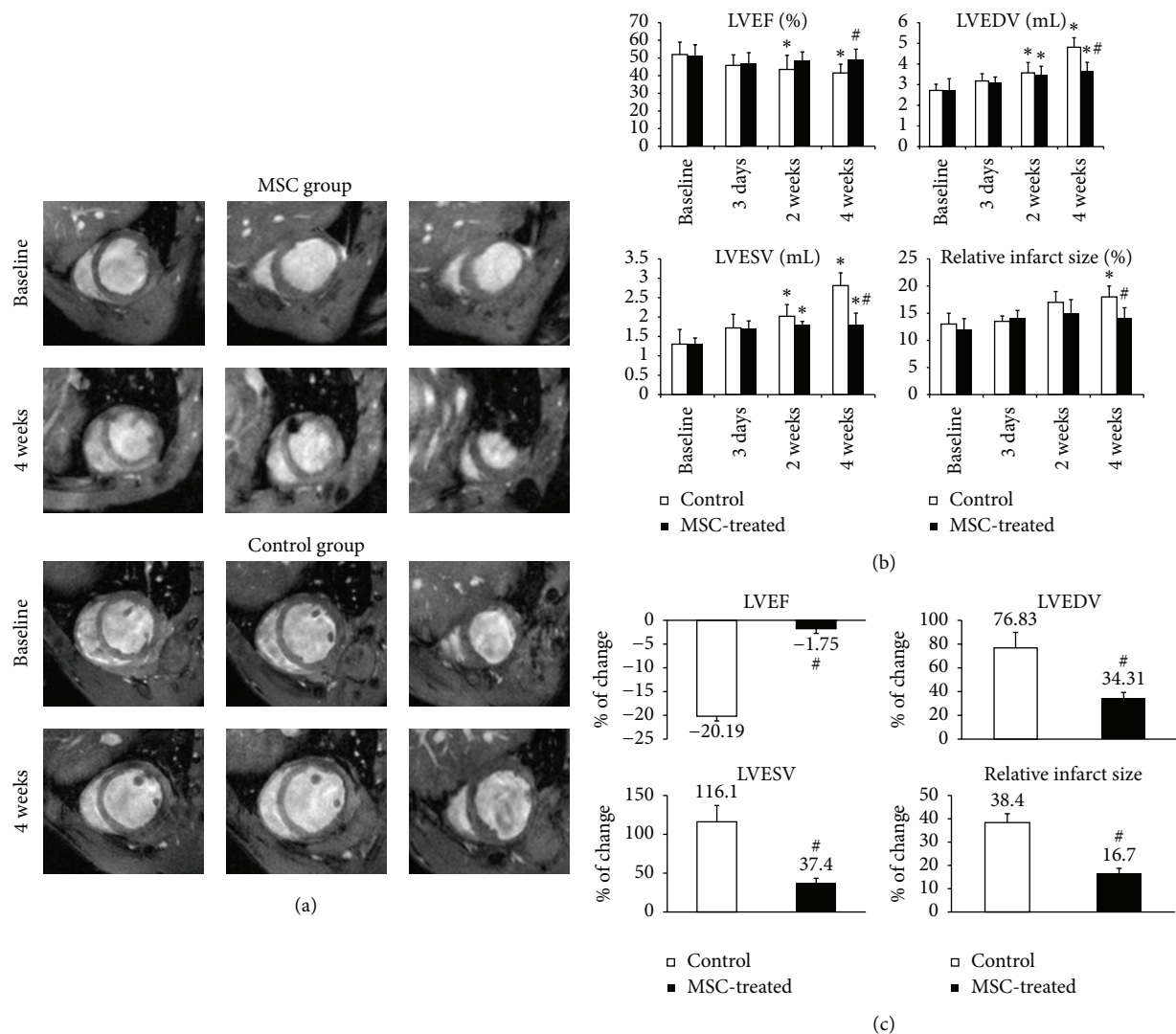


FIGURE 2: MRI assessment of cardiac morphology and function. (a) The typical course after myocardial infarction including progressive scar thinning, left ventricular dilatation, and functional deterioration was observed in both groups at baseline. However, serial cine-MRI studies between baseline and 4 weeks showed that MSCs injection resulted in moderated LV dilatation and dysfunction compared with controls (b–c). $N = 9, 9, 8, 8$ for MSCs group and $N = 10, 9, 9, 8$ for control group at each time point. * $p < 0.05$ versus baseline; # $p < 0.05$ versus control.

MSCs transplantation is a promising method to treat myocardial infarction and heart failure due to their proliferation and differentiation potentials. Understanding the fate of grafted stem cells is critical not only in the development of effective stem cell therapies but also in understanding the underlying mechanisms of therapeutic benefits. Therefore, a sensitive, noninvasive imaging technology is desperately needed for in vivo tracking the transplanted stem cells regarding temporal cell location, distribution, viability, and functional status. MRI is currently considered a standard tool to assess the cardiac structure and function due to its versatility, accuracy, and reproducibility and has been most frequently applied in the clinical trials [6–8, 22].

Several researchers have demonstrated that MSCs transplantation can improve cardiac function and reduce the degree of scar tissue [23–25], supported by our results. But

there were other studies reporting a negative or no discernable functional benefits between MSCs-treated and control hearts [26–28]. Reasons for the inconsistencies include all aspects of cell therapy such as different levels of cardiac impairment, species and animal age, variations in the time, and methods of cell delivery and the number of cells injected. In this study, we injected MSCs at 7 days after MI instead of 2 weeks applied in our previous study [17], which resulted in a significant functional improvement by MSCs injection. The benefits were expected according to a research by Hu et al. [29], focusing on the optimal timing of cell transplantation after MI. They found that the functional improvement was significantly pronounced with injection at 1 week after MI compared to any other time points including immediately and 2 weeks after MI, because at that moment the inflammatory responses were much weaker and the scar tissue had

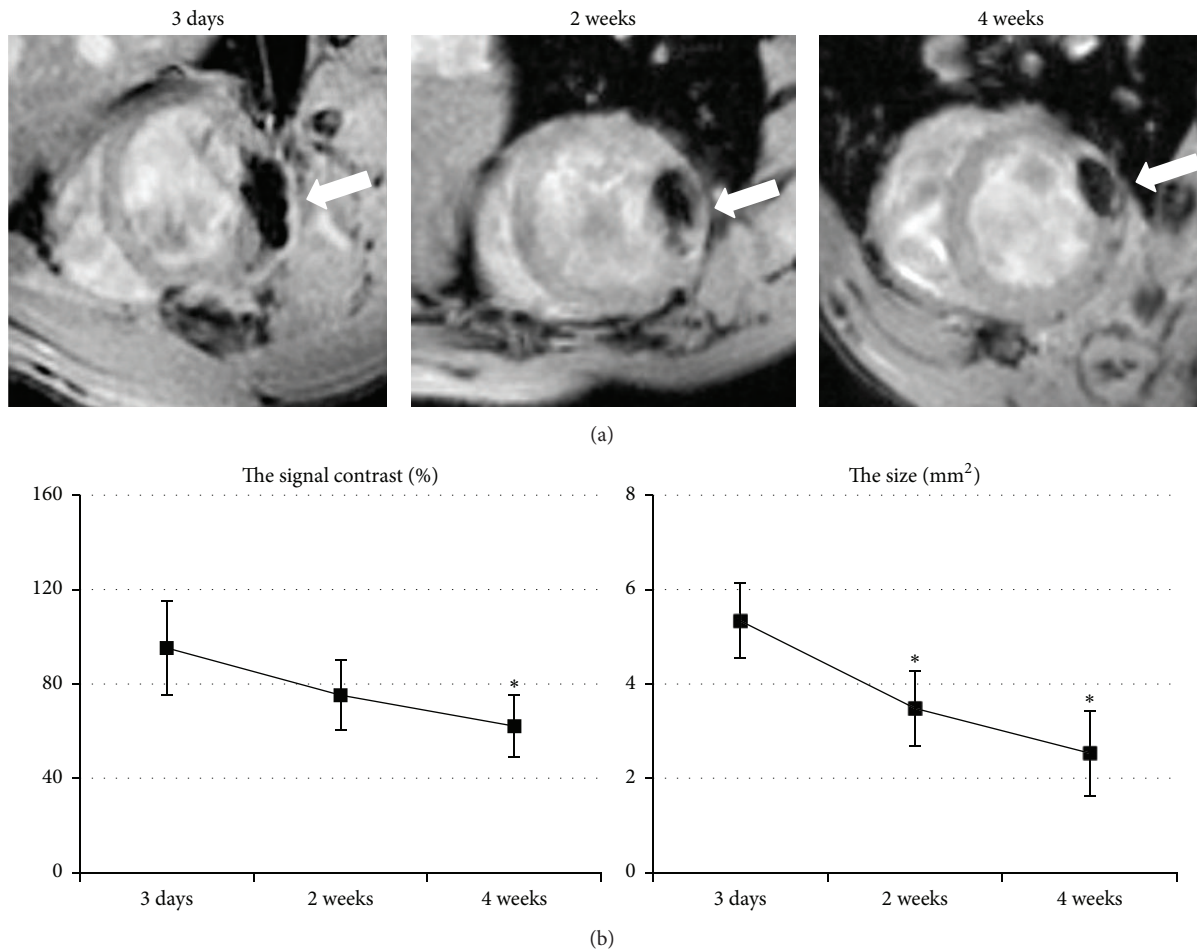


FIGURE 3: In vivo tracking of the MSCs after transplantation. (a) Persistent MR hypointensities caused by MPIOs were detected at all time points at the site of injection after transplantation (arrows). (b) As time progressed, the signal gradually weakened and the area decreased. $N = 9, 9, 8$ at each time point * $p < 0.05$ versus 3 days.

not yet formed. A further explanation for the discrepancy between studies is that different imaging tools have been used to assess cardiac function. Echocardiography has been regularly used to measure cardiac function in rodent hearts due to their convenience. However, its accuracy and reproducibility are controversial [16], and the measurements are less accurate than cine-MRI when applied to asymmetric, infarcted rat hearts. However, MRI is not commonly used to study rodent heart function due to their small size and quite high heart rate (>300 beats/min). The 7T cine-MRI method used in this study yielded excellent contrast between myocardium and blood and resulted in high-definition, volumetric images from which ESV and EDV could be accurately measured [16, 30, 31].

Studies have reported that MRI can in vivo track the fate of grafted stem cells labeled with MPIO, and the MPIOs do not affect cell viability, proliferation, differentiation, or therapeutic effects [32–34]. However, several studies have challenged the reliability of iron-particle tracking the transplanted stem cells [13, 18], because iron particles may be engulfed by macrophages after stem cells died and decomposed, which may interfere with MRI to distinguish the

survival stem cells from the dead ones. In line with our previous study [17], we also demonstrated that the number of survival MSCs decreased progressively over time after successful cell injection, and iron particles distribution was consistent with the macrophages. These findings indicated that MRI could not identify whether the MPIOs arose from the survival MSCs or macrophages. Therefore, we suggested that iron particles are not a reliable marker to monitor the transplanted stem cells viability and retention but localize the injection site in vivo.

Of note, although the cell retention was quite poor, MSCs maintained their protective effect against progressive LV remodeling and dysfunction after myocardial infarction. The underlying mechanisms of this functional improvement remain unclear; previous reports suggested that the therapeutic effects of transplanted cells on LV remodeling and function might be independent of cell retention or transdifferentiation [24, 35]. One recent study showed that intramyocardial transplantation of MSCs after acute MI could improve cardiomyocytes' glucose metabolism and cardiac function [36]. According to their results, the potential mechanism of this phenomenon might be the simultaneous activation of mTOR

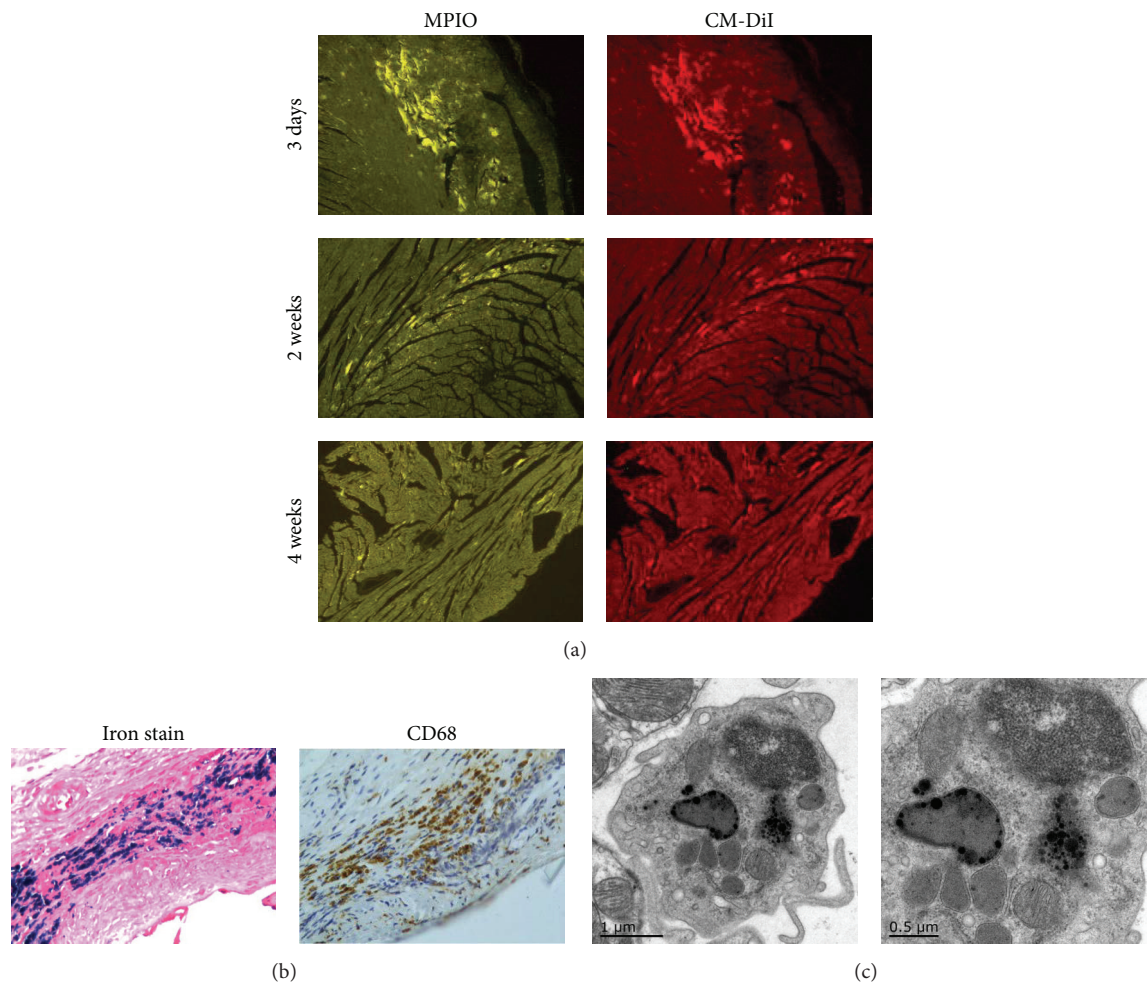


FIGURE 4: MSCs retention in recipient hearts. (a) The number of dual-labeled MSCs decreased over time. At 4 weeks, almost no positive cells were detected (original magnification $\times 50$). (b) Sections stained for iron and CD68 at 4 weeks showed that most of the iron-positive cells (blue cytoplasm) were CD68-positive cardiac macrophages (brown cytoplasm) (original magnification $\times 200$). (c) Representative electron micrographs demonstrated MPIOs engulfment inside a macrophage.

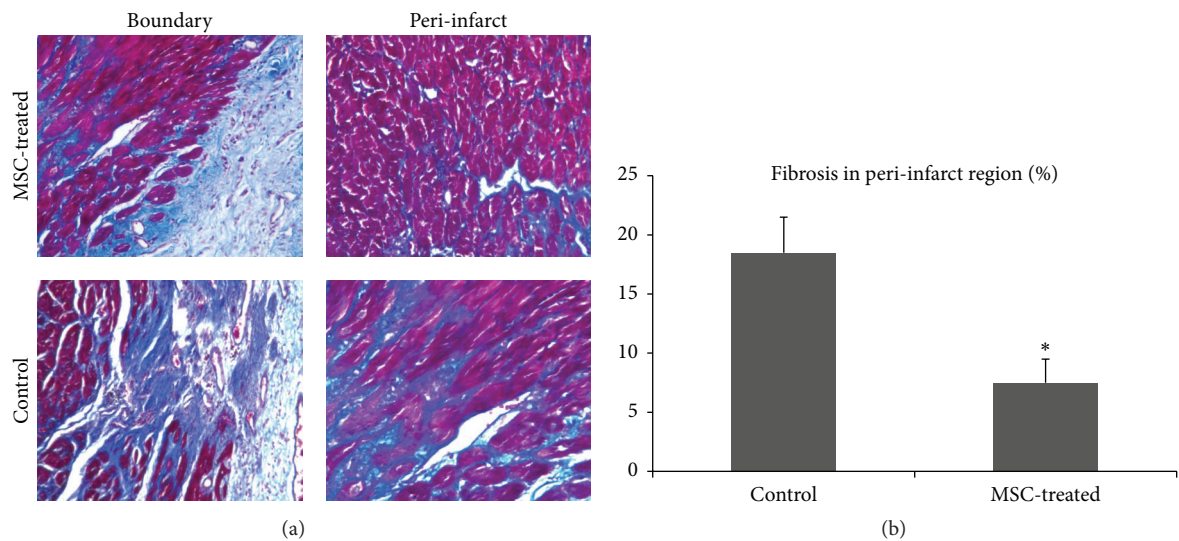


FIGURE 5: Myocardial fibrosis in peri-infarct area 4 weeks after transplantation. (a) Masson staining showed that, in control hearts, the border of myocardial infarction was more irregular and the fibrosis was more pronounced (original magnification $\times 200$). (b) Quantification of fibrosis. $N = 3$ for each group, * $p < 0.05$ versus control.

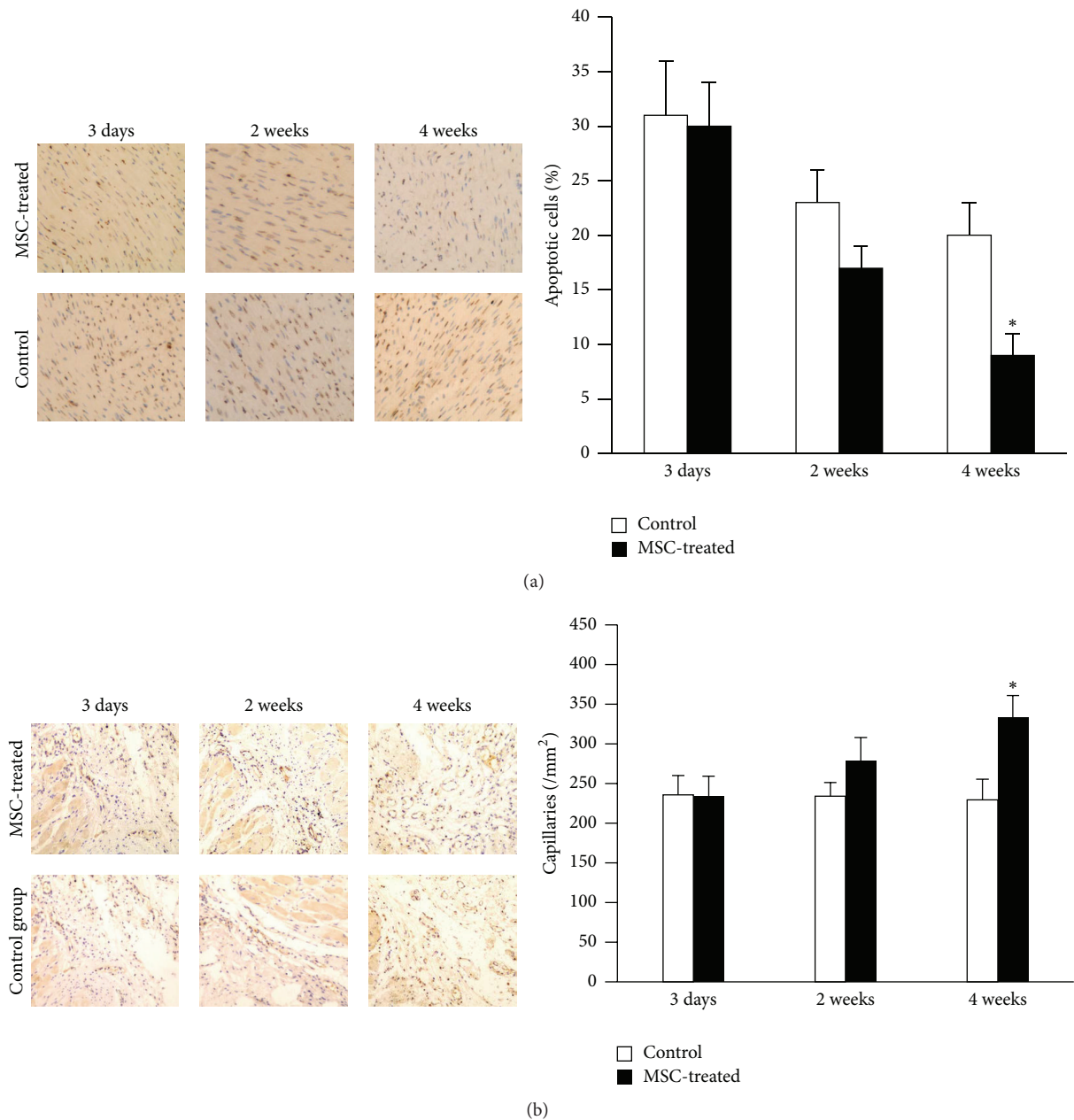


FIGURE 6: Cardiomyocytes apoptosis and capillary density in peri-infarct area after transplantation. (a) TUNEL staining and apoptosis. (b) CD31 staining and capillary density (original magnification $\times 200$). $N = 3$ for each group and $*p < 0.05$ versus control.

signal transduction pathways through paracrine, thus promoting myocardial glucose metabolism and ATP production, which leads to improvement of cardiac function. Other study found the enhancement of angiogenesis via paracrine effect with increased expression of vascular endothelial growth factor (VEGF) resulted in the improved myocardial function [37]. Similarly, our results also revealed MSCs injection significantly increased angiogenesis and reduced myocardial apoptosis and collagen deposition in the peri-infarct region. We speculated that secretion of certain cytokines might contribute to the paracrine effects, which potentially plays

a critical role in the therapeutic effects on the infarcted hearts rather than transdifferentiation in this case [38, 39].

This study has several limitations. First, the relatively short-term observation prevented definite conclusion of long-term effects of cell therapy. Second, myocardial perfusion imaging was not performed to further confirm the blood flow restoration due to angiogenesis in the MSCs group. Finally, additional laboratory analyses were required to further identify the underlying mechanisms.

In conclusion, iron particles are not a reliable marker for in vivo tracking the long-term fate of MSCs engraftment.

Despite poor cell retention, MSCs moderate left ventricular remodeling after MI due to the enhanced angiogenesis, inhibition of cardiomyocytes apoptosis, and fibrosis.

Competing Interests

The authors declare that there are no competing interests regarding the publication of this paper.

Acknowledgments

This study was supported by a research grant of National Natural Science Foundation of China (81130029). In addition, the authors really appreciate the suggestions from [ASCI]²-2015 Program for helping revise the paper.

References

- [1] M. F. Pittenger and B. J. Martin, "Mesenchymal stem cells and their potential as cardiac therapeutics," *Circulation Research*, vol. 95, no. 1, pp. 9–20, 2004.
- [2] T. J. Povsic and C. M. O'Connor, "Cell therapy for heart failure: the need for a new therapeutic strategy," *Expert Review of Cardiovascular Therapy*, vol. 8, no. 8, pp. 1107–1126, 2010.
- [3] C. Stamm, B. Westphal, H.-D. Kleine et al., "Autologous bone-marrow stem-cell transplantation for myocardial regeneration," *The Lancet*, vol. 361, no. 9351, pp. 45–46, 2003.
- [4] P. Menasché, A. A. Hagège, J.-T. Vilquin et al., "Autologous skeletal myoblast transplantation for severe postinfarction left ventricular dysfunction," *Journal of the American College of Cardiology*, vol. 41, no. 7, pp. 1078–1083, 2003.
- [5] F. Fernández-Avilés, J. A. San Román, J. García-Frade et al., "Experimental and clinical regenerative capability of human bone marrow cells after myocardial infarction," *Circulation Research*, vol. 95, no. 7, pp. 742–748, 2004.
- [6] K. C. Wollert, G. P. Meyer, J. Lotz et al., "Intracoronary autologous bone-marrow cell transfer after myocardial infarction: the BOOST randomised controlled clinical trial," *The Lancet*, vol. 364, no. 9429, pp. 141–148, 2004.
- [7] S. Janssens, C. Dubois, J. Bogaert et al., "Autologous bone marrow-derived stem-cell transfer in patients with ST-segment elevation myocardial infarction: double-blind, randomised controlled trial," *The Lancet*, vol. 367, no. 9505, pp. 113–121, 2006.
- [8] K. Lunde, S. Solheim, S. Aakhus et al., "Intracoronary injection of mononuclear bone marrow cells in acute myocardial infarction," *The New England Journal of Medicine*, vol. 355, no. 12, pp. 1199–1209, 2006.
- [9] R. Uemura, M. Xu, N. Ahmad, and M. Ashraf, "Bone marrow stem cells prevent left ventricular remodeling of ischemic heart through paracrine signaling," *Circulation Research*, vol. 98, no. 11, pp. 1414–1421, 2006.
- [10] E. L. Olivares, R. H. Costa-e-Sousa, J. P. S. Werneck-de-Castro et al., "Cellular cardiomyoplasty in large myocardial infarction: can the beneficial effect be enhanced by ACE-inhibitor therapy?" *European Journal of Heart Failure*, vol. 9, no. 6-7, pp. 558–567, 2007.
- [11] C. Peng, K. Yang, P. Xiang et al., "Effect of transplantation with autologous bone marrow stem cells on acute myocardial infarction," *International Journal of Cardiology*, vol. 162, no. 3, pp. 158–165, 2013.
- [12] N. Nagaya, T. Fujii, T. Iwase et al., "Intravenous administration of mesenchymal stem cells improves cardiac function in rats with acute myocardial infarction through angiogenesis and myogenesis," *American Journal of Physiology—Heart and Circulatory Physiology*, vol. 287, no. 6, pp. H2670–H2676, 2004.
- [13] Y. Amsalem, Y. Mardor, M. S. Feinberg et al., "Iron-oxide labeling and outcome of transplanted mesenchymal stem cells in the infarcted myocardium," *Circulation*, vol. 116, no. 11, pp. 138–145, 2007.
- [14] T. Buck, P. Hunold, K. U. Wentz, W. Tkalec, H. Joachim Nesser, and R. Erbel, "Tomographic three-dimensional echocardiographic determination of chamber size and systolic function in patients with left ventricular aneurysm: comparison to magnetic resonance imaging, cineventriculography, and two-dimensional echocardiography," *Circulation*, vol. 96, no. 12, pp. 4286–4297, 1997.
- [15] F. Grothues, G. C. Smith, J. C. C. Moon et al., "Comparison of interstudy reproducibility of cardiovascular magnetic resonance with two-dimensional echocardiography in normal subjects and in patients with heart failure or left ventricular hypertrophy," *The American Journal of Cardiology*, vol. 90, no. 1, pp. 29–34, 2002.
- [16] D. J. Stuckey, C. A. Carr, D. J. Tyler, and K. Clarke, "Cine-MRI versus two-dimensional echocardiography to measure in vivo left ventricular function in rat heart," *NMR in Biomedicine*, vol. 21, no. 7, pp. 765–772, 2008.
- [17] N. Ma, H. Cheng, M. Lu et al., "Magnetic resonance imaging with superparamagnetic iron oxide fails to track the long-term fate of mesenchymal stem cells transplanted into heart," *Scientific Reports*, vol. 5, article 9058, 2015.
- [18] E. M. Winter, B. Hogers, L. M. van der Graaf, A. C. Gittenberger-de Groot, R. E. Poelmann, and L. van der Weerd, "Cell tracking using iron oxide fails to distinguish dead from living transplanted cells in the infarcted heart," *Magnetic Resonance in Medicine*, vol. 63, no. 3, pp. 817–821, 2010.
- [19] W. Wang, Q. Jiang, H. Zhang et al., "Intravenous administration of bone marrow mesenchymal stromal cells is safe for the lung in a chronic myocardial infarction model," *Regenerative Medicine*, vol. 6, no. 2, pp. 179–190, 2011.
- [20] J. M. Hill, A. J. Dick, V. K. Raman et al., "Serial cardiac magnetic resonance imaging of injected mesenchymal stem cells," *Circulation*, vol. 108, no. 8, pp. 1009–1014, 2003.
- [21] Y. Yang, A. Schumacher, Y. Yang et al., "Monitoring bone marrow-originated mesenchymal stem cell traffic to myocardial infarction sites using magnetic resonance imaging," *Magnetic Resonance in Medicine*, vol. 65, no. 5, pp. 1430–1436, 2011.
- [22] G. P. Meyer, K. C. Wollert, J. Lotz et al., "Intracoronary bone marrow cell transfer after myocardial infarction: eighteen months' follow-up data from the randomized, controlled BOOST (Bone marrow transfer to enhance ST-elevation infarct regeneration) trial," *Circulation*, vol. 113, no. 10, pp. 1287–1294, 2006.
- [23] S. Zhang, J. Ge, A. Sun et al., "Comparison of various kinds of bone marrow stem cells for the repair of infarcted myocardium: single clonally purified non-hematopoietic mesenchymal stem cells serve as a superior source," *Journal of Cellular Biochemistry*, vol. 99, no. 4, pp. 1132–1147, 2006.
- [24] L. B. Balsam, A. J. Wagers, J. L. Christensen, T. Kofidis, I. L. Weissmann, and R. C. Robbins, "Haematopoietic stem cells adopt mature haematopoietic fates in ischaemic myocardium," *Nature*, vol. 428, no. 6983, pp. 668–673, 2004.

- [25] A. A. Kocher, M. D. Schuster, M. J. Szabolcs et al., "Neovascularization of ischemic myocardium by human bone-marrow-derived angioblasts prevents cardiomyocyte apoptosis, reduces remodeling and improves cardiac function," *Nature Medicine*, vol. 7, no. 4, pp. 430–436, 2001.
- [26] W. Dai, S. L. Hale, B. J. Martin et al., "Allogeneic mesenchymal stem cell transplantation in postinfarcted rat myocardium: short- and long-term effects," *Circulation*, vol. 112, no. 2, pp. 214–223, 2005.
- [27] A. Deten, H. C. Volz, S. Clamors et al., "Hematopoietic stem cells do not repair the infarcted mouse heart," *Cardiovascular Research*, vol. 65, no. 1, pp. 52–63, 2005.
- [28] A. A. Mangi, N. Noiseux, D. Kong et al., "Mesenchymal stem cells modified with Akt prevent remodeling and restore performance of infarcted hearts," *Nature Medicine*, vol. 9, no. 9, pp. 1195–1201, 2003.
- [29] X. Hu, J. Wang, J. Chen et al., "Optimal temporal delivery of bone marrow mesenchymal stem cells in rats with myocardial infarction," *European Journal of Cardio-Thoracic Surgery*, vol. 31, no. 3, pp. 438–443, 2007.
- [30] S. L. M. A. Beeres, F. M. Bengel, J. Bartunek et al., "Role of imaging in cardiac stem cell therapy," *Journal of the American College of Cardiology*, vol. 49, no. 11, pp. 1137–1148, 2007.
- [31] V. Fuster, J. Sanz, J. F. Viles-Gonzalez, and S. Rajagopalan, "The utility of magnetic resonance imaging in cardiac tissue regeneration trials," *Nature Clinical Practice Cardiovascular Medicine*, vol. 3, supplement 1, pp. S2–S7, 2006.
- [32] C. A. Carr, D. J. Stuckey, L. Tatton et al., "Bone marrow-derived stromal cells home to and remain in the infarcted rat heart but fail to improve function: an in vivo cine-MRI study," *American Journal of Physiology—Heart and Circulatory Physiology*, vol. 295, no. 2, pp. H533–H542, 2008.
- [33] F. Drey, Y.-H. Choi, K. Neef et al., "Noninvasive in vivo tracking of mesenchymal stem cells and evaluation of cell therapeutic effects in a murine model using a clinical 3.0 T MRI," *Cell Transplantation*, vol. 22, no. 11, pp. 1971–1980, 2013.
- [34] D. L. Kraitichman, A. W. Heldman, E. Atalar et al., "In vivo magnetic resonance imaging of mesenchymal stem cells in myocardial infarction," *Circulation*, vol. 107, no. 18, pp. 2290–2293, 2003.
- [35] O. Agbulut, S. Vandervelde, N. Al Attar et al., "Comparison of human skeletal myoblasts and bone marrow-derived CD133⁺ progenitors for the repair of infarcted myocardium," *Journal of the American College of Cardiology*, vol. 44, no. 2, pp. 458–463, 2004.
- [36] M. Cai, R. Shen, L. Song et al., "Bone Marrow Mesenchymal Stem Cells (BM-MSCs) improve heart function in swine myocardial infarction model through paracrine effects," *Scientific Reports*, vol. 6, Article ID 28250, 2016.
- [37] H.-F. Tse, C.-W. Siu, S.-G. Zhu et al., "Paracrine effects of direct intramyocardial implantation of bone marrow derived cells to enhance neovascularization in chronic ischaemic myocardium," *European Journal of Heart Failure*, vol. 9, no. 8, pp. 747–753, 2007.
- [38] T. Kinnaid, E. S. Burnett, M. S. Shou et al., "Local delivery of marrow-derived stromal cells augments collateral perfusion through paracrine mechanisms," *Circulation*, vol. 109, no. 12, pp. 1543–1549, 2004.
- [39] M. Gnecci, H. He, O. D. Liang et al., "Paracrine action accounts for marked protection of ischemic heart by Akt-modified mesenchymal stem cells," *Nature Medicine*, vol. 11, no. 4, pp. 367–368, 2005.

Research Article

Transplanted Endothelial Progenitor Cells Improve Ischemia Muscle Regeneration in Mice by Diffusion Tensor MR Imaging

Xin-Gui Peng,¹ Yingying Bai,¹ Judy R. James,² Darya P. Shlapak,² and Shenghong Ju¹

¹Jiangsu Key Laboratory of Molecular and Functional Imaging, Department of Radiology, Zhongda Hospital, Medical School, Southeast University, Nanjing, China

²Department of Radiology, University of Mississippi Medical Center, Jackson, MS, USA

Correspondence should be addressed to Shenghong Ju; jsh0836@hotmail.com

Received 7 March 2016; Revised 7 July 2016; Accepted 25 July 2016

Academic Editor: Ping Wang

Copyright © 2016 Xin-Gui Peng et al. This is an open access article distributed under the Creative Commons Attribution License, which permits unrestricted use, distribution, and reproduction in any medium, provided the original work is properly cited.

Endothelial progenitor cells (EPCs) play an important role in repairing ischemia tissues. Diffusion tensor imaging (DTI) was applied to detect the architectural organization of skeletal muscle. This study investigated the feasibility and accuracy of using the DTI to evaluate effectiveness of EPCs treatment. Mouse bone marrow-derived EPCs were isolated, cultured, characterized, and transplanted to hindlimb ischemia mice model. DTI was performed on the hindlimb at postischemia time points. The edema regions of diffusion restriction (high signal in diffusion weighted imaging) were decreased in the ischemic muscle of EPCs treated mice after 14 days compared with the controls. These results from DTI show the lower apparent diffusion coefficient and eigenvalues (λ_1 , λ_2 , and λ_3) and the higher fractional anisotropy and fiber counts of ischemic muscle on 7 and 14 days after EPCs treatment compared to the controls. There was a significant correlation between fiber counts calculated by DTI and survival fibers evaluated by histological section ($r = 0.873$, $P < 0.01$). Our study demonstrated that the time frame for muscle fiber regeneration after EPCs transplantation was significantly shortened *in vivo*. DTI could be a useful tool for noninvasive evaluation of muscle tissue damage and repair in animal models and patient with ischemic diseases.

1. Introduction

There has been evidence of an age-related increase in the lower-extremity peripheral arterial disease in the United States [1]. After ischemia, inflammation, apoptosis, and necrosis happened in local tissue [2, 3], then muscle regeneration was followed by activation of myogenic cells if revascularization can be built [4].

In recent years, there has been growing interest in using stem cells and differentiated progenitor cells as a therapeutic method for the patients with severe ischemic coronary artery or peripheral arterial disease who did not participate in revascularization procedures [5–7]. In 1999, it was first reported that bone marrow-derived endothelial progenitor cells (EPCs) contributed to neovascularization in ischemic tissues [8]. EPCs migrating to ischemic tissue and organs did not always participate in neovessels formation but rather produced a variety of proangiogenic cytokines and

growth factors to promote proliferation and migration of preexisting endothelial cells [9–11]. However, the patients with background diseases, such as aging, diabetes, hypercholesterolemia, hypertension, and smoking, may reduce the number and function of circulating/BM EPCs [9]. In our previous study, the cytokines secretion function of diabetic EPCs was significantly decreased compared to normal cell [12]. Stem cell based strategies will expect improving the current therapies.

Recent studies have shown that diffusion tensor imaging (DTI) may detect the architecture of regenerating skeletal muscle or remodeling left ventricle after ischemic injury following EPCs injection [13, 14]. DTI observed that the free diffusion of water in tissue is restricted by membranes and other cellular constituents in physiological or pathological condition, which is orientation dependent for elongated structures, such as nerve fibers and muscle fibers. Orientation dependency was obtained through measuring the diffusion

in at least six directions and the diffusion tensor eigenvalues (λ_1 , λ_2 , and λ_3) can be calculated, which represent the three-dimensional characteristics [15]. Apart from evaluation of the eccentricity of the diffusion ellipsoid by fractional anisotropy (FA), muscle fiber was visualized by fiber tractography. And apparent diffusion coefficient (ADC) displays the size of the diffusing compartment.

In the present study, we focused on two objectives: (1) to examine whether intracardiac transplantation of bone marrow-derived EPCs promotes tissue recovery after hindlimb ischemia and (2) to demonstrate the feasibility and accuracy of *in vivo* DTI in the evaluation of muscle fiber regeneration in a mouse model with hindlimb ischemia.

2. Materials and Methods

2.1. Isolation and Culture of EPCs. All animal experiments were approved by the Institutional Animal Care and Use Committee of the Medical School of Southeast University (approval ID: SYXK-2010.4987). EPCs were isolated from the tibias and femurs of 4-week-old male C57BLKS/J mice (Shanghai Laboratory Animal Center of the Chinese Academy of Science) as previously described [16]. Six mice were anaesthetized with inhaled isoflurane (1.0–1.5%, KeYuan, Shandong, China) and then killed by cervical dislocation. Aspirated bone marrow was mixed with heparin (100 U/mL, heparin sodium, Shanghai No. 1 Biochemical & Pharmaceutical Co., Ltd., China) in phosphate-buffered saline (PBS, Boster Biological Technology Co., Ltd., China). The mononuclear cell fraction was obtained from a Lymphoprep density gradient (human lymphocytes separation medium, HaoYang Biological Manufacture Co., Tianjin, China) after centrifugation (400 g, 25 minutes; Sigma-Aldrich, St. Louis, USA). The mononuclear cell fraction was collected, washed, and centrifuged. The collected cell pellet was suspended in the growth factor supplemented EBM-2 (Lonza, Switzerland) and plated on fibronectin (Sigma-Aldrich, St. Louis, MO) coated flasks (Corning Inc., NY). After 4 days in culture, nonadherent cells were removed by washing with PBS one time. The culture was maintained through days 7–10. Spindle-shaped cells were observed after 4 days. EPCs were collected for further experiments after 15 days.

2.2. EPCs Phenotype Assessment. EPCs were primarily characterized by the use of phase contrast microscopy to evaluate morphology. To assess the endothelial phenotype of EPC colonies, the cells were incubated with acLDL-Dil (Invitrogen Corporation, Carlsbad, CA) diluted at 25 mg/mL concentration in a culture medium for 4 h at 37°C. Lectin binding was analyzed using fluorescein isothiocyanate- (FITC-) conjugated UEA-1-lectin (Invitrogen Corporation). Cells were then examined under a fluorescence microscope (Zeiss, Germany). Immunocytochemistry was used to analyze the expression of various progenitor and endothelial lineage markers [17–19], including CD34 (Santa Cruz Biotechnology Inc., Santa Cruz, CA), CD133 (Abnova Corporation, Taiwan), and CXCR4 (Abcam Biochemical, Cambridge,

UK). Cell nuclei were stained with 4',6-diamidino-2-phenylindole (DAPI, Beyotime Institute of Biotechnology, Haimen, China). Alexa 488-labeled secondary antibodies were examined with confocal microscopy (Olympus, LEXT, Japan). The cell immunofluorescence of CD34, CD133, and CXCR4 was repeated three times, respectively, and averaged among all specimens to measure the positive ratio of the marker. Flow cytometry was performed using a fluorescence activated cell sorter caliber instrument (Becton Dickinson, San Jose, CA) as described previously [18]. The rat monoclonal antibodies, PE-CD34 (BD), fluorescein isothiocyanate-CD133 (eBioscience), PE-VEGF (BD), and PE-CD31 (BD), were used to stain for mouse hematopoietic stem cell and endothelial markers.

2.3. Mouse Model of Hindlimb Ischemia and EPCs Transplantation. Athymic nude male mice (Shanghai Laboratory Animal Center of the Chinese Academy of Science) at the age of 5–7 weeks and weighing 15–20 g were anesthetized with inhaled isoflurane (1.0–1.5%, KeYuan). The right femoral artery was exposed and excised with an electrocoagulator (GD350-S3, Hutong Co., Ltd., Shanghai, China) from the proximal origin of the femoral artery to the bifurcation into the saphenous and popliteal arteries [6]. After surgery, micro-CT (MCT-II08, Junhe Co., Ltd., Suzhou, China) was used to record the vascular condition and to evaluate this model by an intracardiac injection of barium sulfate (80% w/v, Meisheng, Fujian, China).

After being anesthetized with isoflurane (1%), forty-eight mice were randomly assigned to a blinded intracardiac delivery of control saline (150 μ L each), 1×10^6 cultured EPCs (150 μ L each) after 24 hours of surgery.

2.3.1. MRI Scans. All MR experiments were carried out using a 7.0 T small animal magnetic resonance system (Bruker PharmaScan, Ettlingen, ParaVision 5.1 software, Germany). For *in vivo* MR acquisition, anesthesia was induced by inhalation of a mixture of air and 3% isoflurane and maintained by a mixture of oxygen containing 0.5% to 1% isoflurane, respectively. The mouse was positioned supine inside the surface coil and placed in the scanner and monitored using a small animal instrument monitor.

Diffusion weighted images (DWI) of the ischemic hindlimb indicated the presence of edema in the ischemic muscle. The diffusion weighted images were performed at 1, 3, 7, 14, 21, and 28 days after ischemia ($n = 5$ per time point) to study the change in ischemic damage using an echo planar imaging sequence with parameters of repetition time/echo time of 2500/30 ms, b -value of 500 s/mm², matrix of 128 \times 128, field of view of 3.5 cm \times 3.5 cm, slice thickness of 1 mm, and a number of excitations of 1. The area of the edema (white signal in DWI) was measured using Image J software (National Institutes of Health, Bethesda, USA). *In vivo* DTI was performed at a time point according to the following experimental procedure. A spin echo sequence with bipolar diffusion gradients was used to acquire 10 different diffusion directions and five reference images (repetition time/echo time of 5000/28 ms, b -value of 0 and 500 s/mm², bandwidth of 250000 Hz at the same FOV, and slice locations of DWI)

for a total acquisition time of 5 min. The pixel intensities of the diffusion tensor imaging data set were fitted by using the b matrix to obtain the diffusion tensor maps. All imaging gradients were taken into account in the calculation of the b matrix [20]. The MR indices were calculated pixel by pixel and averaged for a circular region of interest of 150–180 pixels ($6\text{--}7\text{ mm}^2$) positioned with the gastrocnemius muscle (Figure 1). From the tensor maps, eigenvalues (λ_1 , λ_2 , and λ_3), mean ADC, and FA were calculated using the software of ParaVision 5.1 (Bruker PharmaScan MRI), where $\text{ADC} = \text{trace}/3$ and

$$\text{FA} = \frac{\sqrt{(\lambda_1 - \lambda_2)^2 + (\lambda_1 - \lambda_3)^2 + (\lambda_2 - \lambda_3)^2}}{\sqrt{2(\lambda_1^2 + \lambda_2^2 + \lambda_3^2)}}. \quad (1)$$

Fiber tracking was performed using a software program (DTI Studio, version 2). The FA threshold was set at 0.1 to avoid missing fibers in regions of low FA, and the angular threshold was set low at 20° , at which the fiber tracking stopped if the fiber orientation changed by greater than 20° in adjacent voxel locations in the track. The area of the edema in gastrocnemius muscle was selected to measure the fiber count.

2.3.2. Histological Analysis. To detect the EPCs muscle recovery effect after ischemic injury, the two groups of mice were sacrificed immediately with a mixture of air and 5.0% isoflurane after *in vivo* analysis at days 1, 3, 7, 14, 21, and 28 after ischemia ($n = 3\text{--}4$ per time point). Each mouse was perfused transcardially with phosphate-buffered saline, followed by freshly prepared 4% paraformaldehyde (Reagent No. 1 Factory of Shanghai Chemical Reagent Co., Ltd., China) in 0.1M phosphate buffer (pH 7.4). Gastrocnemius muscles were fixed, dehydrated, embedded, and transversely sectioned into $5\text{ }\mu\text{m}$ pieces (six sections per sample) for hematoxylin and eosin (H&E, Boster Biological Technology Co., Ltd., China) to detect muscle recovery after ischemia injury and Masson's staining (Shanghai Hongqiao Lexiang Medical Reagent Technology Co., Ltd., China) was used to examine muscle fibers. The general rule in Masson's staining is that the less porous tissues are colored by the smallest molecule dye; whenever a dye of large molecular size is able to penetrate, it always does so at the expense of the smaller molecule. The normal muscle cells have small pores and the red dye is able to penetrate, while the red dye is pulled out of the collagen because of the quite porous structure. After ischemia, the larger pores of the injured muscle cell lead to the disappearance of the red color. To examine the difference in the ischemic muscle fiber recovery between the two groups, we calculated the area of red color as survival muscle fiber in Masson's staining. The region of red staining was performed with a histological semiquantitative procedure developed with the MATLAB software (The MathWorks, Natick, Mass.). The artificial areas, such as blood vessels, were manually excluded by a pathologist. Five random microscopic fields were captured in Masson's stained sections of each mouse in each group. The percent of survival muscle fiber was

calculated by the following formula, averaged among all fields from a mouse:

$$\begin{aligned} &\text{Survival muscle fiber (\%)} \\ &= 100 \times \frac{\text{the area of survival muscle fiber}}{\text{the total tissue area}}. \end{aligned} \quad (2)$$

We measured the average value of these five random microscopic fields per sample (mouse).

Microvessel densities of muscle were calculated from serial sections stained with anti-mouse CD31 (Santa Cruz Biotechnology Inc., Santa Cruz, CA) antibody after being treated for 7 days. CD31 positive vessels were counted from five different fields within each mouse and expressed as the average number of microvessels per square millimeter (mean \pm SD) [18].

Hindlimb salvage after ischemia was evaluated after treatment. The outcomes of the treatments for ischemic hindlimbs were measured by three parameters, that is, hindlimb salvage, foot necrosis, and autoamputation, on day 28 after the treatment. The percentages of those measurements were used to compare and evaluate the treatment responses from mice receiving treatment of the control saline and EPCs.

2.4. Statistical Analysis. All statistical analyses were performed using SPSS software (SPSS for Windows, version 11.0, 2001; SPSS, Chicago, IL). Numerical data were reported as mean values \pm standard deviation (SD). Statistical significance was evaluated with an independent-sample t -test for comparison between 2 groups or by ANOVA for multiple comparisons. The Bonferroni procedure was used to correct for multiple comparisons. For statistical comparisons of the relation between the fiber count calculated by DTI and the survival fiber evaluated by Masson's staining, a correlation test was applied. A P value of less than 0.05 was considered to indicate a statistically significant difference.

3. Results

3.1. Characteristics of EPCs. Bone marrow-derived mononuclear cells were isolated and cultured for 7 days. These cells' shape changed from globe-like to spindle-like one (Figure 2(a)). These cells were stained positively by indirect immunofluorescent staining for the markers of hematopoietic stem cells and progenitor cells, CD34, CD133, and CXCR4 (Figure 2(a)). Further examination showed the positive ratio of CD34, CD133, and CXCR4 was about 81%, 76%, and 68%, respectively. Endothelial cell phenotype was characterized by assessing acLDL-Dil uptake and FITC conjugated UEA-1-lectin binding (Figure 2(b)). The ratio of double positive was about 81%. The cells were, therefore, confirmed as bone marrow-derived EPCs. The results of flow cytometry showed the expression levels of CD34 (52.73%), CD133 (14.28%), and VEGF receptor 2 (61.63%) (Figures 3(a)–3(g)). These cells also expressed CD31 (3.26%), which is a specific marker of endothelial cell. After being cultured 30 days, CD34 positive rate of cells decreased to 15.65% (Figure 3(h)).

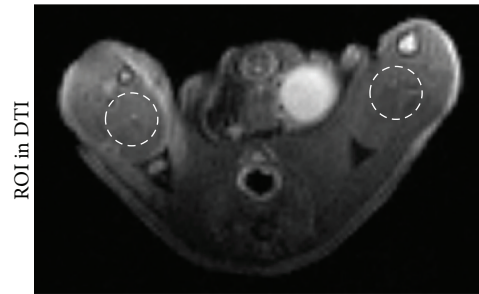


FIGURE 1: The example of regions of interest (ROI) for FA, ADC, λ_1 , λ_2 , and λ_3 value of the gastrocnemius. ROI was drawn manually at the ischemic gastrocnemius muscle in DTI maps to measure the FA, ADC, λ_1 , λ_2 , and λ_3 maps, respectively.

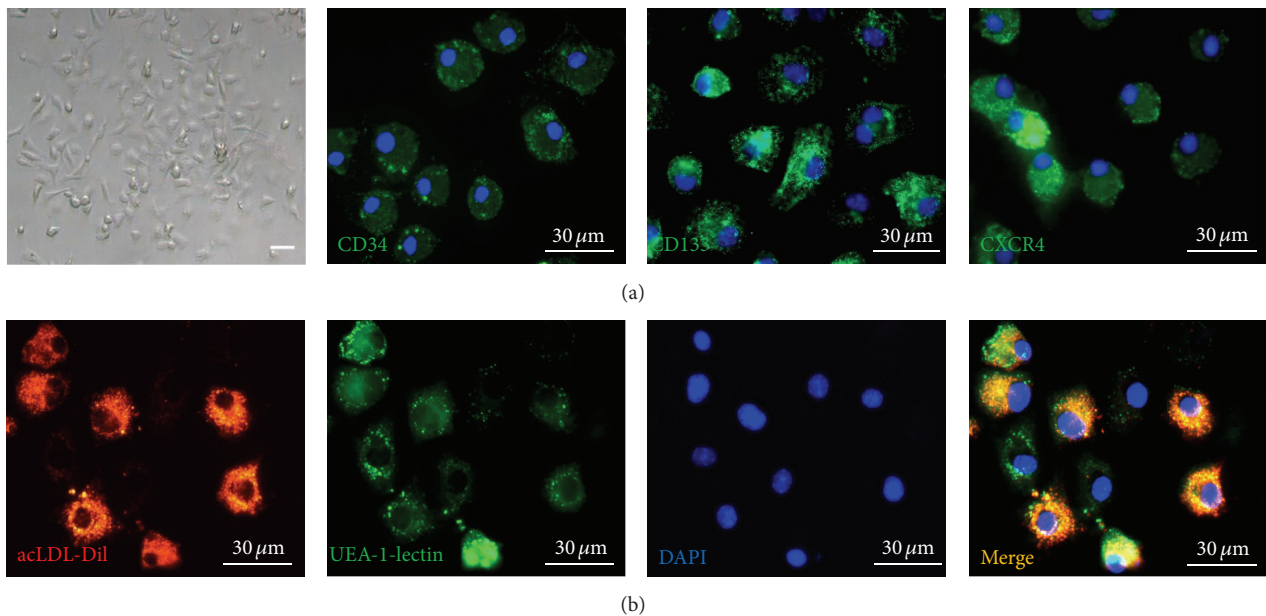


FIGURE 2: Morphological changes and immunocytochemical analysis in mouse bone marrow-derived EPCs. (a) MNCs changed from globe-like shape to being thin and flat and then round and fusiform at day 7 (bar = 30 μm). These cells were positive by indirect immunofluorescent staining for the markers of hematopoietic stem cells and progenitor cells, CD34, CD133, and CXCR4 (bar = 30 μm). (b) The EPCs were able to take up Dil-labeled acetylated low-density lipoprotein (LDL) and bind the endothelial-specific lectin FITC-labeled lectin after 14 days in culture, which were colocalized in >95% cell (bar = 30 μm).

3.2. Evaluation of Hindlimb Ischemia Model. Figure 4(a) was the diagram of the study and treatment methods. Immediately after surgery, the skin color of the right hindlimb turned pale compared with the left normal limb. Micro-CT was performed to detect the dead end in the proximal origin of the right femoral artery (Figure 4(b)).

3.3. Muscle Regeneration in the Ischemic Hindlimb after EPCs Treatment

3.3.1. DWI and DTI In Vivo. Higher signal in diffusion weighted images of the ischemic hindlimb indicated the edema area of diffusion restriction in the ischemic muscle. The regions of edema in the ischemic muscle at day 14 after treatment with EPCs were smaller than that of control group (Figures 5(a) and 5(b)). At days 1 and 3 after treatment, the ADC in the ischemic muscle increased and the FA value

decreased, but there was no difference between the EPCs treated and the control group. However, on days 7 and 14 after treatment, there were significant differences between the EPCs treated and the control group. The ADC values of the ischemic hindlimbs in the EPCs transplantation group were lower than in the control group and the FA values of the ischemic muscle in the EPCs treated mice were higher than that of the control mice (Figures 5(c)–5(e)). Immediately after ischemia, λ_2 and λ_3 increased. Seven to fourteen days after treatment, λ_1 , λ_2 , and λ_3 of the ischemia muscle in the EPCs group were lower compared to the control group (Figures 5(f)–5(h)). In addition, the fiber count of ischemic muscles treated by EPCs was higher than those treated with saline at 28 days (Figures 5(i) and 5(j)).

3.3.2. Masson's Staining. At day 3 after treatment, there was no difference in survival fiber between the two groups.

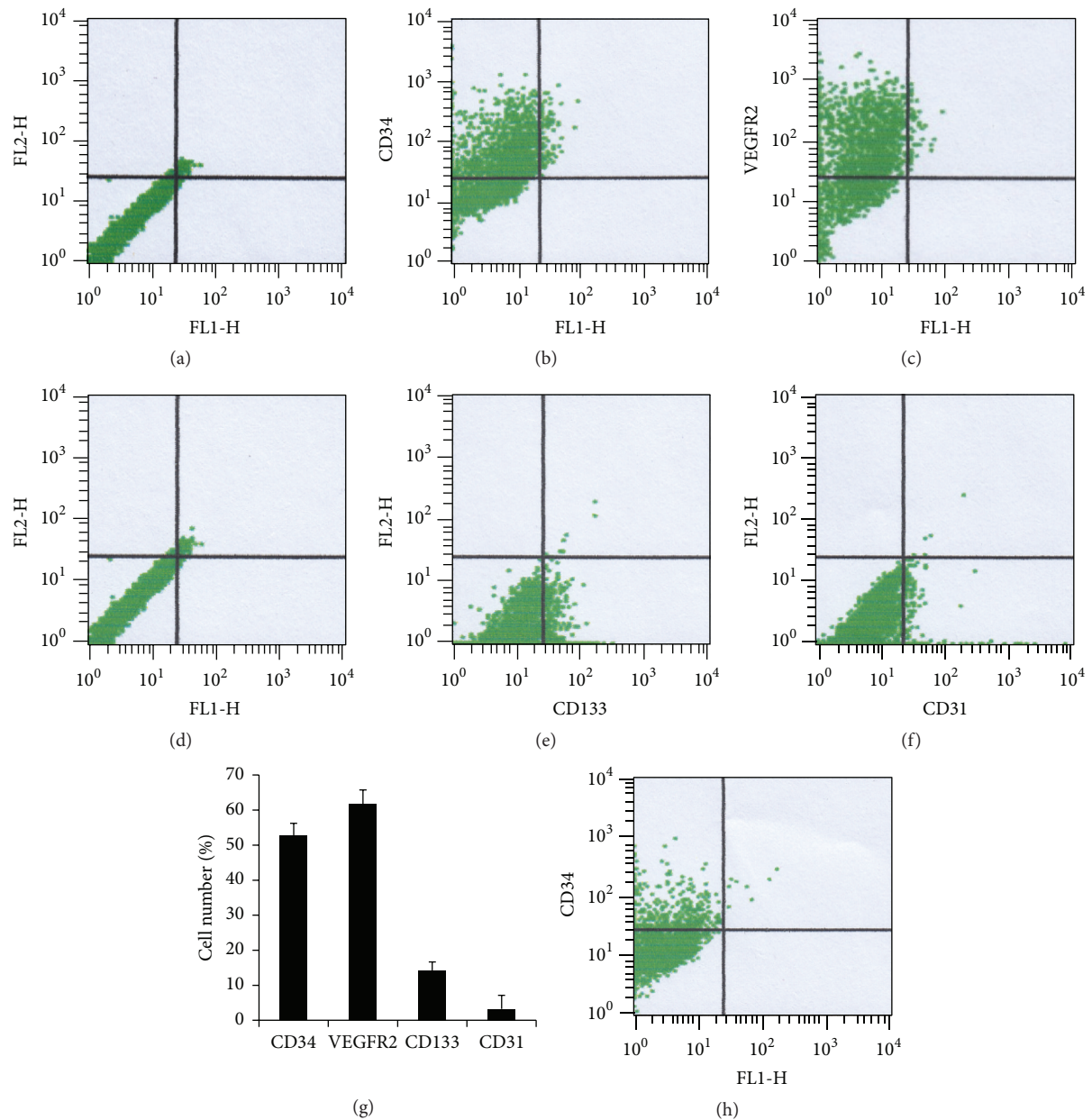


FIGURE 3: In FACS analyses, EPCs cultured for 15 days were positive for CD34 ((b), 52.73%), VEGFR2 ((c), 61.63%), CD133 ((e), 14.28%), and the mature endothelial-specific marker CD31 ((f), 3.26%). Isotype controls were used in the FACS analyses ((a), (d)). A bar graph (g) showed that the positive rate of CD34, VEGFR2, CD133, and CD31. After being cultured for 30 days, the EPCs were positive for CD34 ((h), 15.65%).

However, Masson's staining showed that there was a greater expansion of the survival fibers after ischemia at 28 days than at day 3. In the control group, histological examination of muscle sections at day 28 after treatment showed fibrosis areas and numerous necrotic muscular fibers in the ischemic hindlimb (Figures 6(a) and 6(b)). In contrast, in ischemic mice treated with EPCs for 28 days, fibrosis and the number of necrotic muscular fibers were significantly reduced. The percentage of survival muscular fibers in the ischemic mice treated with EPCs was onefold higher than that of control group (Figure 6(b)). In addition, the majority of muscle fibers were intact. There was a significant correlation between fiber

counts calculated by DTI and survival fiber evaluated by histopathology ($r = 0.874$, $P < 0.01$) (Figure 6(c)).

3.3.3. Capillary Density Measurement. Immunohistochemical analysis of the ischemic tissue samples with the CD31 marker revealed that the number of capillaries in ischemic muscle from mice treated with EPCs for 14 days was more significant than that of the saline treated control group ($P < 0.05$) (Figures 6(d) and 6(e)).

3.3.4. Tissue Salvage after EPC Treatment. A significant decrease in autoamputation of the ischemic hindlimbs in

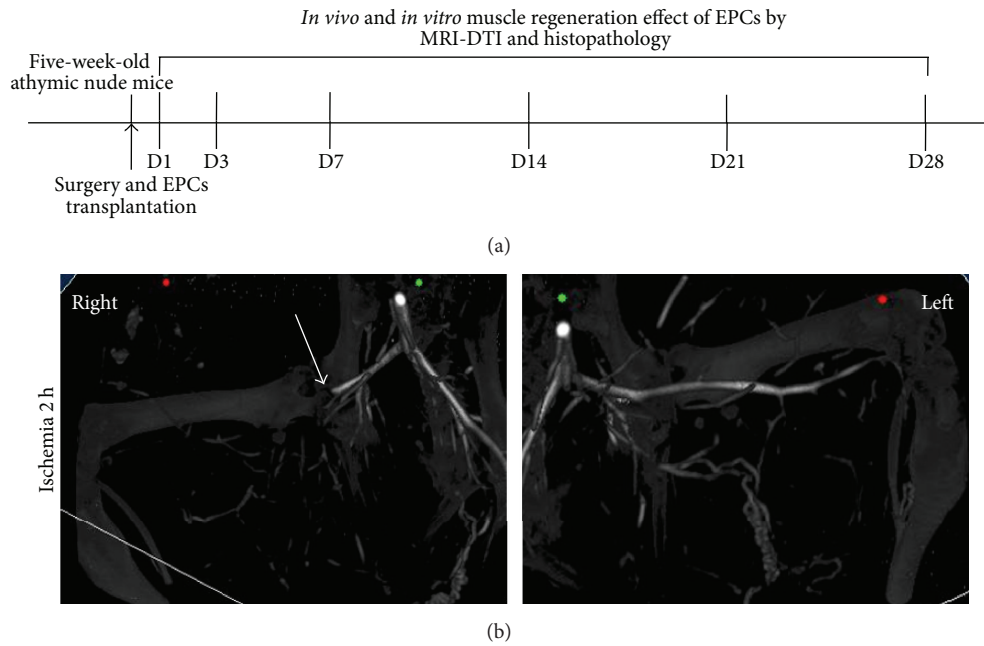


FIGURE 4: Diagram of the EPCs tracking and treatment evaluation methods (a); representative imaging of micro-CT (b) performed after development of hindlimb ischemia 2 hour. The proximal origin of the right femoral artery was terminated (arrow).

the EPC treated group was observed after EPC treatment as compared to animals treated with the saline (control group). In the control group, injured limbs were preserved only in 3 of 12 mice (25%), whereas foot necrosis and autoamputation developed in 5 (41.7%) and 4 (33.3%) mice. In contrast, limbs were salvaged in 8 of 15 mice (53.3%) in the EPC treated group. Furthermore, foot necrosis was limited to 4 mice (26.7%), and only three animals (20%) experienced spontaneous limb amputation. The outcomes were significantly different between the EPCs treated group and the control ($P < 0.01$).

4. Discussion

In this study, we applied DTI to determine the dynamic changes in tissue repair and muscle fiber regeneration between the EPCs treated group and the control saline group following induced hindlimb ischemia. Furthermore this study also demonstrated that the transplanted bone marrow-derived EPCs improved muscle fiber regeneration.

Chargé and Rudnicki reported that the degeneration and necrosis of the muscle fibers after ischemia result in increased permeability and were accompanied by the activation of inflammatory and myogenic cell [4]. If the collateral circulation could not be built, the incidence rate of limb necrosis, autoamputation, and disability increased significantly [21]. Bone marrow-derived EPCs that contributed to neovascularization in ischemic tissues were reported [9, 22, 23]. In this study, we demonstrated the therapeutic effect of EPCs in the hindlimb ischemia model. The area of bright signal in diffusion imaging after EPCs treatment decreased more quickly compared with control mice *in vivo*, and the numbers of survival fibers were also higher than that of the control mice.

Sotak suggested that the decreased ADC value indicated cell swelling and extracellular diffusion restriction in brain tissue [24]. Compared to brain cell swelling, myocyte swelling resulted in increased ADC value and diffusivity after acute ischemia in skeletal muscle [25, 26]. In our study, we also demonstrated the relationship between ADC and myocyte size, where the areas with swollen myocytes were characterized by higher ADC. The muscle regeneration process is from the outer regions to the inner regions [27]. In our study, treatment with EPCs promoted ischemic muscle recovery with smaller regions of edema in the hindlimb. The ADC value in the EPCs treated group was lower compared to the control group and the area of edema in ischemic muscle was also smaller after 14 days. The results demonstrated that EPCs transplantation promoted tissue recovery *in vivo*. Furthermore, the results of FA, eigenvalues, and fiber counts from DTI suggested that the muscle fibers regeneration after ischemia was better in the transplanted EPCs group than in the control group. Strijkers et al. demonstrated that the increase in three eigenvalues is because of lengthened myocytes on day three after ischemia [28]. The histological findings also indicated a more complete recovery of the muscle fiber in the EPCs treated group versus the control group. In addition, there was a strong relationship between the survival muscle fibers measured by Masson's staining and fiber counts evaluated by DTI.

However, compared to Heemskerk et al.'s report [27], the repair time for ischemic muscles was longer in our study. We found that two factors contributed to this difference. One of the factors was that the induced methods of hindlimb ischemia models were different. In our study, the right femoral artery was excised with an electrocoagulator from the proximal origin of the external iliac artery to the bifurcation

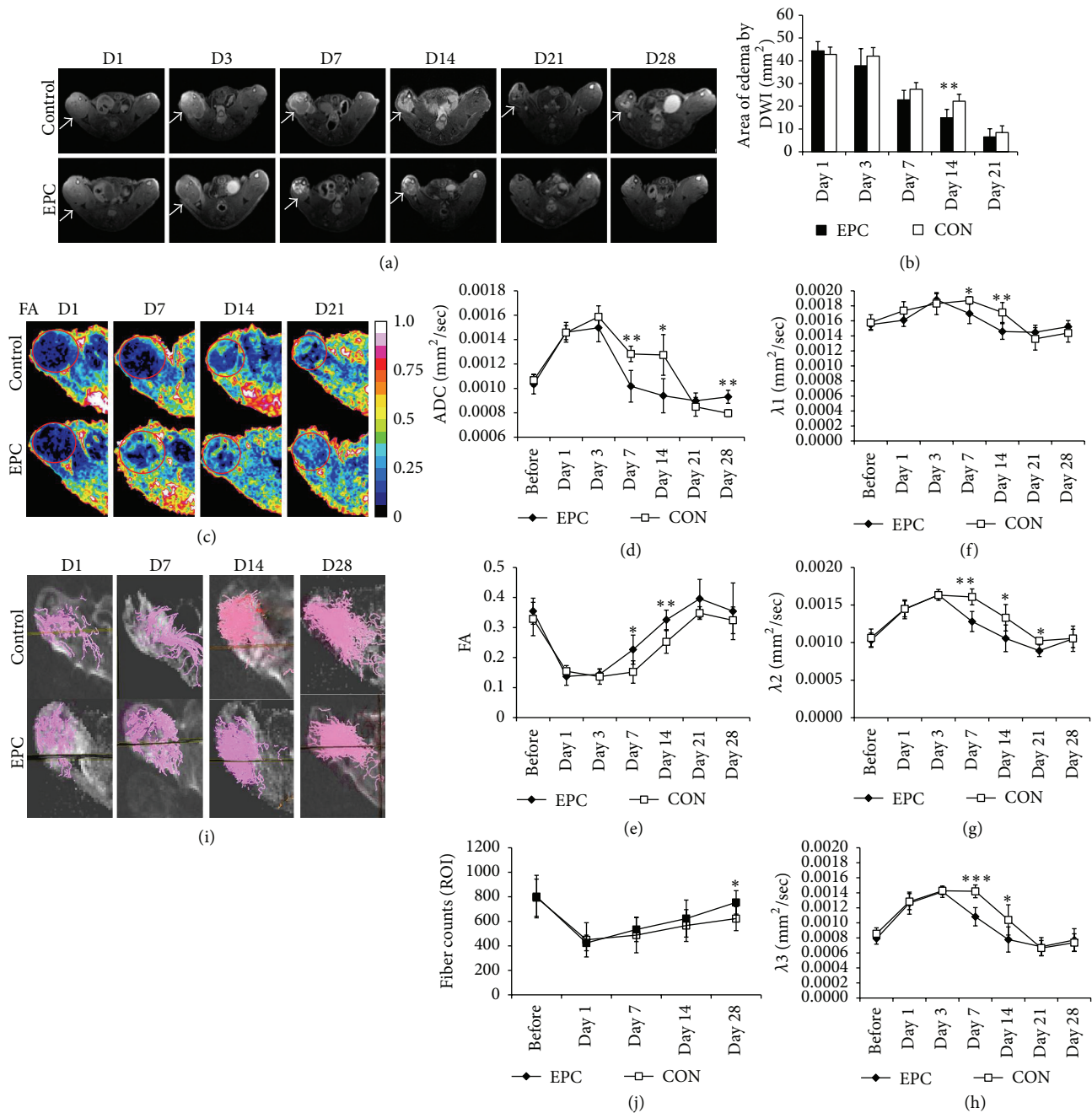


FIGURE 5: *In vivo* ischemic muscle regeneration effect of EPCs by MR-DTI. (a): Representative DWI at 1, 3, 7, 21, and 28 days in ischemic gastrocnemius muscles in control media injected and EPCs transplanted mice (high signal in DWI indicated diffusion restriction, white arrowhead). A bar graph (b) showed that administration of EPCs significantly reduced the region of edema at day 14 after EPCs transplantation. (c) Representative pixel maps of FA at 1, 7, 14, and 21 days (red circle). Line graphs showed that ADC (d), FA (e), λ_1 (f), λ_2 (g), and λ_3 (h) of EPCs transplantation improved better than that of control group at days 7 and 14 after ischemia. (i) Representative fiber tracking maps at 1, 3, 7, and 28 days. The fiber counts (j) in ischemic gastrocnemius muscles at day 28 after EPCs transplantation were more than those of control group. * $P < 0.05$, ** $P < 0.01$, and *** $P < 0.001$.

into saphenous and popliteal arteries, which induced more severe ischemia compared to ligation. The other factor was that the kind of mouse variety used was different. The wild type mice were used in their study; the nude mice were used in our study. The thymus of nude mice was vestigial, resulting in being incapable of producing mature T-cells [29].

Studies suggest that T-cells play an important role in the development of collateral blood vessels [2, 30]. Therefore, our work indicated that the longer muscle regeneration time required in nude mice may, in part, explain the immune dysfunction that caused the delay in the ischemic muscle fiber recovery.

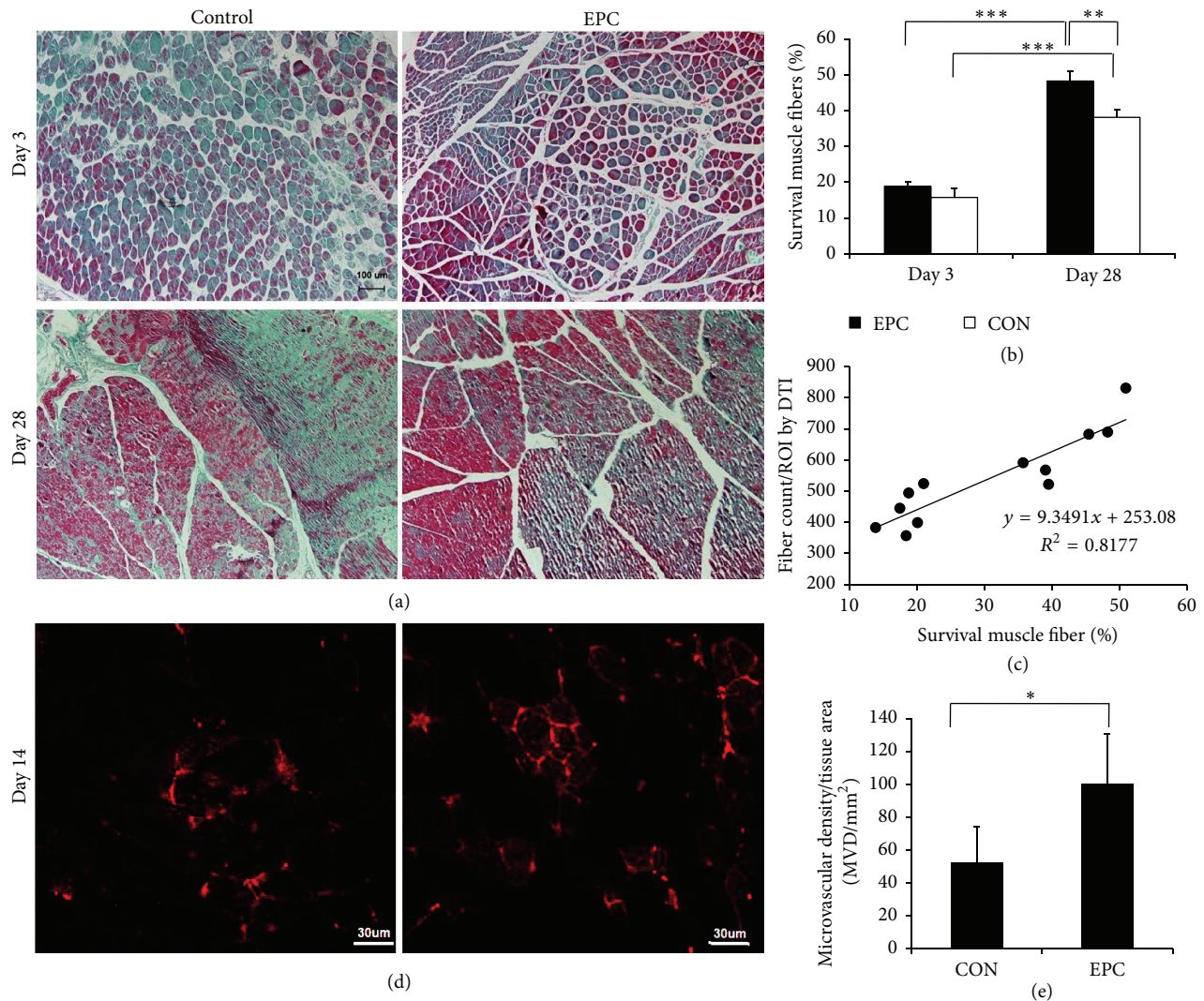


FIGURE 6: Histologic specimens obtained from ischemia muscle. (a) At days 3 and 28, almost complete tissue recovery using Masson's staining was found in the EPCs treated group. However, in the control group, multiple inflammations and collagen were found (bar = 100 μm). (b) A bar graph showed that the survival muscle fibers of mice treated with EPCs were greater than with the control group. Data is expressed as mean \pm SD, * $P < 0.05$. (c) A line graph showed the correlations between survival muscle fibers by histological method and fiber count measured by DTI ($r = 0.874$, $P < 0.01$). (d) The microvascular density was measured by staining ischemia tissues with CD31 on day 14 after treatment. The EPC treatment augmented vessel density of the ischemic hindlimb (bar = 30 μm). (e) A bar graph showed that the microvascular density (MVD) in the group treated with EPCs was significantly increased compared with that of the control group. * $P < 0.05$, ** $P < 0.01$, and *** $P < 0.001$.

Brain DTI studies are usually acquired with a b -value of 1000 s/mm^2 . However, lower value of 400–600 s/mm^2 for muscle imaging was recommended because the minimized echo time could maximize the muscle signal (lower T2 relaxation time compared to brain tissue) [31]. Compared to the brain white matter with high anisotropy ($\text{FA} \geq 0.7$) using approximately 30 gradient directions and the muscle tissue with low FA values (about 0.25), the gradient directions number was about 10 [31, 32]. S. Sinha and U. Sinha demonstrated that there was no significant difference in coefficient of variation from 6- and 13-diffusion gradient acquisitions in human calf muscles at 1.5 T [33].

There were some limitations in this study. First, the MR images were not matched with histologic slices perfectly, so

the DTI data did not compare with the histologic detail change. Second, susceptibility artifacts from bone/tissue and air/tissue interface effects on a 7.0 T MR scanner were up to several times greater than those on 1.5 T or 3.0 T scanners, particularly the echo planar based DTI [34]. We used the surface coil and contact closely with the thighs to help decrease the artifacts.

5. Conclusion

Our results indicated that the tissue repair and ischemic muscle fiber regeneration after EPCs treatment were significantly better than those of the control group. We demonstrated that the DTI was useful for longitudinally evaluating the

regeneration of ischemia muscle fibers after EPCs transplanted treatment in a mouse model with hindlimb ischemia. We propose that DTI can be used for noninvasive evaluation of muscle tissue damage and repair in animal models and patients with ischemic diseases.

Abbreviations

ADC: Apparent diffusion coefficient
 DTI: Diffusion tensor imaging
 DWI: Diffusion weighted imaging
 EPC: Endothelial progenitor cell
 FA: Fractional anisotropy
 MRI: Magnetic resonance imaging.

Competing Interests

The authors declare that there are no competing interests regarding the publication of this article.

Acknowledgments

This work was supported by grant from the National Nature Science Foundation of China (NSFC, no. 81525014, no. 81371538, and no. 81501523) and Jiangsu Provincial Special Program of Medical Science.

References

- [1] M. H. Criqui, A. Fronek, E. Barrett-Connor, M. R. Klauber, S. Gabriel, and D. Goodman, "The prevalence of peripheral arterial disease in a defined population," *Circulation*, vol. 71, no. 3, pp. 510–515, 1985.
- [2] E. Stabile, M. S. Burnett, C. Watkins et al., "Impaired arteriogenic response to acute hindlimb ischemia in CD4-knockout mice," *Circulation*, vol. 108, no. 2, pp. 205–210, 2003.
- [3] E. Stabile, T. Kinnaird, A. La Sala et al., "CD8+ T lymphocytes regulate the arteriogenic response to ischemia by infiltrating the site of collateral vessel development and recruiting CD4+ mononuclear cells through the expression of interleukin-16," *Circulation*, vol. 113, no. 1, pp. 118–124, 2006.
- [4] S. B. P. Chargé and M. A. Rudnicki, "Cellular and molecular regulation of muscle regeneration," *Physiological Reviews*, vol. 84, no. 1, pp. 209–238, 2004.
- [5] F. Dong, J. Harvey, A. Finan, K. Weber, U. Agarwal, and M. S. Penn, "Myocardial CXCR4 expression is required for mesenchymal stem cell mediated repair following acute myocardial infarction," *Circulation*, vol. 126, no. 3, pp. 314–324, 2012.
- [6] K. Harhour, A. Kebir, B. Guillet et al., "Soluble CD146 displays angiogenic properties and promotes neovascularization in experimental hind-limb ischemia," *Blood*, vol. 115, no. 18, pp. 3843–3851, 2010.
- [7] S. MacLean, W. S. Khan, A. A. Malik, S. Anand, and M. Snow, "The potential of stem cells in the treatment of skeletal muscle injury and disease," *Stem Cells International*, vol. 2012, Article ID 282348, 9 pages, 2012.
- [8] T. Takahashi, C. Kalka, H. Masuda et al., "Ischemia- and cytokine-induced mobilization of bone marrow-derived endothelial progenitor cells for neovascularization," *Nature Medicine*, vol. 5, no. 4, pp. 434–438, 1999.
- [9] C. Alev, M. Ii, and T. Asahara, "Endothelial progenitor cells: a novel tool for the therapy of ischemic diseases," *Antioxidants and Redox Signaling*, vol. 15, no. 4, pp. 949–965, 2011.
- [10] D. P. Sieveking and M. K. C. Ng, "Cell therapies for therapeutic angiogenesis: back to the bench," *Vascular Medicine*, vol. 14, no. 2, pp. 153–166, 2009.
- [11] J. C. Ryu, B. P. Davidson, A. Xie et al., "Molecular imaging of the paracrine proangiogenic effects of progenitor cell therapy in limb ischemia," *Circulation*, vol. 127, no. 6, pp. 710–719, 2013.
- [12] Y.-Y. Bai, X.-G. Peng, B.-H. Wang, Y.-L. Wan, and S. Ju, "Effects of stem cell microenvironment on bone marrow-derived endothelial progenitor cells from diabetic mice," *Experimental and Clinical Cardiology*, vol. 20, no. 7, pp. 1057–1068, 2014.
- [13] A. Gianella, U. Guerrini, M. Tilenni et al., "Magnetic resonance imaging of human endothelial progenitors reveals opposite effects on vascular and muscle regeneration into ischaemic tissues," *Cardiovascular Research*, vol. 85, no. 3, pp. 503–513, 2010.
- [14] M.-T. Wu, W.-Y. I. Tseng, M.-Y. M. Su et al., "Diffusion tensor magnetic resonance imaging mapping the fiber architecture remodeling in human myocardium after infarction: correlation with viability and wall motion," *Circulation*, vol. 114, no. 10, pp. 1036–1045, 2006.
- [15] A. M. Heemskerk, T. K. Sinha, K. J. Wilson, Z. Ding, and B. M. Damon, "Quantitative assessment of DTI-based muscle fiber tracking and optimal tracking parameters," *Magnetic Resonance in Medicine*, vol. 61, no. 2, pp. 467–472, 2009.
- [16] R. Chen, H. Yu, Z.-Y. Jia, Q.-L. Yao, and G.-J. Teng, "Efficient nano iron particle-labeling and noninvasive MR imaging of mouse bone marrow-derived endothelial progenitor cells," *International Journal of Nanomedicine*, vol. 6, pp. 511–519, 2011.
- [17] T. Asahara, A. Kawamoto, and H. Masuda, "Concise review: circulating endothelial progenitor cells for vascular medicine," *Stem Cells*, vol. 29, no. 11, pp. 1650–1655, 2011.
- [18] X.-Y. Wang, S. Ju, C. Li et al., "Non-invasive imaging of endothelial progenitor cells in tumor neovascularization using a novel dual-modality paramagnetic/near-infrared fluorescence probe," *PLoS ONE*, vol. 7, no. 11, Article ID e50575, 2012.
- [19] X.-L. Mai, Z.-L. Ma, J.-H. Sun, S.-H. Ju, M. Ma, and G.-J. Teng, "Assessments of proliferation capacity and viability of New Zealand rabbit peripheral blood endothelial progenitor cells labeled with superparamagnetic particles," *Cell Transplantation*, vol. 18, no. 2, pp. 171–181, 2009.
- [20] J. Mattiello, P. J. Basser, and D. Le Bihan, "The b matrix in diffusion tensor echo-planar imaging," *Magnetic Resonance in Medicine*, vol. 37, no. 2, pp. 292–300, 1997.
- [21] C. Kalka, H. Masuda, T. Takahashi et al., "Transplantation of ex vivo expanded endothelial progenitor cells for therapeutic neovascularization," *Proceedings of the National Academy of Sciences of the United States of America*, vol. 97, no. 7, pp. 3422–3427, 2000.
- [22] E. Chavakis, M. Koyanagi, and S. Dimmeler, "Enhancing the outcome of cell therapy for cardiac repair: progress from bench to bedside and back," *Circulation*, vol. 121, no. 2, pp. 325–335, 2010.
- [23] Y.-Y. Bai, L. Wang, X.-G. Peng et al., "Non-invasive monitoring of transplanted endothelial progenitor cells in diabetic ischemic stroke models," *Biomaterials*, vol. 40, pp. 43–50, 2015.
- [24] C. H. Sotak, "The role of diffusion tensor imaging in the evaluation of ischemic brain—a review," *NMR in Biomedicine*, vol. 15, no. 7-8, pp. 561–569, 2002.

- [25] A. M. Heemskerk, M. R. Drost, G. S. Van Bochove, M. F. M. Van Oosterhout, K. Nicolay, and G. J. Strijkers, "DTI-based assessment of ischemia-reperfusion in mouse skeletal muscle," *Magnetic Resonance in Medicine*, vol. 56, no. 2, pp. 272–281, 2006.
- [26] R. H. Fan and M. D. Does, "Compartmental relaxation and diffusion tensor imaging measurements in vivo in λ -carrageenan-induced edema in rat skeletal muscle," *NMR in Biomedicine*, vol. 21, no. 6, pp. 566–573, 2008.
- [27] A. M. Heemskerk, G. J. Strijkers, M. R. Drost, G. S. Van Bochove, and K. Nicolay, "Skeletal muscle degeneration and regeneration after femoral artery ligation in mice: monitoring with diffusion MR imaging," *Radiology*, vol. 243, no. 2, pp. 413–421, 2007.
- [28] G. J. Strijkers, A. Bouts, W. M. Blankesteyn et al., "Diffusion tensor imaging of left ventricular remodeling in response to myocardial infarction in the mouse," *NMR in Biomedicine*, vol. 22, no. 2, pp. 182–190, 2009.
- [29] M. Pelleitier and S. Montplaisir, "The nude mouse: a model of deficient T-cell function," *Methods and Achievements in Experimental Pathology*, vol. 7, pp. 149–166, 1975.
- [30] T. Couffinhal, M. Silver, M. Kearney et al., "Impaired collateral vessel development associated with reduced expression of vascular endothelial growth factor in apoe^{-/-} mice," *Circulation*, vol. 99, no. 24, pp. 3188–3198, 1999.
- [31] B. M. Damon, "Effects of image noise in muscle diffusion tensor (DT)-MRI assessed using numerical simulations," *Magnetic Resonance in Medicine*, vol. 60, no. 4, pp. 934–944, 2008.
- [32] D. K. Jones, "The effect of gradient sampling schemes on measures derived from diffusion tensor MRI: a Monte Carlo Study," *Magnetic Resonance in Medicine*, vol. 51, no. 4, pp. 807–815, 2004.
- [33] S. Sinha and U. Sinha, "Reproducibility analysis of diffusion tensor indices and fiber architecture of human calf muscles in vivo at 1.5 Tesla in neutral and plantarflexed ankle positions at rest," *Journal of Magnetic Resonance Imaging*, vol. 34, no. 1, pp. 107–119, 2011.
- [34] R. Kuo, M. Panchal, L. Tanenbaum, and J. V. Crues III, "3.0 Tesla imaging of the musculoskeletal system," *Journal of Magnetic Resonance Imaging*, vol. 25, no. 2, pp. 245–261, 2007.

Research Article

***In Vivo* Tracking of Systemically Administered Allogeneic Bone Marrow Mesenchymal Stem Cells in Normal Rats through Bioluminescence Imaging**

Juan Cao,^{1,2} Shike Hou,^{1,2} Hui Ding,^{1,2} Ziquan Liu,^{1,2} Meijuan Song,^{1,2} Xiaojing Qin,³ Xue Wang,^{1,2} Mengyang Yu,^{1,2} Zhiguang Sun,^{1,2} Jinyang Liu,^{1,2} Shuli Sun,^{1,2} Peixin Xiao,^{1,2} Qi Lv,^{1,2} and Haojun Fan^{1,2}

¹Institute of Disaster Medicine and Public Health, Affiliated Hospital of Logistic University of Chinese People's Armed Police Force, Tianjin, China

²Key Laboratory of Emergency and Disaster Medicine in Chinese People's Liberation Army (PLA), Tianjin 300162, China

³Department of Pathology, Affiliated Hospital of Logistic University of Chinese People's Armed Police Force, Tianjin, China

Correspondence should be addressed to Qi Lv; lvqi68@163.com and Haojun Fan; haojunfan86@163.com

Received 22 March 2016; Revised 26 May 2016; Accepted 3 July 2016

Academic Editor: Ping Wang

Copyright © 2016 Juan Cao et al. This is an open access article distributed under the Creative Commons Attribution License, which permits unrestricted use, distribution, and reproduction in any medium, provided the original work is properly cited.

Recently, mesenchymal stem cells (MSCs) are increasingly used as a panacea for multiple types of disease short of effective treatment. Dozens of clinical trials published demonstrated strikingly positive therapeutic effects of MSCs. However, as a specific agent, little research has focused on the dynamic distribution of MSCs after *in vivo* administration. In this study, we track systemically transplanted allogeneic bone marrow mesenchymal stem cells (BMSCs) in normal rats through bioluminescence imaging (BLI) in real time. *Ex vivo* organ imaging, immunohistochemistry (IHC), and RT-PCR were conducted to verify the histological distribution of BMSCs. Our results showed that BMSCs home to the dorsal skin apart from the lungs and kidneys after tail vein injection and could not be detected 14 days later. Allogeneic BMSCs mainly appeared not at the parenchymatous organs but at the subepidermal connective tissue and adipose tissue in healthy rats. There were no significant MSCs-related adverse effects except for transient decrease in neutrophils. These findings will provide experimental evidences for a better understanding of the biocharacteristics of BMSCs.

1. Introduction

Mesenchymal stem cells (MSCs) are self-renewing, multipotent progenitor cells with the potential to differentiate into multiple mesoderm lineages. Many animal models have demonstrated the remarkable tropic, nonimmunogenic, and immunosuppressive characteristics of these cells in injured tissues [1, 2]. Due to their properties of accessibility and convenient expansion, clinical research on MSCs has increased in the past twenty years. MSCs have been described as a promising source for the cell-based treatment of miscellaneous complicated disorders, such as graft-versus-host disease [3, 4], cardiocerebrovascular disease [5], spinal cord injury [6, 7], hepatic diseases [8], and respiratory disease

[9, 10]. Although there is a consensus regarding the *in vitro* characteristics of MSCs, there are outstanding issues concerning the localization and persistence of MSCs *in vivo* after administration. Furthermore, the safety of injecting of foreign cells such as these is another major obstacle in the clinical setting.

Bioluminescence imaging (BLI) detects visible light emitted by cells labeled with luminescent enzymes, such as luciferase, when these enzymes react with their specific bioluminescent substrates [11]. BLI can noninvasively track luciferase-transduced cells implanted in living animals in real time. This method of substantial utility has already facilitated the design of therapeutic strategies using MSCs in various animal models, including models of tumorous

diseases, ischemia- and reperfusion-induced acute kidney injury (AKI), myocardial damage, stroke, and other diseases [12–15]. However, visible light is limited in the depth of tissue penetration. Thus, this technique is mainly used for imaging of small animals, such as mice. Herein, we show that bioluminescent imaging can reveal dynamic information detailing the distribution and tropism of BMSCs in a larger rat model. More interestingly, we revealed that the homing organs of BMSCs in rats are not the same as in mice. Additionally, we carried out a safety assessment of the administered BMSCs through histological and serology tests, providing an experimental basis for the use of these stem cells in research.

2. Material and Methods

2.1. Lentivirus Vector and BMSC Transduction. MSCs were isolated from the bone marrow of normal Wistar rats purchased from Cyagen Biosciences. According to the minimal criteria proposed by the International Society for Cellular Therapy (ISCT) [16], the cells were subjected to flow cytometry to examine the expression of specific surface antigens (Figure S1 in Supplementary Material available online at <http://dx.doi.org/10.1155/2016/3970942>). The BMSCs displayed a typical MSC morphology, exhibiting a fibroblast-like shape or flat polygonal appearance. They were plastic adherent and were maintained in tissue culture flasks. When the BMSCs were approximately 80 to 90% confluent, they were dissociated with trypsin-EDTA and split at a 1:2 ratio.

The culture-expanded BMSCs were seeded in six-well plates at a density of 1×10^5 cells per well. 24 h later, the medium was removed and replaced with growth medium and a polybrene solution (1 mL per well). Polybrene was added at a final concentration of $5 \mu\text{g/mL}$. The lentivirus vector expressing both the GFP and luciferase genes (purchased from GENECHEN, Shanghai, China) was thawed and added at a multiplicity of infection of 4. After 8 h of incubation, the medium was replaced with fresh medium, and the flask was returned to the incubator. Three days later, to quantify the transduction efficiency, Luc-GFP-BMSCs were stained with Hoechst 33342 (FANBO, Beijing, China) for 5 min. Then, the cells were visualized and analyzed using an inverted fluorescence microscope (DMI 3000B, Leica, Germany) in five randomly selected fields of view.

2.2. Multilineage Differentiation of Luc-GFP-BMSCs. Cultured-expanded Luc-GFP-BMSCs at passage six were used to evaluate the *in vitro* differentiation abilities of the cells in accordance with the manufacturer's recommendations (Cyagen Biosciences, USA). For adipogenic induction, Luc-GFP-BMSCs were subculture-expanded in six-well plates at 2×10^4 cells/cm² in growth medium containing 10% fetal bovine serum and 5% penicillin-streptomycin as well as glutamine. The cells were fed every three days until they reached 100% confluency. Then, the growth medium was changed to 2 mL of induction medium, which consisted of fetal bovine serum, penicillin-streptomycin, glutamine, insulin, rosiglitazone, and dexamethasone. Three days later, the medium was replaced with maintenance

medium containing fetal bovine serum, penicillin-streptomycin, and insulin. 24 h later, the medium was changed back to induction medium, and the cycle of induction/maintenance was repeated three times. After five cycles of induction/maintenance, the cells were cultured in maintenance medium for an additional three days. Three weeks later, adipose cells were observed after being stained with Oil Red O. To induce osteogenic differentiation, Luc-GFP-BMSCs were seeded in growth medium at a density of 3×10^4 cells/cm² for one day at 37°C in a 5% CO₂ humidified incubator. Then, the growth medium was aspirated from each well and 2 mL of osteogenic differentiation medium containing fetal bovine serum, penicillin-streptomycin, glutamine, ascorbate, β -glycerophosphate, and dexamethasone was added, and the medium was changed every three days. Three weeks later, the cells were fixed with 2 mL of a 4% formaldehyde solution and stained with Alizarin red.

2.3. Animals. Adult male Wistar rats weighing 170 ± 10 g were provided by the Experimental Animal Center of the Military Medical Science Academy of the People's Liberation Army of China. The rats were maintained in an animal laboratory under a temperature of 25°C at all times, fed with commercial rodent chow and given free access to water, and were allowed to acclimate for one week. All animals received humane care in compliance with the *Guide for the Care and Use of Laboratory Animals* published by the National Institutes of Health. The study protocol was approved by the Laboratory Animal Ethics Committee of the Affiliated Hospital of the Logistical College of the Chinese People's Armed Police Forces.

2.4. In Vitro Imaging. To assess the luciferase expression of the transduced BMSCs, different numbers of Luc-GFP-BMSCs (0.1, 0.2, 0.3, 0.4, and 0.5×10^4 /well) were seeded into a 96-well plate in 100 μL of growth medium, and D-luciferin solution (D-luciferin, 150 $\mu\text{g/mL}$, Gold Biotechnology, Inc., USA) was added at room temperature. After 10 min of incubation, the cells were imaged using an *in vivo* imaging system (IVIS) (PerkinElmer, IVISSPE, USA). The bioluminescent signals were analyzed using Living Image Software 4.5.

2.5. In Vivo Imaging of Luc-GFP-BMSCs. Luc-GFP-BMSCs (2×10^6) suspended in 1 mL of phosphate-buffered saline (PBS) were injected into the tail vein of rats, and this group was labeled the Luc-GFP-BMSC transplantation group (Luc-GFP-BMSCs group, $n = 5$). Phosphate-buffered saline alone was used as a control. For the *in vivo* imaging of aim cells, rats were anesthetized with 2% pentobarbital sodium (50 mg/kg) and injected intraperitoneally with D-luciferin (150 mg/kg body weight) 10 min before imaging. Then, the animals were placed in the imaging chamber. *In vivo* BLI was performed at 1.5, 2.5, 18, and 22 h and 1, 2, 3, 7, 10, 14, and 30 days after Luc-GFP-BMSC injection. Regions of interest (ROIs) were drawn manually using Living Image 4.5 Software (Caliper Life Sciences) to evaluate the relative signal intensity emitted. The photon radiance of the experimental animals was expressed as photons per second per centimeter squared

per steradian within the ROIs. The animals were imaged over a period of one month, after which they were sacrificed, and their tissues were harvested for PCR and IHC analyses.

To locate cell homing visually, four days after injection, immediately after acquiring photographic images *in vivo*, five animals were sacrificed. The skin of the back, the vertebral column, and other organs were removed and placed in Petri dishes. BLI of the tissues was carried to identify the Luc-GFP-BMSCs. Then, tissues showing BLI signals were fixed in 4% paraformaldehyde for further IHC analysis.

2.6. Immunohistochemistry. To verify the histological distribution of Luc-GFP-BMSCs after transplantation, tissues fixed in 4% paraformaldehyde were dehydrated and embedded in paraffin. Paraffin-embedded sections of 5 μm were prepared on poly-L-lysine-coated slides according to standard protocols. The slides were incubated with an anti-GFP antibody (Abcam, London, England) diluted 1:50 in PBS overnight at 4°C. For primary antibody detection, a mouse immunohistochemistry (ABC) kit (ZSGB-BIO, Beijing, China) was used. The sections were stained with a DAB kit. Counterstaining was performed with hematoxylin. GFP-positive cells were then counted under a light microscope in six high-power fields in three sections and scored based on whether they were tissue associated.

Furthermore, we detected GFP-positive cells in tissues via IHC to verify the advanced histological distribution of Luc-GFP-BMSCs at one day after transplantation.

2.7. RT-PCR. Total RNA for PCR was extracted with an RNeasy kit (Solarbio Science & Technology, Beijing, China), including a DNase digestion step to exclude contaminating DNA. Reverse transcription was performed using a Quant Script kit (TIANGEN BIOTECH, Beijing, China) for 1 h at 37°C. The primer sequences for the target gene were as follows: firefly luciferase-F: ACTGGGACGAAGACGAACAC and firefly luciferase-R: GGCGACGTAATCCACGATCT. PCR was carried out for the relative quantification of target gene copy numbers in relation to the β -actin transcript.

2.8. Blood Sampling. To examine the systemic response to wild-type BMSC transplantation, blood was collected from the inferior vena cava of anaesthetized rats at one day (1-day group; $n = 6$), four days (4-day group; $n = 6$), or one month (1-month group; $n = 6$) after the transplantation of wild-type BMSCs. The control group, which was injected only with PBS (control group; $n = 6$), was examined as well. The serum concentrations of blood urea nitrogen (BUN), creatinine (Cr), aspartate transaminase (AST), and alanine transaminase (ALT) were determined using automatic dry chemical analysis methods (VITROS 5600 Integrated System, Johnson, America). Routine blood test measurements were conducted with an automatic hematology analyzer (SYSMEX XN-1000, Japan).

2.9. Histopathology Evaluation. Tissue samples collected from the 1-day, 4-day, and 1-month groups were fixed in 10% formalin and subsequently embedded in paraffin following standard methods. Sections with a thickness of 5 μm were cut

and mounted on glass slides and then deparaffinized. Finally, the slides were stained with hematoxylin and eosin (H&E). The slides were relabeled using Arabic numbers, followed by double-blinded examination by two pathologists.

2.10. Statistical Analysis. All of the presented data are expressed as the mean \pm standard deviation (SD). Statistical analyses were performed using SPSS version 22.0. Differences between different groups were examined using Student's *t*-test or analysis of variance. *P* values < 0.05 were considered significant.

3. Results

3.1. Transduction of BMSCs. BMSCs were incubated in six-well plates at 1×10^5 cells/well for 24 h, following infection with 4×10^5 Lenti-Luc-GFP-lentivirus particles (MOI = 4). After 3 days of incubation, the transduction efficiency was approximately 76.45%, as evaluated under a fluorescence microscope (Figure 1(a)). There was no difference between the transduced BMSCs and wild-type BMSCs in terms of morphology. The expression of GFP was stable for at least 60 days under constant culture conditions.

3.2. In Vitro Characterization of the Pluripotential Capacity. To confirm the multilineage differentiation capacity of the Luc-GFP-BMSCs, the ability of Luc-GFP-BMSCs to differentiate into cells showing adipogenic and osteopenia patterns was investigated. Luc-GFP-BMSCs at passage 6 could differentiate into both adipocytes, as demonstrated by Oil Red O staining (Figure 1(b)), and osteoblasts, as assessed via Alizarin red staining (Figure 1(c)). Moreover, the differentiated cells still stably express GFP (Figures 1(b) and 1(c)).

3.3. In Vitro Imaging. The activity of luciferase was assessed through bioluminescence imaging (BLI) (Figure 1(d)). As shown in Figure 1(e), the imaging of different numbers of cells *in vitro* revealed a linear correlation between the BLI signal and cell numbers ($R^2 = 0.9918$), indicating that the reporter gene could be used for tracking and quantifying the transplanted BMSCs in small living animals.

3.4. Dynamic Distribution of BMSCs Monitored with an IVIS after Systemic Administration in Normal Rats. Next, we infused Luc-GFP-BMSCs into normal Wistar rats via tail vein injection and then dynamically monitored the bioluminescence imaging of luciferase activity with an IVIS in the following month. As shown in Figure 2, the BLI image results revealed that BMSCs delivered to fully immunocompetent allogeneic hosts predominantly resided in the lungs and lower back areas (Figures 2(a) and 2(c)). The BLI signals in the lung decreased over time and were absent at three days after injection *in vivo*. By imaging in both supine and prone positions, we found that the BMSCs migrated to the lower back after tail vein injection. There were two peaks of BLI signals observed in the lower back, at 24 h and seven days after vein injection. The imaging signals decreased over time and were completely absent 14 days after transplantation (Figures

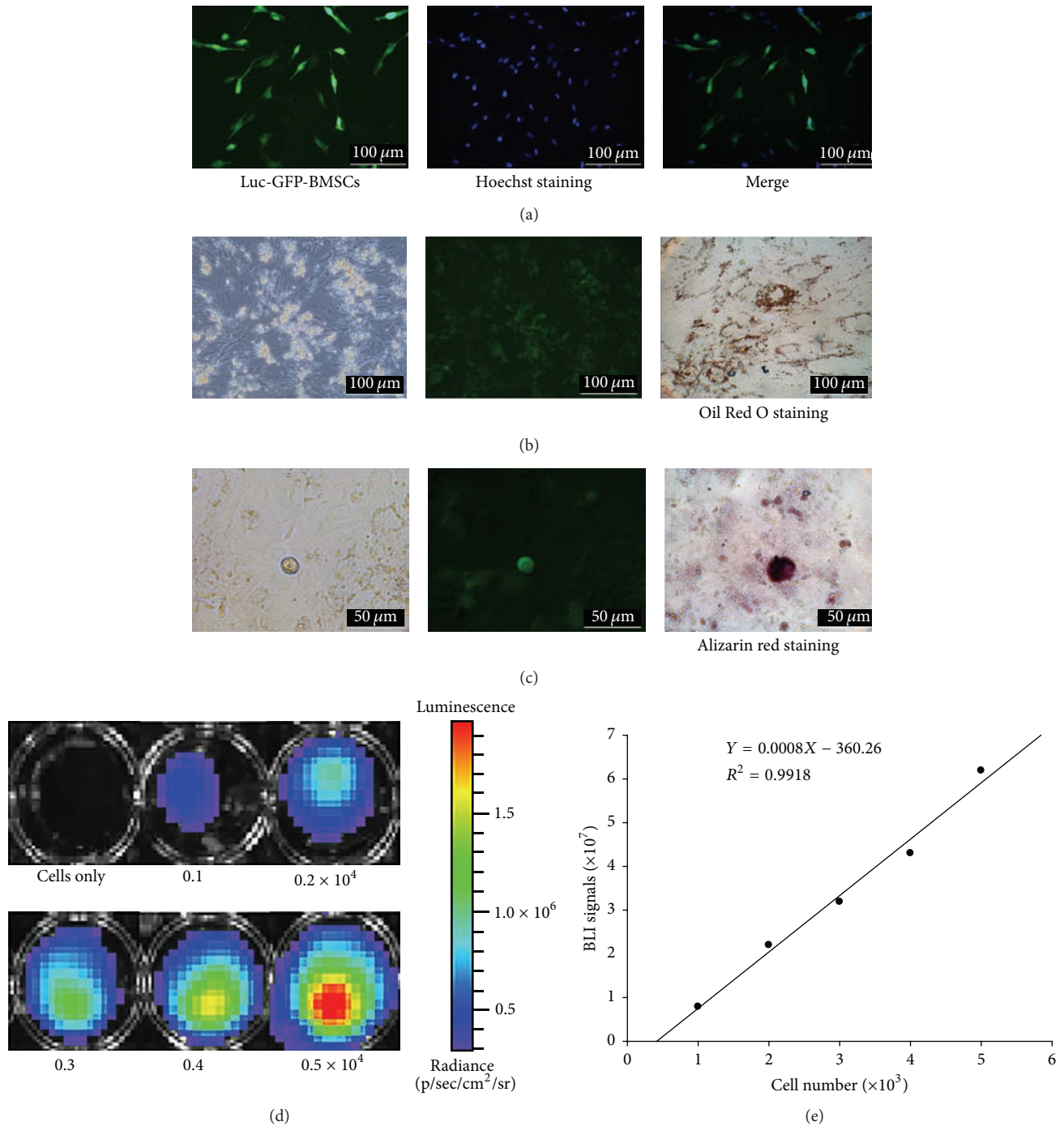


FIGURE 1: Characterization of rats treated with Luc-GFP-BMSCs. (a) GFP expression in Luc-GFP-BMSCs. The transduction efficiency was estimated by comparing the number of GFP-positive cells with the total cells via Hoechst staining. (b and c) The capability of Luc-GFP-BMSCs to differentiate according to an adipocyte or osteopenia pattern was verified by staining with Oil Red O and Alizarin red, respectively. After adipocyte and osteopenia differentiation, the cells still express GFP. (d) BLI of varying numbers of Luc-GFP-BMSCs *in vitro*. Representative images of at least three independent experiments. (e) Quantitative analysis revealed a strong linear relationship between cell numbers and the BLI signal ($R^2 = 0.9918$).

2(b) and 2(d)). One month later, we still failed to find any signals in the animals.

3.5. Histological Distributions of the Transplanted BMSCs. To evaluate the distribution of Luc-GFP-BMSCs in different

organs after injection, we injected the rats with D-luciferase intraperitoneally and isolated various rat organs, including the lungs, kidneys, heart, intestines, liver, skin of the lower back, spine, and spleen at four days after vein injection of Luc-GFP-BMSCs. The BLI signals were assessed in these organs,

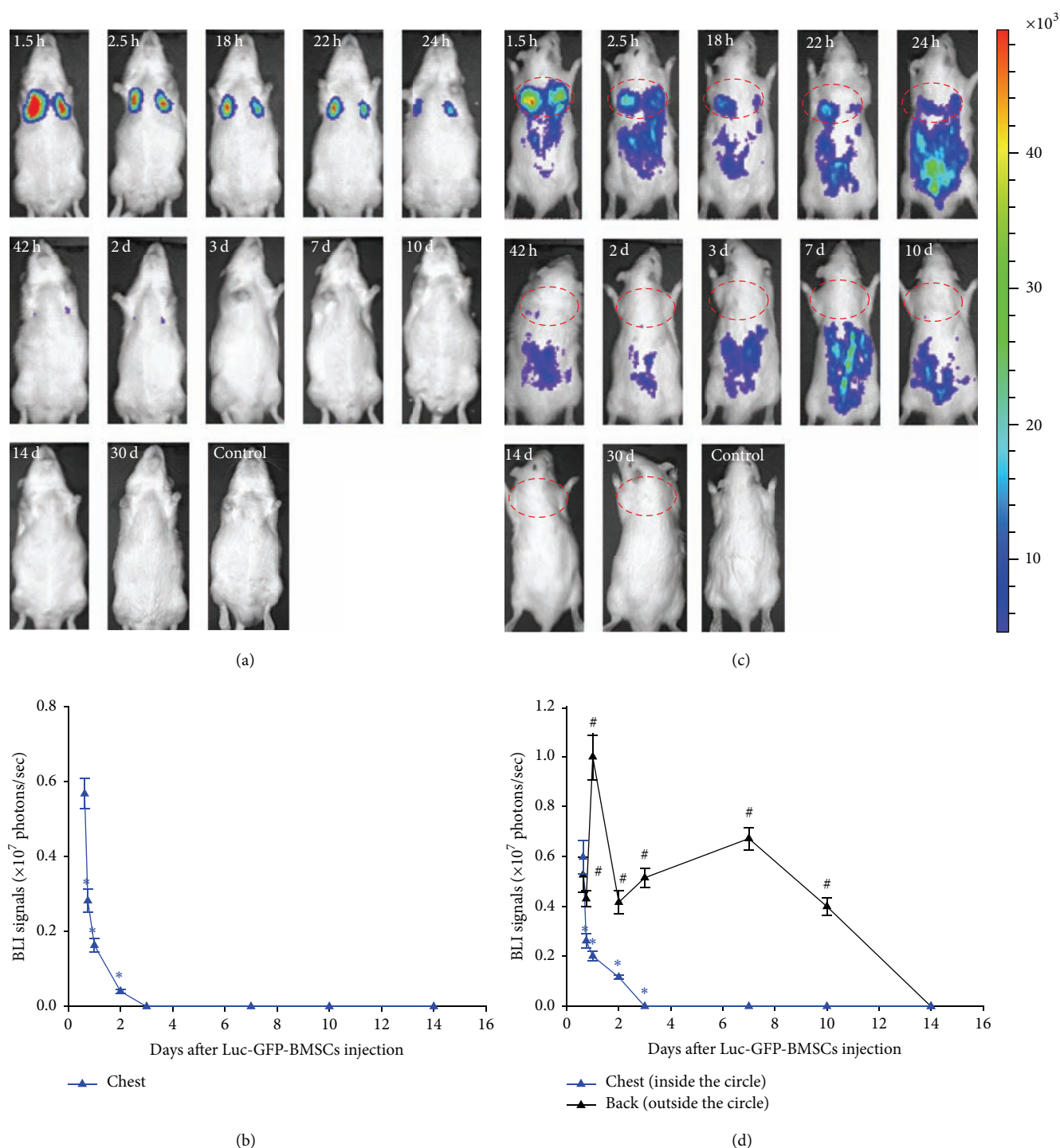


FIGURE 2: BLI of the transplanted Luc-GFP-BMSCs *in vivo*. (a and c) Luc-GFP-BMSCs suspended in PBS were injected into normal rats, while PBS alone was injected as a control. Cells were imaged at different time points, showing initial detention in the lungs and gradual concentration in the back, demonstrating that BMSCs may possess a tissue-specific binding capacity for some organs. However, the signals disappeared at day 14, revealing the final loss of transplanted BMSCs in normal rats. (b and d) Quantitative analysis of BLI signals in the chest and back. Bioluminescence activity steadily decreased over time in the chest. However, in the back, significant enhancement occurred at one and seven days after injection. * $P < 0.05$ versus BLI signals in the chest at 1.5 h ($n = 5$); # $P < 0.05$ versus BLI signals in the back at 1.5 h ($n = 5$).



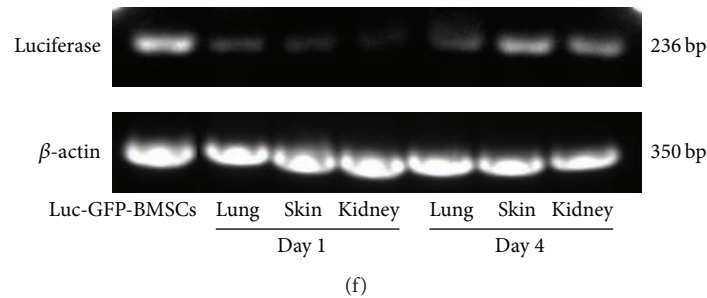


FIGURE 3: Distribution of the transplanted Luc-GFP-BMSCs within different organs. (a) BLI signals were diffusely distributed on the back *in vivo* at 4 days after injection. (b) IVIS photographs of dissected lungs (1), hearts (2), spleens (3), vertebral columns (4), intestines (5), livers (6), kidneys (7), and the skin of the lower back (8), showing direct confirmation of bioluminescence activity; Luc-GFP-BMSCs were localized to the kidneys, lungs, and the skin of the lower back ($n = 5$). (c) Immunohistochemically stained kidneys, lungs, and skin collected at 1 day as well as 4 days after injection. The specific position and positive cell counts were determined. (d and e) Positively stained cells in the lungs, kidneys, and skin were counted, and the migration of BMSCs appeared to be tissue associated over time. $n = 5$, and * presents $P < 0.01$. (f) The expression of the firefly luciferase gene was detected via RT-PCR. β -actin was used as a loading control. Target gene expression was found in the lungs, kidneys, and skin of animals at 1 day as well as 4 days after injection. Representative images of at least three independent experiments.

and the results showed that positive signals were detectable in the lungs, kidneys, and skin of the backs of normal rats (Figures 3(a) and 3(b)).

Furthermore, we detected GFP-positive cells in organs exhibiting BLI signals via immunohistochemistry to verify the advanced histological distribution of Luc-GFP-BMSCs. IHC was performed on the lung, kidney, and dorsal skin tissues. At one day after transplantation of Luc-GFP-BMSCs, GFP-positive cells were found in the conjunctive area between the blood vessels and alveoli. Although there were still BLI signals detected in isolated lungs at four days after injection, the IHC results showed that the positive cells were mainly located in the connective tissue and adipose tissue of the hilus pulmonis, but not the lungs (Figure 3(c)). Similarly, BMSCs were located in the connective tissue and adipose tissue of the renal hilum, but not the renal parenchyma. In the skin tissue, GFP-positive cells mainly appeared in the subepidermal connective tissue as well as the adipose tissue (Figure 3(c)). Consistent with the BLI results, the greatest number of GFP-positive cells was found in the lungs at one day after injection (Figure 3(d)), and four days later, the number of GFP-positive cells in the dorsal skin was greater than in other organs (Figure 3(e)). RT-PCR results also verified the presence of Luc-GFP-BMSCs in the above organ tissues: lung, kidney, and skin (Figure 3(f)). Furthermore, consistent with *in vivo* imaging result, BMSC colonization of specific organs was not found by RT-PCR and IHC detection (Figures 4(a) and 4(b)).

3.6. Safety Evaluation. No death occurred in the experimental groups, and clinical signs of dyspnea did not appear throughout the experiment. The morphometric analyses failed to detect any tumors or neoplasms in all animals. HE staining demonstrated that there was no dysplasia in MSC homing organs in the 1-day, 4-day, and 1-month groups (Figure 5). Moreover, as shown in Table 1, there was no significant difference in the biological markers of the kidney and liver ($P > 0.05$) between the experimental groups and the

control. Routine blood tests verified a reduction in the white cell count, especially for neutrophils ($P < 0.05$), resulting in a relative increase in the percentage of lymphocytes ($P < 0.05$) in the 4-day group compared with the control. However, one month later, the neutrophil count had returned to normal and was not significantly different than in the control (Table 2).

4. Discussion

Cell therapies are currently expected to provide cures for a wide variety of diseases as short effective routine therapies in clinical settings [17]. In clinical practice, in terms of the immune reaction, the perfect donor cells would be autologous [13]. However, autologous cells have obvious shortcomings. For example, in patients with diseases of the blood or immune system, their own cells are unsuitable for application. Due to showing low expression of immune antigens, allogeneic MSCs are an attractive cell resource for various complicated and refractory diseases [18]. The present study employed allogeneic cells, and we choose intravenous injection as the transplantation route to closely imitate clinical settings, as this route is commonly used in humans.

There is controversy about the homing feature of systemically administered BMSCs. The fate of BMSCs in living animals is related to many factors, such as their origins, the number of cells, and delivery routes. Tracking studies have demonstrated that transplanted human or allergenic BMSCs initially reside in the lungs and then egress to the liver and spleen in SCID mice [19, 20]. Eggenhofer et al. found that allergenic mouse BMSCs did not migrate beyond the lungs after intravenous infusion [21]. The differences in the distribution of BMSCs among these studies might be related to the origins of the cells, the host animal type, and the applied detection methods. Unlike the above studies, we injected allergenic BMSCs into normal rats (a larger animal subject). Our results showed that the majority of BMSCs localized to the lungs, kidneys, and loose connective tissue under the

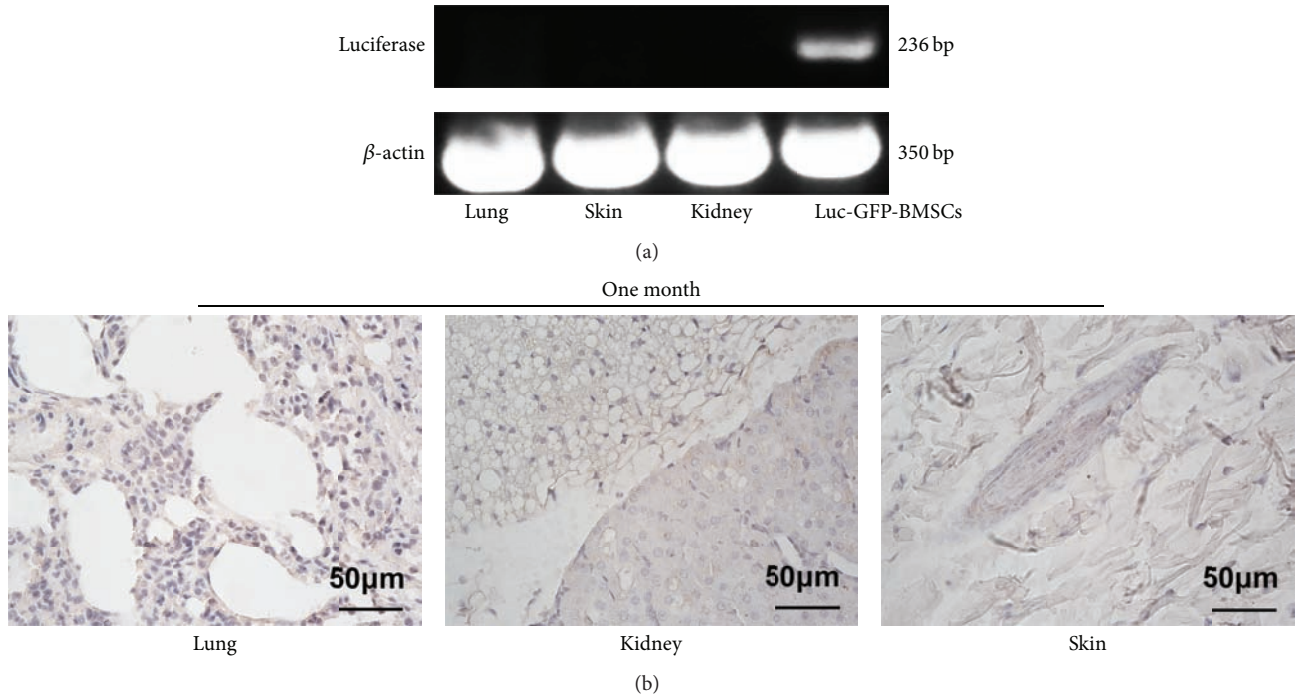


FIGURE 4: Detection of Luc-GFP-BMSCs in tissues at one month after injection. (a) The expression of the firefly luciferase gene was detected via RT-PCR. β -actin was used as a loading control. Target gene expression was not found in the lungs, kidneys, or skin. $n = 5$. Representative images of at least three independent experiments. (b) Immunohistochemistry detection of GFP. The absence of GFP-positive cells verified the BLI results at one month after injection ($n = 5$).

TABLE 1: Changes in the routine blood tests of the four study groups.

	Control	1-day	4-day	1-month
WBC ($\times 10^9/L$)	10.19 ± 3.42	6.95 ± 1.13	8.12 ± 1.81	7.49 ± 1.82
RBC ($\times 10^{12}/L$)	7.10 ± 0.85	6.57 ± 0.37	6.77 ± 0.20	7.43 ± 0.25
PLT ($\times 10^9/L$)	1020.50 ± 165.04	942 ± 133.95	1049.00 ± 83.606	936.17 ± 123.89
LYMPH ($\times 10^9/L$)	7.68 ± 2.40	5.55 ± 0.89	6.96 ± 1.51	5.80 ± 1.67
NEUT ($\times 10^9/L$)	2.02 ± 0.96	1.20 ± 0.28	$0.97 \pm 0.27^*$	1.39 ± 0.25
LYMPH%	76.18 ± 5.20	79.98 ± 2.04	$85.80 \pm 2.50^*$	76.87 ± 4.51

Control: animals injected with PBS only; 1-day: animals examined 1 day after transplantation of BMSCs (2×10^6); 4-day: animals examined 4 days after transplantation of BMSCs (2×10^6); 1-month: animals examined 1 month after transplantation of BMSCs (2×10^6).

Results are shown as the mean \pm SD ($n = 6$).

* $P < 0.05$ versus control.

epithelia of the back after tail vein injection. In accordance with previous studies, a large number of IV-injected BMSCs were trapped within the first filtering organ rich in capillaries because the mean size of the suspended BMSCs is larger than that of capillaries [22]. In this work, we found that the BMSCs were inclined to undergo passive clustering after systemic infusion in the lungs and kidneys, but homing to the epithelia of the back may be an active phenomenon. BMSCs are not circulating cells, which must attach to the extracellular matrix for survival and growth. Accordingly, when such cells are disaffiliated from this context, they may be tracked using certain extracellular matrix-derived signals for survival. Regarding their secondary distribution, BMSCs mainly concentrate in loose connective tissue and adipose tissue under the epithelia. Even in the lungs and kidneys,

they did not appear in the parenchyma, but in the connective tissue and adipose tissue of the hilus pulmonis and renal hilum at 4 days after injection.

By view from both supine and prone position, we firstly found that the dorsal skin is another organ attracting MSCs. IHC test showed that Luc-GFP-BMSCs locate in the loose connective tissue of the dorsal skin. Considering that BMSCs can easily differentiate into adipocytes *in vitro*, we hypothesize that the administered BMSCs are drawn by signals from the extracellular matrix of adipocytes and that the loose connective tissue is convenient for BMSCs to move through and proliferate. Different from the muscular tissue (heart and skeletal muscle), loose connective tissues have more space which may be suitable for the residing of MSCs. Moreover, dermal fibroblast secretes stromal cell-derived factor-1,

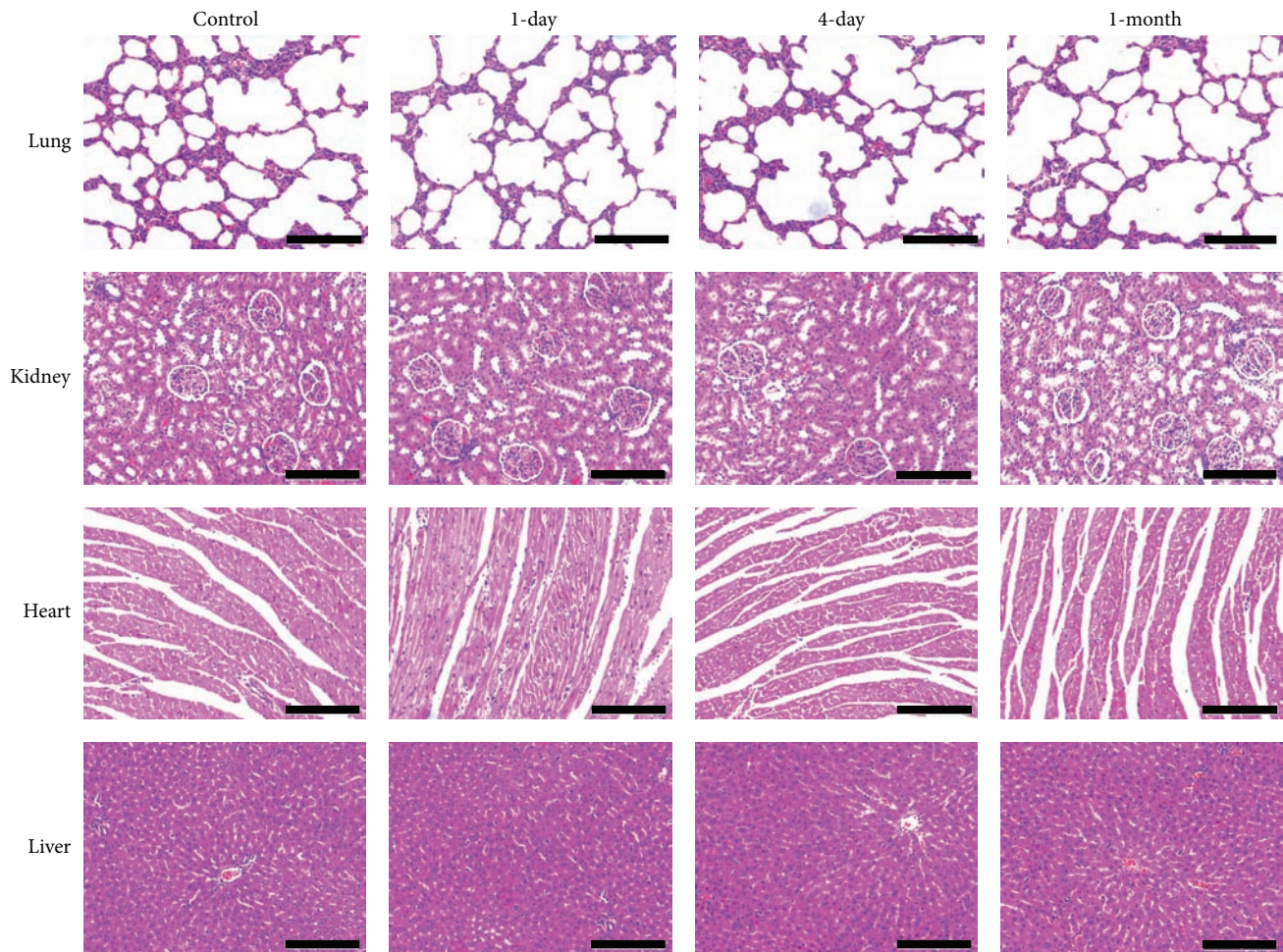


FIGURE 5: Light photomicrographs of tissue sections (HE). Compared with the control, there were no pathologic changes in the experimental groups. $n = 6$; scale bar = $100\ \mu\text{m}$.

TABLE 2: Serum AST, ALT, Cr, and BUN levels in the four study groups.

	Control	1-day	4-day	1-month
AST (U/L)	106.5 ± 22.28	124.60 ± 10.69	105.67 ± 18.46	99.17 ± 19.19
ALT (U/L)	34.00 ± 8.60	38.60 ± 5.18	34.50 ± 3.62	31.17 ± 4.12
Cr ($\mu\text{mol/L}$)	30.67 ± 6.02	27.21 ± 3.56	29.67 ± 2.52	31.00 ± 2.37
BUN (mmol/L)	5.55 ± 0.49	4.76 ± 1.08	5.43 ± 0.70	5.38 ± 0.89

Control: animals injected with PBS only; 1-day: animals examined 1 day after transplantation of BMSCs (2×10^6); 4-day: animals examined 4 days after transplantation of BMSCs (2×10^6); 1-month: animals examined 1 month after transplantation of BMSCs (2×10^6).

Results are shown as the mean \pm SD ($n = 6$).

a key chemokine which recruits circulating MSCs through the SDF-1 α /CXCR4 pathway [23, 24]. As to the reason of BMSCs' selective recruitment to dorsal skin, we cannot give an exact explanation, which may need further research to answer this phenomenon in our following studies.

Previously, it was believed that MSCs repair damaged tissues through a transdifferentiation mechanism [25], and targeted delivery routes of the cells to injured organs would therefore be essential for effective therapy. These cells are also typically regarded as one of the notable landmarks in the progress of all forms of cell

therapies. To cause greater numbers of MSCs to concentrate in injured tissues, researchers have attempted diverse injection strategies, leading to the detainment of MSCs in other target filtering organs. However, persistent engraftment and differentiation of implanted MSCs *in vivo* have rarely been detected. Many investigators have found that transplanted MSCs show short survival *in vivo*, and they exert a considerable influence on diseases that do not depend on the number of cells homing to the targeted organ [26, 27]. The life of transplanted MSCs *in vivo* is too short to explain the significant functional improvement

of infarcted organs by differentiation. Thus, the routes for MSC administration do not appear to be as important in clinical applications. Thus, intravenous administration may be sufficient.

Our data from follow-up studies of transplanted BMSC survival using BLI demonstrated that BMSCs cannot survive for a long period. These results are similar to those of previous studies. There are three possible explanations for the observed localization of the administered BMSCs. (1) Mesenchymal cell adhesion to the extracellular matrix generates tensional integrity, which is a physiological cellular process that is necessary for cell differentiation, survival, and growth. In contrast, after administration and suspension in blood, MSCs lose their cell/matrix interactions, which will induce programmed death. This type of apoptosis is known as anoikis [28]. We believe that anoikis likely plays an important role in the disappearance of MSCs in this context because MSCs are not circulating cells and require extracellular matrix-derived signals for survival, and the deprivation of these signals in the vasculature might induce anoikis. (2) In the present study, we employed immunocompetent rats without the application of immunosuppressive agents during the whole experiment. The innate immune system, which is responsible for the removal of transplanted cells, may be activated by allogeneic MSCs. Some researchers believed that MSCs would not induce an immune response by themselves, but fetal bovine serum (FBS), which is widely used in cell culture and cannot be removed using phosphate-buffered saline, stimulates immunogenicity [29]. In a clinical setting, to avoid such risks, the adoption of autologous serum should be considered, as it has been found that autologous human serum results in more rapid expansion of MSCs [30]. (3) The kidney is a metabolic organ with abundant blood flow. It is known that the excretion of many drugs is closely related to renal function. Our data showed that BMSCs migrated to the kidneys and then disappeared from this organ. Another study [31] provided direct evidence that 1% of BMSCs that were present in the glomerular and peritubular capillaries were TUNEL positive. Together, these findings suggest that this process may contribute to the declining number of BMSCs after administration. Continued attrition of the very small number of cells eventually results in the disappearance of all cells. However, in this work, instead of the glomerular capillaries, we discovered BMSCs in the loose connective tissue around the peritubular capillaries. It is unknown if such a situation occurs occasionally or is related to different sampling times. Perhaps the kidney represents a secondary route of metabolism, but not the major one. Thus, larger, randomized, placebo-controlled preclinical animal trials need to be carried out to address the question of where MSCs are going.

The present study also investigated the short- and middle-term safety of allogeneic BMSC transplantation. Unlike pharmaceutical drugs, we are unable to produce MSCs in complete compliance with the relevant regulations in the laboratory [32]. However, we made all possible attempts to avoid potential adverse events after BMSC transplantation, such as bacteriological contamination, using a cell incubation period of less than 60 days and not exceeding 10 passages

in culture. The experimental groups were followed up after one day, four days, and one month, and all animals exhibited an absence of tumorigenesis and injured tissues. Histological analysis of the experimental groups showed that all animals did not display any hyperplasia or tissue inflammation. There was no significant difference between the experimental groups and the control in terms of biological markers of the kidney and liver. Although infused MSCs were found to cause a reduction in neutrophils count at 4 days after injection, the sample sizes are too small to reach a definitive conclusion about whether allogeneic BMSC transplantation causes the white cell count to decrease. However, we think that care should be taken because of the observed phenomenon, and statistical analyses of large samples of blood cell count data associated with MSC-based therapies will be needed for future evaluations of long-term safety.

In summary, our results demonstrate that systemically administered BMSCs in healthy rats are short-lived and mainly migrate to the lungs, kidneys, and the skin of the lower back. Interestingly, in histological analysis, the BMSCs show lipophilicity. They collect in the adipose tissue, and a small number are located in the loose connective tissue around the blood vessels of the hilus pulmonis and renal hilum. The reasons for this distribution pattern are not fully understood. Safety assessment failed to detect any adverse effects in the animals over a short period. Thus, BMSCs may be an ideal candidate for cell-based therapy in preclinical animal studies and, subsequently, for clinical trials, but long-term follow-up safety assessments are needed.

Competing Interests

The authors declare that they have no competing interests.

Acknowledgments

This research was supported by the National Natural Science Foundation of China (81202105, 71533008) and the Tianjin Science and Technology Project (14ZCDZSY00033, 15JCY-BJC28500, and 13JCQNJC12900-2013).

References

- [1] B. J. Jones and S. J. McTaggart, "Immunosuppression by mesenchymal stromal cells: from culture to clinic," *Experimental Hematology*, vol. 36, no. 6, pp. 733–741, 2008.
- [2] M. R. Reagan and D. L. Kaplan, "Concise review: mesenchymal stem cell tumor-homing: detection methods in disease model systems," *Stem Cells*, vol. 29, no. 6, pp. 920–927, 2011.
- [3] I. B. Resnick, C. Barkats, M. Y. Shapira et al., "Treatment of severe steroid resistant acute GVHD with mesenchymal stromal cells (MSC)," *American Journal of Blood Research*, vol. 3, no. 3, pp. 225–238, 2013.
- [4] M. Introna, G. Lucchini, E. Dander et al., "Treatment of graft versus host disease with mesenchymal stromal cells: a phase I study on 40 adult and pediatric patients," *Biology of Blood and Marrow Transplantation*, vol. 20, no. 3, pp. 375–381, 2014.
- [5] J. Bartunek, A. Behfar, D. Dolatabadi et al., "Cardioprotective stem cell therapy in heart failure: the C-CURE (Cardioprotective stem Cell therapy in heart failURE) multicenter randomized

- trial with lineage-specified biologics,” *Journal of the American College of Cardiology*, vol. 61, no. 23, pp. 2329–2338, 2013.
- [6] S. Karamouzian, S. N. Nematollahi-Mahani, N. Nakhaee, and H. Eskandary, “Clinical safety and primary efficacy of bone marrow mesenchymal cell transplantation in subacute spinal cord injured patients,” *Clinical Neurology and Neurosurgery*, vol. 114, no. 7, pp. 935–939, 2012.
 - [7] S. Forostyak, P. Jendelova, and E. Sykova, “The role of mesenchymal stromal cells in spinal cord injury, regenerative medicine and possible clinical applications,” *Biochimie*, vol. 95, no. 12, pp. 2257–2270, 2013.
 - [8] M.-E. M. Amer, S. Z. El-Sayed, W. A. El-Kheir et al., “Clinical and laboratory evaluation of patients with end-stage liver cell failure injected with bone marrow-derived hepatocyte-like cells,” *European Journal of Gastroenterology and Hepatology*, vol. 23, no. 10, pp. 936–941, 2011.
 - [9] A. Skrahin, R. K. Ahmed, G. Ferrara et al., “Autologous mesenchymal stromal cell infusion as adjunct treatment in patients with multidrug and extensively drug-resistant tuberculosis: an open-label phase 1 safety trial,” *The Lancet Respiratory Medicine*, vol. 2, no. 2, pp. 108–122, 2014.
 - [10] J. G. Wilson, K. D. Liu, H. Zhuo et al., “Mesenchymal stem (stromal) cells for treatment of ARDS: a phase 1 clinical trial,” *The Lancet Respiratory Medicine*, vol. 3, no. 1, pp. 24–32, 2015.
 - [11] J. R. D. Wet, K. V. Wood, D. R. Helinski, and M. DeLuca, “Cloning of firefly luciferase cDNA and the expression of active luciferase in *Escherichia coli*,” *Proceedings of the National Academy of Sciences of the United States of America*, vol. 82, no. 23, pp. 7870–7873, 1985.
 - [12] K.-S. Jang, K.-S. Lee, S.-H. Yang, and S.-S. Jeun, “In vivo tracking of transplanted bone marrow-derived mesenchymal stem cells in a murine model of stroke by bioluminescence imaging,” *Journal of Korean Neurosurgical Society*, vol. 48, no. 5, pp. 391–398, 2010.
 - [13] C. Xia and J. Cao, “Imaging the survival and utility of pre-differentiated allogeneic MSC in ischemic heart,” *Biochemical and Biophysical Research Communications*, vol. 438, no. 2, pp. 382–387, 2013.
 - [14] W. Zhuo, L. Liao, Y. Fu et al., “Efficiency of endovenous versus arterial administration of mesenchymal stem cells for ischemia-reperfusion-induced renal dysfunction in rats,” *Transplantation Proceedings*, vol. 45, no. 2, pp. 503–510, 2013.
 - [15] M. E. Aanstoots, D. P. Regan, R. J. Rose, L. S. Chubb, and N. P. Ehrhart, “Do mesenchymal stromal cells influence microscopic residual or metastatic osteosarcoma in a murine model?” *Clinical Orthopaedics and Related Research*, vol. 474, no. 3, pp. 707–715, 2016.
 - [16] M. Dominici, K. Le Blanc, I. Mueller et al., “Minimal criteria for defining multipotent mesenchymal stromal cells. The International Society for Cellular Therapy position statement,” *Cytotherapy*, vol. 8, no. 4, pp. 315–317, 2006.
 - [17] A. Tyndall, “Mesenchymal stem cell treatments in rheumatology—a glass half full?” *Nature Reviews Rheumatology*, vol. 10, no. 2, pp. 117–124, 2014.
 - [18] F. Gao, S. M. Chiu, D. A. Motan et al., “Mesenchymal stem cells and immunomodulation: current status and future prospects,” *Cell Death and Disease*, vol. 7, no. 1, Article ID e2062, 2016.
 - [19] S. Kidd, E. Spaeth, J. L. Dembinski et al., “Direct evidence of mesenchymal stem cell tropism for tumor and wounding microenvironments using in vivo bioluminescent imaging,” *Stem Cells*, vol. 27, no. 10, pp. 2614–2623, 2009.
 - [20] S. M. Albarenque, R. M. Zwacka, and A. Mohr, “Both human and mouse mesenchymal stem cells promote breast cancer metastasis,” *Stem Cell Research*, vol. 7, no. 2, pp. 163–171, 2011.
 - [21] E. Eggenhofer, V. Benseler, A. Kroemer et al., “Mesenchymal stem cells are short-lived and do not migrate beyond the lungs after intravenous infusion,” *Frontiers in Immunology*, vol. 3, article 297, Article ID Article 297, 2012.
 - [22] S. Schrepfer, T. Deuse, H. Reichenspurner, M. P. Fischbein, R. C. Robbins, and M. P. Pelletier, “Stem cell transplantation: the lung barrier,” *Transplantation Proceedings*, vol. 39, no. 2, pp. 573–576, 2007.
 - [23] C. Quan, M. K. Cho, Y. Shao et al., “Dermal fibroblast expression of stromal cell-derived factor-1 (SDF-1) promotes epidermal keratinocyte proliferation in normal and diseased skin,” *Protein and Cell*, vol. 6, no. 12, pp. 890–903, 2015.
 - [24] S.-B. Zhou, J. Wang, C.-A. Chiang, L.-L. Sheng, and Q.-F. Li, “Mechanical stretch upregulates SDF-1 α in skin tissue and induces migration of circulating bone marrow-derived stem cells into the expanded skin,” *Stem Cells*, vol. 31, no. 12, pp. 2703–2713, 2013.
 - [25] M. F. Pittenger and B. J. Martin, “Mesenchymal stem cells and their potential as cardiac therapeutics,” *Circulation Research*, vol. 95, no. 1, pp. 9–20, 2004.
 - [26] A. F. Wise, T. M. Williams, M. B. G. Kiewiet et al., “Human mesenchymal stem cells alter macrophage phenotype and promote regeneration via homing to the kidney following ischemia-reperfusion injury,” *American Journal of Physiology—Renal Physiology*, vol. 306, no. 10, pp. F1222–F1235, 2014.
 - [27] Y. Yao, J. Huang, Y. Geng et al., “Paracrine action of mesenchymal stem cells revealed by single cell gene profiling in infarcted murine hearts,” *PLoS ONE*, vol. 10, no. 6, Article ID e0129164, 2015.
 - [28] J.-B. Michel, “Anoikis in the cardiovascular system: known and unknown extracellular mediators,” *Arteriosclerosis, Thrombosis, and Vascular Biology*, vol. 23, no. 12, pp. 2146–2154, 2003.
 - [29] J. L. Spees, C. A. Gregory, H. Singh et al., “Internalized antigens must be removed to prepare hypoimmunogenic mesenchymal stem cells for cell and gene therapy,” *Molecular Therapy*, vol. 9, no. 5, pp. 747–756, 2004.
 - [30] O. Honmou, K. Houkin, T. Matsunaga et al., “Intravenous administration of auto serum-expanded autologous mesenchymal stem cells in stroke,” *Brain*, vol. 134, no. 6, pp. 1790–1807, 2011.
 - [31] F. Tögel, Y. Yang, P. Zhang, Z. Hu, and C. Westenfelder, “Bioluminescence imaging to monitor the in vivo distribution of administered mesenchymal stem cells in acute kidney injury,” *American Journal of Physiology—Renal Physiology*, vol. 295, no. 1, pp. F315–F321, 2008.
 - [32] D. G. Halme and D. A. Kessler, “FDA regulation of stem-cell-based therapies,” *New England Journal of Medicine*, vol. 355, no. 16, pp. 1730–1735, 2006.